Orientational topology of layered systems and reinforcement learning in active matter

Inaugural-Dissertation

zur Erlangung des Doktorgrades
der Mathematisch-Naturwissenschaftlichen Fakultät
der Heinrich-Heine-Universität Düsseldorf

vorgelegt von

Paul Arne Monderkamp
aus Düsseldorf

Düsseldorf, April 2023

aus dem Institut für Theoretische Physik II: Weiche Materie
der Heinrich-Heine-Universität Düsseldorf

Gedruckt mit der Genehmigung der
Mathematisch-Naturwissenschaftlichen Fakultät der
Heinrich-Heine-Universität Düsseldorf

Referent: Prof. Dr. Hartmut Löwen

Korreferent: Prof. Dr. Jürgen Horbach

Tag der mündlichen Prüfung: 18. Juli, 2023

I came into physics for the meaning of life. I believe I know now, what is a rod.

Abstract

The largest fraction of research attention in this thesis is dedicated to the study of topological defects in the regular layered structure of colloidal smectic liquid crystals. Liquid crystals are materials which, due to characteristic particle shapes, display a plethora of interesting ordered phases, depending on, for instance, density. At intermediate densities, elongated particles tend to align, into so-called nematic ordering. Additionally, at high densities, they display a tendency to reside in layers, called a smectic phase. These ordered phases are accompanied by local disruptions in their ordered structure, so-called topological defects. In ch. 1, I introduce the necessary fundamentals to understand the topological concepts, applied in the corresponding publications in ch. 3. Furthermore, the Monte-Carlo simulation protocol is elaborated, which marks my main contribution to the scientific publications on smectic liquid crystal topology (**P1**, **P2**, **P3** and **P4**). Over the course of these scientific publications, we investigate how the concept of topological defect charges, known from nematic liquid crystals, generalises to the defects, which are inherent to smectics (**P1**,**P3**). We present how grain boundaries can be classified with these charges. We furthermore show that the rigidity of the smectic structure causes the formation of so-called tetratic defect pairs. These resemble points in two, and line defects in three dimensions. Even though, in three dimensions, topological charge is not strictly conserved, we find that it can result from the smectic rigidity (**P2**). Lastly, in this part on liquid crystals, we explore how graph-theoretical approaches can be used to interpret the structure of systems composed of chiral particles (**P4**).

This thesis contains a study of the application of reinforcement learning to an active swimmer. In our case, we equip single microswimmers in Brownian dynamics simulations with the means to intelligent steering via tabular Q-learning (**P5**). Details on the physical model as well as a simple, illustrative example for a problem, solved with tabular Q-learning algorithm, can be found in ch. 2. Our research provides a model for the understanding of autonomous decision-making in biological microorganisms, as well as for the design of intelligent microrobotic machines. The swimmer utilises his capabilities to learn to navigate through complicated, random environments. We find, that it not only outperforms suitable reference cases, but the strategy also generalises well to classes of environments, unknown until after the training.

The last scientific publication in this thesis comprises a study of the equilibrium statistics of carrier-cargo complexes (**P6**). These represent microscopic particles,

which possess the ability to engulf smaller cargo particles. This is relevant, for instance, for quantitative methods in medicine or the study of biological objects such as vesicles or phagocytes. The main findings of this work are obtained via density functional theory: the formation of carrier-cargo complexes can be tuned by carrier and cargo densities. Furthermore, the theory predicts structural properties of the mixture. The theoretical results are complimented by Monte-Carlo simulation. The Monte-Carlo simulation protocol, which I contribute to this work is the same, which is applied in the equilibration of liquid crystal phases, summarised in ch. 1.4. The theory itself is extensively discussed in the main text of the publication.

Kurzfassung

Der größte Teil der Forschung in dieser Arbeit ist der Studie topologischer Defekte in der geschichteten Struktur kolloidaler smektischer Flüssigkristalle gewidmet. Flüssigkristalle sind Materialien, welche durch die charakteristischen Formen der einzelnen Teilchen eine Fülle an interessanten geordneten Phasen aufweisen. Diese hängen mitunter von der Dichte ab. Bei mittleren Dichten haben längliche Teilchen die Eigenschaft sich vornehmlich parallel auszurichten. Dies definiert die sogenannte nematische Ordnung. Zusätzlich entsteht bei hohen Dichten eine geschichtete Struktur, die sogenannte smektische Phase. Diese geordneten Phasen werden häufig durch topologische Defekte lokal unterbrochen. In Kapitel 1 werden die notwendigsten Grundlagen vermittelt, welche in den jeweiligen Publikationen, welche in Kapitel 3 präsentiert werden, angewandt werden. Außerdem wird das generelle Monte-Carlo Simulationsprotokoll erläutert, mit welchem die Simulationsergebnisse generiert wurden, die ich zu den wissenschaftlichen Veröffentlichungen zur Topologie der smektischen Flüssigkristalle beigetragen habe. (**P1**, **P2**, **P3** und **P4**). Wir erforschen, wie sich das Konzept der topologischen Defektladungen, welches aus den nematischen Flüssigkristallen bekannt ist, auf topologische Defekte in Smektischen Flüssigkristallen verallgemeinern lässt (**P1**,**P3**). Außerdem demonstrieren wir, wie Grenzlinien (sogenannte grain boundaries) mit dem Konzept der topologischen Ladungen klassifiziert werden können. Es zeigt sich, dass die Festigkeit der smektischen Struktur die Bildung von sogenannten tetratischen Defektpaaren erzeugt. Diese haben in zwei Dimensionen die Form von Punktladungen und sind in drei Dimensionen linienförmig. Obwohl topologische Ladungen dieser Objekte in drei Dimensionen nicht gesetzmäßig streng erhalten sind, zeigen wir, dass Ladungserhaltung als Konsequenz der Festigkeit der smektischen Struktur folgen kann (**P2**). Zuletzt erforschen wir, in diesem Teil über Flüssigkristalle, wie Graphentheorie für das Verständnis komplizierter Strukturen chiraler Teilchen nutzbar ist (**P4**).

Diese Arbeit beinhaltet eine Studie zur Anwendung von Reinforcement Learning auf einen aktiven Schwimmer. In unserer Arbeit statten wir Mikroschwimmer in einer Simulation Brownscher Dynamik mit der Fähigkeit aus, intelligent zu steuern. Dies geschieht mit der Hilfe eines tabularen Q-Learning Algorithmus (**P5**). Details zu dem physikalischen Modell, sowie ein illustratives Beispiel für ein Q-Reinforcement Learning Problem, werden in Kapitel 2 präsentiert. Unsere Arbeit leistet sowohl einen Beitrag zum Verständnis autonomer Entscheidungsfindung in biologischen Mikroorganismen, als auch ein Modell zum Entwurf von intelligenten mikroskopischen Maschinen. Der Schwimmer nutzt seine Fähigkeiten, um durch

komplizierte zufällige Umgebungen zu navigieren. Wir stellen fest, dass er die Fähigkeit besitzt, besser zu navigieren als angemessene vergleichbare Schwimmer ohne Reinforcement Learning. Außerdem kann er seine Strategie erfolgreich auf Arten von Umgebungen anzuwenden, welche bis nach Ende des initialen Trainings unbekannt sind.

Der letzte wissenschaftliche Artikel in dieser Arbeit ist eine Studie der Equilibriumstatistik von Carrier-Cargo Komplexen. (**P6**). Diese repräsentieren mikroskopische Teilchen, welche die Fähigkeit besitzen kleinere Cargo-Teilchen aufzunehmen. Dies ist beispielsweise relevant für quantitative Methoden in der Medizin oder das Verständnis von Vesikeln oder Phagozyten. Die Hauptergebnisse dieser Arbeit stammen aus Dichtefunktionaltheorie: Die Entstehung von Carrier-Cargo Komplexen wird hauptsächlich durch die Dichten der Carrier und Cargos beeinflusst. Außerdem ist die Theorie in der Lage, strukturelle Eigenschaften der Mischung vorherzusagen. Diese Ergebnisse werden mit Monte-Carlo Simulationen verglichen. Diese folgt demselben Protokoll, welches auf die Simulation der Flüssigkristalle angewandt wird und in Kapitel 1.4 zusammengefasst wird. Die Theorie selber wird ausführlich im Haupttext der Veröffentlichung diskutiert.

Eidesstattliche Versicherung

Ich versichere an Eides Statt, dass die Dissertation von mir selbständig und ohne unzulässige fremde Hilfe unter Beachtung der „Grundsätze zur Sicherung guter wissenschaftlicher Praxis an der Heinrich-Heine-Universität Düsseldorf“ erstellt worden ist.

Düsseldorf, _____ _____

Preface

The content of this dissertation is based on articles that I co-authored, and that have been published in/ submitted to peer-reviewed scientific journals. These articles are reproduced in ch. 3 and are listed in the following (in topical order):

- **P1** P. A. Monderkamp* , R. Wittmann*, L. B. G. Cortes, D. G. A. L. Aarts, F. Smallenburg, and H. Löwen,
  Topology of Orientational Defects in Confined Smectic Liquid Crystals,
  Phys. Rev. Lett. **127**, 198001 (2021),
  * P. A. Monderkamp and R. Wittmann have equally contributed to the manuscript.

- **P2** P. A. Monderkamp, R. Wittmann, M. te Vrugt, A. Voigt, R. Wittkowski, and H. Löwen,
  Topological fine structure of smectic grain boundaries and tetratic disclination lines within three-dimensional smectic liquid crystals,
  Phys. Chem. Chem. Phys. **24**, 15691 (2022)

- **P3** R. Wittmann, P. A. Monderkamp, J. Xia, L. B. G. Cortes, I. Grobas, P. E. Farrell, D. G. A. L. Aarts and H. Löwen
  Smectic structures in button-like confinements: experiment and theory,
  arXiv:2303.01425 (2023),

- **P4** P. A. Monderkamp, R. S. Windisch, R. Wittmann and H. Löwen,
  Network topology of interlocked chiral particles,
  accepted for publication at J. Chem. Phys.,
  arXiv:2301.09541 (2023),

- **P5** P. A. Monderkamp, F. J. Schwarzendahl, M. A. Klatt and H. Löwen,
  Active particles using reinforcement learning to navigate in complex motility landscapes,
  MLST, 3, 045024 (2022),

- **P6** R. Wittmann, P. A. Monderkamp and H. Löwen
  Statistics of carrier-cargo complexes,
  arXiv:2303.04005 (2023),

Detailed author contributions to the scientific publications above are specified in ch. 3.

Acknowledgements

Foremost, I express my gratitude towards Prof. Dr. Hartmut Löwen, who most obviously enabled this thesis on multiple levels. He gave me this opportunity by providing my Bachelor-, Master- and doctorate positions. Most of what I know about theoretical physics and scientific work in general, I know from him. I remain happily indebted for this investment.

I thank Prof. Dr. Jürgen Horbach, for providing excellent mentorship throughout this doctorate. He would always have an open door and find time to share his extensive knowledge on specific computer simulation techniques, which has proven invaluable on many such occasions.

Towards Dr. René Wittmann I am grateful, above all, for his patience. If I had to make a list of quintessential factors for the success of our research projects, *Renés patience* would make it at least into the top five.

I thank my family, Kerstin, Uli, Hannah and Jürgen, for their ongoing love and support. Also without my friends, this would not have been possible. In particular, I would like to express my gratitude towards Lukas Fischer for being there, especially during the initial semesters of the bachelor. I could not have done it without you.

I also send gratitude towards all colleagues and collaborators. Especially Dr. Louis B. G. Cortes and Dr. Lorenzo Caprini for letting me use their unpublished data in the first chapter of this thesis.

Special thanks also to Claudia Stader and Joachim Wenk for Your untiring contributions to all my work!

I would like to thank You, Valeska for Your love and patience as well as emotional and intellectual support. I am truly fortunate to have You. Lastly, I thank Lasse for modelling for all the machine learning content and providing constant calm and serenity, especially during turbulent times.

Contents

List of Figures

Chapter 1

Liquid crystal topology

Four out of the six publications in this thesis are dedicated to the study of the topology of defects in liquid crystal phases (**P1**, **P2**, **P4**, **P3**). This chapter aims to introduce the reader into the prerequisite knowledge for understanding those articles. It elaborates mostly on the concepts, which are typically not explicitly contained in scientific publications, but are usually implied knowledge. Therefore, I hope, that the reader will be able to appreciate the publications in ch. 3 thoroughly.

Section 1.1 explains what liquid crystals are in the first place and why they are interesting and important. In Sec. 1.2, the concept of defects in their regular structure is explained from the ground up. Section 1.3 discusses a simple toy system of two rods on a lattice, to develop an intuition for the causes of nematic alignment. Lastly, Sec. 1.4 discusses the aspects of the simulation procedure, used throughout this thesis (the above articles, as well as **P6**).

1.1 What are liquid crystals?

Liquid crystals are a most curious class of materials. This umbrella term refers, in general, to a range of materials, which gain their remarkable and occasionally unexpected properties through the peculiarity of the constituting particles. These are the microscopic subunits, which take virtually arbitrary shapes across different types of liquid crystals. This causes properties, which can neither be exclusively associated with liquids, nor with crystals, but rather in between. The scientific world distinguishes most prominently between two classes: *(i)* thermotropic liquid crystals, composed of molecules with sizes around the nano-scale, where the characteristic shapes emerge from the architecture of the individual molecules and *(ii)* lyotropic liquid crystals, denoting macro-molecules on the micron-scale, dispersed in a fluid solvent. Nowadays, these macro-molecules are often synthesised colloids, where the geometry of the particles depends on the creativity and technical proficiency of the creator [1–4].

Anyone who has boiled spaghetti in a pot, has handled nails in a toolbox, or has looked upon cookies in a cookie jar, will testify, that the particular arrangement of the objects in question vastly depends on the respective particle geometry.

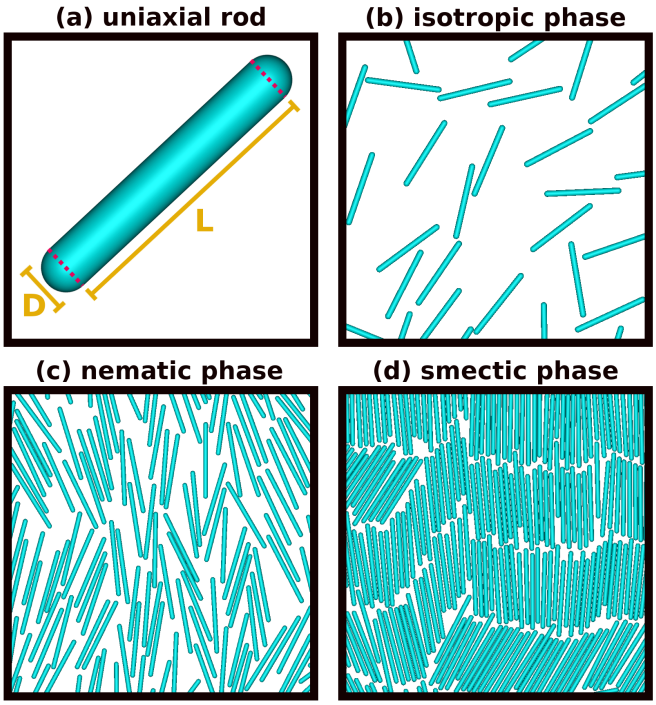

Figure 1.1: Schematic depiction of the liquid crystal particles, which are the focus of this thesis, and three excerpts of simulation snapshots of three typical bulk phases. **(a)**: Uniaxial rod, defined by a cylinder with length L and spherical caps with diameter D on each end. **(b)**: Isotropic phase, found at low packing fractions, characterised by uniform distribution of the rods across space, and isotropic distribution of the orientations. **(c)**: Nematic phase, found at intermediate packing fractions, where the particles tend to globally align, with uniform distribution of positions. **(d)**: Smectic phase at high densities. To occupy the volume most efficiently, the rods align and additionally stack in layers.

Spaghetti and nails can be efficiently packed by aligning them along their long axes, whereas flat cookies tend to stack perpendicular to their principle plane. Such it is also with liquid crystals. In lyotropic liquid crystals, which are the focus of this thesis, short-ranged hard-body interactions between particles govern the phase behaviour. In order to fill the volume occupied by the dispersion most efficiently, e.g., flat particles often stack, while elongated particles align. Therefore, the study of liquid crystals is a study of ordering and packing phenomena [5–9].

The centre of research attention in this thesis are lyotropic liquid crystals, composed of uniaxial hard rods (see Fig. 1.1). In those, the phase behaviour, for a given rod aspect ratio, is determined by the density. At different densities, different

mesophases emerge *, among which this thesis is foremost interested in the so-called *smectic* phase, which occurs at high packing fractions.

The structure of the smectic phase is best understood, by first considering the phases, which occur at low densities. At sufficiently low densities, the particles rarely come into contact. They move therefore almost freely across the accessible space, while also rotating freely (see Fig. 1.1.**(b)**), resulting in uniform distribution of the positions and isotropic distribution of orientations. Therefore, this phase is called the *isotropic* phase. With increasing packing fraction, the material undergoes a phase transition. Through the elongated shapes, the particles display a strong tendency for local alignment along their long axis, while retaining a uniform distribution in space. This phase is denoted the *nematic* phase (see Fig. 1.1.**(c)**). Upon further increase of the packing fraction, the liquid crystal undergoes yet another phase transition. The rods start packing into layers, breaking up the uniform distribution of the positions in the nematic phase (see Fig. 1.1.**(d)**) [11–15].

This apparent wealth of ordered phases lends itself to a vast range of applications, e.g., as coatings with a sophisticated surface chemistry [16, 17] or in functional materials in technical applications. One of the most prominent of the latter are displays containing liquid crystals (LCD), where steering of the local orientation of the rods through confinement as well as electromagnetic fields enables external control of the translucency of individual screen pixels [18, 19].

The detailed structure of the liquid crystal, i.e., the positions and orientations of the constituent particles, is typically described in terms of a space-dependent number density $\rho(\mathbf{r})$ (often also expressed alternatively as packing fraction $\eta(\mathbf{r}) = \rho(\mathbf{r})V_{\mathrm{rod}}$, with the volume of a single particle V_{rod}) and a local orientation $\hat{\mathbf{n}}(\mathbf{r})$ †, commonly referred to as *director*. In experiment and simulation, both quantities are typically understood as mean local quantities and are usually sampled, from configurations of particles through local averaging [20–22]. Coarse-grained continuum theories approach the investigation of the liquid crystal by resolving these quantities directly [23–26].

1.2 Liquid crystal defects in two dimensions

The regular structure of a bulk liquid crystal phase may be disrupted by a range of various factors, such as fluctuations [27, 28] or external influences such as electromagnetic fields [29–33], confinement [34–45] or the insertion of obstacles [46–52]. In liquid crystals, composed of hard rods, for instance, confinement to finite cavities leads to an alignment of the elongated particles with the outer walls

*_meso-_ from *ancient greek*: *middle-* hinting at their partially ordered structure setting them between liquid and crystalline matter [10].

†For the purposes of this thesis, $\hat{\mathbf{n}}$ can be viewed as a conventional vector field with $\|\hat{\mathbf{n}}\| = 1$, with $\hat{\mathbf{n}} = -\hat{\mathbf{n}}$, to accommodate for the apolarity of the rods.

of the container or the surfaces of hard obstacles [53–57]. These external constraints enter into competition with the liquid crystal's tendency to retain an ordered bulk structure throughout the hole domain. More specifically, this leads to a formation of defects, which are associated with locations in space, where the director $\hat{\mathbf{n}}$ is ill-defined and jumps discontinuously.

The study of defects is of particular importance to the understanding of liquid crystal materials. Similarly to, e.g., (metallic) solids where the presence of defects has dramatic impact on the material properties [58–60], so-called topological charges in liquid crystals are descriptive of physical properties such as type and strength of deformations [8, 61–63]. Additionally, since topological defects are often associated with conservation laws, akin to, for instance, charge conservation in classical electrodynamics, the underlying topological theory is equipped with a predictive power: topological theorems dictate, that the total topological charge within a confinement is determined by the topology/connectivity of the confining container. This enables one to predict large amounts of information about the deformations, present in a material, only from the container [20, 21, 53–57].

In nematic liquid crystals in two dimensions, these defects, so-called disclinations, are commonly singular points, while in three dimensions, they often take the shape of elongated defect lines. This has been well studied and classified with the help of group-theory, which describes the conservation and recombination laws of topological defect charges in nematic liquid crystals in different dimensions and environments [61, 64–66]. In smectic liquid crystals however, which break the uniformity of the nematic phase through their characteristic layering, the emerging defect structures take more complicated shapes such as edge dislocations in two dimensions [67–72] (cf. Fig. 1.1.**(d)**, where one layer terminates, the two adjacent layers splay out) and focal conics in three dimensions [73–76]. Both types of defects are commonly associated with the layer structure. Since the orientational ordering, which is characteristic for the nematic phase, is also inherent to the smectics, the emerging defects can often additionally be interpreted in terms of the topology of the director field $\hat{\mathbf{n}}$.

The concept of the following section (Sec. 1.2.1) is well established knowledge from literature and is reiterated to serve as an introduction to nematic liquid crystal topology. The subsequent section (Sec. 1.2.2) elaborates on the generalisation of the concept from nematics to smectic liquid crystals. That section is largely based on the insight gained in **P1**, **P2** and **P3**.

The topology of defects in the layer structure, presented in Sec. 1.2.3, is once again, well established in literature. This introductory section aims to explain how topological charges are treated from the viewpoint of layers smectics. This concept forms the basis for the analysis performed in publication **P4**.

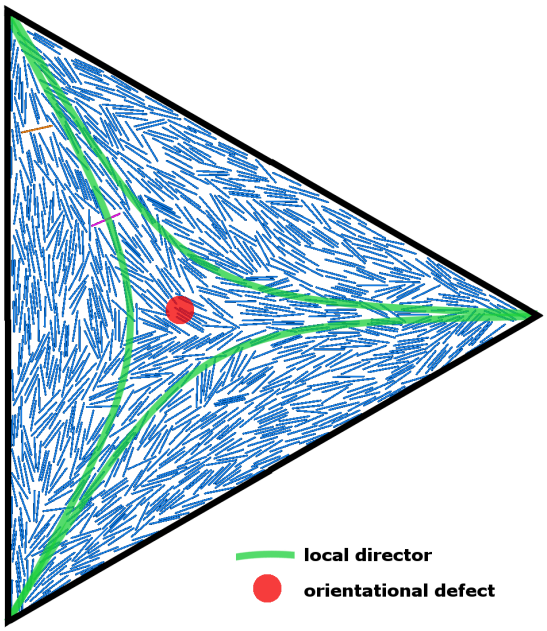

Figure 1.2: Simulation snapshot of a nematic liquid crystal featuring a defect in the mean local orientation/director $\hat{\mathbf{n}}$ in the middle of the confinement. Locally, the long axes of the rods point into the corners. This forces a defect in the middle, where $\hat{\mathbf{n}}$ jumps discontinuously. The green lines serve as guide to the eye for the local director. The topological charge of the defect (cf. Eq. (1.2)) is $Q = -1/2$.

1.2.1 Orientational defects in nematic liquid crystals

Since the topological model for the orientational defects in the director $\hat{\mathbf{n}}$ of a smectic liquid crystal derives from the description of the defects in a nematic liquid crystal, this section elaborates the topology of two-dimensional nematic defects first.

In Fig. 1.2, a simulated snapshot of a nematic liquid crystal, confined to a two-dimensional cavity with almost hard walls, is depicted. Due to the hardness of the walls, the rods tend to favour parallel wall alignment [77, 78]. Since the wall segments feature different orientations, the rods are prohibited from assuming a state in which all long axes point into the same direction, leading to a space-dependent $\hat{\mathbf{n}}(\mathbf{r})$. Most notably, the rods locally point into the corners, resulting in a star-shaped geometry with three spikes in the field lines of $\hat{\mathbf{n}}$ (indicated by the green lines). Inevitably this leads to a singular point in the centre, where $\hat{\mathbf{n}}$ is ill-defined and across which $\hat{\mathbf{n}}$ jumps discontinuously. The director in the close

vicinity around this defect may be approximated as

$$\hat{\mathbf{n}}(\mathbf{r}) = \begin{pmatrix} \cos(Q\phi) \\ \sin(Q\phi) \end{pmatrix}, \tag{1.1}$$

where ϕ denotes the polar angle of the position $\mathbf{r} = r(\cos(\phi), \sin(\phi))$ and $r = \|\mathbf{r}\|$. Here, Q represents the topological charge of the defect. In Fig. 1.2, the value of Q is equal to $-1/2$.

In general, for any two-dimensional director field $\hat{\mathbf{n}} = (\hat{n}_1, \hat{n}_2)$, the topological charge of a defect is equal to the *winding number* of $\hat{\mathbf{n}}$. This is the total in-plane rotation of the direction of the field, along a path that goes around the defect once, in counter-clockwise direction. It can be calculated as

$$Q = \frac{1}{2\pi} \oint_{\mathcal{C}(\kappa)} \left[\hat{n}_1(\kappa) \frac{\partial \hat{n}_2(\kappa)}{\partial \kappa} - \hat{n}_2(\kappa) \frac{\partial \hat{n}_1(\kappa)}{\partial \kappa} \right] \mathrm{d}\kappa, \tag{1.2}$$

where $\mathcal{C}(\kappa)$ is a closed path with $\oint_{\mathcal{C}(\kappa)} \mathrm{d}\kappa = 2\pi$ [21, 61]. The charge, defined in this manner, is a conserved quantity in two dimensions, which behaves in many ways comparable to conventional particles with electromagnetic charges [79–81]. Defects of different charges may, for instance, recombine/annihilate. Details on the group-theoretical treatment of topological charges are discussed in Sec. 2.3 of publication **P2**.

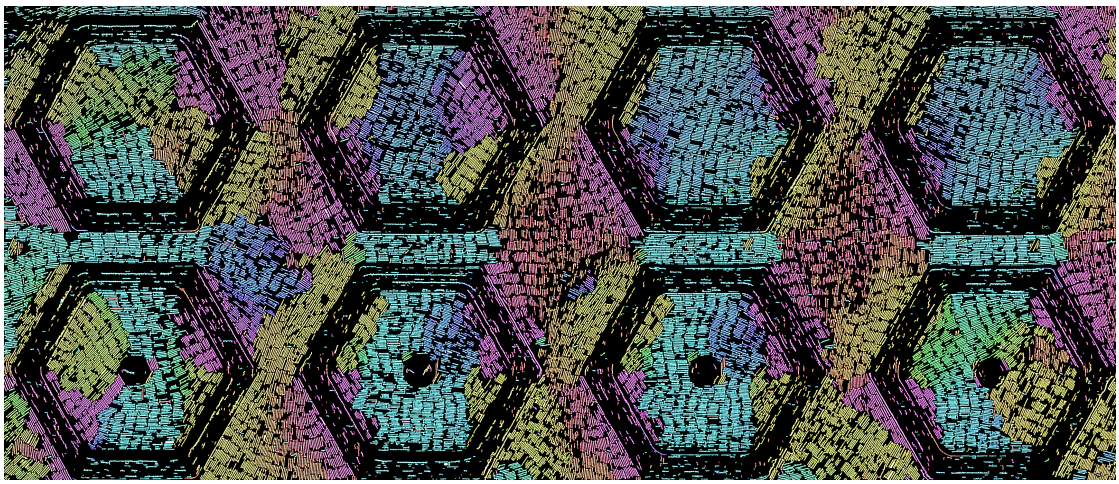

Figure 1.3: Experimental snapshots of a smectic liquid crystal composed of rods in a quasi two-dimensional environment. The picture is taken under a light microscope from the bottom glass pane of a cavity, filled with colloidal silica rods in aqueous NaCl-solution (experimental details are described in ref. [54]). The rods display a visible tendency to align with the hexagonal black walls, exemplified by the orientational colour coding. The liquid crystal displays domain formation, each with intrinsic uniform orientation. Those are separated by relatively sharp boundaries, which can be identified as defects in the director $\hat{\mathbf{n}}$. These can be analysed with the topological theory, presented in Sec. 1.2.2. (image received by the courtesy of Dr. Louis B. G. Cortes, unpublished personal correspondence)

1.2.2 Orientational defects in smectic liquid crystals

The previous section (Sec. 1.2.1) elaborates on the behaviour of topological defects in the orientational field $\hat{\mathbf{n}}(\mathbf{r})$ in nematic liquid crystals. This section now discusses how the concept of the orientational defects in nematics generalises to the smectic phase: upon increase of the packing fraction, a hard-rod nematic liquid crystal undergoes a phase transition into the smectic phase, where the particles arrange into characteristic layers [11–15]. In Fig. 1.3, an experimental snapshot of a two-dimensional smectic liquid crystal, observed under a light microscope, is shown. The bulk structure of the liquid crystal is obstructed by an arrangement of hexagonal walls and additionally hexagonal obstacles within the hexagons in the bottom row. The hexagonal walls serve both as *(i)* confinement for the liquid crystal within and *(ii)* hexagonal obstacles to the bulk structure on the outside. The colour coding represents the orientations of the rods. It can be seen, that the smectic liquid crystal prefers the formation of domains, with largely uniform orientations and layer structure.

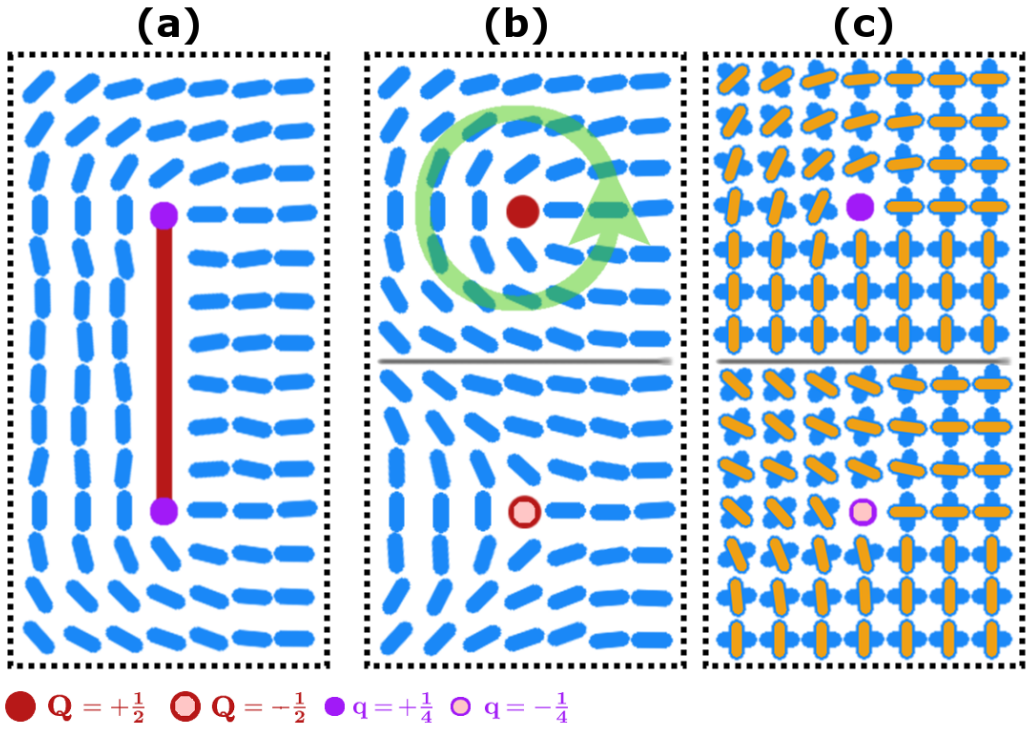

Figure 1.4: Schematic of the classification of topological defects in two dimensions, present as discontinuities in the director field $\hat{\mathbf{n}}(\mathbf{r})$. The topological charge of a defect corresponds to the net rotation of $\hat{\mathbf{n}}(\mathbf{r})$ traversing the defect in counter-clockwise direction (indicated by the circular arrow in (b, top)) around the defects. **(a)**: The schematic shows an exemplary line defect of total charge $Q = 1/2$. Due to the preferred difference in orientation angles of $\pi/2$, the line defects can be classified as two isolated tetratic point defects of charge $q = 1/4$, sitting on the ends. **(b)**: Schematic of point defects for particles of π rotational symmetry with charges $Q = +1/2$ (top) and $Q = -1/2$ (bottom). The $Q = +1/2$ charge is analogous to the line defect in (a), which can be thought of as a stretched version of this point defect. **(c)**: Point defects for particles with $\pi/2$ rotational symmetry. Charges are $q = +1/4$ (top) and $q = -1/4$ (bottom). For ease of observing the continuous rotation, the two main axes are decorated differently. (figure and caption reproduced and adapted from [21] licensed under CC BY 3.0)

These domains are separated by grain boundaries, which represent extended discontinuities in the director field $\hat{\mathbf{n}}$ across which the director jumps, in analogy to the points defects, presented in the previous section (Sec. 1.2.1). Since local orientational ordering is also inherent to the smectic phase, and since these grain

boundaries represent discontinuities in the director field $\hat{\mathbf{n}}$, they are eligible for classification through topological charges [20, 21, 54].

In Fig. 1.4.**(a)** a schematic of an elongated grain boundary is shown. Considering the total rotation around the defect, it shows that this defect carries a charge of $Q = 1/2$. For comparison, Fig. 1.4.**(b)** shows point defects with $Q = 1/2$ (top) and $Q = -1/2$ (bottom). Indeed, the grain boundary in Fig. 1.4.**(a)** can be obtained, through continuous deformation, from the $Q = 1/2$ defect in Fig. 1.4.**(b)**. This can be envisioned by splitting the picture of the $Q = 1/2$ point defect visually in top- and bottom half, directly through the middle of the defect, and then stretching the defect and the surrounding field in vertical direction like molten cheese or chewing gum, thereby stretching the point defect into a line (unrelated to the true viscoelastic properties of the physical material).

The topological charge distribution within grain boundaries can be further resolved due to the strong preference of smectic layers to form a tilt angle of $\pi/2$ across grain boundaries [82–84]. This results in a tendency for the rotation of the rods to occur at the end-points, which can be visualised, by analysing the hard-rod system with an order parameter, which measures tetratic order. Perfect tetratic order occurs, when all particles are at 0 or $\pi/2$ angles to each other. The end-points on the grain boundaries can be interpreted as quarter-integer tetratic point charges, which constitute the total charge of the defect. The grain boundary in Fig. 1.4.**(a)** with $Q = 1/2$ is composed of two $q = 1/4$ end-point defects [20, 21, 54].

To elucidate this concept further, two isolated tetratic defects with charges are shown in Fig. 1.4.**(c)**: $q = 1/4$ (top) and $q = -1/4$ (bottom). These tetratic point charges are local discontinuities in the orientation of particles with fourfold rotational symmetry (e.g. squares or crosses, such as here). For ease of observation of the continuous rotation around the defect, one principal axes of the particles is coloured in orange.

1.2.3 Layer defects in smectic liquid crystals

The previous section (Sec. 1.2.2) elaborates on the analysis of the topology of a smectic structure by considering the grain boundaries as orientational defects with a fine-structure. The conventional treatment in literature of the topology of a smectic liquid crystal, happens from the viewpoint of the smectic layers [67–76]. This approach is explained in this section, and forms the basis for the analysis, performed in publication **P4**.

A defect in the layer structure is defined as a singular location in space, where multiple layers meet at an angle, i.e., layers terminate. A schematic of such a defect is depicted in Fig. 1.5, where $n = 3$ layers converge into a single point. As the layer structure (black lines) around this defect is continuously deformed around the defect, it can be classified in terms of the total rotation of the rods. Since in smectic structures, the particles typically possess a preferred angle to the layers,

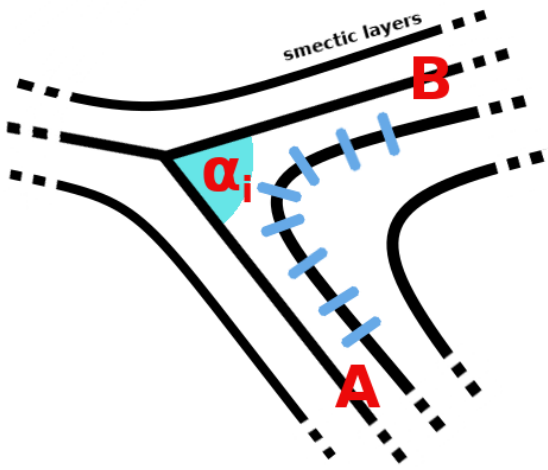

Figure 1.5: Schematic of a topological defect in a smectic liquid crystal as considered via the layers (black lines) of particle positions. The defect is a point, where a number of layers meet at an angle, thereby perturbing the regular smectic bulk structure. The defect strength can be quantified by a layer topological charge Q, computed through the total rotation of the rods (blue) around the defect, divided by 2π similar as in defects in the director field $\hat{\mathbf{n}}$ (see Sec. 1.2.1). Between two outgoing layers **A** and **B**, at an angle α_i, the rotation angle of the rods is equal to $\alpha_i - \pi$. Consequently, the total layer topological charge around the defect can be obtained via summation over all incident layers: $Q = 1 - n/2$. The charge of the depicted defect with star shape is $Q = -1/2$, since $n = 3$, consistent with the orientational topological charges (cf. depiction of confined nematic in Fig. 1.2).

the rotation of the rods equates to the rotation of the layers around the point defect [85–89].

As visible, the rotation of a rod $\Delta\phi_i$ $(i = 1, ..., n)$, between two incident layers **A** and **B** is equal to $\alpha_i - \pi$, where α_i denotes the angles between both layers. Accordingly, the charge of the defects, computed from the total rotation around the defect, is equal to $Q = (\sum_i^n \Delta\phi_i)/2\pi = (1 - n/2)$ [85–89].

To assure that this definition of the charges is indeed topological, i.e., the sum of confined charges matches the topology of the finite container and local charge conservation persists, additional considerations are usually made, that involve the inclusion of density minima as topological objects [85–89].

To illustrate this, an exemplary simulated configuration is depicted in Fig. 1.6. The particle snapshot is shown in Fig. 1.6.**(a)**. The rods display layering, mutual local alignment as well as parallel alignment with the boundaries of the cavity, as expected at this packing fraction ($\eta = 0.75$, aspect ratio $L/D = 15$). The external

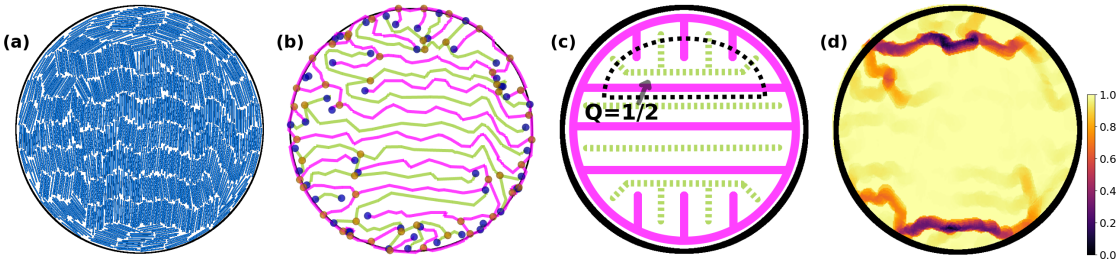

Figure 1.6: Topological analysis of confined hard-rod smectics from the viewpoint of the layers. **(a)**: Particle snapshot from Monte-Carlo simulation in circular confinement. The particles display a visual tendency to align and form layers, as expected at this packing fraction. **(b)**: The layers from the particle configuration are labelled in magenta. In order to obtain a picture, where the layer topological charges are conserved, the minima in between layers (*half-layers*, green) are explicitly considered as charge bearing (positive charges are blue, negative brown). To obtain global charge conservation, the boundaries can be designated to the original particle layer network. **(c)**: Schematic of the defectious layer configuration. Summing the layer defects within the dashed circle shows that the system features regions with layer topological charge $Q = 1/2$, distributed between both layer species, close to the top bottom of the confinement. **(d)**: Orientational order parameter field $\mathcal{S}(\mathbf{r})$, visualising the defects in the orientations $\hat{\mathbf{n}}$. It can be seen, that $\mathcal{S}$ is decreased, where the layer structure in (b) displays defects. Since both defects are single grain boundaries, they contain orientational topological charges $Q = 1/2$, each. It shows how orientational and layer charge pictures are consistent in terms of the total charges.

constraints from the confinement clearly prohibit the intrinsic preference of the smectic liquid crystal to form a bulk structure with defect-free, undeformed, parallel and equidistant layers. As such, the system is expected to display the formation of defects. The detailed layer structure is depicted in Fig. 1.6.**(b)**. A meaningful topological charge conservation is obtained via the explicit consideration of the density minima (green) in between the smectic layers (magenta) as topological entities. Those are, due to their intermediate positions between smectic layers, typically denoted as half-layers [85–89]. The outer walls are associated with the smectic layers, which introduces boundary defects.

The depiction in Fig. 1.6.**(b)** shows a large defect free central domain, with largely parallel layers and half-layers. Above and below this are two regions with a multitude of short layers, orthogonal to the central domain. A simplified schematic of this characteristic structure is shown in Fig. 1.6.**(c)**. It indicates that the two defect regions contain layer defects whose topological charge sums up to $Q = 1/2$

each. At the same time, the rest of the confinement is charge neutral.

In Fig. 1.6.**(d)**, the orientational order parameter field $\mathcal{S}(\mathbf{r}) = |\langle \exp(i2\phi)\rangle|$ of the system is shown. Minima in $\mathcal{S}(\mathbf{r})$ are associated with defects in $\hat{\mathbf{n}}$. It prominently shows two grain boundaries in the top and bottom of the cavity, where $\mathcal{S}$ is significantly decreased. Both possess an orientational topological charge $Q = 1/2$, which can be inferred from the particle configuration in Fig. 1.6.**(a)**, from the layer networks in Fig. 1.6.**(b)**, or from the Euler characteristic $\chi = 1$ of the confinement. This consideration displays, how both pictures of topological charges are consistent with respect to the total amount of charges in a defectious region.

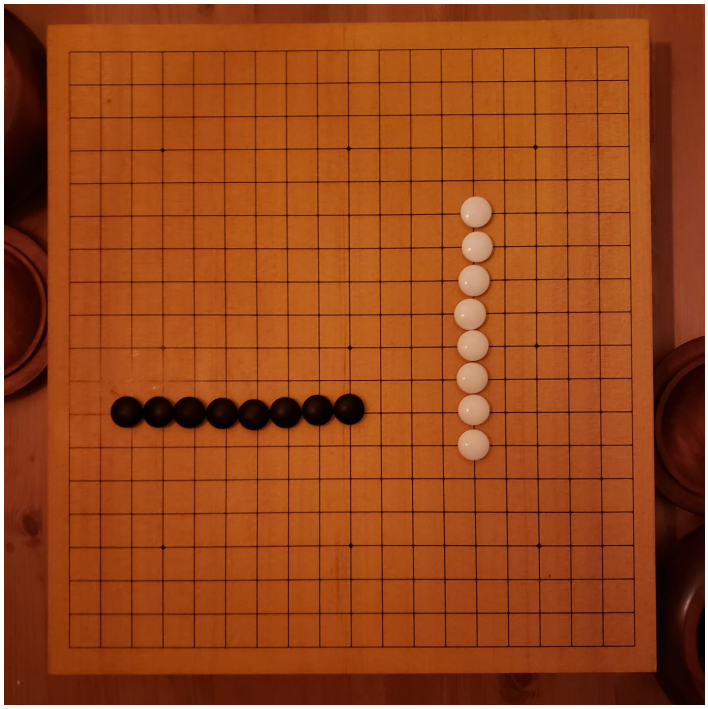

Figure 1.7: Hard-rod system on a finite square lattice realised on a Goban (board of the game of Go). The board is a lattice of thin lines, on which white and black stones are placed. These, placed connected and in rows, generates a system of two rods on a square lattice. We analyse this as an instructive toy system, which can investigated with the help of classical statistical mechanics, by assigning a probability distribution to the configurations. This allows for the exact calculation of statistical properties such as a partition function and entropy, which is in general not possible for hard-rod systems in two or three dimensions with continuous orientations and positions of an arbitrary number of N rods.

1.3 Two-rod system on a finite square lattice

Unfortunately, it is quite a common fallacy to assume, that the term "entropy" is more or less synonymous with the word "disorder" [90, 91]. This, however, can raise wrong expectations towards many natural phenomena, since in liquid crystals, entropy often plays a crucial constructive role in the formation of ordered phases [92–94]. This section shall address this misconception by analysing a simple toy system of two hard rods on a square lattice. In this system, the positions of the rods are discretised and only two orientations, horizontal and vertical, are possible.

In Fig. 1.7 a photograph of a *Goban*, a board from the game of *Go*, is shown. The board features black and white stones, placed horizontally or vertically adjacent

on the vertices of a square lattice of size 19×19. Stones placed in this manner, here of length eight, symbolise the vertices which are occupied by the respective rods. Since any vertex can only be occupied by a single stone, the rods symbolise hard-body repulsion. The simplicity of this model allows for the explicit calculation of thermodynamical quantities such as entropy with the standard tools, given by classical statistical mechanics [95].

This consideration aims to provide a very basic intuitive understanding of the role of entropy, as derived from the microscopic, i.e., particle-resolved statistical mechanics, in the context of alignment phenomena and the formation of mesophases in hard-rod liquid crystals. It features furthermore confinement (to a square box), which is a reoccurring theme throughout the publications in this thesis (**P1**, **P2**, **P4**, **P3**).

To obtain an appropriate analogy to the alignment phenomena, present in real hard-rod liquid crystals, we assume that the rods can discretely diffuse and rotate about the lattice. The two rods display short-ranged, hard-body repulsion and so, the interaction potential can be defined as

$$V(\{\mathcal{P}_n\}) = \begin{cases} \infty & \text{if } i \neq j \text{ and } \mathcal{P}_i \cap \mathcal{P}_j \neq \emptyset \\ 0 & \text{else.} \end{cases} \tag{1.3}$$

Here, $\mathcal{P}_n$ denotes the set of points occupied by the n-th rod ($n = 1, ..., N$). The set-intersection operator is denoted by $\cap$ and $\emptyset$ denotes the empty set. The argument $\{\mathcal{P}_n\}$ denotes the set of all $\mathcal{P}_n$, for which the interaction energy is considered. Note that this definition is valid for more than two rods. This interaction essentially describes, that while the rods randomly propagate about the lattice, overlaps never occur. At the same time, because all possible configurations have the same energy $V = 0$, all are occupied with the same probability

$$p_k = \frac{1}{Z(L_\square, L_\bullet)}, \tag{1.4}$$

where k indexes the configurations. [95–99]. The total number of configurations is denoted by Z, which depends on the size (i.e, number of vertices) of the square lattice in one direction $L_\square$ and the length of the rods $L_\bullet$ (number of occupied vertices).

These individual states, which resolve the microscopic positions of the individual rods (short *microstates*) are in real physical systems, however, usually inaccessible and also uninteresting. When considering, e.g, a cubic meter of breathable air, containing around 10^{23} individual gas particles, one is usually concerned, instead, with macroscopic observables such as temperature or pressure [95,99]. A *macrostate* can be defined by these macroscopic observables, and encompasses all microstates, which result in the same macroscopic observables. In the case of our two-rod system, we are interested in whether the two rods are parallel, or whether the two

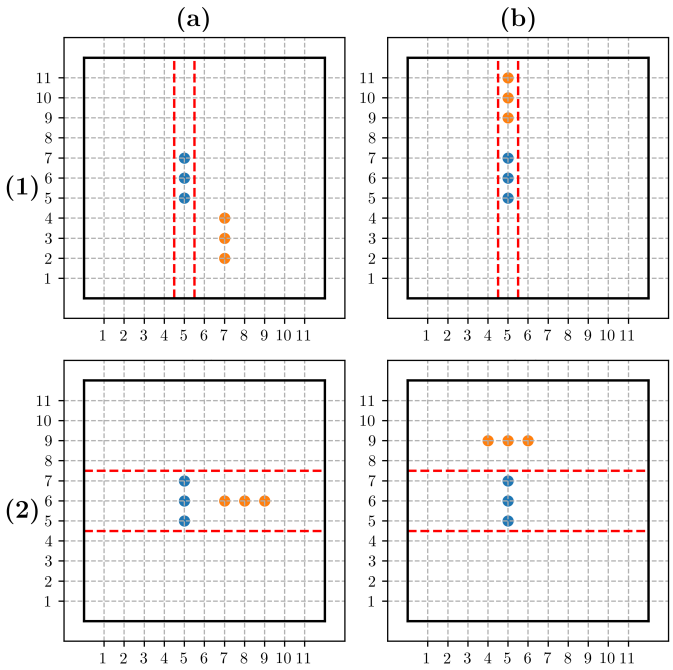

Figure 1.8: Schematic of one possible partition of all possible configurations of two hard rods on a two-dimensional square lattice, facilitating the computation of the number of states $Z(L_\square, L_\bullet)$ as a function of box length $L_\square$ and rod length $L_\bullet$. In order to assign probabilities to either **(1)**: perpendicular or **(2)**: parallel macrostates for given $L_\square$ and $L_\bullet$, one calculates the amount of respective configurations. All states can be classified, by the second particle (orange) being **(a)**: to the side **(b)**: above or below, the designated first particle (blue), within the respective bands, indicated by the dashed red lines. In this schematic $L_\bullet = 3$ and $L_\square = 11$. This analysis can be applied with any combination of $L_\bullet$ and $L_\square$.

rods are perpendicular as a function of the system parameters lattice length $L_\square$ and rod length $L_\bullet$. Accordingly, we define a parallel macrostate and a perpendicular macrostate. The respective probability for the parallel macrostate is given by

$$P_\parallel(L_\square, L_\bullet) = \frac{Z_\parallel(L_\square, L_\bullet)}{Z(L_\square, L_\bullet)} = \frac{Z_\parallel(L_\square, L_\bullet)}{Z_\parallel(L_\square, L_\bullet) + Z_\perp(L_\square, L_\bullet)}, \tag{1.5}$$

with the number of microstates $Z_\parallel$, where the rods are parallel, and the number of microstates $Z_\perp$, where the rods are perpendicular. Both quantities depend on $L_\square$ and $L_\bullet$. Analogously, the probability for perpendicularity is

$$P_\perp(L_\square, L_\bullet) = \frac{Z_\perp(L_\square, L_\bullet)}{Z(L_\square, L_\bullet)} = \frac{Z_\perp(L_\square, L_\bullet)}{Z_\parallel(L_\square, L_\bullet) + Z_\perp(L_\square, L_\bullet)}. \tag{1.6}$$

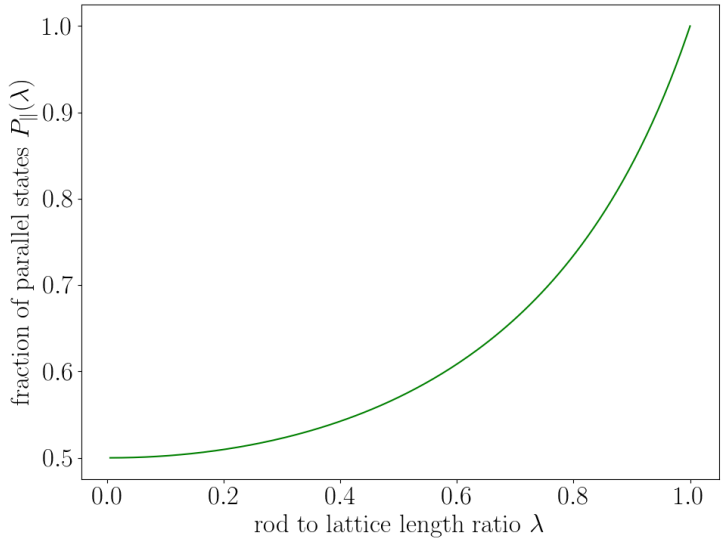

Figure 1.9: Fraction of parallel configurations $P_\parallel(\lambda)$ of two rods on a square lattice as a function of the ratio λ of the length of the rod $L_\bullet$ to the length of the confining box $L_\square$. P ranges between 1/2 for isotropy and 1, for guaranteed alignment.

The number of microstates $Z_\parallel$ and $Z_\perp$ can be calculated explicitly, as shown in Fig. 1.8. The figure shows a schematic of a possible further partitioning, which simplifies the calculation. For instance, the number of configurations where the rods are parallel but do not lie on a single line aligned (Fig. 1.8.**(1a)**, orange outside red dashed lines) is equal to $2(L_\square + 1 - L_\bullet)^2 L_\square(L_\square - 1)$. Each rod has $(L_\square + 1 - L_\bullet)$ possible positions on the line along its vertical, combined with $L_\square(L_\square - 1)$ combinations for the two rods along the horizontal, as well as a factor of 2, for the microstates, when both rods are horizontal. The other terms follow through similar combinatoric computations. Accordingly, the number of parallel microstates reads as

$$\begin{aligned} Z_\parallel(L_\square, L_\bullet) =& 2(L_\square + 1 - L_\bullet)^2 L_\square(L_\square - 1) + \\ & 2(L_\square + 2 - 2L_\bullet)(L_\square + 1 - 2L_\bullet) L_\square \Theta(L_\square - 2L_\bullet), \end{aligned} \tag{1.7}$$

where $\Theta(x)$ denotes the Heaviside step function with the convention $\Theta(0) = 1$. The number of perpendicular microstates reads as

$$Z_\perp(L_\square, L_\bullet) = 2(L_\square + 1 - L_\bullet)^2 (L_\square - L_\bullet)(L_\square + L_\bullet). \tag{1.8}$$

In Fig. 1.9, the probability for parallelity $P_\parallel$ (cf. Eq. (1.5)) is shown as a function of $\lambda = L_\bullet / L_\square$. Since $L_\square$ can be arbitrarily large, λ can take the value of any rational

number. When the rods have lengths $L_\bullet = 1$ ($\lambda = 1/L_\square$), i.e., the smallest possible value corresponding to hard spheres, there is no distinction possible between parallel and perpendicular. Consequently $P_\parallel(1/L_\square) = P_\perp(1/L_\square) = 1/2$. On the other hand, when $L_\bullet = L_\square$, i.e., λ =1, perpendicularity is impossible. Therefore $P_\parallel(1) = 1$.

The quantity $2P_\parallel - 1 \in [0, 1]$ can be thought of as an order parameter for the continuous transition of the system from a disordered isotropic state, where all orientations are present with equal probability, into an orientationally ordered state. This may give a good intuition for, e.g., the spontaneous alignment, which happens at the isotropic to nematic phase transition in hard-rod liquid crystals. The term *phase transition*, is in the strict sense of the word, not applicable to the lattice two-rod system, discussed in this section. It is reserved for a range of phenomena in nature, which fulfil a special set of criteria, most prominently reside in the thermodynamic limit ($N \to \infty$, $V \to \infty$, $N/V = \text{const}$) [95, 100, 101].

We can, in general, identify the entropy S of a macrostate, given its partition function, i.e., the total number of microstates Z via:

$$S = \frac{\partial}{\partial T} k_\mathrm{B} T \ln Z = k_\mathrm{B} \ln Z, \tag{1.9}$$

if Z is temperature independent [‡]. Here k_B denotes the Boltzmann constant [102].

Since $P_\parallel > 1/2$ (cf. Fig. 1.9), the difference in entropy for the two macrostates

$$S_\parallel - S_\perp = k_\mathrm{B} \ln \left(\frac{Z_\parallel}{Z_\perp} \right) = k_\mathrm{B} \ln \left(\frac{P_\parallel}{1 - P_\parallel} \right) \geq 0 \tag{1.10}$$

is always greater than 0 and diverges as λ approaches 1 and therefore $P_\parallel$ approaches 1. For all values $\lambda < 1$, this particular system will, over the course of its physical evolution, randomly switch between higher and lower entropy macrostates, parallel and perpendicular.

This discussion illustrates how the entropy in hard repulsive systems is directly linked to the amount of states, which a system can occupy. Furthermore, the entropy of the aligned state is always larger than the orthogonal state, and this effect increases with length of the rods. This might serve as an analogy for understanding ordering transitions in nature, such as the isotropic to nematic phase transition in liquid crystals. Here, beyond a certain rod aspect ratio or density, the entropy associated with translational freedom of motion along the long axes,

[‡]Note that this notation assumes the canonical ensemble, as utilised also in Sec. 1.4 for the simulation. The partial derivative is taken at constant V and N. The absence of temperature dependence, with only hard interactions in this section, simplifies the calculations of the entropy. There are several justifications for why the terms in the partition functions, regarding the translational and angular momenta can be neglected for the computation of the entropy of lyotropic liquid crystals in general, and thus also for the lattice rod system. One, which shall suffice for this context, is the diminished influence of inertial effects on microscopic particles in solution (overdamped dynamics).

outweighs the entropy associated with freedom of rotation. Unlike the example discussed in this section, the liquid crystal usually does not switch freely between isotropic and ordered state, but remains in the ordered state that features the higher entropy [5, 92, 93].

1.4 Canonical Monte-Carlo method for liquid crystals

The name *Monte-Carlo method* apparently derives from the gambling habits of an uncle of Stanislav Ulam, one of the original inventors of this technique. It is stated by Nikolas Metropolis himself, one of the inventors, that it references a famous casino in Monaco, due to the probabilistic nature of the algorithm [103]. It has evolved into a highly versatile method, which finds itself applicable in, for instance, optimisation problems and the numerical solution of integrals [104, 105]. Among these, it is famously utilised today, to solve problems in *machine learning* [106–108] and to model the seemed randomness of the financial market [109,110]. The method remains a powerful tool for the study of the statistical mechanics of multi-particle systems [111, 112].

The basic scheme samples the configuration space of all particles, by starting at an arbitrary configuration and iteratively generating new configurations by generating trial displacements, which are accepted according to the probability P given by the *Metropolis criterion* [112, 113]

$$P = \min\left(1, e^{-\frac{\Delta U}{k_\mathrm{B}T}}\right), \tag{1.11}$$

where ΔU designates the change in energy of the system, k_B is the Boltzmann constant and T the temperature. The total number of trial configurations is highly dependent on the considered system and typically requires fundamental knowledge about the problem. Moreover, the particular choice of trial displacement is quite flexible, but must be chosen such that the algorithm is not biased towards a certain configuration/region of the configuration space [102, 114].

This probabilistic approach has several major properties: *(i)* when applying this scheme to finding extrema of an arbitrary function, it does not require the explicit evaluation of gradients, contrary to minimisation algorithms such as *gradient descent*, which might, in a sufficiently complicated setting, either be entirely impossible, or at least computationally unfeasible. *(ii)* In the same context, the algorithm possesses the ability to overcome local minima, due to the finite probability of accepting a trial move towards an upward slope. *(iii)* Lastly, and most crucially for the simulation of multi-particle systems, all possible configurations are sampled according to the probability given by the Boltzmann factor $\exp(-U/(k_\mathrm{B}T))$ in the canonical ensemble [96, 97]. Accordingly, the goal of the Monte-Carlo simulation is commonly to obtain a state, which reflects an equilibrium configuration that

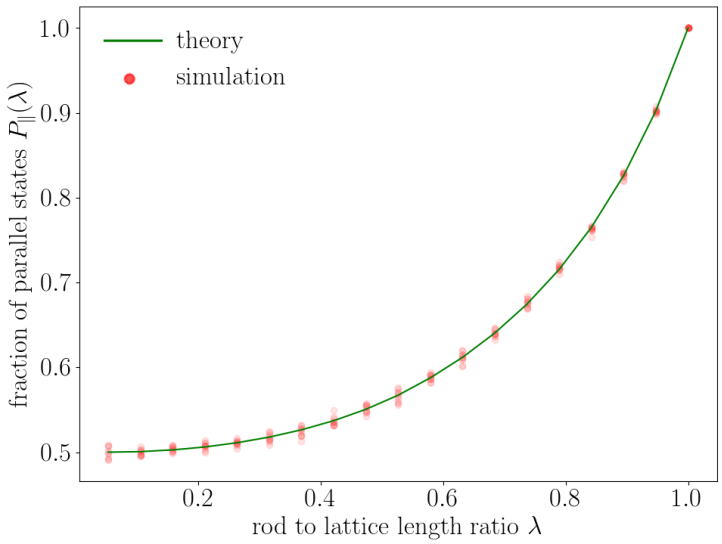

Figure 1.10: Fraction of parallel configurations $P_\parallel(\lambda)$ of two rods on a square lattice (as already depicted in Fig. 1.9). The analytical solution (green solid line) is complemented by simulation results obtained via Monte-Carlo simulation for $L_\square = 19$ (orange points). As visible through the agreement of the simulation with the exact result, the Monte-Carlo simulation samples the configuration space according to the correct probability distributions, approximating the exact result. We show the results of ten independent simulation runs per $L_\bullet \in \{1, 2, ..., 19\}$.

minimises the free energy

$$F = U - TS. \tag{1.12}$$

In other words, if done properly, the system resides in a state, which is determined by the competition of the entropy and the internal energies associated with soft interactions, such as soft interaction potentials or external potentials such as soft confining walls. In pure hard-body systems, the Boltzmann factor is globally equal to 1 and the configuration space is sampled accordingly. The goal is, to obtain a configuration, which reflects an equilibrium state with maximal entropy.

To illustrate the simplicity but effectiveness of Monte-Carlo simulation, we recollect the two-rod system from the previous section (Sec. 1.3). In Fig. 1.10, the solution to the fraction of parallel states $P_\parallel(\lambda)$ for two rods on a square lattice is shown, again. The green line shows the exact analytical solution, depicted in Fig. 1.9 (see Sec. 1.3). In addition, the same quantity obtained via Monte-Carlo simulation, is now indicated as orange points The simulation simply generates 10^4 valid overlap-free configurations, from which the relative frequencies are extracted. The figure shows ten independent simulation results runs per $L_\bullet \in \{1, 2, ..., 19\}$, indicated by the orange dots. It is visible, that the fractions, obtained via simulation,

approximate the exact solution.

1.4.1 Compression protocol for self-assembly of ordered phases

Large parts of the craft of proper Monte-Carlo simulation is to enable the system to reside in a state which reflects a true equilibrium configuration[§]. While this can never be fully guaranteed, without additional techniques, which enable the calculation of free energy F or entropy S [115, 116], precautions can be made, such as an unbiased displacement function and an appropriate equilibration protocol. An example for the latter is briefly introduced in this section.

The general discussion of the Monte-Carlo scheme in the previous section (Sec. 1.4) prescribes to initialise the physical system at an arbitrary random configuration before running the Monte-Carlo scheme. However, the fundamental reason why any ordered phase exists at all in hard-rod liquid crystals, is due to the lack of space at higher densities, which forces the rods into alignment and/or positional order. Accordingly, guessing a random configuration, which fits into the simulation volume, is equivalent to guessing the result of the simulation in the first place. Therefore, a simulation protocol is necessary, which allows for the random initialisation at low densities and subsequent transition into ordered phases. Further specifics of the simulation procedure, regarding the individual publications, are given by the respective sections in ch. 3 (**P1**, **P2**, **P4**, **P3**, **P6**). This section describes the general scheme.

We follow compression schemes, where we initialise the particle configuration randomly at low volume fraction, several orders of magnitude below the volume fraction of interest. The positions of the particles are uniformly randomised across the simulation volume. The orientations of the particles are uniformly randomised on the unit sphere S_2 in three dimensions and on the unit circle S_1 in two dimensions. The system resides in an isotropic phase.

All liquid crystal publications in this thesis feature confinement. In order to obtain a state at a high packing fraction, the size of the cavity is gradually decreased after initialisation. In order to be able to shrink the cavity, without generating unphysical configurations, i.e., a particle sitting inside a hard wall, the confining walls are modelled as soft walls, with a very steep interaction potential. One such possibility is given by a cut-off WCA potential

$$V(x) = \begin{cases} \Phi(x_0) + \Phi'(x_0)(x - x_0) & \text{for } x \leq x_0, \\ \Phi(x) & \text{for } x_0 > x, \end{cases} \tag{1.13}$$

where $\Phi(x)$ denotes the standard 12-6-WCA potential [117]. Here, x can denote, i.e, the distance of the particle on the outside of the walls to the inside, where $V = 0$ and x_0 denotes an arbitrary cut-off, beyond which the potential is linearised.

[§]except Monte-Carlo simulation being applied to out-of-equilibrium Brownian dynamics (with an appropriate displacement function) or the investigation of non-equilibrium states. The discussion of both is far out of scope for this brief section.

The shrinking of the simulation volume is performed sufficiently slowly, such that the simulated system can be considered close to equilibrium for any given volume throughout the compression. This is to enable the system to reach a final configuration at the end of the simulation, which most accurately reflects an equilibrium, instead of getting quenched into a kinetically arrested state, which features an unfavourable free energy.

The algorithm can be expected to reach equilibrium drastically faster in the isotropic phase, because the particles are relatively far apart, and there are extremely little rejected trial moves due to the absence of particle overlap. Therefore, the compression rate, with which the simulation volume is shrunk, is typically varied. This is usually done, in order to save computation time. In the projects in this thesis, we utilise two slightly different approaches: *(i)* employing a two-phase compression, where we quickly compress the system, with a constant compression rate, to a packing fraction, where self-assembly is expected. In liquid crystals, this corresponds to just below the bulk isotropic to nematic phase transition. Reaching this regime, the simulation enters a second compression phase, with a drastically reduced compression rate to allow the systems to equilibrate into the ordered phases. *(ii)* Employing a single-phase compression, where the compression rate explicitly depends on the simulation progress but is drastically faster in the beginning of the simulation. This can be expressed as (see e.g. **P4**):

$$\eta(\tau) = \eta(\tau) = (\eta_1 - \eta_0)\tau^{\frac{1}{3}} + \eta_0, \tag{1.14}$$

where $\tau \in [0, 1]$ denotes the fraction of performed trial moves (in the beginning of the simulation $\tau = 0$, in the end $\tau = 1$). Additional numerical indicators, which can be sampled to investigate how well the simulation reflects equilibrium, are discussed in more detail in Appendix A of publication **P4**.

1.5 Topological grain boundaries beyond liquid crystals

The concept of grain boundaries, which possess a topological charge, that splits into end-points, such as introduced in Sec. 1.2.2 is a remarkably general topological idea. To illustrate this, Fig. 1.11 shows simulation results for a two-dimensional out-of-equilibrium system of spherical active Brownian particles [118–121] (cf. Sec. 2.1), which repel through a standard 12-6-WCA potential. Active particles typically feature the so-called motility induced phase separation, i.e., a coexistence between a dense and a dilute phase. This collective phenomenon occurs due to the intrinsic persistence of active particles, even in the absence of attractive interactions [118,122]. Furthermore, within these clusters, spontaneous velocity alignment can be observed [123, 124].

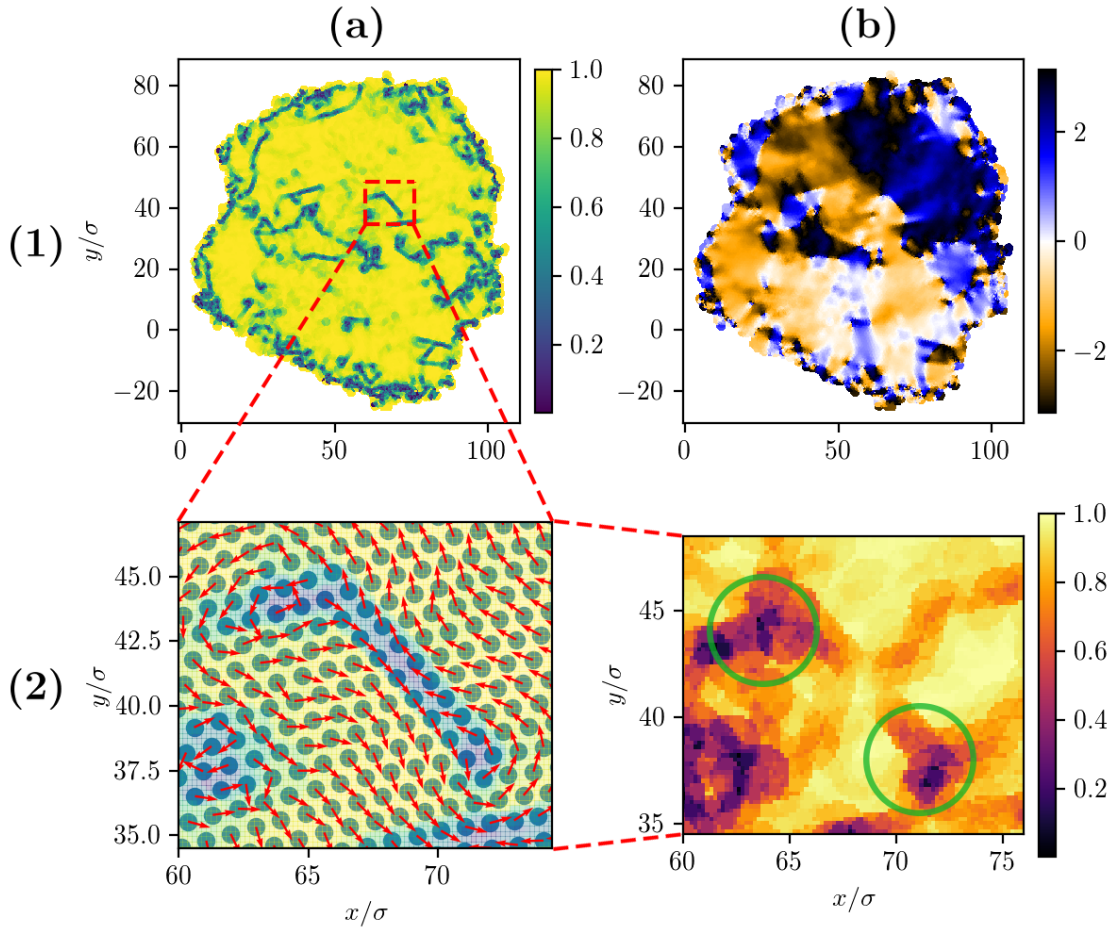

Figure 1.11: Topological grain boundaries in a cluster of active Brownian particles for a system showing motility induced phase separation. Within the cluster, the particles velocities are spontaneously aligned. **(a1)**: Polar order parameter $\mathcal{P}(\mathbf{r})$ of normalised velocities displaying grain boundaries. **(b1)**: Local polar angle of the velocities in radian. It is visible, that $\mathcal{P}$ displays grain boundaries, at which the orientation angle jumps discontinuously. **(a2)**: Particles (dots) and normalised velocities around a local grain boundary (blue background). Across the grain boundary, the angular discrepancy $\Delta\phi$ is equal to π. **(b2)**: Nematic order parameter $\mathcal{S}(\mathbf{r})$. Due to the angular discrepancy $\Delta\phi = \pi$, the polar grain boundary splits into two apolar (nematic) end point charges with $\mathcal{Q} = 1/2$ each, encircled in green (raw data received by courtesy of Dr. Lorenzo Caprini, unpublished personal correspondence).

The polar order parameter $\mathcal{P} = |\langle \exp(i\phi) \rangle|$, where ϕ denotes the polar angles of the velocities, is shown in Fig. 1.11.**(a1)**, as a scalar field. It distinctively displays

large regions with $\mathcal{P} \approx 1$, i.e., domains with strongly aligned velocities. Across the grain boundaries where $\mathcal{P} \approx 0$, the polar angles discontinuously jump, as visible in Fig. 1.11.**(b1)**, where $\phi(\mathbf{r})$ (in radian) is displayed. In Fig. 1.11.**(a2)**, the local particle configuration is shown around a grain boundary in the centre of the cluster. It is visible how, across the grain boundary, the polar angle of the velocities jumps by $\Delta\phi = \pi$. At the end-points of the grain boundary, a continuous rotation of the velocities can be observed. The total rotation of the polar angle around the defect is 2π. As such, this defects carries a topological charge $\mathcal{Q} = 1$. Since the rotation occurs around the end-points, the polar grain boundary splits into two apolar (nematic) end-point defects with $\mathcal{Q} = 1/2$ each, as visible in Fig. 1.11.**(b2)** (encircled in green). This is analogous to how the charge of a grain boundary in apolar smectic systems splits into two constituting tetratic defects (cf. Sec. 1.2.2).

Chapter 2

Reinforcement learning in active matter systems

This chapter aims to equip the reader with the tools to appreciate publication **P5** in ch. 3, which is an application of *reinforcement learning* to a simple *active matter* system. To this end, Sec. 2.1 introduces the concept of the *active Brownian particle*. The reinforcement learning algorithm, used in this context, is set into the broader context of *machine learning*, and discussed in detail in Sec. 2.2.

2.1 What is active matter?

All the publications in this thesis, except **P5**: *Active particles using reinforcement learning to navigate in complex motility landscapes*, are studies of systems which are considered to reside in thermodynamical equilibrium. While this is an extremely appropriate assumption to understand the physics of, e.g., liquid crystals, the majority of systems which we encounter in our everyday life are, in fact, not in equilibrium. For instance, every piece of electrical machinery consumes energy and radiates heat. The human perception of temperature is largely based on temperature gradients. We ourselves are out-of-equilibrium systems [125, 126]. Indeed, one of the fundamental bases for biological life is the consumption of nutrients through particle exchange. The term active matter describes any object, or ensemble of objects, which consumes energy from its surroundings and turns it into a self-propelled motion.

A simple model/dynamics to describe self-propelled microorganisms, such as biological swimmers or active colloids, is given by the so-called active Brownian particle [118, 127]. *Active* designates the aforementioned conversion of ambient energy into a self-propelled motion. *Brownian* corresponds to the subjection to Brownian motion, i.e., random noise in the equations of motion, representing translational and/or rotational diffusion. In the context of publication **P5**, we equip an active Brownian particle with the means of intelligent decision-making through a machine learning algorithm. This model shall *(i)* show avenues for the engineering of intelligent microscopic robotic components [128] and *(ii)* provide

a model for autonomous steering in biological microorganisms, which is based on active decision-making.

2.1.1 Equations of motion of the active Brownian particle in 2d

The active Brownian particle model is characterised by its equation of motion, which can be written in terms of the corresponding Langevin equation [129]:

$$\dot{\mathbf{r}}(t) = \hat{\mathbf{u}}(t)v_0 + \sqrt{2D_\mathrm{t}}\xi(t) \tag{2.1}$$

$$\dot{\phi} = \sqrt{2D_\mathrm{r}}\zeta(t). \tag{2.2}$$

Here, $\mathbf{r}$ is the position of the particle and $\hat{\mathbf{u}} = (\cos\phi, \sin\phi)$ is the orientation of the particle. The self propulsion velocity of the particle is denoted by v_0. D_t and D_r denote translational and rotational diffusion coefficient, respectively. The Brownian random forces are implemented via Gaussian noises ξ and ζ, which fulfil:

$$\langle \xi(t) \rangle = 0 \tag{2.3}$$

$$\langle \xi_i(t)\xi_j(t') \rangle = \delta(t-t')\delta_{ij} \tag{2.4}$$

$$\langle \zeta(t) \rangle = 0 \tag{2.5}$$

$$\langle \zeta(t)\zeta(t') \rangle = \delta(t-t'). \tag{2.6}$$

The angle brackets denote an average over the realisations of the Gaussian noise [118, 127]. In practise, the equations of motion are solved by writing a formal solution in the form

$$\mathbf{r}(t) - \mathbf{r}(0) = \int_0^t \dot{\mathbf{r}}(t')dt', \tag{2.7}$$

which enables one to calculate noise averaged quantities such as the mean squared displacement

$$\left\langle (\mathbf{r}(t) - \mathbf{r}(0))^2 \right\rangle = 4D_\mathrm{t}t + \frac{2v_0^2}{D_\mathrm{r}^2}\left(tD_\mathrm{r} - 1 + e^{-tD_\mathrm{r}}\right) \approx \frac{2v_0^2}{D_\mathrm{r}^2}\left(tD_\mathrm{r} - 1 + e^{-tD_\mathrm{r}}\right) \tag{2.8}$$

utilising Eqs. (2.3), (2.4) and $\langle \hat{\mathbf{u}}(t) \cdot \hat{\mathbf{u}}(0) \rangle = e^{-tD_\mathrm{r}}$ [130]. In typical experimental active systems, we can neglect the translational noise given by D_t, since its contribution to the dynamics often ranks several orders of magnitude below the rotational noise [118].

2.1.2 Mean first passage time and augmentation with intelligent steering

Microscopic robots may, for instance, be used to perform minimal invasive medicine through targeted drug delivery in the human body [131–135]. In this application, the time and the reliability with which a robot reaches its target, e.g., a specific cancer cell, are crucial factors in the efficiency and cost of the therapy.

In many relevant medical applications, the distance a over which the particle travels, is much greater than the length scale on which its trajectory is persistent, due to self propulsion (persistence length v_0/D_r). We therefore consider the diffusive behaviour in the long-time regime with the effective diffusion constant $v_0^2/(2D_\mathrm{r})$. In this case, the mean time of first passage of an active Brownian particle over the distance a in any direction, scales as

$$t_\mathrm{fp}(\to a) \propto \frac{a^2 D_\mathrm{r}}{v_0^2}. \tag{2.9}$$

Here, travelling by a in either direction is counted as passage [136]. Even in this idealised case, the scaling of the first passage time is suboptimal. In a more applied setting, e.g., a microrobot travelling through human veins, no better results are to be expected. This is because for medical applications, e.g., with drug delivery, the direction of the travel usually matters. For a directed first passage, i.e., travelling a certain distance in a certain direction, the mean time of first passage diverges to infinity [136].

These considerations show, that it seems extremely unpractical, to say the least, to inject simple active Brownian particles into a patient, and hope for delivery. To this end, it makes sense, to augment the microrobots with a means of intelligent steering, such that the random Brownian motion turns into a directed, guided motion. In publication **P5**, we model this with a reinforcement learning algorithm. This gives an additional term in the equation of motion Eq. (2.2) for the orientation, which turns into

$$\dot{\phi} = \sqrt{2D_\mathrm{r}}\zeta(t) + \omega_Q(\mathbf{r}(t), t). \tag{2.10}$$

In this new equation for the orientation, $\omega_Q(\mathbf{r}(t), t)$ represents the steering strategy, i.e., an angular velocity, which the particle exerts on its own orientation. In the next section (Sec. 2.2), we give a general and simple explanation of the basic functionality of the applied algorithm.

2.2 What is reinforcement learning?

Reinforcement learning is a category of machine learning algorithms, which in turn describes a subset of *artificial intelligence (AI)*. In a general sense, artificial intelligence is any machine, which emulates the intelligent problem-solving capabilities, that can be found in biological intelligence [106, 107, 137]. This can be a fixed set of instructions, given in the form of a number of conditional statements, or a dynamic set of instructions which may evolve upon acquisition of data. The latter defines a machine learning algorithm [138, 139].

The basic functionality of teaching an artificial intelligence (agent) through reinforcement learning, is based on defining a set of operations, called *actions*, which the agent may perform. Furthermore, the agent is given a certain amount of information, defining its *state*. It decides on an action, depending on the state, in which it resides, on the basis of its artificial brain. The artificial brain represents some form of data storage and can vary with the specific implementation. Among the most common are *neural networks*, or *Q-matrix tables*. The latter is used in publication **P5**. In general, the goal of training the agent is to optimise its brain towards a specific task. To this end, it is given the ability to distinguish whether the task has been successfully completed. The agent is trained by trial and error, updating the brain accordingly [140]. To elucidate how the above concepts are applied in publication **P5**, the next section (Sec. 2.2.1) discusses a simple example of reinforcement learning problem, namely a path finding problem on a finite lattice, solved with tabular Q-learning.

2.2.1 Target finding on a finite lattice

This section aims to explain tabular Q-learning, which is applied in publication **P5**. In this section, we elucidate the basic functionality by explaining its application to a simple example, namely a target finding problem on a finite lattice. A schematic of the problem is shown in Fig. 2.1. An artificial intelligence (agent, symbolised by the dog) is placed anywhere on a finite lattice (symbolised by the square boxes). The objective is, to enable the agent to navigate reliably to the lattice position of a target (symbolised by the snack), irrespective of the starting point. In order to build a reinforcement learning model, one needs to decide, what information the agent receives. All possible positions on the lattice are indexed arbitrarily, but uniquely. The agent knows the index of its current location. In the case depicted in Fig. 2.1, this defines the state space of 32 states. One furthermore defines the actions, which the agent can perform in order to solve the given task. Here, the agent may go one discrete step in each vertical and horizontal direction. These actions are also uniquely indexed, e.g., going right $\widehat{=}$ 1, going up $\widehat{=}$ 2, going left $\widehat{=}$ 3, going down $\widehat{=}$ 4.

The artificial brain, which encodes the strategy of the agent, is given by a simple

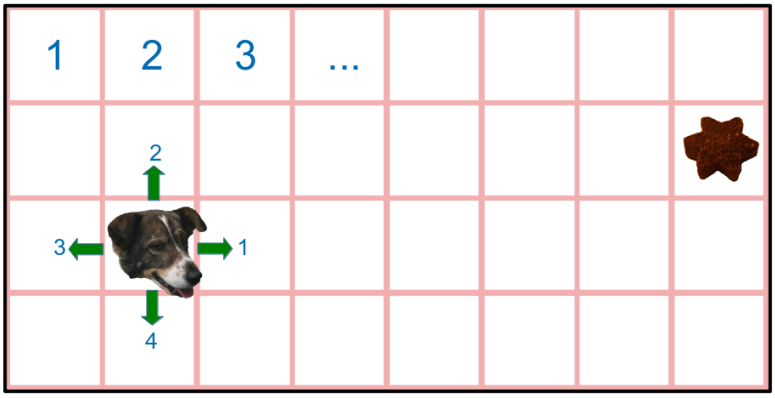

Figure 2.1: Schematic of the setup for target finding on a finite lattice. The artificial intelligence (represented by the dog) learns to navigate towards a goal (represented by the snack, right). The boxes define the states, and are uniquely indexed ($i \in \{1, 2, 3, ..\}$). The actions going in a certain direction ($\{\rightarrow, \uparrow, \leftarrow, \downarrow\}$) are also uniquely indexed ($j \in \{1, 2, 3, 4\}$). The navigation strategy is encoded in the matrix elements $\mathcal{Q}_{ij}$. The objective of the reinforcement learning algorithm is to optimise $\mathcal{Q}$ towards an optimal strategy.

matrix, commonly denoted as $\mathcal{Q}$, giving the algorithm Q-learning its name. The strategy, which the agent executes, can be simply stated by:

$$\text{action in state i} = \arg\max_j(\mathcal{Q}_{ij}). \tag{2.11}$$

In other words, in any given state, the agent performs the action, which corresponds to the column with the highest value in row i, corresponding to its current state index.

In order to obtain a matrix, which represents the best possible navigation strategy, the agent performs the task a fixed number of M times. One single execution is denoted as an *episode*. Throughout the training procedure, the agent either performs an action, which is chosen at random, or performs an action, dictated by the matrix Q. The a priori probability to perform a random action in the first place, instead of dictated by Q, is commonly denoted as ϵ, which is decreased over the course of the training procedure, for instance linearly as

$$\epsilon(m, M) = 1 - \frac{m}{M}, \tag{2.12}$$

where m denotes the current episode and M the total number of episodes. This decreasing probability of executing a random action reflects the lack of knowledge of the agent in the beginning, and on the other hand, the confidence in the trained strategy, at the end of the training.

The optimisation of the matrix Q is performed through the formula

$$\mathcal{Q}_{ij}^{\text{new}} = \mathcal{Q}_{ij}^{\text{old}} + \alpha \left(\mathcal{R} + \gamma \max_{k}(\mathcal{Q}_{i'k}) - \mathcal{Q}_{ij}^{\text{old}} \right), \tag{2.13}$$

which is applied after each executed action [141,142]. Here, i denotes the state prior to the performed action with index j, chosen through Eq. (2.11). $\mathcal{R}$ denotes the instantaneous reward, according to the outcome of the action. In this example, it may be $\mathcal{R} = 1$, only if the agent reaches the target. The term $\gamma \max_k(\mathcal{Q}_{i'k})$ enables the agent to value rewards in the future of the episode. $\max_k(\mathcal{Q}_{i'k})$ denotes the value in the i'-th row after the action. The *discount rate* $\gamma \in [0, 1]$ quantifies how much the agent values future rewards against instantaneous rewards, and is typically chosen close to 1. Finally, the parameter $\alpha \in [0, 1]$ denotes the learning rate. At $\alpha = 0$, the agent learns nothing, while at $\alpha = 1$, the algorithm displays no convergence, since the update via Eq. (2.13), deletes previous experience immediately. In practice, α is typically chosen close to 0. After all M episodes are performed, the hope is to receive a matrix Q, which enables the agent to navigate to the target efficiently, irrespective of the initial position [141, 142].

Chapter 3

Scientific publications

P1 Topology of Orientational Defects in Confined Smectic Liquid Crystals

Reproduced from

P. A. Monderkamp, R. Wittmann, L. B. G. Cortes, D. G. A. L. Aarts, F. Smallenburg and H. Löwen,
Topology of Orientational Defects in Confined Smectic Liquid Crystals,
Phys. Rev. Lett. **127**, 198001 (2021),

Digital Object Identifier (DOI): `https://doi.org/10.1103/PhysRevLett.127.198001`

Statement of contribution

R. Wittmann and I contributed equally to this publication.
R. Wittmann, H. Löwen, and I developed the model for the topological charge distribution.
D. G. A. L. Aarts and L. B. G. Cortes performed the experiments.
I performed the numerical simulations, with mentoring by F. Smallenburg, who designed an algorithm for the detection of tetratic point charges.
I designed the figures.
R. Wittmann and I wrote the paper and finalised the manuscript.
Funding and overseeing was provided by D. G. A. L. Aarts and H. Löwen. All authors contributed text associated with their respective expertise in the paper and supplemental material.

I would like to specifically acknowledge the work of the anonymous referee, who provided extraordinarily helpful insight and gave considerable inspiration for classifying the quarter charges explicitly as tetratic point charges.

P1.1 Paper: Topology of orientational defects in confined smectic liquid crystals

PHYSICAL REVIEW LETTERS **127,** 198001 (2021)

Editors' Suggestion Featured in Physics

Topology of Orientational Defects in Confined Smectic Liquid Crystals

Paul A. Monderkamp,[1] René Wittmann,[1,*] Louis B. G. Cortes,[2] Dirk G. A. L. Aarts,[3] Frank Smallenburg,[4] and Hartmut Löwen[1]

[1]*Institut für Theoretische Physik II: Weiche Materie, Heinrich-Heine-Universität Düsseldorf, Universitätsstraße 1, 40225 Düsseldorf, Germany*

[2]*School of Applied and Engineering Physics, Cornell University, Ithaca, New York 14853, USA*

[3]*Department of Chemistry, Physical and Theoretical Chemistry Laboratory, University of Oxford, South Parks Road, Oxford OX1 3QZ, United Kingdom*

[4]*Laboratoire de Physique des Solides, CNRS, Université Paris-Saclay, 91405 Orsay, France*

(Received 8 March 2021; revised 28 June 2021; accepted 22 September 2021; published 3 November 2021)

We propose a general formalism to characterize orientational frustration of smectic liquid crystals in confinement by interpreting the emerging networks of grain boundaries as objects with a topological charge. In a formal idealization, this charge is distributed in pointlike units of quarter-integer magnitude, which we identify with tetratic disclinations located at the end points and nodes. This coexisting nematic and tetratic order is analyzed with the help of extensive Monte Carlo simulations for a broad range of two-dimensional confining geometries as well as colloidal experiments, showing how the observed defect networks can be universally reconstructed from simple building blocks. We further find that the curvature of the confining wall determines the anchoring behavior of grain boundaries, such that the number of nodes in the emerging networks and the location of their end points can be tuned by changing the number and smoothness of corners, respectively.

DOI: 10.1103/PhysRevLett.127.198001

Topological defects are ubiquitous in ordered states of matter [1–5] and thus also emerge as a characteristic feature of liquid crystals [6–11], which exhibit various degrees of positional and orientational ordering [6,12–17]. Frustrated orientational order in nematic liquid crystals typically manifests itself in the form of singular points or lines. Defects of this type may spontaneously form and annihilate in bulk due to fluctuations [18], external influences such as electromagnetic fields [19–23], changes in temperature [24,25], or active motion [26–28]. In these processes, the defect strength, quantified by a half-integer topological charge Q, is subject to a universal conservation law [29,30]. The formation of topological defects can further be triggered in a controlled manner through confining the particles [31–47] or inserting an obstacle [48–55]. In this case, the precise type, number, and location of defects depend on the particular geometry [56–58] and particle properties [43,59–62], due to a delicate balance between elastic distortions and surface anchoring.

The characteristic positional order of smectic liquid crystals breaks the symmetry of the homogeneous nematic phase and affects the elastic properties [6,63]. The constraints associated with the layer structure [64,65] stabilize distortions of the bulk smectic lattice [66,67] which do not exist in nematic liquid crystals [6]. These include purely positional defects called edge dislocations [68–71] but also more complex objects like focal conic domains [72–75]. In many cases, orientational frustration in smectic phases can be well described in terms of topological defects in the nematic order that is inherent to the symmetry of the smectic phase. However, in the paradigmatic case of confined two-dimensional lyotropic systems, the formation of grain boundaries largely dominates over strong elastic deformations [76–78]. At these grain boundaries, the nematic order present in the bulk smectic phase breaks down, hindering a classification of the emerging orientational patterns in terms of nematic topology alone.

In this Letter, we demonstrate that extremely confined smectic systems can be effectively described in terms of topological defects in the tetratic order due to the strong preference of smectic layers to tilt at a grain boundary by approximately 90°. The tetratic topology is thus not only important in systems with tetratic bulk symmetry [79–82] but also a vital ingredient to a comprehensive picture of frustrated smectics. In detail, we identify quarter-integer tetratic disclinations, which materialize in pairs at the extremities of grain boundaries, as the elementary topological unit of smectic liquid crystals. In turn, the notion of a nematic disclination expands to a spatially extended defect structure whose half-integer charge follows from the sum of its tetratic components, thereby acting as a spatial charge distribution, as exemplified in Fig. 1. To unveil the full implications of coexisting nematic and tetratic order, we use particle-resolved computer simulations and colloidal experiments on hard rods to create different defect structures in a large range of two-dimensional geometries.

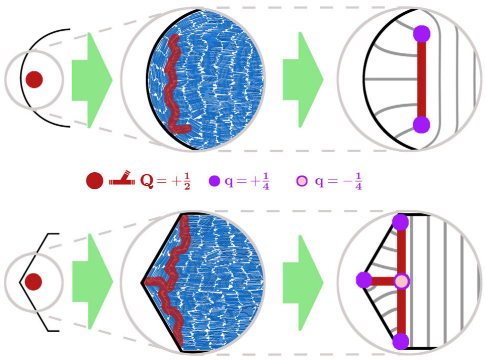

FIG. 1. Topological characterization of grain boundaries in confined smectic liquid crystals. Left: coarse-grained topological structure with an idealized nematic disclination of half-integer charge Q induced by the presumed planar alignment with the nearby wall. Middle: particle-resolved simulation snapshots of hard rods with highlighted grain boundaries in the form of a line close to a circular wall (top row) and a network induced by corners (bottom row). Right: continuum model with quarter-integer tetratic point charges q at the end points and nodes, which can be interpreted as the distribution of the spatially extended charge Q.

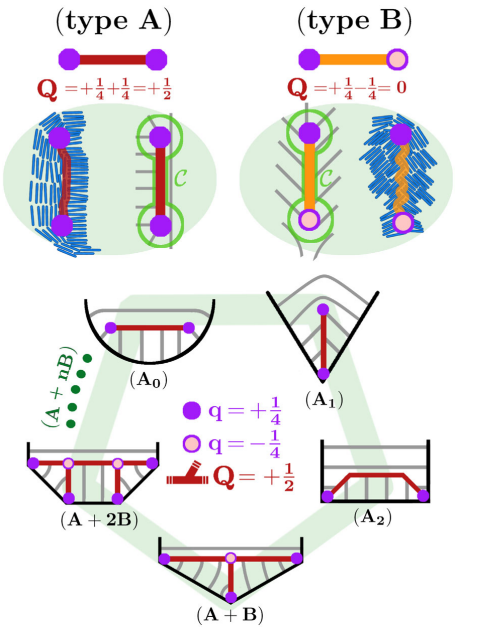

FIG. 2. Survey of grain boundaries with different connectivities in smectic liquid crystals at a convex confining wall. Top: composition of the two fundamental building blocks with total nematic charge $Q = 1/2$ (type A, red line) and $Q = 0$ (type B, orange line), determined by the tetratic quarter charges q (dots) at the end points. The illustration of bulk orientational ordering depicts a typical arrangement of the surrounding rods and a schematic continuum picture with idealized straight grain boundaries separating regions of perpendicular smectic layers (grey lines). The closed contour $\mathcal{C}$ (green line) highlights the contribution of the tetratic end points to $Q = \sum q$. Bottom: relation between the geometry-dependent manifestations of $Q = +1/2$ grain-boundary networks (red) in smectics confined to polygons. The simplest structure (A_m) only contains one type-A defect with $m \in \{0, 1, 2\}$ of its end points attached to a corner of the confining wall. In general, complex networks $(A + nB)$ can form, which amounts to adding n building blocks of type B. Approaching the limit $n \to \infty$, the network detaches from the increasingly smooth corners, gradually reverting to (A_0), as the tetratic defects in the type-B branches annihilate [83].

Defining the grain boundaries connecting different types of tetratic disclinations as fundamental building blocks, we provide the basic toolbox to characterize the more complex smectic defect networks emerging in the presence of multiple corners, as illustrated in Fig. 2. Thereby, our approach visualizes the topological charge conservation $\sum q = \sum Q = 1$ for both individual tetratic point defects q and defect networks with nematic charge Q, whose typical connectivity depends on the curvature landscape of the confining wall.

To create the smectic structures for each confinement, we perform canonical Monte Carlo (MC) simulations on $N = 1000$ hard discorectangles [84] of aspect ratio $p = 15$ within two-dimensional cavities, bounded by WCA-like soft walls [85,86]; see Supplemental Material [83]. We randomly initialize the system at a low area fraction $\eta_0 \ll 1$. The system is quickly compressed at a rate of $\Delta\eta_1 = 4.15 \times 10^{-7}$ per MC cycle to an area fraction $\eta_1 \approx 0.29$, where the isotropic-nematic transition is expected [87]. We subsequently compress the system at a lower rate $\Delta\eta_2 = 4.625 \times 10^{-8}$ per MC cycle until the system reaches the target area fraction of $\eta_2 = 0.75$ and exhibits smectic order. This protocol ensures that the system is close to equilibrium at all times. After equilibration, we use cluster analysis to identify domains with different orientational order and generate statistics. For each state, we determine local nematic $S(\mathbf{r})$ and tetratic $T(\mathbf{r})$ order parameter fields to identify the composition of topological defects [83].

On the experimental side, we analyze smectic structures emerging at the bottom of tailored cavities at sedimentation-diffusion equilibrium of colloidal silica rods [77]. The synthetic rods [88] have a small polydispersity in length and diameter. They are dispersed into a 1 mM NaCl aqueous solution [78], which leads to a short-ranged repulsion and effective hard-rod-like interactions. The degenerate planar anchoring at the bottom wall allows us to capture images of quasi-two-dimensional smectic states in the horizontal plane. Using bright-field

microscopy with an objective of high numerical aperture, we can discriminate most rods and thus determine the local order.

Our numerical observations are summarized in Fig. 3. The common feature of all structures is a large, defect-free central domain, characteristic for the bridge state [76–78]. The detailed appearance of the topological defects, however, sensitively depends on the confining geometry. To verify that the overall topology is universal, we decorate [83] all representative snapshots with a defect structure assembled from the building blocks in Fig. 2. By doing so, we recognize in each system in Fig. 3 two separate grain-boundary networks representing a $Q = +1/2$ charge each, while the remaining defects do not carry any nematic charge Q as a whole. The intriguing dependence of the emerging defect networks on the geometric properties of the confining wall can be perceived according to the schematic cycle in Fig. 2, as laid out in the following three paragraphs.

The most common defects are linear grain boundaries of the general type A, which we further discriminate by the location of the two positively charged tetratic end points, cf. Fig. 2. The circular cavity in Fig. 3 typically features two opposing bulk defects of subtype A_0, i.e., both end points possessing isolated tetratic signals are detached from the wall. Therefore, the orientation of rods around the perimeter changes continuously and all particles within the system belong to a single domain. Upon switching from the uniformly curved circular confinement to different polygons, the grain boundaries usually extend towards the corners, such that the tetratic defects anchor at the wall. The invariance of our topological picture can be illustrated by considering confinements with smooth corners [83]. The example of a rounded equilateral triangle in Fig. 3 indicates

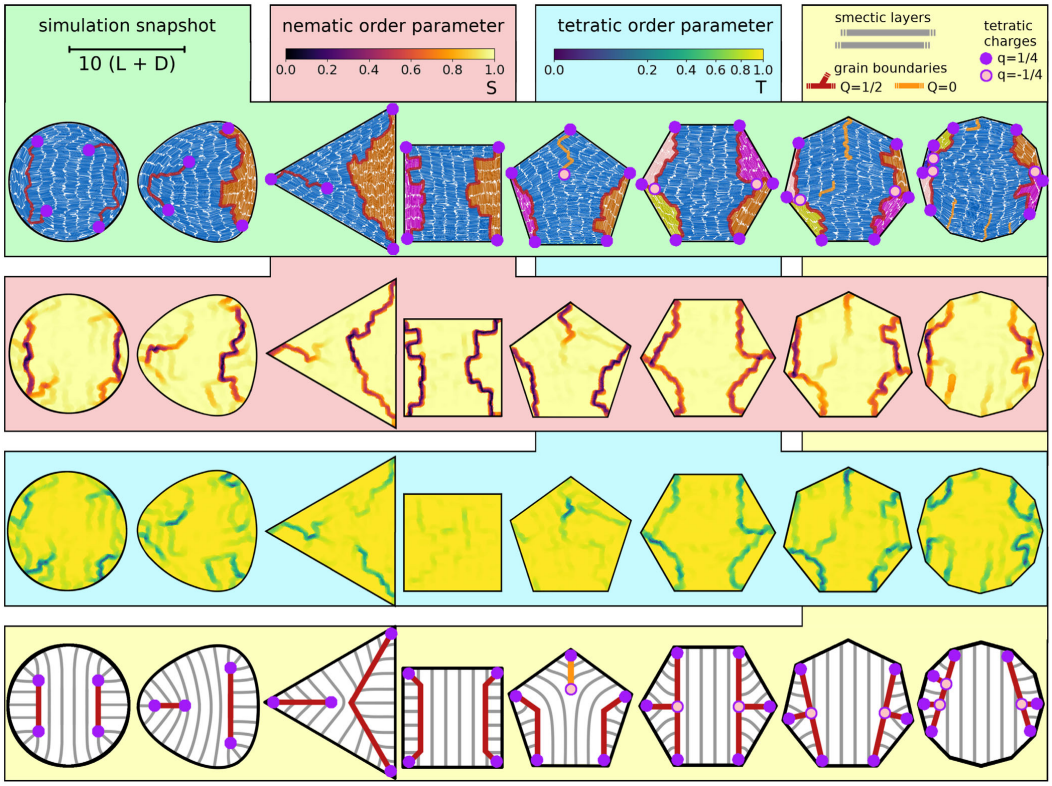

FIG. 3. Topological defect structure of representative simulations for hard rods with aspect ratio $p = 15$ in different convex confining geometries. Top row: particle snapshots with superimposed networks of grain boundaries and isolated tetratic point defects, compare Fig. 2. The color of the rods highlights individual domains according to cluster analysis. Second row: nematic order parameter field $S(\mathbf{r})$. Third row: tetratic order parameter field $T(\mathbf{r})$. Point defects at the confining wall are not visible. Bottom row: idealized continuum interpretation of the depicted snapshots, as detailed in the Supplemental Material [83].

that one grain boundary turns into a true domain boundary, i.e., a type-A_2 defect, as both its end points move towards two of the three corners. The second grain boundary gradually turns into a type-A_1 defect, as one end point attaches with the remaining corner and the other end extends into the center of the large domain. This structure is most pronounced in the limit of sharp corners. We further observe that a grain boundary of type A_1 gradually contracts to a $Q = +1/2$ point defect upon decreasing the opening angle [83]. Turning to a square cavity in Fig. 3, the additional corner can accommodate the loose end point of the type-A_1 defect, resulting in the eponymous bridge structure [76,77] with two parallel type-A_2 domain boundaries, as in circular confinement, but with perfect tetratic bulk order.

Following in Fig. 3 a sequence of geometries represented by regular polygons, the increasing number of $q = +1/4$ charges at each corner is compensated accordingly by negative bulk charges. We thus introduce an additional type-B building block representing a pair of tetratic $q = \pm 1/4$ charges. This overall charge-neutral object with $Q = 0$ either occurs on its own (at edge dislocations in the bulk or attached to a single corner) or attaches with its negative end to other building blocks, forming a large network of grain boundaries, cf. Fig. 2. In particular, the pentagon can accommodate an individual type-B defect in addition to the two type-A_2 domain boundaries also found in square confinement (notice the difference with the free-standing type-A_1 defect with $Q = 1/2$ in the triangle). The hexagon typically features two parallel type-$(A + B)$ networks, each separating two small domains from the central bridging layers and resembling a type-A defect, like in the square, with an attached type-B defect emerging from the additional corner in the middle.

The addition of further corners allows for the formation of complex type-$(A + nB)$ networks, which contain n nodes with $q = -1/4$ and $n + 2$ branches ending on a $q = +1/4$ charge. The typical defect structure, however, gradually reverts to that in circular confinement, closing the cycle in Fig. 2. The defect networks in Fig. 3 thus detach from the confining wall, as adjacent pairs of opposite tetratic charges annihilate. Grain boundaries between pairs of defects close to annihilation typically induce only a small tilt between smectic layers, such that their nematic signal weakens and qualitatively resembles the tetratic signal (contrast, e.g., the free-standing type-B defects in the pentagon and heptagon). In general, the degree of the annihilation increases with increasing opening angle at the corners [83].

To demonstrate the experimental relevance of our classification scheme, we analyze in Fig. 4 microscopy images of colloidal rods for their orientational order, here focusing on a hexagonal domain. The experimental defect networks are typically less complex than those in the pure hard-rod simulations [83], due to the higher elasticity of the smectic layers. Nonetheless, the defect networks found consist of the same fundamental building blocks, confirming the broad applicability of our approach. Additionally, our simulation results match the previously reported experiments in square [77] and circular [78] confinement, and hence the same analysis is directly suitable to those experiments as well.

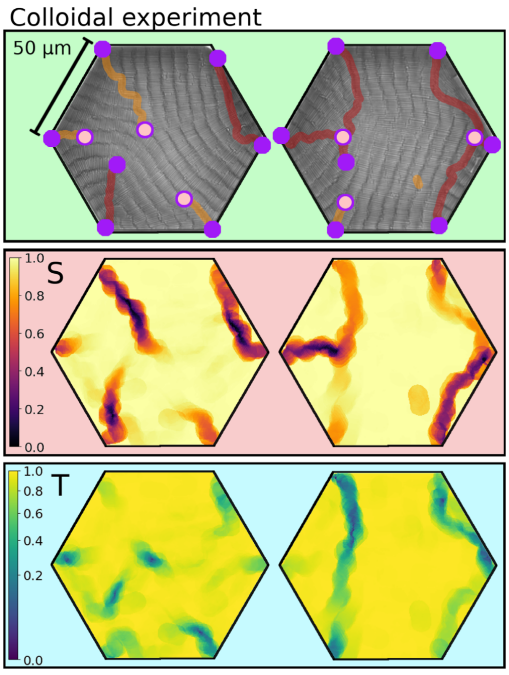

FIG. 4. Two selected sets of experimental reference data in hexagonal confinement, presented as in Fig. 3. Shown are bare bright-field microscopy images with $N = 1400 \pm 150$ colloidal rods of effective hard-rod aspect ratio $p_{\mathrm{eff}} = 10.6$ in the field of view and the extracted order parameters.

Beyond the chosen methodology, our topological toolbox can be readily employed to illustrate the coexisting nematic and tetratic orientational order of frustrated smectics in free-energy based theoretical studies [15,78,89–91], granular experiments [80–82] or molecular systems [92–94]. Regarding nonconvex confinements [78] or two-dimensional manifolds [65,95], our set of building blocks can be supplemented by a line connecting two negative tetratic charges. A generalized approach can shed more light on intersecting surfaces of grain boundaries in three-dimensions. One central implication of our analysis is that the motion of grain boundaries can be tracked through tetratic point defects, providing additional insights into the dynamics of smectics [96–99] and their nucleation [100–102], which is particularly interesting for biologically inspired nonequilibrium systems

like self-propelled rods [103–106] or growing bacterial colonies [107–109] as candidates for active smectics.

Finally, we expect that the classification of the fine structure of defects on the length scale of individual particles put forward in this work will be helpful to analyze quenched or undercooled systems, in particular those where the symmetry of an ordered phase is broken by grain boundaries that may still impose a preferred alignment between adjacent domains. One possible example would be fine-grained polycrystals, which are challenging to distinguish from amorphous solids on the single-particle level [110]. More generally, those methods could lead to a better understanding of defects in complex solids (such as protein [111] or aerosol [112] crystals) relevant for photonics [113], phononics [114] and metamaterials [115].

The authors would like to thank Daniel de las Heras, Axel Voigt, Raphael Wittkowski, and Michael te Vrugt for helpful discussions. This work was supported by the German Research Foundation (DFG) within project LO 418/20-2.

P. M. and R. W. contributed equally to this work.

*rene.wittmann@hhu.de

[1] P. M. Chaikin and T. C. Lubensky, *Topological Defects* (Cambridge University Press, Cambridge, England, 1995), pp. 495–589.
[2] N. D. Mermin, Rev. Mod. Phys. **51**, 591 (1979).
[3] T. W. B. Kibble, J. Phys. A **9**, 1387 (1976).
[4] A. Moor, A. F. Volkov, and K. B. Efetov, Phys. Rev. B **90**, 224512 (2014).
[5] Y. Liu, Z. Wang, T. Sato, M. Hohenadler, C. Wang, W. Guo, and F. F. Assaad, Nat. Commun. **10**, 2658 (2019).
[6] P.-G. de Gennes and J. Prost, *The Physics Of Liquid Crystals* (Clarendon Press, Oxford, 1993).
[7] M. Kleman and O. D. Lavrentovich, *Soft Matter Physics—An Introduction* (Springer-Verlag, Berlin, 2003).
[8] G. P. Alexander, B. G. -g. Chen, E. A. Matsumoto, and R. D. Kamien, Rev. Mod. Phys. **84**, 497 (2012).
[9] K. Sentker, A. W. Zantop, M. Lippmann, T. Hofmann, O. H. Seeck, A. V. Kityk, A. Yildirim, A. Schönhals, M. G. Mazza, and P. Huber, Phys. Rev. Lett. **120**, 067801 (2018).
[10] S. Čopar, N. A. Clark, M. Ravnik, and S. Žumer, Soft Matter **9**, 8203 (2013).
[11] L. Radzihovsky, Phys. Rev. Lett. **125**, 267601 (2020).
[12] R. Teerakapibal, C. Huang, A. Gujral, M. D. Ediger, and L. Yu, Phys. Rev. Lett. **120**, 055502 (2018).
[13] P. Bolhuis and D. Frenkel, J. Chem. Phys. **106**, 666 (1997).
[14] L. Mederos, E. Velasco, and Y. Martínez-Ratón, J. Phys. Condens. Matter **26**, 463101 (2014).
[15] R. Wittmann, C. E. Sitta, F. Smallenburg, and H. Löwen, J. Chem. Phys. **147**, 134908 (2017).
[16] S. Dussi, N. Tasios, T. Drwenski, R. van Roij, and M. Dijkstra, Phys. Rev. Lett. **120**, 177801 (2018).
[17] V. F. D. Peters, M. Vis, A. G. García, H. H. Wensink, and R. Tuinier, Phys. Rev. Lett. **125**, 127803 (2020).
[18] G. P. Crawford and S. Zumer, *Liquid Crystals in Complex Geometries: Formed by Polymer and Porous Networks* (CRC Press, London, 1996), https://doi.org/10.1201/9781482272796.
[19] Y. Reznikov, O. Ostroverkhova, K. D. Singer, J.-H. Kim, S. Kumar, O. Lavrentovich, B. Wang, and J. L. West, Phys. Rev. Lett. **84**, 1930 (2000).
[20] Y. Gu and N. L. Abbott, Phys. Rev. Lett. **85**, 4719 (2000).
[21] H. Stark, Phys. Rev. E **66**, 032701 (2002).
[22] P. E. Cladis, W. van Saarloos, P. L. Finn, and A. R. Kortan, Phys. Rev. Lett. **58**, 222 (1987).
[23] D. R. Link, J. E. Maclennan, and N. A. Clark, Phys. Rev. Lett. **77**, 2237 (1996).
[24] T. Ohzono and J.-i. Fukuda, Soft Matter **8**, 11552 (2012).
[25] C. D. Muzny and N. A. Clark, Phys. Rev. Lett. **68**, 804 (1992).
[26] X.-Q. Shi and Y.-Q. Ma, Nat. Commun. **4**, 3013 (2013).
[27] V. Narayan, S. Ramaswamy, and N. Menon, Science **317**, 105 (2007).
[28] A. Chardac, L. A. Hoffmann, Y. Poupart, L. Giomi, and D. Bartolo, arXiv:2103.03861 [Phys. Rev. X (to be published)].
[29] W. Fulton, *Algebraic Topology—A First Course* (Springer-Verlag, Berlin, 1995).
[30] B. Senyuk, Q. Liu, S. He, R. D. Kamien, R. B. Kusner, T. C. Lubensky, and I. I. Smalyukh, Nature (London) **493**, 200 (2013).
[31] O. D. Lavrentovich and E. M. Terentjev, Zh. Eksp. Teor. Fiz. **91**, 2084 (1986).
[32] O. D. Lavrentovich, Liq. Cryst. **24**, 117 (1998).
[33] Y.-K. Kim, S. V. Shiyanovskii, and O. D. Lavrentovich, J. Condens. Matter Phys. **25**, 404202 (2013).
[34] O. J. Dammone, I. Zacharoudiou, R. P. A. Dullens, J. M. Yeomans, M. P. Lettinga, and D. G. A. L. Aarts, Phys. Rev. Lett. **109**, 108303 (2012).
[35] O. V. Manyuhina, K. B. Lawlor, M. C. Marchetti, and M. J. Bowick, Soft Matter **11**, 6099 (2015).
[36] J. Dzubiella, M. Schmidt, and H. Löwen, Phys. Rev. E **62**, 5081 (2000).
[37] Y. Trukhina and T. Schilling, Phys. Rev. E **77**, 011701 (2008).
[38] S. Varga, Y. Martínez-Ratón, and E. Velasco, J. Phys. Condens. Matter **26**, 075104 (2014).
[39] P. E. Brumby, H. H. Wensink, A. J. Haslam, and G. Jackson, Langmuir **33**, 11754 (2017).
[40] A. H. Lewis, I. Garlea, J. Alvarado, O. J. Dammone, P. D. Howell, A. Majumdar, B. M. Mulder, M. Lettinga, G. H. Koenderink, and D. G. A. L. Aarts, Soft Matter **10**, 7865 (2014).
[41] S. Kralj and A. Majumdar, Proc. R. Soc. A **470**, 20140276 (2014).
[42] A. Majumdar and A. Lewis, Liq. Cryst. **43**, 2332 (2016).
[43] I. C. Gârlea, P. Mulder, J. Alvarado, O. J. Dammone, D. G. A. L. Aarts, M. P. Lettinga, G. H. Koenderink, and B. M. Mulder, Nat. Commun. **7**, 12112 (2016).
[44] M. V. Kurik and O. D. Lavrentovich, Sov. Phys. Usp. **31**, 196 (1988).
[45] X. Yao and J. Z. Y. Chen, Phys. Rev. E **101**, 062706 (2020).
[46] E. Basurto, P. Gurin, S. Varga, and G. Odriozola, Phys. Rev. Research **2**, 013356 (2020).
[47] K. H. Kil, A. Yethiraj, and J. S. Kim, Phys. Rev. E **101**, 032705 (2020).

[48] P. Poulin, V. Cabuil, and D. A. Weitz, Phys. Rev. Lett. **79**, 4862 (1997).
[49] R. W. Ruhwandl and E. M. Terentjev, Phys. Rev. E **56**, 5561 (1997).
[50] D. Andrienko, G. Germano, and M. P. Allen, Phys. Rev. E **63**, 041701 (2001).
[51] S. Čopar, T. Porenta, V. S. R. Jampani, I. Muševič, and S. Žumer, Soft Matter **8**, 8595 (2012).
[52] J. M. Ilnytskyi, A. Trokhymchuk, and M. Schoen, J. Chem. Phys. **141**, 114903 (2014).
[53] S. Püschel-Schlotthauer, V. Meiwes Turrin, C. K. Hall, M. G. Mazza, and M. Schoen, Langmuir **33**, 2222 (2017).
[54] B. Senyuk, Q. Liu, Y. Yuan, and I. I. Smalyukh, Phys. Rev. E **93**, 062704 (2016).
[55] K. Chen, O. J. Gebhardt, R. Devendra, G. Drazer, R. D. Kamien, D. H. Reich, and R. L. Leheny, Soft Matter **14**, 83 (2018).
[56] T. Araki, F. Serra, and H. Tanaka, Soft Matter **9**, 8107 (2013).
[57] M. G. Campbell, M. Tasinkevych, and I. I. Smalyukh, Phys. Rev. Lett. **112**, 197801 (2014).
[58] I. C. Gârlea, O. Dammone, J. Alvarado, V. Notenboom, Y. Jia, G. H. Koenderink, D. G. A. L. Aarts, M. P. Lettinga, and B. M. Mulder, Sci. Rep. **9**, 20391 (2019).
[59] G. van Anders, D. Klotsa, N. K. Ahmed, M. Engel, and S. C. Glotzer, Proc. Natl. Acad. Sci. U.S.A. **111**, E4812 (2014).
[60] J. Alvarado, B. M. Mulder, and G. H. Koenderink, Soft Matter **10**, 2354 (2014).
[61] M. Chiappini, T. Drwenski, R. van Roij, and M. Dijkstra, Phys. Rev. Lett. **123**, 068001 (2019).
[62] D. Revignas and A. Ferrarini, Phys. Rev. Lett. **125**, 267802 (2020).
[63] J. P. F. Lagerwall and F. Giesselmann, ChemPhysChem **7**, 20 (2006).
[64] V. Poénaru, Commun. Math. Phys. **80**, 127 (1981).
[65] R. A. Mosna, D. A. Beller, and R. D. Kamien, Phys. Rev. E **86**, 011707 (2012).
[66] B. G. -g. Chen, G. P. Alexander, and R. D. Kamien, Proc. Natl. Acad. Sci. U.S.A. **106**, 15577 (2009).
[67] T. Machon, H. Aharoni, Y. Hu, and R. D. Kamien, Commun. Math. Phys. **372**, 525 (2019).
[68] R. B. Meyer, B. Stebler, and S. T. Lagerwall, Phys. Rev. Lett. **41**, 1393 (1978).
[69] P. Chen and C.-Y. D. Lu, J. Phys. Soc. Jpn. **80**, 094802 (2011).
[70] C. Zhang, A. M. Grubb, A. J. Seed, P. Sampson, A. Jákli, and O. D. Lavrentovich, Phys. Rev. Lett. **115**, 087801 (2015).
[71] R. D. Kamien and R. A. Mosna, New J. Phys. **18**, 053012 (2016).
[72] M. Kléman and O. Lavrentovich, Eur. Phys. J. E **2**, 47 (2000).
[73] J. P. Bramble, S. D. Evans, J. R. Henderson, T. J. Atherton, and N. J. Smith, Liq. Cryst. **34**, 1137 (2007).
[74] Y. H. Kim, D. K. Yoon, M.-C. Choi, H. S. Jeong, M. W. Kim, O. D. Lavrentovich, and H.-T. Jung, Langmuir **25**, 1685 (2009).
[75] D. B. Liarte, M. Bierbaum, R. A. Mosna, R. D. Kamien, and J. P. Sethna, Phys. Rev. Lett. **116**, 147802 (2016).
[76] T. Geigenfeind, S. Rosenzweig, M. Schmidt, and D. de las Heras, J. Chem. Phys. **142**, 174701 (2015).
[77] L. B. G. Cortes, Y. Gao, R. P. A. Dullens, and D. G. A. L. Aarts, J. Phys. Condens. Matter **29**, 064003 (2017).
[78] R. Wittmann, L. B. G. Cortes, H. Löwen, and D. G. A. L. Aarts, Nat. Commun. **12**, 623 (2021).
[79] Y. Li, H. Miao, H. Ma, and J. Z. Y. Chen, Soft Matter **9**, 11461 (2013).
[80] V. Narayan, N. Menon, and S. Ramaswamy, J. Stat. Mech. (2006) P01005.
[81] M. González-Pinto, F. Borondo, Y. Martínez-Ratón, and E. Velasco, Soft Matter **13**, 2571 (2017).
[82] A. D.-D. Armas, M. Maza-Cuello, Y. Martínez-Ratón, and E. Velasco, Phys. Rev. Research **2**, 033436 (2020).
[83] See Supplemental Material at http://link.aps.org/supplemental/10.1103/PhysRevLett.127.198001 for a detailed description of the physical model, simulation procedure and analysis of the observed topological structures. We also discuss some additional simulation results for different isosceles triangles, triangles with rounded corners and explore the dependence on system size, aspect ratio and density.
[84] C. Vega and S. Lago, Comput. Chem. **18**, 55 (1994).
[85] H. C. Andersen, D. Chandler, and J. D. Weeks, J. Chem. Phys. **56**, 3812 (1972).
[86] N. Metropolis, A. W. Rosenbluth, M. N. Rosenbluth, A. H. Teller, and E. Teller, J. Chem. Phys. **21**, 1087 (1953).
[87] M. A. Bates and D. Frenkel, J. Chem. Phys. **112**, 10034 (2000).
[88] A. Kuijk, D. V. Byelov, A. V. Petukhov, A. van Blaaderen, and A. Imhof, Faraday Discuss. **159**, 181 (2012).
[89] R. Wittmann, M. Marechal, and K. Mecke, J. Phys. Condens. Matter **28**, 244003 (2016).
[90] M. Y. Pevnyi, J. V. Selinger, and T. J. Sluckin, Phys. Rev. E **90**, 032507 (2014).
[91] J. Xia, S. MacLachlan, T. J. Atherton, and P. E. Farrell, Phys. Rev. Lett. **126**, 177801 (2021).
[92] J. Jeong and M. W. Kim, Phys. Rev. Lett. **108**, 207802 (2012).
[93] J.-P. Michel, E. Lacaze, M. Goldmann, M. Gailhanou, M. de Boissieu, and M. Alba, Phys. Rev. Lett. **96**, 027803 (2006).
[94] D. Coursault, B. Zappone, A. Coati, A. Boulaoued, L. Pelliser, D. Limagne, N. Boudet, B. H. Ibrahim, A. de Martino, M. Alba *et al.*, Soft Matter **12**, 678 (2016).
[95] E. Allahyarov, A. Voigt, and H. Löwen, Soft Matter **13**, 8120 (2017).
[96] J. K. G. Dhont, *An Introduction to Dynamics of Colloids* (Elsevier, New York, 1996), vol. 2.
[97] E. Grelet, M. P. Lettinga, M. Bier, R. van Roij, and P. van der Schoot, J. Phys. Condens. Matter **20**, 494213 (2008).
[98] R. Kurita, S. Mitsui, and H. Tanaka, Phys. Rev. Lett. **119**, 108003 (2017).
[99] M. Chiappini, E. Grelet, and M. Dijkstra, Phys. Rev. Lett. **124**, 087801 (2020).
[100] T. Schilling and D. Frenkel, Phys. Rev. Lett. **92**, 085505 (2004).
[101] R. Ni, S. Belli, R. van Roij, and M. Dijkstra, Phys. Rev. Lett. **105**, 088302 (2010).

[102] A. Cuetos, E. Sanz, and M. Dijkstra, Faraday Discuss. **144**, 253 (2010).
[103] M. Bär, R. Großmann, S. Heidenreich, and F. Peruani, Annu. Rev. Condens. Matter Phys. **11**, 441 (2020).
[104] N. Kumar, R. K. Gupta, H. Soni, S. Ramaswamy, and A. K. Sood, Phys. Rev. E **99**, 032605 (2019).
[105] A. Maitra, P. Srivastava, M. C. Marchetti, S. Ramaswamy, and M. Lenz, Phys. Rev. Lett. **124**, 028002 (2020).
[106] M. C. Bott, F. Winterhalter, M. Marechal, A. Sharma, J. M. Brader, and R. Wittmann, Phys. Rev. E **98**, 012601 (2018).
[107] D. van Holthe tot Echten, G. Nordemann, M. Wehrens, S. Tans, and T. Idema, arXiv:2003.10509.
[108] Z. You, D. J. G. Pearce, and L. Giomi, Sci. Adv. **7**, abc8685 (2021).
[109] K. Copenhagen, R. Alert, N. S. Wingreen, and J. W. Shaevitz, Nat. Phys. **17**, 211 (2021).
[110] H. Zhang and Y. Han, Phys. Rev. X **8**, 041023 (2018).
[111] D. S. Tsekova, D. R. Williams, and J. Y. Heng, Chem. Eng. Sci. **77**, 201 (2012).
[112] U. Dusek, G. Frank, L. Hildebrandt, J. Curtius, J. Schneider, S. Walter, D. Chand, F. Drewnick, S. Hings, D. Jung *et al.*, Science **312**, 1375 (2006).
[113] L. Lu, J. D. Joannopoulos, and M. Soljačić, Nat. Photonics **8**, 821 (2014).
[114] G. Yi and B. D. Youn, Struct. Multidiscip. Optim. **54**, 1315 (2016).
[115] Y.-F. Wang, Y.-Z. Wang, B. Wu, W. Chen, and Y.-S. Wang, Appl. Mech. Rev. **72**, 040801 (2020).

P1.2 Supplemental material: Topology of orientational defects in confined smectic liquid crystals

Supplemental Material: Topology of orientational defects in confined smectic liquid crystals

Paul A. Monderkamp,[1] René Wittmann,[1] Louis B. G. Cortes,[2]
Dirk G. A. L. Aarts,[3] Frank Smallenburg,[4] and Hartmut Löwen[1]

[1] *Institut für Theoretische Physik II: Weiche Materie, Heinrich-Heine-Universität Düsseldorf, Universitätsstraße 1, 40225 Düsseldorf, Germany*
[2] *School of Applied and Engineering Physics, Cornell University, Ithaca, NY 14853, USA*
[3] *Department of Chemistry, Physical and Theoretical Chemistry Laboratory, University of Oxford, South Parks Road, Oxford OX1 3QZ, United Kingdom*
[4] *Laboratoire de Physique des Solides, CNRS, Université Paris-Saclay, 91405 Orsay, France*

(Dated: September 22, 2021)

1. NUMERICAL METHODS

A. Model system

We model our system as fluid of hard discorectangles that are defined as rectangles with length L and width D capped by two half discs with diameter D, interacting via pure excluded-volume interaction [1]. We focus on particles with length-to-width ratio $p = L/D = 15$. The coordinates of the particles are defined via their position vectors $\mathbf{r}_n$ and orientation vectors $\hat{\mathbf{u}}_n = (\cos\varphi_n, \sin\varphi_n)^T$, where φ_n is the angle of the nth particle with an arbitrary fixed axis. The particles are confined within various two dimensional cavities as depicted in Fig. 3 in the main manuscript. To force particles from the outside of the cavity to the inside, we model the interaction of the particles with the walls as a soft cut-off Weeks-Chandler-Anderson (WCA) potential [2]. To determine the interaction energy of the particles with the walls in our model, we consider the discoidal caps sitting at $\mathbf{r}_n \pm L/2\ \hat{\mathbf{u}}_\mathbf{n}$. Defining the relative positions x_+ and x_- of both discs to the walls of the confinement, we compute the wall energy of the nth rod as

$$V(\mathbf{r}_n, \hat{\mathbf{u}}_\mathbf{n}) = V(x_+) + V(x_-) \tag{S.1}$$

with the potential

$$V(x) = \begin{cases} \Phi(x_0) + \Phi'(x_0)(x - x_0) & \text{for } x \leq x_0 \\ \Phi(x) & \text{for } x_0 > x \end{cases} \tag{S.2}$$

providing a version, linearized below $x_0 = D/2$ and thus extended to the outside of the cavity, of the regular WCA-potential

$$\Phi(x) = \begin{cases} 4\epsilon \left[\left(\frac{D}{x}\right)^{12} - \left(\frac{D}{x}\right)^{6} \right] + \epsilon & \text{for } x/D \leq 2^{\frac{1}{6}} \\ 0 & \text{for } x/D > 2^{\frac{1}{6}} \end{cases}, \tag{S.3}$$

where we use the energy scale $\epsilon = 10\ k_\mathrm{B}T$ to mimic nearly hard walls, thereby imposing a bias for planar surface anchoring.

B. Simulation procedure

We study systems at constant particle number N and constant temperature T using standard canonical Monte-Carlo simulations. We define the area fraction of the confined particles as $\eta = NA_\mathrm{HDR}/\mathcal{A}$ with the area of a hard discorectangle

$$A_\mathrm{HDR} = LD + \frac{\pi D^2}{4} \tag{S.4}$$

and the area $\mathcal{A}$ of the confining geometry, assuming hard walls at $x = 0$. We focus on the study of smectic states at an area fraction $\eta \approx 0.75$, where the smectic phase is stable in bulk [3].

Every simulation runs for at least 10^7 Monte-Carlo cycles. One cycle consists of N trial moves where we randomly choose one particle and, by equal probability, either displace it or rotate it. The particles are displaced by changing

their x- and y-coordinates by $\Delta_{x,y} \in [-\Delta^{\max}_{x,y}, \Delta^{\max}_{x,y}]$. Rotation is done by displacing the orientation vector $\hat{\mathbf{u}}_n$ along its orthogonal by $\Delta_{\hat{\mathbf{u}}} \in [-\Delta^{\max}_{\hat{\mathbf{u}}}, \Delta^{\max}_{\hat{\mathbf{u}}}]$ and then renormalizing. The whole trial step is accepted with the standard acceptance probability $P_{\rm acc} = \min(e^{\beta\Delta U}, 1)$ [4] where ΔU is the total change in the energy of the system. The rate with which particle trial moves are accepted depends on $\Delta^{\max}_{x,y}$ and $\Delta^{\max}_{\hat{\mathbf{u}}}$. Those quantities are adjusted over the course of the simulation to stabilize the acceptance rate at about 0.1.

To obtain the desired high-density states, we initialize our simulation by randomly placing all N particles within an augmented confinement, such that the initial area fraction is $\eta_0 \ll 1$. We then follow a compression protocol to bring the system slowly to the desired density. This is done at sufficiently low compression rates to allow the system to reach thermodynamic equilibrium at each density. Specifically, the compression procedure is divided into two stages: a first one where we increase the area fraction of by shrinking the confinement with a relatively high compression rate $\Delta\eta_1 = 4.15 \times 10^{-7}$ per MC-cycle to an area fraction $\eta_1 \approx 0.29$ where nematic ordering starts to occur. This is observed to lie slightly below the area fraction of the isotropic to nematic phase transition [5]. Once the system reaches η_1 we reduce the compression rate to $\Delta\eta_2 = 4.625 \times 10^{-8}$ per MC-cycle and compress further until the desired target area fraction η_2 (we typically choose $\eta_2 = 0.75$) is reached and we sample the results. As there is a significant difference between nematic and smectic states in a square cavity, we equilibrated the systems confined to square cavities at compression rates that were slower than those for the other geometries by a factor of four.

C. Data analysis

In this section, we define the local quantities, we use characterize the structure of the confined systems. The central quantities to our topological analysis are the nematic

$$S(\mathbf{r}) = \left|\langle e^{i2\varphi_n}\rangle_{\mathbf{r}}\right| \tag{S.5}$$

and the tetratic

$$T(\mathbf{r}) = \left|\langle e^{i4\varphi_n}\rangle_{\mathbf{r}}\right| \tag{S.6}$$

orientational order parameters, where the angled brackets $\langle ...\rangle_{\mathbf{r}}$ denote the average over all particles which intersect a local circle around $\mathbf{r}$ with radius $\xi = 5D$. $S(\mathbf{r})$ and $T(\mathbf{r})$ take values in the interval $[0, 1]$, where 0 denotes low local orientational order and 1 corresponds to high local orientational order. Furthermore we measure the local nematic director angle $\psi_2(\mathbf{r})$ and tetratic director angle $\psi_4(\mathbf{r})$ as

$$\psi_m(\mathbf{r}) = \frac{1}{m}\arccos\left(\Re\left(\frac{\langle e^{im\varphi_n}\rangle_{\mathbf{r}}}{|\langle e^{im\varphi_n}\rangle_{\mathbf{r}}|}\right)\right) \tag{S.7}$$

with $m \in \{2, 4\}$ and the real part $\Re(...)$ of a complex number. The normalized nematic $\hat{\mathbf{n}}(\mathbf{r})$ and tetratic director fields $\hat{\mathbf{t}}(\mathbf{r})$ are defined as $\hat{\mathbf{n}}(\mathbf{r}) = \cos(\psi_2)\hat{\mathbf{e}}_{\mathbf{x}} + \sin(\psi_2)\hat{\mathbf{e}}_{\mathbf{y}}$ and $\hat{\mathbf{t}}(\mathbf{r}) = \cos(\psi_4)\hat{\mathbf{e}}_{\mathbf{x}} + \sin(\psi_4)\hat{\mathbf{e}}_{\mathbf{y}}$, respectively.

To facilitate the identification of grain boundaries and to determine the number of the domains within the confinement, we perform a cluster analysis on the final equilibrated configuration based on the inter-particle distances and the relative orientations. We chose the pairwise domain criterion such that two particles k and l are assigned to the same domain if (i) the distance of their position vectors is smaller than a threshold $|\mathbf{r}_k - \mathbf{r}_l| \leq 1.3\ (L + D)$ and (ii) their relative orientation follows the criterion

$$|\hat{\mathbf{u}}_k \cdot \hat{\mathbf{u}}_l| \geq 0.95\,. \tag{S.8}$$

To further identify the fine structure of the system, we draw bonds between neighboring particles that we consider to be in the same smectic layer. For each particle i with position $\mathbf{r}_i$ and orientation $\mathbf{u}_i$, we also define the vector $\mathbf{u}^{\perp}{}_i$, which is taken to be perpendicular to $\mathbf{u}_i$. We then consider two possible neighbors: the particle that is closest to the point $\mathbf{r}_i + \mathbf{u}^{\perp}{}_i$ and the particle that is closest to $\mathbf{r}_i - \mathbf{u}^{\perp}{}_i$. By closest, we here mean the distance of the chosen point to any point on the particle's surface. A chosen particle j on each side of particle i is now considered a neighbor if

1. $|\hat{\mathbf{u}}_i \cdot \hat{\mathbf{u}}_j| > 0.9$, and
2. $|\mathbf{r}_{ij} \cdot \hat{\mathbf{u}}_i| < 0.45L$, and
3. $|\mathbf{r}_{ij} \cdot \hat{\mathbf{u}}_j| < 0.45L$,

where $\mathbf{r}_{ij} = \mathbf{r}_i - \mathbf{r}_{\mathbf{j}}$. To ensure symmetry, we remove any bonds from particle i to j where particle j is not bonded to particle i.

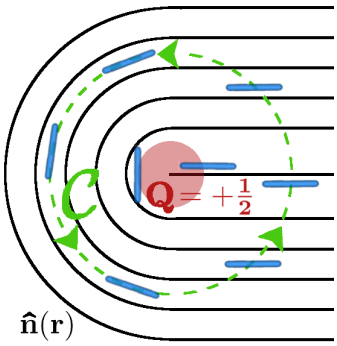

FIG. 1: Schematic depictions of the topological charge of a singularity in the director field $\hat{\mathbf{n}}(\mathbf{r})$, illustrated for a point-like $Q = +1/2$ disclination. The topological charge is calculated according to Eq. (S.9) via the winding number along a closed contour $\mathcal{C}$ (green). Circling around the defect once, the particles orientation changes by an angle of π, which results in $q = +1/2$.

2. CHARACTERIZING THE TOPOLOGICAL DEFECT STRUCTURE

A. Topological charge conservation of pointlike nematic bulk and boundary defects

To introduce the fundamental topological concepts relevant to determine and interpret the charge of a defect, we first reiterate the established methods for a fluid with pure nematic symmetry. Nematic orientational order of uniaxial liquid crystals is described by the director field $\hat{\mathbf{n}}(\mathbf{r})$, with the identification $\hat{\mathbf{n}} \equiv -\hat{\mathbf{n}}$, reflecting the apolarity of the particles. To determine the charge of the topological defects emerging in a two-dimensional system, we consider a closed contour $\mathcal{C}$ with one revolution in counter-clockwise direction, as illustrated in Fig. 1, assuming that $\mathcal{C}$ does not pass any points or regions with a discontinuous $\hat{\mathbf{n}}(\mathbf{r})$. Hence, the local orientation of the director will always return to its initial value, when traversing once along a given $\mathcal{C}$ from any starting point. This results in the topological charge Q, defined as the number of revolutions of the director relative to those of $\mathcal{C}$, being always a multiple of $1/2$, see Fig. 1a for an example with $Q = 1/2$. Introducing a parametrization κ of the contour $\mathcal{C}(\kappa)$, the topological charge can be explicitly calculated according to [6, 7]

$$Q = \frac{1}{2\pi} \oint_{\mathcal{C}(\kappa)} \left[\hat{\mathbf{n}}(\kappa) \times \frac{\partial \hat{\mathbf{n}}(\kappa)}{\partial \kappa} \right] d\kappa \,, \tag{S.9}$$

where $\oint_{\mathcal{C}(\kappa)} d\kappa = 2\pi$. Since Q takes only discrete values but must change continuously whilst continuously altering the path $\mathcal{C}$ in a region without singularities, it has to be constant in such a region [8]. Moreover, the total charge within a given domain can be computed as the sum of individual charges.

In a confined system, the external boundary induces a particular alignment of the particles, which is preferably parallel to the walls in case of hard rods at a hard wall. This typically enforces the formation of defects. If all particles obey a strong tangential anchoring condition at each point of the boundary, then the sum of all topological charges is determined by the Euler characteristic $\chi = 1$ of the simply-connected confining domains considered here [8]. The corresponding fundamental law of charge conservation reads

$$\sum_i Q_i = 1 \,, \tag{S.10}$$

where the index i labels all defects in the system.

The topological defects occurring in nematic liquid crystals can be generally classified according to their location relative to the confining walls as bulk, boundary or virtual defects [9, 10]. The charge of a bulk defect determined according to Eq. (S.9) is not affected by the presence of the boundary. A boundary defect indicates a violation of the anchoring condition. This is particularly the case at a corner, i.e., a singular point of the boundary curvature, which is not compatible with the symmetry of the director field $\hat{\mathbf{n}}(\mathbf{r})$. The sudden jump of $\hat{\mathbf{n}}(\mathbf{r})$ when traversing the confining wall can be related to the deficiency angle $\tau = 180° - \alpha$ at the corner of opening angle α, which leads to

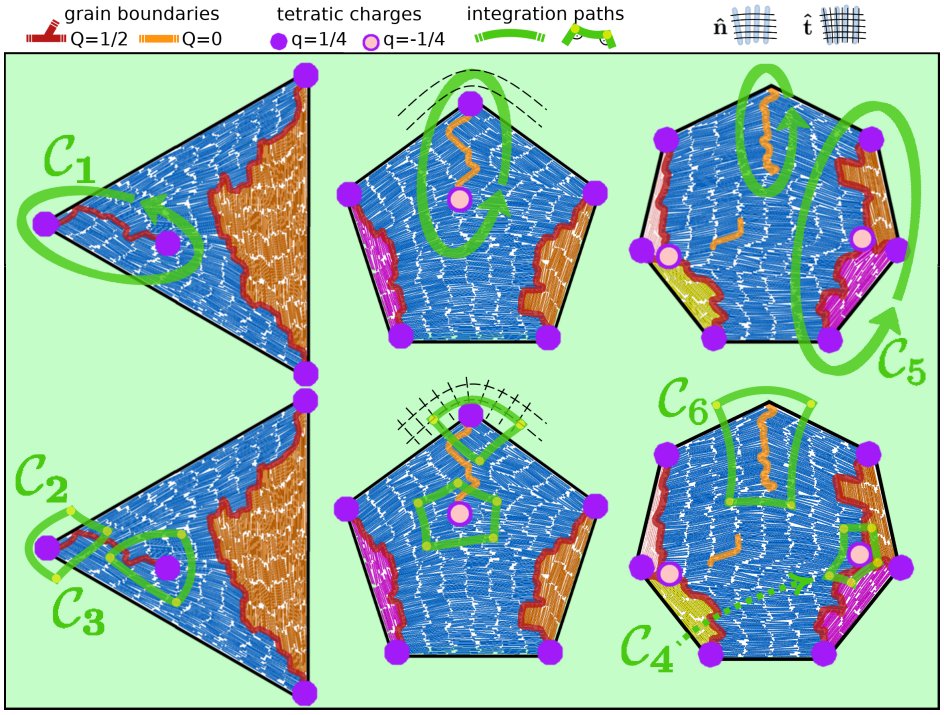

FIG. 2: Overview of how to determine the topological charge distribution (superimposed points and lines) within different simulation snapshots. Each defect represents a discontinuity in the director field, which can be enclosed by a closed contour $\mathcal{C}$ (green paths), only traversing regions with a continuous director. Virtually extending the director fields to the region outside the cavity (representative black lines) allows to assign a topological bulk charge to each defect, irrespective of its connectivity with the system boundaries. The labeled contours are explicitly referred to in the text. **Top row:** The nematic director field $\hat{\mathbf{n}}(\mathbf{r})$is parallel to the rod axes and thus discontinuous at a grain boundary. Every network of grain boundaries, i.e., an assembly of interconnected nematic line defects can be assigned a charge Q as a whole by integrating up the local rotation angle of $\hat{\mathbf{n}}(\mathbf{r})$ along $\mathcal{C}$, according to Eq. (S.9). **Bottom row:** The field lines of the tetratic director $\hat{\mathbf{t}}(\mathbf{r})$ are both parallel and perpendicular to the rod axes and thus continuous at a grain boundary with typical deficiency angle 90°, while the rotation of the field happens around the end points. The charge $q = 1 - c/4$ of these tetratic defects follows from Eq. (S.12) and can be directly inferred from counting the number c of 90°-corners (yellow points) of a polygonal integration loop $\mathcal{C}$ on top of the field lines. A grain-boundary network can therefore be understood as a consolidation of isolated tetratic defects. As one principal axis of $\hat{\mathbf{t}}(\mathbf{r})$ is always equal to $\hat{\mathbf{n}}(\mathbf{r})$, the nematic charge of such a network always equals the total tetratic charge of its end points and nodes according to Eq. (S.13), compare contour $\mathcal{C}_1$ with $\mathcal{C}_2$ and $\mathcal{C}_3$. Grain boundaries with a deficiency angle $< 90°$ can only be assigned a topological charge $q = Q$ as a whole, see contour $\mathcal{C}_6$.

the common definition [7, 9, 11] $m = k/2 - \tau/(2\pi)$ of a of a boundary charge m, where k takes integer values. The corresponding conservation law generalizing Eq. (S.10) then reads

$$\sum_i \left(m_i + \frac{\tau_i}{2\pi} \right) + \sum_j Q_j = 1 \,, \tag{S.11}$$

with the bulk defect charges Q_j. Finally, a virtual defect represents a director field which does not uniformly align with the boundary, such that the center of this distortion can be thought to lie outside the actual system [10]. For smectic liquid crystals, which also exhibit positional order, the interpretation of the defect structure, described in the remainder of this section, requires further care.

B. Nematic and tetratic topological charge within smectic grain boundaries

In this section we describe the classification of topological defects in a smectic fluid, which are of central interest in our simulations and experiments. Regarding the spatially extended defect structure represented by the emerging smectic grain boundaries, a clear distinction between bulk and boundary defects is not always possible. For example, depending on the local curvature of the wall, we observe a continuous transition between grain-boundary lines representing pure bulk defects and those with one or both end points attached to the boundary (see, e.g., Fig. 7). On a second level of our classification, the end points of grain boundaries themselves can be identified as tetratic bulk or boundary defects, which could be classified along the lines of Sec. 2 A. However, in what follows, we seek for a unifying virtual treatment for all defects, irrespective of their location, which we illustrate for both nematic and tetratic order in Fig. 2.

As a first step, we introduce a virtual extension of the director field that is tangential to the boundary and continuously circulates each corner in the outside region. Hence, we avoid the ambiguity arising from the angular deficiency at the corners and treat all defects as bulk defects, compare, e.g., the contour $\mathcal{C}_1$ in Fig. 2. This picture allows us to associate a well-defined topological charge $Q \in \{\pm 1/2, \pm 1, \pm 3/2 \ \ldots\}$, determined via Eq. (S.9), with any defect in the nematic order, irrespective of its spatial extension and connectivity with the boundary, see Fig. 2 for representative examples. A point-like defect at the system boundary, in particular, is thus interpreted as a virtual defect with half-integer topological charge $Q = m + \tau/(2\pi)$, such that the charge conservation law for internal bulk charges from Eq. (S.10), which applies to our classification, is recovered from Eq. (S.11). This concept is best justified regarding the detachment of defects from the boundary in polygons with rounded corners, as detailed in Sec. 5 B.

As a second step, we apply the continuum assumption of a tilt angle between smectic layers at opposite sides of grain boundaries that is exactly 90°. Therefore, each grain boundary is compatible with tetratic orientational order, described by the director field $\hat{\mathbf{t}}(\mathbf{r})$, which is similar to the nematic director field $\hat{\mathbf{n}}(\mathbf{r})$ but with the identification $\hat{\mathbf{t}} \equiv \ -\hat{\mathbf{t}} \equiv \hat{\mathbf{e}}_z \times \hat{\mathbf{t}} \equiv -\ \hat{\mathbf{e}}_z \times \hat{\mathbf{t}}$ of both parallel and perpendicular orientations ($\hat{\mathbf{e}}_z$ is the unit vector perpendicular to the two-dimensional system). The topological charge q of a tetratic defect is always a multiple of $1/4$ and can be defined analogously to Eq. (S.9) as

$$q = \frac{1}{2\pi} \oint_{\mathcal{C}(\kappa)} \left[\hat{\mathbf{t}}(\kappa) \times \frac{\partial \hat{\mathbf{t}}(\kappa)}{\partial \kappa} \right] d\kappa \,, \tag{S.12}$$

where the closed contour $\mathcal{C}$ may traverse grain boundaries, which is forbidden for a nematic director field. This allows us to identify two isolated point-like tetratic defects at the end points of a grain boundary. For example, the contours $\mathcal{C}_2$ and $\mathcal{C}_3$ in Fig. 2 enclose a tetratic bulk defect and a virtual defect at the boundary, respectively.

As a third step, we apply the same continuum assumption to networks of grain boundaries, which reveals the location of additional tetratic point defects at the nodes, which represent a junction point of three grain boundaries, compare, e.g., the contour $\mathcal{C}_4$ in Fig. 2. For the convex confinement shapes considered in our work, we typically observe defect networks of total nematic charge $Q = 1/2$, consisting of n nodes and $n + 2$ end points with tetratic charge $q = -1/4$ and $q = +1/4$, respectively. This decomposition reflects the fact that the nematic charge

$$Q = \sum_j q_j \tag{S.13}$$

of a defect equals the sum of all tetratic point charges q_j enclosed by the same contour, compare, e.g., the contour $\mathcal{C}_5$ in Fig. 2. Formally, the topological charge of a grain-boundary network is thus exclusively located at its nodes and end points. Globally, the fundamental conservation laws, Eq. (S.10), for the total nematic charge Q and accordingly $\sum_i q_i = 1$ for the total tetratic charge q can be nicely illustrated in terms of the two types A (with $Q = 1/4{+}1/4 = 1/2$) and B (with $Q = 1/4{-}1/4 = 0$) of grain-boundary lines, introduced in the main text as building blocks of the emerging defect structures: we usually identify two $A + nB$ networks, which consist of one type-A and n type-B defect, and a number of standalone type-B grain boundaries.

As a final step, we must decide for which of the observed grain boundaries the continuum assumption is justified and how to classify the defect structures in the case it is not. This issue is dealt with in the following section.

3. DETECTION OF TETRATIC DEFECTS IN FRUSTRATED SMECTICS

A. Local fields of the orientational order parameters

Having introduced a continuum classification of smectic grain boundaries in Sec. 2 B, we now address the defect structure arising from frustrated smectic order in extreme confinement as represented by our simulation data. One

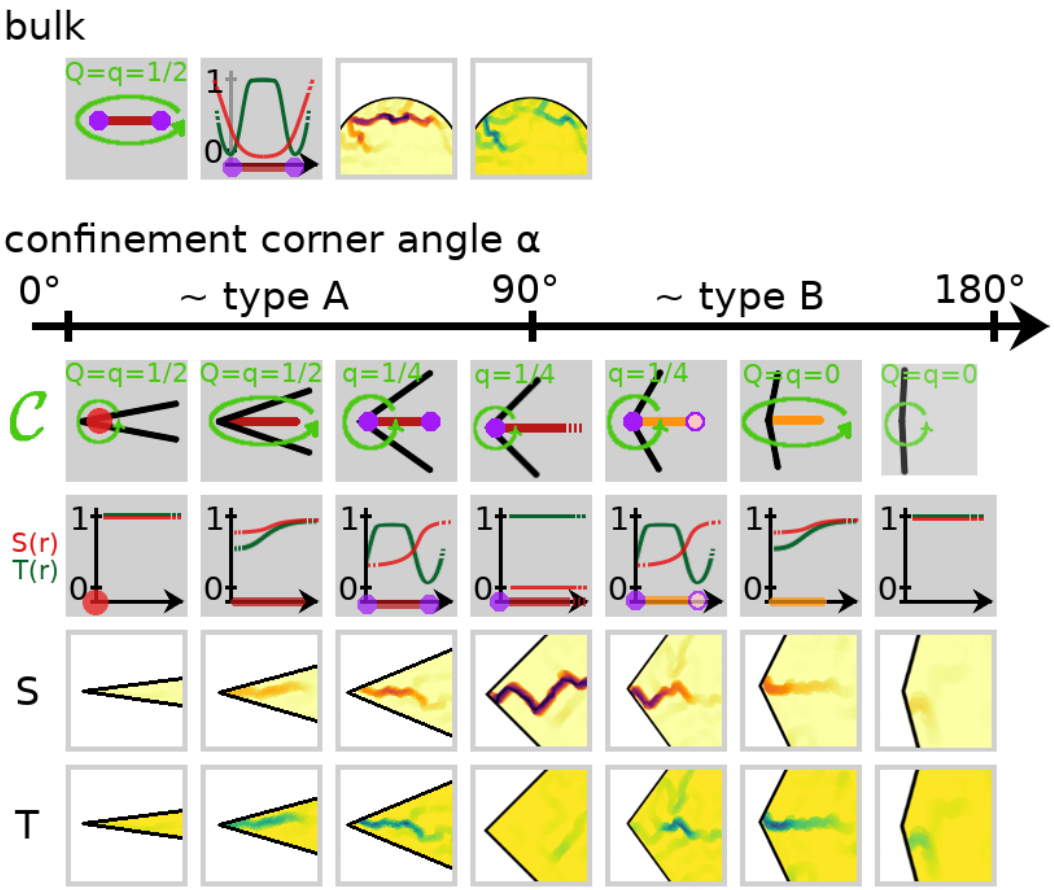

FIG. 3: Schematic illustration of the behavior of the nematic order parameter S (red curves) and the tetratic order parameter T (green curves) along a grain-boundary line (horizontal coordinate in the plots) together with selected fields extracted from the simulation data representing the indicated scenario. We also draw in each case a contour $\mathcal{C}$ (green arrow) that encloses a representative nematic charge Q and/or tetratic charge q. **Top:** type-A bulk defect, typically found in circular confinement. **Bottom:** the typical defect type emerging at a corner of the confining wall depends on the opening angle α. If no tetratic point charges are drawn at the endpoints of a grain boundary, we consider these as partially annihilated. Further details are given in the text.

way to visualize the emerging topological defects is through the local profiles of the nematic order parameter S and the tetratic order parameter T. If a grain-boundary line is located in the bulk, i.e., not attached to the boundary, its topological structure is unambiguously revealed by these fields. As emphasized in Fig. 3, the lines along which the S field is close to zero are clearly visible, whereas the tetratic signal in the middle of the line is not distinguishable from the background. However, the T field is low at both ends of the line, indicating the two end-point defects. If a grain-boundary network is connected to the wall, both the strength of the signal in the order parameters (deviation from the bulk value one) along a grain boundary and the observed type of the free-standing defects typically depends on the opening angle α of the adjacent corner, as illustrated in Fig. 3 and detailed in the following. Corners with $\alpha \simeq 90°$ induce ideal grain boundaries with with $S \simeq 0$ and promote perfect tetratic ordering throughout the system. The tetratic end point defects are fully located on the system boundary and can therefore not be resolved in the T

field. Departing from the particular case $\alpha \simeq 90°$, the tetratic order along a grain boundary is also frustrated close to the confining wall. For $45° \lesssim \alpha \lesssim 90°$ and $90° \lesssim \alpha \lesssim 135°$ the nematic signal along a grain-boundary line opposes the tetratic signal (S increases when T decreases and vice versa). For both $0° \lesssim \alpha \lesssim 45°$ and $135° \lesssim \alpha \lesssim 180°$ the tetratic charges no longer provide isolated signals, i.e., they are partially merged to a line defect whose order parameter field qualitatively resembles the nematic one. Such a grain boundary does not accommodate perpendicular smectic layers, compare, e.g., the contour $\mathcal{C}_6$ in Fig. 2. In the limit $\alpha \to 180°$, adjacent smectic layers are parallel and there is no topological defect. This corresponds to a type-B grain boundary, typically observed for $\alpha \gtrsim 90°$, whose oppositely charged tetratic endpoints are completely annihilated. In the opposite case, $\alpha \to 0°$, there is a point defect of charge $Q = q = 1/2$ in the corner, corresponding to the two merged endpoints of a type-A defect, generally preferred for $\alpha \lesssim 90°$.

The given thresholds for the opening angle α reflect the different symmetry inherent to the nematic and tetratic order. The resulting intuition helps to predict the expected type of defect induced by a corner. In particular if there is only a single grain-boundary line, the information in the order-parameter field can be used as a basis for the decision whether or not to assign isolated tetratic end points to the defect, as indicated in Fig. 3. Regarding, however, the variety of possible defect structures laid out in Sec. 4, we take a cue from our domain criterion described in Sec. 1 C and attach a branch of type B to a grain-boundary network only if it separates two different domains. Otherwise, we consider the endpoints of such a building block as annihilated and no such branch is drawn into our schematic defect structures.

B. Tetratic defect analysis based on smectic layers

To provide an alternative point of view on tetratic defects in frustrated smectics, we focus our analysis on the smectic layers, instead of the particle-resolved picture in the previous section. Our main goals are to provide a deterministic distinction between isolated and (partially) annihilated defects and to explicitly detect boundary defects. In the frustrated smectic configurations we consider here, many of the smectic layers are tilted to some degree, and as a result the particles are not aligned perpendicular to the direction of the smectic layer. Hence, the difference in nematic orientation across a grain boundary can be significantly different from $\pi/2$, resulting in a low local tetratic order parameter near the grain boundary. As a result, pinpointing defects based on the tetratic order parameter is not easy in practice. We thus require a more robust way of identifying the topological defects associated with the tetratic order in frustrated smectic liquid crystals from our simulation data.

To circumvent the difficulties associated with the local order parameter field, we determine the directions and connectivity of the smectic layers. Specifically, we consider two particles to be in the same smectic layer based on a bonding criterion that takes into account the positions and orientations of pairs of particles, see Sec.1 C for details. We then draw a smoothened center line along the length of each layer to mark its direction. The smoothening is performed by first determining an overall direction for the smectic layer (taken to be perpendicular to the nematic director of all particles in the layer), and then applying a low-pass filter to the component of the particle positions perpendicular to this director. We can now use these lines to guide us in identifying the behavior of the tetratic director as we move through the system. Along the center line of the smectic layers, the orientation of the tetratic director varies smoothly. Moreover, we can connect two lines by green arrows that are either parallel, or meet at an approximately perpendicular junction, such that the tetratic director can be assumed to vary smoothly along this connection. The resulting closed lines allow us to locate the defects in the tetratic order, as illustrated in Fig. 4. To do this, we consider two types connections between smectic layers. First, between two parallel smectic layers within the same smectic domain, we can draw direct connections perpendicular to the two smectic layers, denoted by double-headed green arrows. Second, when a smectic layer terminates against the side of another layer, such that the last particle in the first layer lies parallel to the smectic direction of the second layer, we draw a single-headed arrow, which by definition crosses an area of low nematic order.

As shown in Fig. 4, it is then possible to identify a topological charge $q = 1 - t/4$ of tetratic defects by counting the number t of turns represented by the tips of the green arrows. In an idealized interpretation of any loop, switching direction at the tip of a green arrow is a turn of 90°, which has no effect on the tetratic order. Following the closed loop in Fig. 4b, we encounter three sharp corners of 90° (with no effect on the tetratic order) plus the smooth rotation of the smectic director by a final 90°, completing the loop. This quarter-turn of the tetratic director indicates the presence of a defect with $q = +1/4$ topological charge. Similarly, closed loops with 5 turns at a right angle, like in Fig. 4c must carry a topological charge of $q = -1/4$. Finally, we should consider non-topological defects that are common in our configurations. These can be either dislocations or simply sudden shifts in a smectic layer perpendicular to its smectic direction, and do not significantly impact the orientations of the particles: they occur in regions of high nematic order. An example is shown in Fig. 4d, with connections between the different layers drawn to show that no topological defects occur, as the closed loop has exactly four sharp corners of 90°.

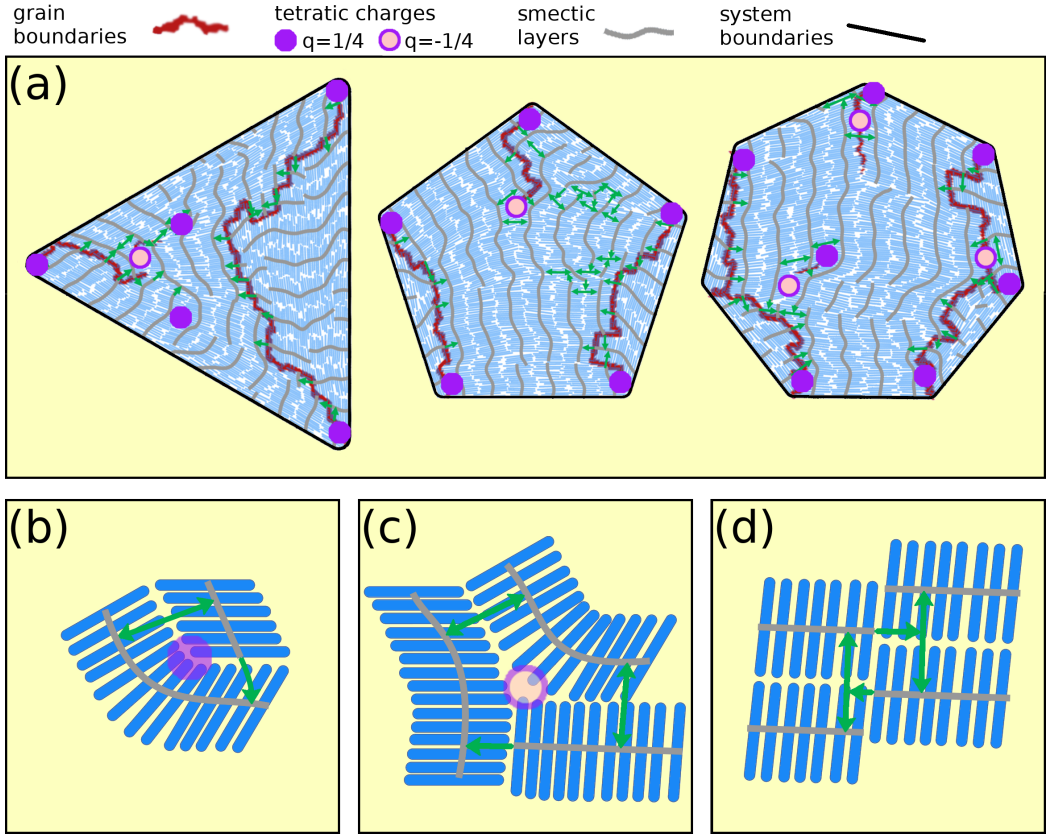

FIG. 4: Detecting tetratic charges based on smectic layers determined by the algorithm outlined in Sec. 1 C. **a)** Exemplary distribution of tetratic point charges in three simulation snapshots. **b-d)** Illustration of how to identify different tetratic charges. The gray lines indicate the detected smectic layers. Green arrows with one or two tips are added manually to indicate connections between these layers in the vicinity of the topological defects. Then the tetratic charge $q = 1 - t/4$ can be read of from the number t of tips. Further details are given in the text.

We can now apply this approach to the simulated configurations, as illustrated in Fig. 4a. For this, it is convenient to include the nematic order parameter field as a background. In particular, as terminations of one smectic layer against another (single-headed green arrows) only occur in regions of low nematic order, in practice we only have to focus on the regions close to the grain boundaries to find tetratic defects. In each figure, we draw only the connections required to identify the topological defects in the system. Then, additional connections between parallel layers are added to narrow down the regions where defects are located. Moreover, as detailed in Sec. 2 B, we assume the tetratic director field to vary smoothly along the outside wall. To reflect this, we draw a smoothened outline of the system boundary in each image. Smectic layers can terminate at the wall, providing an additional connection that should again be interpreted as a rotation by 90° in any closed loop that includes it. In other words, the wall represents a double-headed arrow (which is not drawn for presentation reasons).

We stress that identifying tetratic defects in this way is relatively straightforward. Arrows are drawn manually, but there is usually no freedom of choice: when a smectic layer terminates in a region of low nematic order, it is connected to the perpendicular layer just ahead of it. If no such layer is immediately visible, then occasionally another connection in this region should be made first to allow the first layer to terminate by drawing an arrow which ends on another perpendicular arrow (see, e.g., on the right-hand side of the heptagon in Fig. 4a. The only freedom of choice

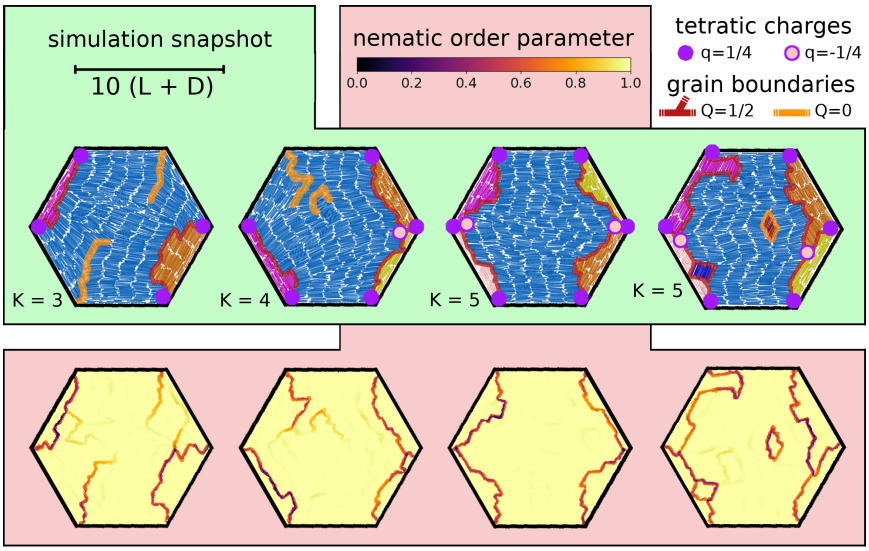

FIG. 5: Comparison of representative bridge states with K domains as labeled from simulations of $N = 1000$ hard rods confined to a hexagonal cavity. The corresponding relative frequencies are given in Tab. I. The structure on the right illustrates that we do not count singular domains located in the middle of the cavity, as described in the caption of Tab. I. **Top row:** particle snapshots with superimposed grain-boundary networks (compare Fig. 2 in main manuscript). **Second row:** nematic order parameter field $S(\mathbf{r})$.

in this method occurs when it is not clear whether two adjacent smectic lines should be considered perpendicular or parallel. For example, one could imagine continuously deforming the region around the defect pair just to the left of the center of the heptagon in Fig. 4a to be more similar to an edge dislocation, as in Fig. 4d, which would result in the annihilation of the two defects. However, note that any choice leaves the overall topological charge of the system intact, as one would expect.

Compared to the analysis of order-parameter fields, described in Sec. 3 A, our layer-based approach generally resolves a larger number of defect pairs, albeit these are usually close to annihilation. For example, the distribution of tetratic charges in the free-standing grain boundary at the top corner of the heptagon in Fig. 4a corroborates our interpretation of partially annihilated endpoint charges. In conclusion, while both methods provide a solid understanding of the tetratic topology in their own right, the algorithm presented above is perhaps most suitable to track the defect motion in a dynamical setup.

4. RELATIVE FREQUENCIES OF OBSERVED LIQUID CRYSTAL STRUCTURES

In general, each smectic structure in simply-connected confinement features a total topological charge $Q = q = 1$ typically distributed over two $A + nB$ grain-boundary networks (containing one type-A and n type-B building blocks each) and a number of additional type-B grain boundaries. To identify the most likely network composition, we differentiate between the occurring defect structures by counting the number of domains, according to the analysis in Sec. 1 C. Considering hexagonal confinement as an exemplary case, Fig. 5 shows how the number of domains relates to the complexity of the emerging networks: when completely connected to the wall, an $A + nB$ network separates $(n + 2)$ domains.

In Tab. I, we list the relative frequencies for structures labeled according to the number of domains for a range of polygonal confinements. For polygons with smaller numbers of corners, we observe that the average number of domains $\overline{\mathbf{K}}$ increases with increasing number of corners, peaking for dodecagon (12 corners) and tridecagon (13 corners). Further increasing the number of corners, $\overline{\mathbf{K}}$ decreases again, as the confinement gradually approaches a circular shape. This behavior reflects a general trend, which is also reflected by the most frequently observed defect

confinement		number of domains (K)										
(corners)	$\overline{K}$	1	2	3	4	5	6	7	8	9	10	11
circle (0, ∞)	1.64	**0.55**	0.10	0.03	0.01							
triangle (3)	2.34	0.08	**0.53**	0.35	0.03							
square (4)	2.82		0.21	**0.75**	0.03							
pentagon (5)	3.52		0.03	0.45	**0.49**	0.03						
hexagon (6)	4.72			0.05	0.21	**0.68**	0.05					
heptagon (7)	5.16			0.01	0.16	**0.54**	0.25	0.04				
octagon (8)	5.49				0.05	**0.53**	0.32	0.09	0.02			
nonagon (9)	6.17				0.02	0.20	**0.46**	0.26	0.06	0.01		
decagon (10)	6.25				0.02	0.18	**0.40**	0.33	0.06	0.01		
hendecagon (11)	6.76				0.02	0.10	0.27	**0.36**	0.20	0.05		
dodecagon (12)	7.04				0.02	0.08	0.22	**0.35**	0.22	0.08	0.03	0.01
tridecagon (13)	7.05			0.01	0.03	0.09	0.21	**0.30**	0.25	0.10	0.02	
tetradecagon (14)	6.46			0.02	0.05	0.16	0.27	**0.28**	0.26	0.05	0.01	
pentadecagon (15)	5.71		0.02	0.05	0.13	0.23	**0.26**	0.20	0.08	0.03		
hexdecagon (16)	2.97	0.14	**0.28**	0.26	0.16	0.10	0.04	0.01				
icosagon (20)	2.43	0.23	**0.36**	0.24	0.11	0.05	0.01					
triacontagon (30)	1.09	**0.91**	0.08									
tetracontagon (40)	1.88	**0.44**	0.34	0.16	0.05	0.02						

TABLE I: Average number of domains $\overline{K}$ and relative frequencies of structures with **K** domains occurring in our simulations, rounded to two decimal places. The most frequent structure is marked by a boldfaced number. The data are sampled from 1000 simulations for each confinement. For this statistic, we only count domains which align with at least one wall to better reflect the typical defect geometry of the confinement, compare Fig. 5.

structure for a given confinement. The particular distribution for a given polygon depends in detail on the ratio of the side length (determined by the fixed particle number and area fraction) to the length of the rods. For instance, the triacontagonal (30 corners) confinement, for which this ratio is equal to 1.07, displays a relatively large number (compared to 40 corners) of single-domain structures, which can be related to the high probability of a continuous string of rods around the perimeter.

5. ADDITIONAL SIMULATION DATA

The distinctive topology of the defects, we observe in our confined systems, is influenced by various quantities, such as area fraction η_2, geometry of the particles (aspect ratio p), as well as confining geometry and system size (particle number N). To further explore these different aspects, we present in the following sets of simulation data generated with the protocol described in Sec. 1 B. First, we consider additional geometries for the simulation parameters $N = 1000$, $p = 15$ and $\eta_2 = 0.75$ used in the main text. In detail, we exemplify the dependence of the typical length of a grain boundary on the sharpness of the adjacent corner by considering a range of isosceles triangles in Sec. 5 A and discuss the effects of a varying local curvature of the confining walls by the example of different rounded triangles in Sec. 5 B. We then elaborate on the dependence of the topological defect structure on the system size in Sec. 5 C. Finally, to shed light on the relation between simulation and experiment, we explore a range of area fractions and aspect ratios in Sec. 5 D.

A. Isosceles triangles

To study the effect of the of the sharpness of a corner on the typical length of the adjacent grain boundary, we consider in Fig. 6 a range of sharp isosceles triangles. The appearance of the free-standing type-A defect, typically attached to the sharpest corner of the polygons, critically depends on the opening angle, as illustrated in Fig. 3 and depicted in Fig. 6. As elaborated in the main manuscript, the free-standing grain boundary in equilateral triangles tends to protrude deeply into the bulk. For intermediate opening angles, we typically observe that the length of the defect decreases compared to the legs of the triangle and the degree of orientational frustration becomes lower as the tetratic endpoints begin to merge. For angles $\lesssim 15^\circ$ we observe an isolated perfect point defect with $Q = q = +1/2$ as smectic layering is suppressed by the cramped geometry in the vicinity of the tip.

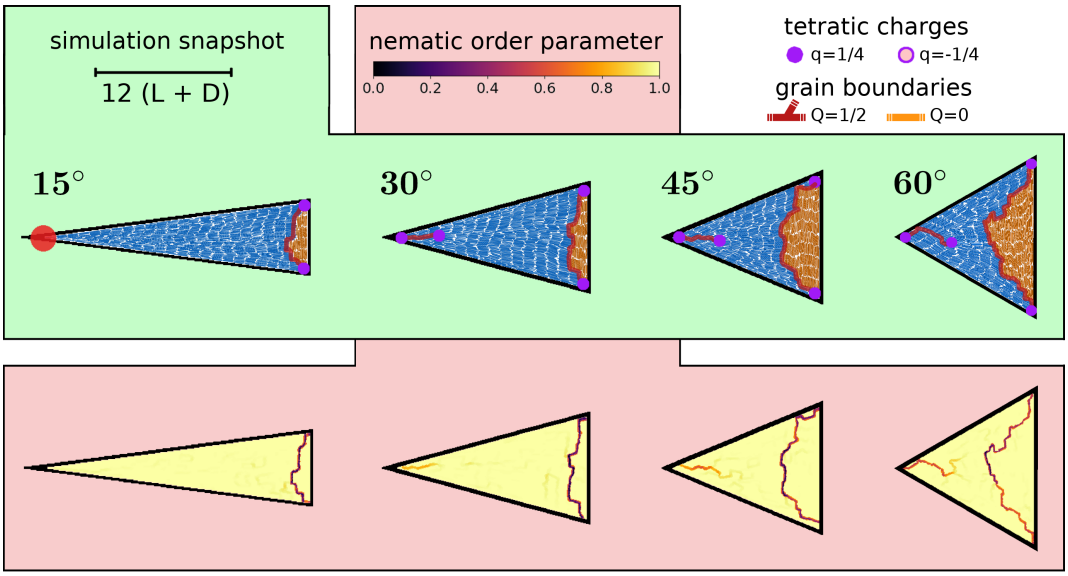

FIG. 6: Topological defect structure of representative simulation results for hard rods with aspect ratio $p = 15$ confined to isosceles triangular cavities with tip angles (as labeled), where the structure shown at 60° coincides with that in Fig. 3 in the main manuscript. Particle snapshots and orientational order parameter field $S(\mathbf{r})$ as in Fig. 5.

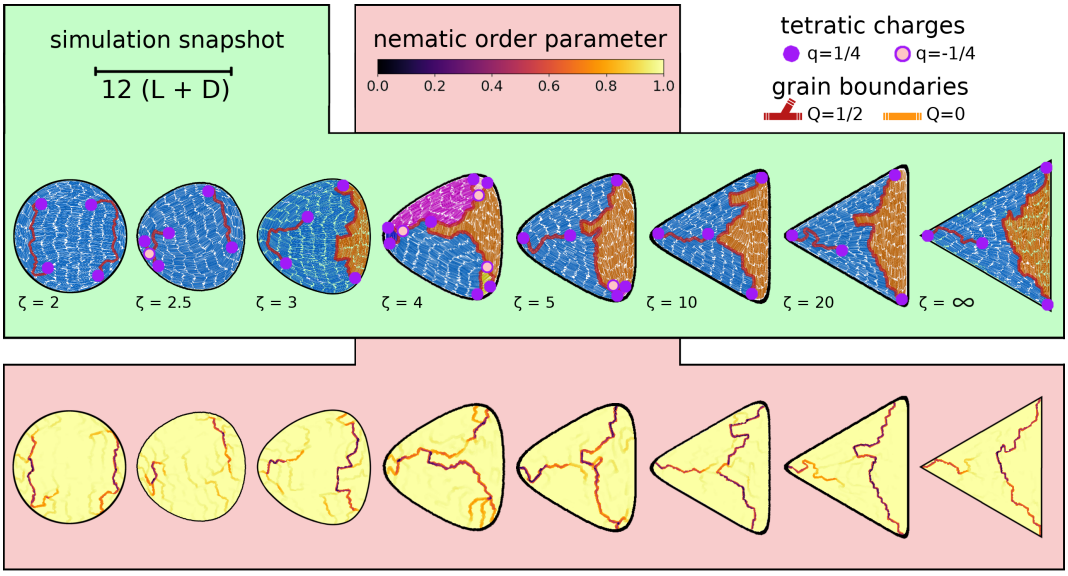

FIG. 7: Topological defect structures of representative simulation results for $N = 1000$ hard rods with aspect ratio $p = 15$ confined to triangular cavities with varying roundness ζ, defined in Eq. (S.14), as labeled. The structures with $\zeta \in \{2,\ 3,\ \infty\}$ coincide with those presented in Fig. 3 in the main manuscript.
Particle snapshots and orientational order parameter field $S(\mathbf{r})$ as in Fig. 5.

B. Rounded triangles

As mentioned in the main manuscript, the curvature of the outer system boundary plays a central role in the formation and resulting topological interpretation of grain-boundary networks. To elaborate on the dependence of the topological defect structure on the curvature of confining cavities, we consider rounded polygons generally defined by the equation

$$1 = \left[\sum_{k}^{M} (\mathbf{r}\cdot\mathbf{b}_k - \mathcal{W})^{\zeta}\right]^{1/\zeta} \tag{S.14}$$

with $\mathbf{r} \in \mathbb{R}^2$, $\mathbf{b}_k = (\cos(k2\pi/M), \sin(k2\pi/M))$ and $\mathcal{W} = \tan(\pi/(2M))\sin(2\pi/M)$, such that M and ζ denote the number and sharpness of the corners, respectively. In particular, $\zeta = 2$ defines a circle and the limit $\zeta \to \infty$ corresponds to sharp corners.

Focusing on $M = 3$, Fig. 7 compares the typical structure for a large range of rounded triangles. For sharp corners with infinite local curvature, the sudden shift in the orientation of the wall causes a frustration of the orientational order directly at the walls, resulting in grain boundaries attached to each corner. The resulting defect structure with two clearly separated domains remains dominant for rounded triangles with $\zeta \gtrsim 4$ throughout. For $\zeta \lesssim 4$, the dominant structure resembles that in circular confinement, characterized by a single domain and two opposite grain-boundary lines on each side of the confinement, which tend to align locally with the confining wall. The degree of attachment to the system boundary, generally decreases with ζ, which demonstrates the convenience of our virtual treatment of boundary defects.

For intermediate values of the roundness parameter around $\zeta \approx 4.0$, where the curvature radius at the corners is comparable to the rod length, we find additional structural elements: the grain boundaries tend to branch out close to the corners, resulting in small domains incorporating one to two smectic layers. Moreover, in this parameter range, we find structures that feature either one, two or three large domains, reflecting a strongly fluctuating connectivity of the defect networks.

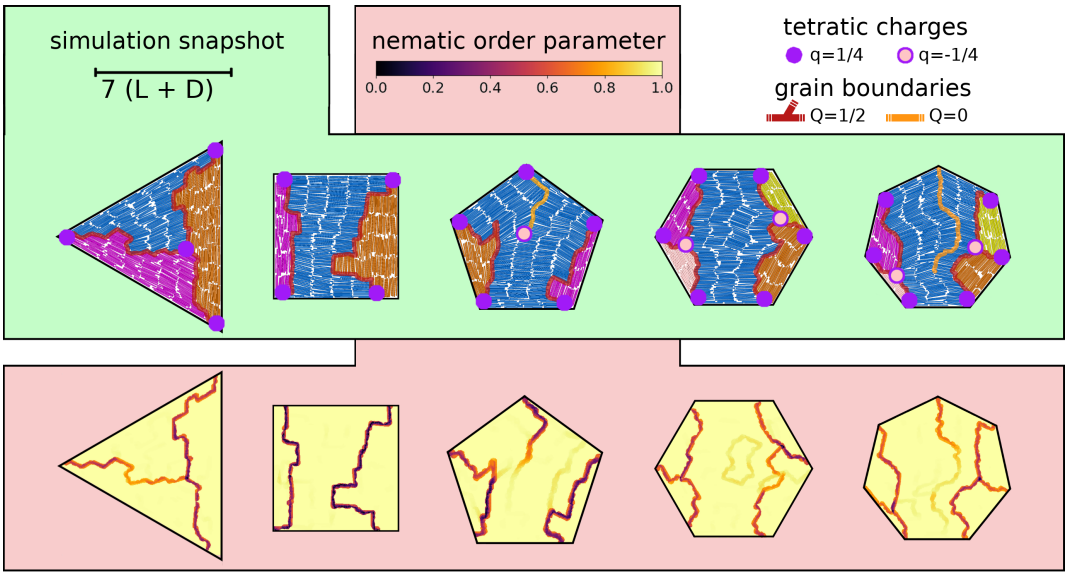

FIG. 8: Topological defect structure of representative simulations for $N = 500$ hard rods with aspect ratio $p = 15$ in a range of regular polygons. Particle snapshots and orientational order parameter field $S(\mathbf{r})$ as in Fig. 5.

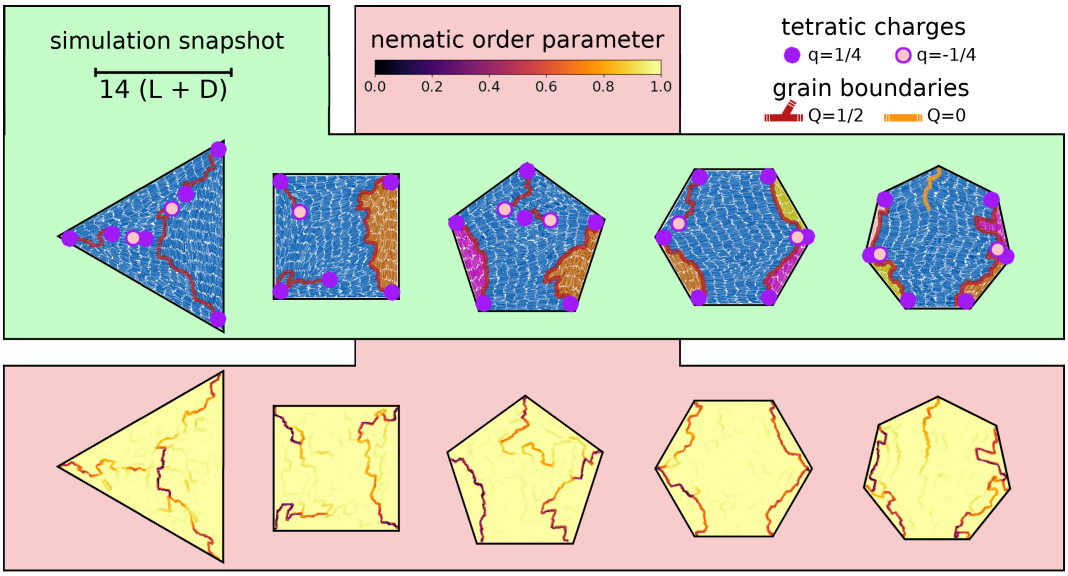

FIG. 9: Topological defect structure of representative simulations for $N = 2000$ hard rods with aspect ratio $p = 15$ in a range of regular polygons. Particle snapshots and orientational order parameter field $S(\mathbf{r})$ as in Fig. 5.

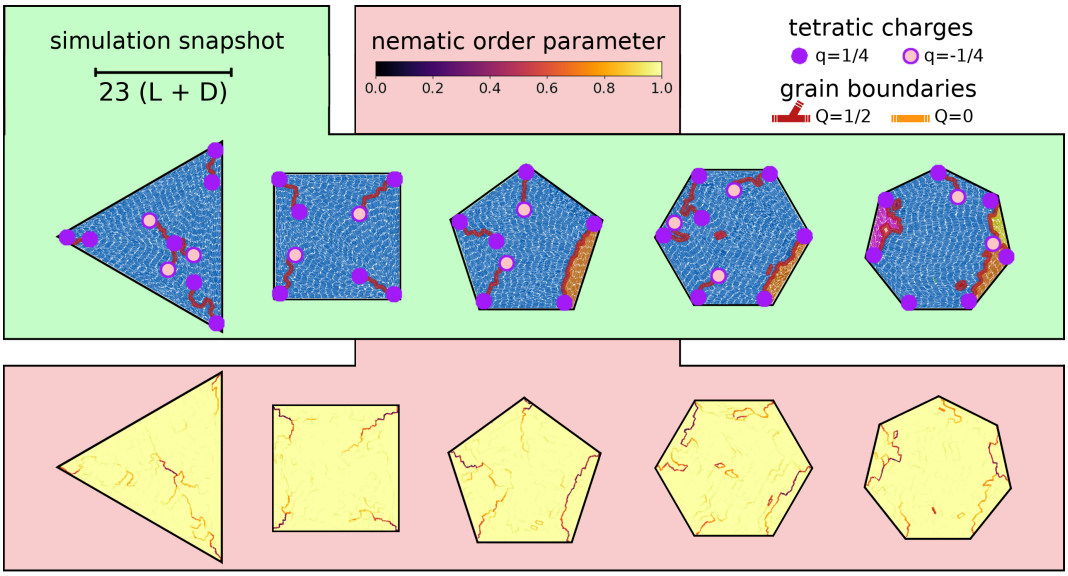

FIG. 10: Topological defect structure of representative simulations for $N = 5000$ hard rods with aspect ratio $p = 15$ in a range of regular polygons. Particle snapshots and orientational order parameter field $S(\mathbf{r})$ as in Fig. 5.

			number of domains (**K**)						
N	sim-#	$\overline{\mathbf{K}}$	**1**	**2**	**3**	**4**	**5**	**6**	**7**
500	1000	4.85			0.03	0.23	**0.62**	0.11	0.01
1000	1000	4.72			0.05	0.21	**0.68**	0.05	
1500	1000	4.62		0.01	0.06	0.33	**0.50**	0.09	0.01
1777	300	3.74	0.01	0.12	0.25	**0.38**	0.22	0.02	
2000	1000	3.71	0.02	0.10	0.31	**0.34**	0.21	0.03	
2500	250	3.30	0.06	0.14	**0.38**	0.31	0.12		
3000	250	2.87	0.11	0.27	**0.35**	0.19	0.07	0.01	
5000	155	3.01	0.14	**0.28**	0.23	0.15	0.19	0.01	

TABLE II: Average number of domains $\overline{\mathbf{K}}$ and relative frequencies of structures with **K** domains in hexagonal cavities as in Tab. I, but for systems with different particle numbers N at area fraction $\eta = 0.75$. The number of simulations from which the data are sampled is given in the second column.

C. Polygons with different particle numbers

The typical extent of the topological defects we observe in extreme confinement, depends on the elastic deformation energy of the smectic layers. On smaller length scales, positional distortions of the smectic layers are favored, whereas bent smectic layers are dominant on larger length scales [6]. This results in the formation of the described networks of grain boundaries in smaller systems while in bigger systems large scale bends, connecting different walls of the confinement, suppress the formation of separated domains. Accordingly, we show in Figs. 8, 9 and 10 exemplary simulation results with different particle numbers N, leaving the area fraction $\eta = NA_{\mathrm{HDR}}/\mathcal{A} = 0.75$ constant for any confinement. In general, we observe that the average number of domains in each confinement decreases with increasing system size, which is statistically quantified in Tab. II. Moreover, the relative length of free-standing type-B grain boundaries is reduced for larger systems, which can be observed, e.g., by comparing the structures in the heptagons.

The extremely confined structures with $N = 500$ particles shown in Fig. 8 display a tendency to develop pronounced positional distortions all across the central bridging domain. This is for instance visible through the slightly rotated dislocated layer in the hexagon and the strong elastic deformations in combination with the almost system-spanning central grain boundary in the heptagon. Moreover, the triangular cavity typically displays a single $Q = 1$ network featuring a positively charged node with $q = +1/4$, separating three equally-sized domains. Strictly speaking, this structure is different from the bridge state, irrespective of the identical set of building blocks. For systems larger than those considered in the main text, the enhanced flexibility leads to a higher frequency of smectic layers interrupting and

			number of domains (**K**)							
η	p	N	$\overline{\mathbf{K}}$	**1**	**2**	**3**	**4**	**5**	**6**	**7**
0.7	10	1147	2.78	0.09	0.32	**0.38**	0.16	0.04	0.01	
	11.5	1301	2.49	0.16	**0.37**	0.32	0.14	0.02		
	13	1454	2.60	0.12	0.33	**0.39**	0.14	0.01		
	15	1659	2.62	0.15	0.28	**0.41**	0.14	0.03		
	18	1965	2.52	0.14	0.33	**0.41**	0.11	0.01		
0.725	10	1188	3.18	0.05	0.20	**0.39**	0.25	0.10	0.01	
	11.5	1347	3.09	0.06	0.20	**0.41**	0.26	0.06	0.01	
	13	1506	3.30	0.04	0.16	**0.40**	0.28	0.11	0.01	
	15	1718	3.23	0.03	0.20	**0.40**	0.25	0.11	0.01	
	18	2036	3.05	0.06	0.21	**0.41**	0.25	0.05	0.01	
0.75	10	1229	3.51	0.03	0.13	**0.35**	0.30	0.16	0.03	
	11.5	1394	3.71	0.01	0.8	0.33	**0.38**	0.17	0.02	0.01
	13	1558	3.57	0.03	0.10	**0.35**	0.34	0.16	0.02	
	15	1777	3.74	0.01	0.12	0.25	**0.38**	0.22	0.02	
	18	2106	3.56	0.03	0.13	0.31	**0.35**	0.17	0.02	

TABLE III: Average number of domains $\overline{\mathbf{K}}$ and relative frequencies of structures with **K** domains in hexagonal cavities as in Tab. I, but for different particle numbers N, area fractions η and aspect ratios $p = L/D$, fixing the ratio 7.5 between side length of the confining hexagon and rod length. The number of simulations is equal to 300 for each row. The parameters $\eta = 0.75$ and $p = 15$ used in all other simulations are highlighted in magenta.

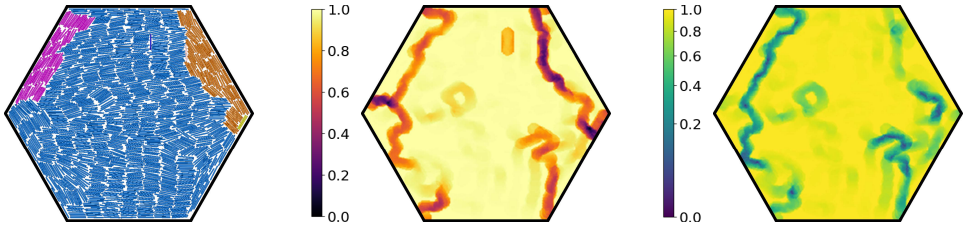

FIG. 11: Particle snapshot, nematic order parameter S and tetratic order parameter T for a representative simulation of hard rods in a hexagon with $N = 1347$, $\eta = 0.725$ and $p = 11.5$.

thus disconnecting the individual grain-boundary networks. In return, this results in a higher frequency of structures with unified neighboring domains, as can be nicely observed for $N = 2000$ in Fig. 9. This behavior is exemplified in a more pronounced way for $N = 5000$ in Fig. 10, depicting a larger number of grain boundaries with partially annihilated tetratic end points, while the length of all grain boundaries relative to the cavity size decreases.

D. Comparison between simulation and experiment

To establish a closer connection to the experimental data shown in the main manuscript, we show in Tab. III a set of simulation data for systems with a constant ratio $a_{\mathrm{hex}}/(L + D) = 7.5$ of the side length of the hexagonal confinement and the rod length. This allows for the formation of seven to eight smectic layers at each side like in the experiment. The remaining parameters are the area fraction η and the rod aspect ratio p.

Keeping the packing fraction fixed, we find that the distribution of the different structures is largely independent of the aspect ratio, although a change in p is accompanied by a relatively big change in the particle number N. This means that the effect described in Sec. 5 C of increasing N is mainly due to increasing the typical length scale of the confinement relative to the particle length. Therefore, the difference of (effective) aspect ratios in our simulations and experiments has no significant effect. In contrast, we observe a clear trend that the distribution of domain numbers shifts to smaller values when the packing fraction η is reduced. In conclusion, structures with more flexible smectic layers as well as less separated domains, which are typical for our colloidal experiment, are best reproduced in our hard-rod simulations for choosing a particle number N and aspect ratio p compatible with the desired number of layers in a given geometry and reducing the packing fraction η, see Fig. 11 for an exemplary structure.

In principle, a closer match between simulation and experiment could likely be reached by taking into account (i) the effects of the slight softness and polydispersity of the silica rods, which also tend to reduce the rigidity of the smectic layers, (ii) the three-dimensional nature of the experiment, which makes it difficult to estimate and compare an explicit packing fraction at the bottom, and (iii) the particular equilibration protocol of the two-dimensional simulation, contrasting the experimental sedimentation process (also note that the compression in our experiments is faster than in Ref. [12], since in this work we use a larger number of rods, which results in a higher osmotic pressure at the bottom of the cavity).

[1] C. Vega and S. Lago, Comput. Chem. **18**, 55 (1994).
[2] H. C. Andersen, D. Chandler, and J. D. Weeks, J. Chem. Phys. **56**, 3812 (1972).
[3] R. Wittmann, C. E. Sitta, F. Smallenburg, and H. Löwen, J. Chem. Phys. **147**, 134908 (2017).
[4] N. Metropolis, A. W. Rosenbluth, M. N. Rosenbluth, A. H. Teller, and E. Teller, J. Chem. Phys. **21**, 1087 (1953).
[5] M. A. Bates and D. Frenkel, J. Chem. Phys. **112**, 10034 (2000).
[6] M. Kleman and O. D. Lavrentovich, *Soft Matter Physics - An Introduction* (Springer-Verlag, 2003).
[7] O. D. Lavrentovich, Liquid Crystals **24**, 117 (1998).
[8] W. Fulton, *Algebraic Topology - A First Course* (Springer-Verlag, 1995).
[9] O. V. Manyuhina, K. B. Lawlor, M. C. Marchetti, and M. J. Bowick, Soft Matter **11**, 6099 (2015).
[10] I. C. Gârlea, P. Mulder, J. Alvarado, O. J. Dammone, D. G. A. L. Aarts, M. P. Lettinga, G. H. Koenderink, and B. M. Mulder, Nat. Commun. **7**, 12112 (2016).
[11] Y.-K. Kim, S. V. Shiyanovskii, and O. D. Lavrentovich, J. Condens. Matter Phys. **25**, 404202 (2013).
[12] R. Wittmann, L. B. G. Cortes, H. Löwen, and D. G. A. L. Aarts, Nat. Commun. **12**, 623 (2021).

P2 Topological fine structure of smectic grain boundaries and tetratic disclination lines within three-dimensional smectic liquid crystals

Published as open access and reproduced from

P. A. Monderkamp, R. Wittmann, M. te Vrugt, A. Voigt, R. Wittkowski, and H. Löwen,
Topological fine structure of smectic grain boundaries and tetratic disclination lines within three-dimensional smectic liquid crystals,
Phys. Chem. Chem. Phys. **24**, 15691 (2022)

with permission from the Royal Society of Chemistry.

Digital Object Identifier (DOI): `https://doi.org/10.1039/D2CP00060A`

Statement of contribution

R. Wittmann, H. Löwen, and I developed the model for the three-dimensional topological charge distribution and tetratic disclination lines.
M. te Vrugt and R. Wittkowski derived the exact mathematical form of the order parameter with the necessary properties and wrote the text in the appendix.
I performed the numerical simulations, designed the figures and wrote the text.
R. Wittmann, M. te Vrugt and I finalised the manuscript.
Funding and overseeing was provided by R. Wittkowski and H. Löwen.
All authors contributed text associated with their respective expertise in the paper and appendix.

P2.1 Paper and appendix: Topological fine structure of smectic grain boundaries and tetratic disclination lines within three-dimensional smectic liquid crystals

Volume 24
Number 26
14 July 2022
Pages 15607–16398

PCCP

Physical Chemistry Chemical Physics

rsc.li/pccp

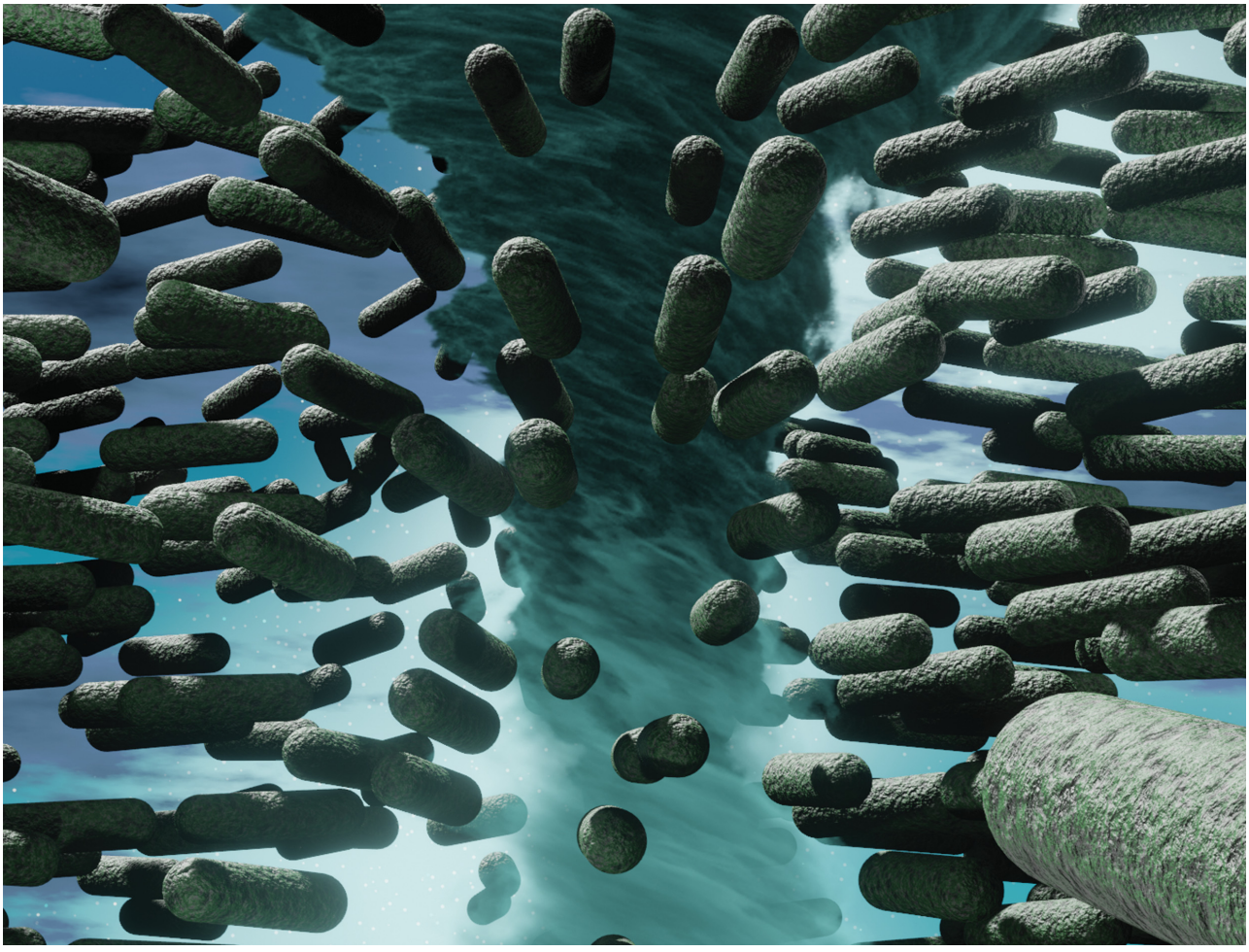

ISSN 1463-9076

ROYAL SOCIETY OF CHEMISTRY

PAPER
René Wittmann *et al.*
Topological fine structure of smectic grain boundaries and tetratic disclination lines within three-dimensional smectic liquid crystals

PCCP

ROYAL SOCIETY OF CHEMISTRY

PAPER

View Article Online
View Journal | View Issue

Cite this: *Phys. Chem. Chem. Phys.*, 2022, **24**, 15691

Topological fine structure of smectic grain boundaries and tetratic disclination lines within three-dimensional smectic liquid crystals

Paul A. Monderkamp, [a] René Wittmann, [a]* Michael te Vrugt, [b] Axel Voigt, [c] Raphael Wittkowski [b] and Hartmut Löwen [a]

Received 5th January 2022,
Accepted 26th April 2022

DOI: 10.1039/d2cp00060a

rsc.li/pccp

Observing and characterizing the complex ordering phenomena of liquid crystals subjected to external constraints constitutes an ongoing challenge for chemists and physicists alike. To elucidate the delicate balance appearing when the intrinsic positional order of smectic liquid crystals comes into play, we perform Monte-Carlo simulations of rod-like particles in a range of cavities with a cylindrical symmetry. Based on recent insights into the topology of smectic orientational grain boundaries in two dimensions, we analyze the emerging three-dimensional defect structures from the perspective of tetratic symmetry. Using an appropriate three-dimensional tetratic order parameter constructed from the Steinhardt order parameters, we show that those grain boundaries can be interpreted as a pair of tetratic disclination lines that are located on the edges of the nematic domain boundary. Thereby, we shed light on the fine structure of grain boundaries in three-dimensional confined smectics.

1 Introduction

Omnipresent throughout a vast range of chemical and physical systems,[1–12] topological defects play a central role in characterizing collective ordering phenomena. As one of the default systems for investigating such ordering phenomena, liquid crystals[13] have been enjoying continuous attention within the physical chemistry and chemical physics communities over the past decades and remain an active field of research.[14] Liquid-crystalline mesophases accompanied by topological defects occur, *e.g.*, in viral colonies,[15] bacterial DNA,[16] biopolymers,[17] and active systems[18–21] realized, *e.g.*, by swarms of bacteria[22–25] or driven filaments.[26,27] Topological analysis even provides a tool for insight into the collective behavior of animals on a macroscopic scale, *e.g.*, shoals of fish, where local coherent swimming is a vital tool in the evasion of predators.[28,29]

The most prominent type of ordering, which is typically found in liquid crystals, is orientational (nematic) ordering, where the characteristically shaped subunits, *i.e.*, molecules or colloidal particles in close proximity, show a tendency to align. This alignment can be induced or enhanced by the system boundaries.[30–32] If the nematic order gets frustrated, *e.g.*, within floating droplets,[33–37] by external confinement,[38–48] near obstacles,[49–58] or on curved surfaces,[59–65] topological defects emerge, which are discontinuities in the ordered structures that can display particle-like properties themselves.[1,20,66–68]

In liquid crystals which feature exclusively orientational order of the fluid particles, so-called nematics, the commonly observed stable defects are singular points in a two-dimensional (2d) plane and curves in three-dimensional (3d) space that are either closed or end on system boundaries. The defect strength in 2d nematic liquid crystals is characterized by a so-called topological charge, which obeys an additive conservation law in analogy to the electric charge. This topological charge is determined by the total change of the preferred local orientation of the fluid on a contour around the defects.[69,70] At higher densities and/or low temperatures, certain liquid crystals form the so-called smectic phase, which additionally displays positional order. Traditionally, the study of defects in smectic liquid crystals is mainly concerned with the purely positional defects, such as edge dislocations[71–74] or complex structures like focal conics.[75–77] However in situations, where frustration of nematic ordering takes a pronounced role, the consideration of the topology of the local orientations has proven insightful.

Smectic liquid crystals are characterized by an intrinsic layering, such that the discontinuities in the local order preferably appear as grain boundaries separating different domains within the fluid. These elongated defects possess a linear shape in two and a planar shape in three dimensions.[78]

[a] *Institut für Theoretische Physik II: Weiche Materie, Heinrich-Heine-Universität Düsseldorf, 40225 Düsseldorf, Germany. E-mail: rene.wittmann@hhu.de*
[b] *Institut für Theoretische Physik, Center for Soft Nanoscience, Westfälische Wilhelms-Universität Münster, 48149 Münster, Germany*
[c] *Institut für Wissenschaftliches Rechnen, Technische Universität Dresden, 01062 Dresden, Germany*

View Article Online
Paper PCCP

The formation of grain boundaries can be enforced when the fluid is confined to a container, such that the local preferred orientation in the system depends heavily on the position. This is in particular the case for colloidal liquid crystals which interact mainly through volume exclusion and possess a strong tendency to maintain a uniform layering, such that the relaxation of external constraints by elastic deformations only plays a minor role (unless favored by the confining topology).[79] For such 2d colloidal liquid crystals, we have previously elaborated that the notion of the emerging domain boundaries as topological objects with coexisting nematic and tetratic charges yields insight into the orientational topology of smectics[80] (for a comprehensive summary see Section 2.3). However, the role of the orientations within smectic liquid crystals still remains to be further understood. This concerns in particular the analysis of three-dimensional systems.

To shed more light on this issue, we present a range of simulation results for confined hard rods, representing colloidal smectic liquid crystals in three dimensions. The confinement causes frustration of the bulk symmetry and induces the formation of topological defects, which are observed and analyzed on the particle scale by treating the local orientations of the rods as indicative of the local director field. As elaborated in Section 2.3, the investigation of orientational topology in three dimensions is more involved, since 3d topological charges do not adhere to an additive charge conservation like their 2d counterparts.[69,81] However, under specific circumstances, this additive charge conservation is recovered. By elaborating on the analogy to the 2d case, we explain the effects of the introduction of the third dimension and investigate the conditions for additive topological charge conservation.

This article is structured as follows: in Section 2, we present our methodology. After elaborating in Section 2.1 on the simulation protocol, we introduce the order parameters used to characterize the simulation results in Section 2.2, while we provide a detailed discussion of the three-dimensional tetratic order parameter in Appendix A. In Section 2.3, we explain the analysis of the topological charge and the details of the charge conservation. In Section 3, we present our results, by first evaluating in Section 3.1 the order parameters to detect and classify the emerging defects in our particle-resolved snapshots. Then we characterize the layer structure and orientations within the two confinements in Section 3.2, where Appendix B provides more detailed account of the cylindrical geometry. We discuss the implications on the topological charge in Section 3.3. Lastly, we conclude in Section 4.

2 Methods

2.1 Simulations

We perform canonical Monte Carlo (MC) simulations of a model for colloidal rods confined to 3d cavities, see Fig. 1. Specifically, we consider soft walls in the shape of cylinders $\{\mathbf{r} \in \mathbb{R}^3 | {r_x}^2 + {r_y}^2 \leq R^2, 0 \leq r_z \leq h\}$ and spherical caps, resembling a drop-like shape, $\{\mathbf{r} \in \mathbb{R}^3 | {r_x}^2 + {r_y}^2 + {r_z}^2 < R^2, r_z > R - h\}$, both of

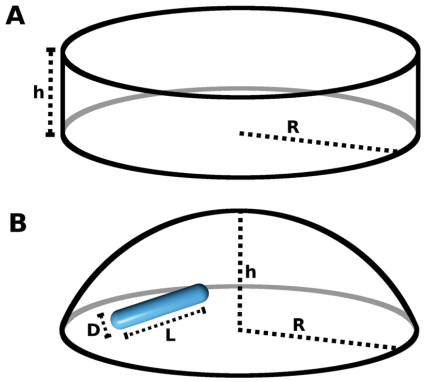

Fig. 1 Schematic depiction of the confinement considered in our simulation of three-dimensional liquid crystals. We simulate the liquid crystals by a system of N spherocylinders with length L and diameter D in confinement to suppress the bulk symmetry of the fluid in order to observe topological defects. (A) Cylindrical cavity with radius R and height h. (B) Spherical-cap cavity with radius R and height h.

radius R and height h. The rods are modeled as hard spherocylinders with aspect ratio $p = L/D = 5$, with core length L and diameter D. Note that in two dimensions, one would require significantly longer rods to observe stable smectic structures.

The pair potential for the particle–particle interaction is given by the standard hard-core repulsion[82]

$$U(\mathbf{r}_i, \mathbf{r}_j, \hat{\mathbf{u}}_i, \hat{\mathbf{u}}_j) = \begin{cases} \infty & \text{for } d_{i,j} \leq D, \\ 0 & \text{for } d_{i,j} > D \end{cases} \quad (1)$$

for spherocylinders with

$$d_{i,j} = \min_{|\alpha,\beta| < \frac{L}{2}} \left\| \mathbf{r}_i + \alpha\hat{\mathbf{u}}_i - (\mathbf{r}_j + \beta\hat{\mathbf{u}}_j) \right\|, \quad (2)$$

where $\mathbf{r}_k$ and $\hat{\mathbf{u}}_k$ are the position and normalized orientation of the k-th rod, respectively. The convexity of the confining cavities enables us to specify a wall–particle interaction potential $V(x)$ by modeling the rods as two virtual point-like particles at $\mathbf{r}_\pm = \mathbf{r}_k \pm (L/2)\mathbf{u}_k$. The interaction potential is then given by

$$V(x) = \begin{cases} \Phi(x_0) + \Phi'(x_0)(x - x_0) & \text{for } x \leq x_0, \\ \Phi(x) & \text{for } x_0 > x, \end{cases} \quad (3)$$

where $|x|$ denotes the minimal perpendicular distance from either of the two points to the wall and $x > 0$ corresponds to the inside of the cavity. The cut-off point, below which $V(x)$ is linear, is chosen as $x_0 = 0.5D$. Moreover, $\Phi(x)$ is the canonical Weeks–Chandler–Andersen-potential

$$\Phi(x) = \begin{cases} 4\varepsilon\left[\left(\frac{D}{x}\right)^{12} - \left(\frac{D}{x}\right)^{6}\right] + \varepsilon & \text{for } x \leq 2^{\frac{1}{6}}D \\ 0 & \text{for } x > 2^{\frac{1}{6}}D, \end{cases} \quad (4)$$

with $\varepsilon = 10k_BT$ (with the Boltzmann constant k_B and the temperature T),[83] mimicking nearly hard walls. In what follows,

View Article Online
PCCP Paper

we consider confinements with fixed footprint radius $R = 4L$ and different heights $h \in [0.3L, 4.5L]$, whereas in Appendix B we discuss additional data for cylinder heights up to $h = 15L$.

To create the smectic structures in our 3d cavities, we follow a compression protocol, where we initialize the system at a low volume fraction $\eta_0 = 5 \times 10^{-3}$ and compress until the volume fraction $\eta_2 = 0.52$ is reached, at which the smectic-A phase is stable in the bulk. Here, the volume fraction η is defined as $\eta = NV_{\mathrm{hsc}}/V_{\mathrm{cav}}$, with the particle number N, the volume of a hard spherocylinder V_{hsc} and the total volume of the confining cavity V_{cav}. Since in each simulation run the particle geometry, the shape and size of the confinement and the final volume fraction are fixed, the particle number N is a variable that gets adjusted accordingly. The values of N we investigate, determined by the parameters above, typically lie between $N \approx 200$ for extremely shallow cavities and $N \approx 3300$ for the tallest cavities with $h = 4.5L$ that are addressed in the main part of this publication.

After initialization at $\eta_0 = 5 \times 10^{-3}$, we perform a large number of MC cycles, each of which consists of a trial displacement or rotation of each particle. The acceptance probability $P = \min\left(1, \exp\left(-\frac{\Delta U}{k_{\mathrm{B}}T}\right)\right)$ is given by the Metropolis criterion from the difference ΔU of the energies (see eqn (1) and (3)) in the system before and after trial move.[84] In detail, we compress the system for 10^6 MC cycles $\sim 10^9$ trial moves with a rate of $\Delta\eta_1 = 2.45 \times 10^{-7}$ per MC cycle to the volume fraction $\eta_1 = 0.25$ and then, in a second stage for 5×10^6 MC cycles $\sim 5 \times 10^9$ trial moves, with a rate $\Delta\eta_2 = 5.4 \times 10^{-8}$ per MC cycle to $\eta_2 = 0.52$. This two-step simulation protocol is implemented such that the majority of the simulation takes place in the regime of the packing fraction where self-assembly into the ordered phases occurs, ensuring a proper equilibration. To calculate average distribution functions and global order parameters, we gather statistics from up to 15 simulation runs.

2.2 Order parameters

We examine the structure of the confined fluid with the help of two orientational order parameters. The first one is the standard nematic order parameter $\mathcal{S}$, associated with orientational ordering of uniaxial particles, which corresponds to the largest eigenvalue of the nematic tensor $\mathcal{Q}$.[13,85] To numerically generate the scalar field $\mathcal{S}(\mathbf{r})$, we sample the nematic tensor within a spherical subsystem of radius $2.5D$ around each point $\mathbf{r}$ as

$$\mathcal{Q}(\mathbf{r}) = \left\langle \frac{3}{2}\hat{\mathbf{u}}_k \otimes \hat{\mathbf{u}}_k - \frac{1}{2}\mathbb{I}_3 \right\rangle_{B_{2.5D}(\mathbf{r})}. \tag{5}$$

Here, the brackets denote an average over all N_B particles contained within the ball $B_{2.5D}(\mathbf{r})$ with the individual orientations $\hat{\mathbf{u}}_k = (\sin\theta_k\cos\phi_k, \sin\theta_k\sin\phi_k, \cos\theta_k)^{\mathrm{T}}$ in spherical coordinates for $k \in \{1,\ldots,N_B\}$, where θ and ϕ are the angles to the z- and x-axes, respectively, and the 3d unit matrix $\mathbb{I}_3$. $\mathcal{S}(\mathbf{r})$ denotes the largest eigenvalue of $\mathcal{Q}(\mathbf{r})$. The mean local orientation $\hat{\mathbf{n}}(\mathbf{r}) = \mathbf{n}(\mathbf{r})/\|\mathbf{n}(\mathbf{r})\|$ of the rods, *i.e.*, the nematic director, can be computed by normalizing the eigenvector $\mathbf{n}(\mathbf{r})$ associated with $\mathcal{S}(\mathbf{r})$, where $\|\cdot\|$ is the Euclidean norm.

As will be discussed later, the favorable nematic bulk symmetry of orientational ordering is broken when the fluid is confined to a cavity. In two dimensions, the topological fine structure of the spatially extended defect lines in the director field $\hat{\mathbf{n}}(\mathbf{r})$ can be investigated using a scalar tetratic order-parameter field, which can be defined as

$$\mathcal{T}_{(2\mathrm{d})}(\mathbf{r}) = \left|\langle \exp(i4\phi_k)\rangle_{B_{2.5D}(\mathbf{r})}\right| \tag{6}$$

for a 2d subsystem with radius $2.5D$, with the imaginary unit i and the 2d polar angle of the k-th particle ϕ_k.[86,87] Note that this tetratic order parameter evaluates to $\mathcal{T}_{2\mathrm{d}} = 1$ when each pair of rods is either mutually parallel or perpendicular.

Similarly, in three dimensions, the discontinuities in the director field typically form grain boundaries, *e.g.*, defect planes. To develop a classification concept in three dimensions, we construct in Appendix A a 3d tetratic order parameter from the Steinhardt order parameters[88]

$$I_l = \sum_{m=-l}^{l} |\langle Y_{lm}\rangle|^2 \tag{7}$$

with the spherical harmonics Y_{lm}. Globally, this tetratic order parameter $\mathcal{T}$ is given by

$$\mathcal{T} = \frac{16\pi}{21N^2}\left|\sum_{m=-4}^{4}\left|\sum_{k=1}^{N} Y_{4m}(\theta_k,\phi_k)\right|^2 - \frac{3}{4}\sum_{m=-2}^{2}\left|\sum_{k=1}^{N} Y_{2m}(\theta_k,\phi_k)\right|^2\right|. \tag{8}$$

This definition results in $\mathcal{T} = 0$ for an isotropic system, where the orientations $\{\hat{\mathbf{u}}_k\}$ are uniformly distributed on the unit sphere S^2 and $\mathcal{T} = 1$ for a system where all orientations are pairwise either parallel or orthogonal, *i.e.*, if we have a local Cartesian coordinate system, where all rods are aligned to either of the axes. Analogously to the 2d tetratic order parameter $\mathcal{T}_{(2\mathrm{d})}$, our definition (8) of $\mathcal{T}$ implies both perfect cubatic ($\mathcal{T} = 1$, $\mathcal{S} = 0$) and perfect nematic order ($\mathcal{T} = 1$, $\mathcal{S} = 1$) as special cases of $\mathcal{T} = 1$, such that we cannot measure this kind of tetratic order in a 3d system with either the standard cubatic[89,90] or the standard nematic order parameter.

We now prove that the 3d tetratic order parameter (8) has the desired properties. First, we show that it is 0 for an isotropic system. In this case, the orientations $\{\theta_k, \phi_k\}$ approach a uniform distribution on the unit sphere S^2, such that the inner sums over k in eqn (8) approach an integral over S^2. This integral vanishes since the spherical harmonics satisfy

$$\int_{S^2} \mathrm{d}\Omega\, Y_{lm}(\theta,\phi) = 0 \tag{9}$$

for $l \neq 0$. Second, we show that it is 1 for a system where all particles are pairwise either parallel or orthogonal. Since $\mathcal{T}$ is by construction invariant under coordinate transformations and since the functions Y_{4m} and Y_{2m} are invariant under parity

View Article Online
Paper PCCP

transformation, we can assume without loss of generality that we have a configuration (Λ) of a particles with orientation $(\theta,\phi) = (\pi/2, 0)$, b particles with orientation $(\theta,\phi) = (\pi, 0)$ and c particles with orientation $(\theta,\phi) = (\pi/2, \pi/2)$ (with $a, b, c \in \mathbb{N}_0$). The order parameter (8) then evaluates to

$$\begin{aligned}\mathcal{T}^{(\Lambda)} &= \frac{16\pi}{21(a+b+c)^2} \\ &\times \left| \sum_{m=-4}^{4} \left| a Y_{4m}\left(\frac{\pi}{2},0\right) + b Y_{4m}(\pi,0) + c Y_{4m}\left(\frac{\pi}{2},\frac{\pi}{2}\right)\right|^2 \right. \\ &\left. - \frac{3}{4}\sum_{m=-2}^{2} \left| a Y_{2m}\left(\frac{\pi}{2},0\right) + b Y_{2m}(\pi,0) + c Y_{2m}\left(\frac{\pi}{2},\frac{\pi}{2}\right)\right|^2 \right| \\ &= 1, \end{aligned} \tag{10}$$

as can be easily confirmed by evaluating eqn (10) using a computer algebra system. Further examples are given in Appendix A.2.

Finally, to generate a local field $\mathcal{T}(\mathbf{r})$ of the tetratic order parameter from our simulation data, we sample the spherical harmonics entering eqn (8) only within local spherical subsystems $B_{2.5D}(\mathbf{r})$, which yields

$$\begin{aligned}\mathcal{T}(\mathbf{r}) = \frac{16\pi}{21} &\left| \sum_{m=-4}^{4} \left| \langle Y_{4m}(\theta_k,\phi_k)\rangle_{B_{2.5D}(\mathbf{r})}\right|^2 \right. \\ &\left. - \frac{3}{4}\sum_{m=-2}^{2} \left| \langle Y_{2m}(\theta_k,\phi_k)\rangle_{B_{2.5D}(\mathbf{r})}\right|^2 \right|, \end{aligned} \tag{11}$$

analogously to the nematic tensor, *cf.* eqn (5).

2.3 Topological charge

Topological defects are identified as discontinuities in the director field $\hat{\mathbf{n}}(\mathbf{r})$, see Fig. 2. In 2d nematic liquid crystals, the types of stable bulk defects are point defects. The strength of the defect, *i.e.*, the degree of deformation of the surrounding fluid, is typically analyzed by a topological charge Q that equates to the total rotation of the director traversing any contour $\mathcal{C}$ around the defect. This charge is given by the winding number that can be explicitly calculated as the closed line integral along the contour $\mathcal{C}$ parametrized by κ, *i.e.*,

$$Q = \frac{1}{2\pi}\oint_{\mathcal{C}(\kappa)} \left[\hat{n}_1(\kappa)\frac{\partial \hat{n}_2(\kappa)}{\partial\kappa} - \hat{n}_2(\kappa)\frac{\partial \hat{n}_1(\kappa)}{\partial\kappa}\right] \mathrm{d}\kappa, \tag{12}$$

where $\oint_{\mathcal{C}(\kappa)} \mathrm{d}\kappa = 2\pi$.[85] Due to the apolarity of the particles, the configuration space of the orientations is a semicircle with end points identified, commonly denoted by S^1/Z_2, *i.e.*, we now consider $\hat{\mathbf{n}}$ to be a headless vector in the sense that we identify $\hat{\mathbf{n}}$ and $-\hat{\mathbf{n}}$.

From a topological point of view, we define the charge *via* the winding number because (since the winding number is a discrete quantity) different contours with different winding numbers can not be continuously transformed into each other, *i.e.*, are not homotopic. All possible contours in the liquid crystal correspond to loops in S^1/Z_2. The fundamental group $\pi_1(S^1/Z_2)$ classifies loops in S^1/Z_2 up to homotopy equivalence.

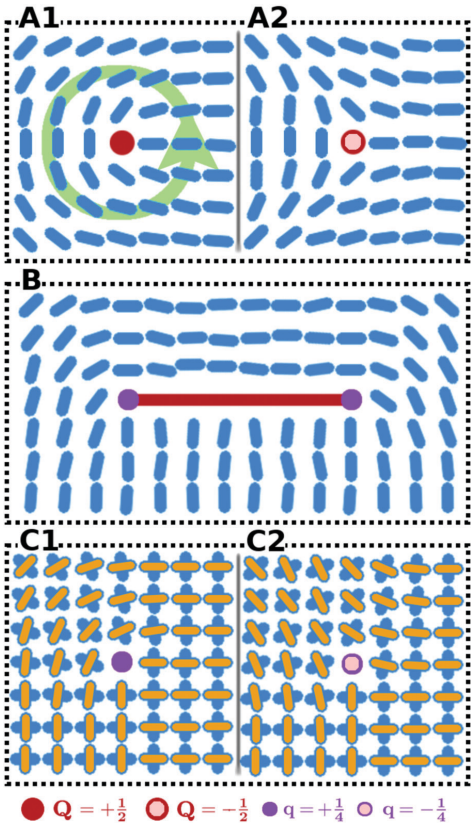

Fig. 2 Schematic of the classification of topological defects in two dimensions, present as discontinuities in the director field $\hat{\mathbf{n}}(\mathbf{r})$. The topological charge of a defect corresponds to the net rotation of $\hat{\mathbf{n}}(\mathbf{r})$ traversing the defect in counter-clockwise direction (indicated by the arrow in A1) around the defects. (A) Point defects for particles of π rotational symmetry with charges $Q = +1/2$ (A1) and $Q = -1/2$ (A2) typically present in nematic liquid crystals. (B) Decomposition of smectic grain boundaries into tetratic point defects. Due to the preferred difference in orientation angles of $\pi/2$, the line defects can be classified as two isolated tetratic point defects of charge $q = \pm 1/4$. The schematic shows an exemplary line defect of total charge $Q = q_1 + q_2 = 1/2$. (C) Point defects for particles with $\pi/2$ rotational symmetry. Charges are $q = +1/4$ (C1) and $q = -1/4$ (C2). For ease of observing the continuous rotation, the two main axes are decorated differently.

Consequently, all possible defects are classified by the fundamental group $\pi_1(S^1/Z_2)$. This group is given by $\mathbb{Z}/2$ with the addition operation +. (The prefactor 1/2 is a convention used in physics that is motivated by the geometric definition of charges *via* the winding number.) Therefore, the possible charges are $Q \in \{k/2 | k \in \mathbb{Z}\}$ and these charges can be added to find the total charge of a combination of two defects. The sum of all charges is a conserved quantity in two dimensions (since it has to match the Euler characteristic of the confinement[91]). As an example, we illustrate $Q = 1/2$ in Fig. 2A1 and $Q = -1/2$ in

Fig. 2A2. Moreover, the number of elements in $\pi_1(S^1/Z_2)$ is infinite, which is exemplified by the fact that the winding number can be any half-integer.

Defects typically observed in 3d nematics are disclination lines, along which the local orientational order is frustrated. (Point defects in three dimensions (hedgehogs) are not considered in this work.) In analogy to the 2d case, topological defects can be classified by considering closed loops in the orientational configuration space, up to homotopy equivalence. One typically analyses the defect in terms of the topology of a planar cross-section perpendicular to the disclination line.[92] Since the configuration space of the orientations in three dimensions is a hemisphere with antipodal points identified, commonly denoted by S^2/Z_2, the rotation of $\hat{\mathbf{n}}(\mathbf{r})$ along $\mathcal{C}$ forms loops in S^2/Z_2, classified by $\pi_1(S^2/Z_2)$. By rotation into the third dimension, all half-integer disclinations can be continuously mapped onto each other. Correspondingly, $\pi_1(S^2/Z_2)$ has only two elements. As a result, for instance, 3d defects with cross-sections like in Fig. 2A1 ($Q = +1/2$) and Fig. 2A2 ($Q = -1/2$) are homotopically equivalent. More specifically, the opposite charges $\pm 1/2$ correspond to opposite paths around half of the base of the hemisphere S^2/Z_2, both connecting two antipodal points. A $+1/2$ defect can be transformed into a $-1/2$ defect by passing the corresponding path in S^2/Z_2 over the north pole of the hemisphere. This implies that (a) the charge defined by eqn (12) is no longer a conserved quantity and (b) it can no longer be used to classify the possible configurations of the nematic liquid crystal up to homotopy equivalence. There are only two topologically distinct configurations left, namely defect and no defect. (The discussion in this paragraph and the previous paragraph follows ref. 69.)

Smectic liquid crystals, which additionally feature layering of the fluid particles, can be treated in the same spirit as nematics by considering a vector field normal to the smectic layers[93,94] or by directly working with the nematic director[95,96] (which coincides with the layer normals in the case of smectic-A order). However, if the smectic layers are sufficiently rigid, which is a prominent feature of colloidal systems, the discontinuities in the layered structure take the distinct form of elongated grain boundaries. Those grain boundaries are lines in two dimensions and planes in three dimensions. Recent insight into the orientational topology of colloidal smectics in two dimensions[80] suggests that these grain boundaries can be analyzed from the viewpoint of orientational topology by associating a topological charge to these defects as a whole. Furthermore, it has been shown that the rotation of the local director occurs mainly around the endpoints of the grain boundaries (see Fig. 2B). Those endpoints can be analyzed as isolated tetratic point defects by superimposing a tetratic director onto the fluid particles, *i.e.*, considering orientations with $\pi/2$ rotational symmetry, where one of the axis points along the main axes of the rods (see Fig. 2C). Due to the preferred difference of $\pi/2$ in the orientation angle across the grain boundary in smectics, those tetratic point defects display quarter charges $Q \in \{k/4 | k \in \mathbb{Z}\}$ (see Fig. 2C). Geometrically speaking, this is a consequence of the fact that the rotation of the director around such a defect (divided by 2π) is an integer multiple of $1/4$ (and not of $1/2$ as for standard nematic defects). Topologically speaking, this is a consequence of the fact that the tetratic order parameter superimposed in Fig. 2C takes values in $(S^1/Z_2)/Z_2$, which is a quarter-circle with end points identified. This order parameter becomes singular only at the endpoints, such that we can classify these endpoints as topological defects by integrating along a closed contour around them without having to pass through a singular point. The fundamental group is $\pi_1\left(\left(S^1/Z_2\right)/Z_2\right) = \mathbb{Z}/4$, where the conventional prefactor has now been set to $1/4$.

An important property of smectic structures is their rigidity due to the additional constraint provided by the positional order. As will be detailed in the results in Section 3, the space occupied by the orientations $\{\hat{\mathbf{u}}_k\}$ is drastically reduced in our simulations of 3d colloidal smectic systems, *i.e.*, all orientations are approximately perpendicular close to the line disclinations. Therefore, it is no longer possible to transform the defects with $Q = +1/2$ into defects with $Q = -1/2$, implying that they are topologically distinct and that the charge Q defined by eqn (12) is effectively a conserved quantity. In this way, we construct a formalism for analyzing the 3d grain boundaries in Section 3 with the help of the previously defined 2d model.[80]

3 Results

3.1 Detection of defects *via* order parameters

Previous studies on 2d smectics in a simply-connected convex confining cavity[79,97,98] have shown the existence of a large, relatively defect-free central domain, encompassing several smectic layers, which connect opposite ends of the cavity. This bridge state can generally be observed for a large range of confinements.[80] Indeed, we find that this reference structure also persists when extending the system into the third dimension.

In our 3d study, we compare typical simulation results, shown both in Fig. 3 from a bird's eye view and in Fig. 4 using a 2d depiction, for two representative systems of hard rods confined to a cylindrical container (column 1) and spherical cap (column 2). The snapshots in Fig. 3A1 and A2 give an indication of the chosen dimensions of the confinement in terms of the dimensions of the individual particles: The height h of both cylinder and spherical cap is $2.4L$, while the diameter $2R$ of the footprint is fixed at $8L$. Both systems display what can be considered a generalized 3d bridge state. This becomes even clearer when considering the bottom view of both systems in Fig. 4A1 and A2. Apparently, the bottom layer of rods in our 3d systems forms 2d bridge states. Due to the symmetry of the cylinder, this structure is also mirrored on the top side. Even though the top surface of the spherical cap is strongly curved, the structure on it still resembles a 2d bridge state.

To study the particle orientation throughout the system in more detail, we examine the topology of the corresponding order-parameter fields. In Fig. 3B1 and B2, we visualize the data points of low nematic order by showing the regions with

View Article Online
Paper PCCP

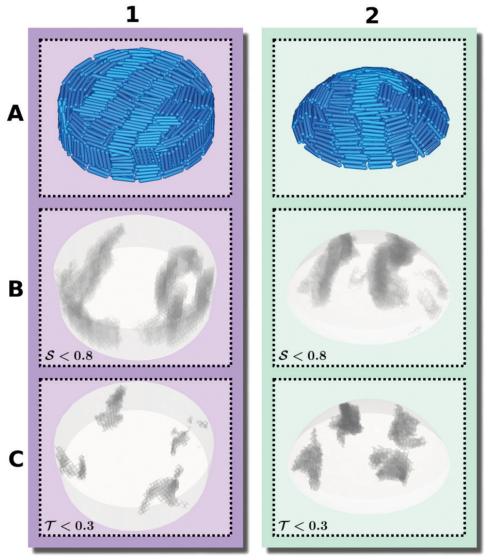

Fig. 3 Exemplary simulation results for two systems of 3d confined smectic liquid crystals. Column 1: cylinder. Column 2: spherical cap. Both systems feature height h = 2.4L and diameter 2R = 8L. Row A: Bird's eye view of the simulated system of hard rods. Row B: 3d visualization of the nematic defects according to the order parameter $\mathcal{S}(\mathbf{r})$. In order to observe the regions of low nematic order, *i.e.*, defect regions, we display the data points with $\mathcal{S}(\mathbf{r}) < 0.8$ as opaque gray clouds. Row C: 3d visualization of the tetratic defects according to the 3d tetratic order parameter $\mathcal{T}(\mathbf{r})$. To visualize the defect regions, we only display the data points with $\mathcal{T}(\mathbf{r}) < 0.3$.

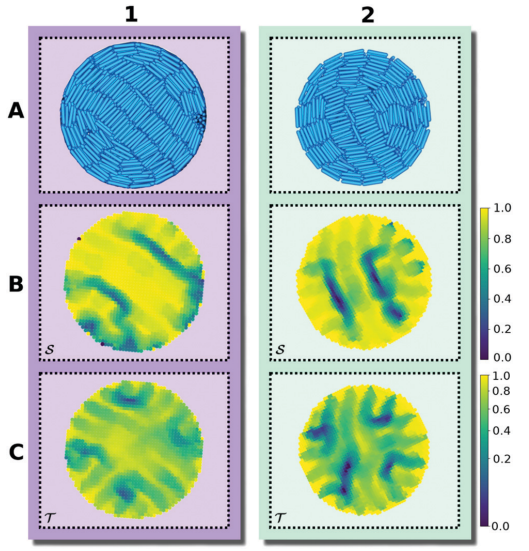

Fig. 4 The same two 3d systems as depicted in Fig. 3, but shown from a 2d perspective. Column 1: cylinder. Column 2: spherical cap. Row A: bottom view of the snapshots to exemplify the structure of the 2d cross-sections. Row B: $\mathcal{S}(\mathbf{r})$ for the system projected onto the horizontal plane. Row C: $\mathcal{T}(\mathbf{r})$ for the system projected onto the horizontal plane.

$\mathcal{S}(\mathbf{r}) < 0.8$ in gray. For both confinements, the resulting plots show a pair of planar disclinations, nestled to the sides of the central bridge domain. These defect planes reach from the top to the bottom of the container, while their shape barely varies along the vertical axis. Moreover, at cross sections of constant height, they have very little contact to the outer walls. This picture is reinforced in Fig. 4B1 and B2, which show the nematic field of the systems projected on the horizontal plane, *i.e.*, the plane perpendicular to the symmetry axis. Indeed, these projections closely resemble the nematic field $\mathcal{S}(\mathbf{r})$ for 2d systems, confirming that the shape of the defect planes varies little along the vertical axis. In addition to these grain-boundary planes, the simulated cylindrical structure gives rise to several spots where $\mathcal{S}(\mathbf{r})$ is significantly decreased at the mantle surface. As can be seen in Fig. 3A1, these spots correspond to locations where layers of single-rod depth align with the cylinder mantle. For the spherical cap, the formation of such domains is largely suppressed by the curved boundary.

Fig. 3C1 and C2 similarly show regions of low 3d tetratic order according to the order parameter $\mathcal{T}(\mathbf{r})$. In analogy to the nematic case, we locate the defects by identifying the regions where this order is minimal. Due to the relatively high sensitivity to orientational fluctuations of $\mathcal{T}(\mathbf{r})$, we display the data points only for $\mathcal{T}(\mathbf{r}) < 0.3$ in gray. It is then clearly visible that the nematic defect planes split into two tetratic defect pillars, each spanning from the bottom plane of the cavity to the top surface. Fig. 4C1 and C2 show the corresponding tetratic order-parameter field for the systems projected on the horizontal plane. This visualization shows that the minima in the order-parameter field are well localized and take an almost point-like shape. This again confirms that the tetratic disclinations in 3d appear as relatively straight lines, parallel to the vertical axis of the confinement.

In general, one identifies orientational defects as singular geometric objects in space, where the local director field $\hat{\mathbf{n}}(\mathbf{r})$ (see eqn (5)) jumps discontinuously. In particular, in 2d/3d liquid crystals with a smectic-A symmetry, the typical difference across any defect is $\pi/2$. As a result, nematic defects can be identified with the help of $\mathcal{S}(\mathbf{r})$. The same angular difference leads to a promotion of tetratic order everywhere except for the endpoints/edges, where the preferred orientation rotates. As a result, we identify a set of tetratic disclination points/lines, with the help of $\mathcal{T}(\mathbf{r})$, that sit on the endpoints/edges of each nematic defect.

3.2 Confined smectic structure

To better understand the structural details of our confined smectics, we consider the number density

$$\rho(r,z) = \frac{1}{NV_0}\sum_{k=1}^{N}\Theta\left(\frac{D}{10} - \sqrt{(z-z_k)^2 + (r-r_k)^2}\right) \qquad (13)$$

of the center positions of the rods, averaged over the azimuth, where r_k and z_k refer to the positions of the particles in

View Article Online
PCCP Paper

cylindrical coordinates. Here, the Heaviside step function is denoted by $\Theta(x)$ and V_0 is the intersection volume of the respective toroidal bin with the container. We further divide by the particle number N, such that $\rho(r, z)$ corresponds to the probability distribution for the position of a single particle. Additionally, we show the local orientational distribution function

$$g_2(r, z) = \langle P_2(\sin\theta_k)\rangle_{B2.5D(r,z)}, \quad (14)$$

of the rods at position (r, z), where $\sin\theta_k$ denotes the orientation of the k-th particle projected into the horizontal plane and $P_2(x)$ is the second Legendre polynomial. To obtain an appropriate resolution, we average within a spherical subsystem of radius $2.5D$.

Both quantities $\rho(r,z)$ and $g_2(r,z)$ are averaged over 15 simulations runs, with different randomized initial states. We show the resulting distribution functions in Fig. 5 for the same confinements of container height $h = 2.4L$ and diameter $2R = 8L$, presented in Section 3.1. For ease of observation, the plots are stretched in the vertical direction. We generally observe for both confinements that the density profiles distinctly show the layering structure of the fluid, reflected by the relatively localized lines close to the outside walls. This indicates, that the positions of the layers are strongly influenced by the planar surface anchoring on the outer walls. While these peaks are less pronounced further inside the cavity, the diagrams show clear indication of horizontal stacking from the bottom to the top of the confinement. We stress that the kind of layering visible in the density profiles happens on the scale of the particle diameter D and should not be confused with smectic layering along the direction of the rod axes of length $L + D$.

Along the vertical axis, the density profile for cylindrical confinement in Fig. 5A1 shows 11 layers of particles within a

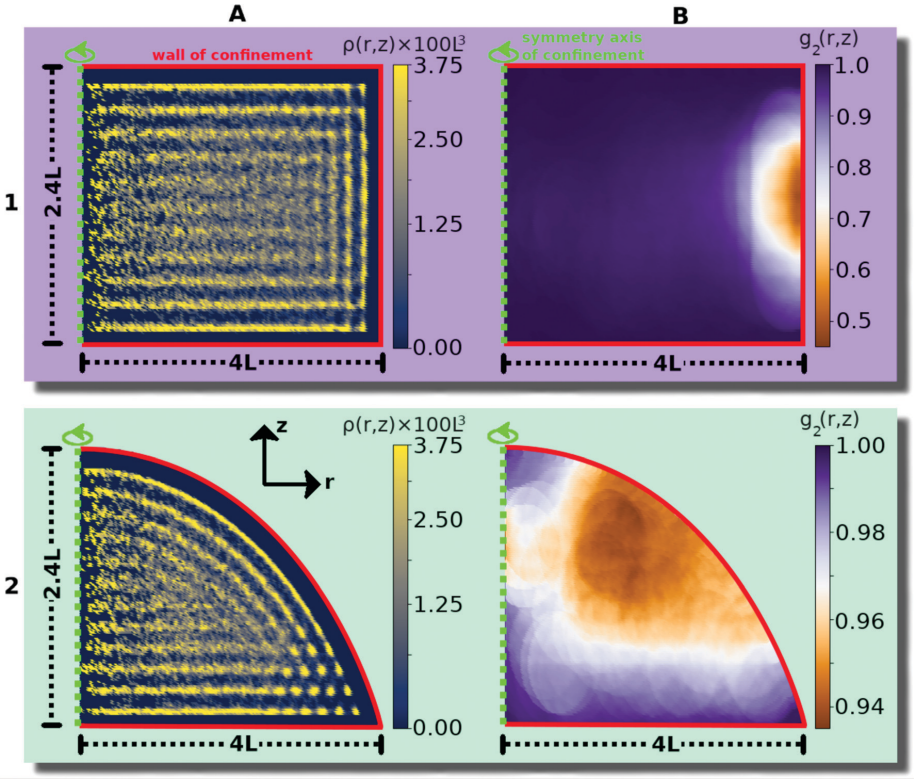

Fig. 5 Averaged structural properties of smectic liquid crystals confined in a cylinder (row 1) and spherical cap (row 2) of height $h = 2.4L$ and diameter $2R = 8L$. All diagrams are shown in cylindrical coordinates, averaged over the azimuth around the vertical center axis of the confinement (shown as a dashed green line). All diagrams are additionally averaged over 15 simulations. Column A: one-particle density $\rho(r, z)$ (defined by eqn (13)). These fields exemplify the layered fluid structure along a radial slice of the confinement, influenced by the planar surface anchoring of the confinement. To improve the contrast, we set the interval of the color bar to [0, 3.75], ensuring that the structures are clearly visible. All values above 3.75 are mapped to 3.75. Column B: correlation $g_2(r, z)$ (defined by eqn (14)) of the orientations at a certain position with the orientations projected into the horizontal plane. This function illustrates the deviation from the preferred horizontal orientation depending on the position within the confinement.

View Article Online
Paper PCCP

length interval of $2.4L = 12D$, indicating that their typical orientation is horizontal. This observation is reinforced in Fig. 5B1, showing that the orientations of the rods strongly correlate with the horizontal plane in almost the whole container. The depicted correlation function additionally indicates the presence of vertical rods close to the mantle of the cylinder, where $g_2(r, z)$ drops to $g_2 \approx 0.3$, consistent with the occasional appearance of vertical rods on the perimeter of the cylinder shown in the snapshot in Fig. 3A1. Accordingly, the density profile in Fig. 5A1 indicates a transition between vertical layers close to the mantle and horizontal layers in all other regions. In the corners, where the horizontal and vertical layers are compatible, we find fairly sharp isolated point-like peaks, exemplifying the high probability of a rod to sit aligned to both neighboring walls.

The density profile for the spherical-cap-shaped container in Fig. 5A2 indicates 12 stacked fluid layers in the middle of the confinement, indicating a stronger compression of the fluid than in the cylinder. Layers which are closer to the curved surface of the container are bent, while those closer to the bottom surface are horizontal. Again, we see localized peaks close to the corner, which are even more pronounced than in the cylindrical container due to the smaller opening angle. Here, the roughly 20 isolated peaks are arranged on an approximately hexagonal grid, representing the structure of rods sitting at an angle of $\pi/2$ to both walls, at approximately the same distances to the perimeter in all simulations. This clearly demonstrates the influence of the extreme confinement. Fig. 5B2 shows the orientational correlation of the rods g_2 with the bottom plane. It is visible that all rods are aligned fairly horizontally within the whole spherical cap (mind the different color scale compared to the cylindrical cavity). Only in the vicinity of the curved surface of the container, $g_2(r, z)$ is slightly reduced to values of $g_2 \approx 0.9$, indicating that the rods rotate slightly out of the horizontal plane when aligning with the curved wall.

To study the effect of confinement height h in more detail, we vary this geometrical parameter from $h = 0.3L$ to $h = 4.5L$ in steps of $0.3L$, performing in each case 15 simulations for each confining geometry. In Fig. 6, we show the resulting nematic order parameter $\mathcal{S}$ and the 3d tetratic order parameter $\mathcal{T}$ evaluated for the entire system as a function of h. For the spherical cap, both order parameters $\mathcal{S}$ and $\mathcal{T}$ globally remain at fairly constant values, irrespective of the confinement height h. In detail, the nematic order parameter settles at $\mathcal{S} \approx 0.5$, while the tetratic order parameter settles at $\mathcal{T} \approx 0.1$, only showing a slight downwards trend. In stark contrast, for cylindrical confinement the tetratic order parameter increases strongly with increasing h, while the nematic order parameter displays a nonmonotonic behavior.

Comparing the ordering behavior in the two types of cavities in more detail, we also observe in Fig. 6 that for the most shallow confinements with $h = 0.3L$ the two values of $\mathcal{T}$ are qualitatively similar, whereas $\mathcal{S}$ takes a slightly lower value in the cylinder than in the cap. For this small height of the cavities, there are practically no effects of the third dimension,

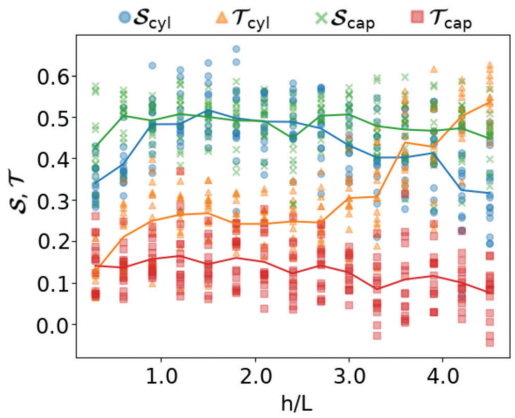

Fig. 6 Nematic order parameter $\mathcal{S}$ and tetratic order parameter $\mathcal{T}$ (see Section 2.2) for the smectic liquid crystals confined to 3d cavities in the shape of cylinders and spherical caps (see Fig. 1). Along the horizontal axis we show a range of confinements with different heights h in units of spherocylinder length L. The vertical axis represents different values of the order parameters evaluated for the entire system. For each confinement, we performed 15 simulations for each value of h. The height h is swept from $h = 0.3L$ up to $h = 4.5L$ in steps of $0.3L$. For each simulation run, we show two sets of data points, corresponding to the two order parameters $\mathcal{S}$ and $\mathcal{T}$. The curves show the order parameters averaged over the 15 simulation runs.

such that, like in a true 2d system, the aspect ratio $p = 5$ of the rods considered here is too small to result in a significant orientational order and much less a smectic bridge state. The fact that the global nematic ordering in the spherical cap is still higher than in the cylinder, relates to the decreased accessible radius of the effective circular confinement. Upon departing from this quasi-2d case by increasing h, the global order generally increases. For the cylinder, however, the nematic order parameter decreases again from $\mathcal{S} \approx 0.5$ to $\mathcal{S} \approx 0.3$, while $\mathcal{T}$ drastically increases from $\mathcal{T} \approx 0.1$ to $\mathcal{T} \approx 0.4$ as soon as $h > 1.5L$. This behavior, which is specific for the cylindrical geometry, can be explained by the fact that we observe a higher fraction of vertical rods on the mantle surface for taller confinements, reducing the global nematic order. In turn, this alignment even leads to an increase of the tetratic order, since the vertical rods are perfectly perpendicular to the central domain, such that the tetratic defects, which are exclusively formed by the horizontal rods, take a smaller percentage of the total system size. This kind of behavior is not observed for the spherical cap due to its curved boundary. For even larger cylinder heights h, the majority of rods aligns with the mantle surface such that the global nematic order increases again. This is studied in detail in Appendix B.

3.3 Topological charge

In Section 3.1, we discussed the detection of the topological defects with the help of the order parameters. As elaborated in Section 2.3, topological defects that span between system boundaries, such as those in Fig. 3 and 4, can be assigned a

topological charge defined *via* the net rotation of the director $\hat{\mathbf{n}}(\mathbf{r})$ along an encircling closed contour. More specifically, these contours can be defined within any cross section parallel to the bottom plane. Note that the sum of all topological charges, defined in this way, is a conserved quantity in 3d only under specific circumstances like in the smectic systems considered here, which can be understood as follows. Imagine, *e.g.*, that Fig. 2A1 and A2 represent cross sections of a 3d nematic system (rather than a purely 2d system). In this case, the $Q = +1/2$ defect from Fig. 2A1 can be transformed into the $Q = -1/2$ defect from Fig. 2A2 by flipping the orientations $\hat{\mathbf{u}}_k$ of all rods individually across the vertical picture axis. This transformation can be performed as a continuous mapping in 3d space, thereby obtaining a $Q = +1/2$ defect from a $Q = -1/2$ or *vice versa*. Additionally, this rotation can occur continuously along a disclination line, resulting in different values for topological charges, depending on the respective chosen cross section.[81] As a result, all possible structures can in principle be either homotopically equivalent to a charge-free structure with $Q = 0$ or to a defect structure with $Q = 1/2$.

In the previous Section 3.2, we elaborated that the confined smectic fluids in our simulations majorly consist of stacked quasi-2d layers. By showing that the 3d systems consist of a number of stacked quasi-2d layers, with no out-of-plane rotation, the defects do not undergo the transitions mentioned above. We thus argue that, in our simulations, the topological charge is equal for all horizontal cross sections, such that we can consistently define charges of any of the defects visible in Fig. 3. Additionally, we observe very similar structures on the top and bottom surface of the cylindrical systems and even on the curved surface of the spherical cap. This similarity of top and bottom structures is a further indication for a persisting structure through all horizontal slices. We can thus assume, to a good degree of approximation, that the director $\hat{\mathbf{n}}(\mathbf{r})$ does not rotate out of the 2d layers the 3d system consists of. This reduces the orientational configuration space from S^2/Z_2 to S^1/Z_2, implying that we can treat the topology in full analogy to the 2d case. In this way, by observing the bottom plane, we can infer that the total topological charge of the nematic grain boundary is equal to $Q = 1/2$ and matches the charge of the 2d counterpart. More specifically, the grain boundaries split into two pillars, *i.e.*, tetratic disclination lines, with $q = 1/4$ each, corresponding to $q = 1/4$ point charges in the cross-sections.

Less frequent exceptions to the ordering behavior described above for the considered confinements are given by the occasional alignment of the rods with the curved surface of the cap-shaped container as well as the small vertical clusters present at the mantle surface of the cylindrical container. The former case does not undergo a transition between $\pm 1/2$ charged cross sections, as no rods are present that are drastically rotated out of plane. This is supported by the fact that the flat projection of the structure on the curved surface still mirrors the structure of the bottom plane. For cylindrical cavities of comparable height, according to our observation, a director field $\hat{\mathbf{n}}(\mathbf{r})$ can most of the time be defined in a neighborhood around the defect, such that the vertical clusters do not influence the topological charges. This is in general no longer the case when the cylinder becomes sufficiently tall. As shown in Appendix B, for $h \gtrsim 5L$ full layers of vertical rods persist throughout several cross sections.

From mathematical topology it follows that for liquid crystals confined to 2d manifolds, the total topological charge in the director field has to match the Euler characteristic χ of the container.[91] The Euler characteristic χ is an algebraic invariant. Accordingly, results of previous work agree for nematic[59] as well as smectic liquid crystals[80] confined to simply-connected convex cavities and for smectics confined to 2d spherical surfaces embedded in 3d.[60] In this work, we have presented examples for 3d simply-connected convex confinements, where the sum of topological charges defined through integrating around a closed contour in a 2d cross section matches the Euler characteristic $\chi = 1$ of this cross section.

4 Conclusion

In this work, we provided an insight into the topology of defects in 3d smectic liquid crystals. In 3d smectic liquid crystals, orientational defects take the shape of extended planar grain boundaries, across which the local preferred direction jumps by an angle of $\pi/2$. Combining the established knowledge of classification of 3d nematic disclination lines with recent insights into the classification of grain boundaries as orientational defects in 2d smectic liquid crystals, we presented a formalism for the analysis of topological charge distribution. We exemplified this formalism on smectic structures in cylindrical and spherical cap containers, obtained using Monte-Carlo simulation.

In the 2d analysis one can utilize the coexistence of nematic and tetratic defects and, with the help of the tetratic order parameter, locate the points where the preferred direction rotates. Accordingly, we introduced a tetratic order parameter which can be readily applied to 3d systems. The 3d tetratic line defects were then analyzed along 2d cross sections.

In a 3d system, the sum of the winding numbers of all defects is not in general a conserved quantity since defects with different winding numbers can be transformed into each other. However, since the confined structures can be interpreted as stacked quasi-2d systems, topological charge behaves akin to electromagnetic charge and follows similar additive conservation laws. We thus found in the simulated systems that the total topological charge matches the Euler characteristic $\chi = 1$ of the containers and splits into two orientational defects, *i.e.*, two grain boundaries with topological charge $Q = 1/2$ each. Those can in turn be split into two tetratic disclination lines with charges $q = 1/4$. In general terms, we find it remarkable that the 2d topological charge, which does not have to be conserved for mathematical reasons in three dimensions, is conserved for physical reasons in the systems considered in this work.

To better understand the physical origin of the pronounced grain boundaries emerging in our confined system, let us recall that a key property of the (hard-core) colloidal system under

View Article Online
Paper PCCP

consideration is the rigidity of the smectic layers, such that the balance between intrinsic structure and external constraints mostly results in extended defects (grain boundaries) rather than elastic deformations. A similar observation has been made for a related 2d system using both microscopic density functional theory and colloidal experiments[79] and we expect that the same mechanism is at work in three dimensions. To get further insight, the confined systems considered in this work could therefore be investigated using density functionals for hard spherocylinders.[99,100] Alternatively, density functional theory also allows to determine elastic parameters of fluids of hard spherocylinders[101] which could then be used to fix the parameters in phenomenological elasticity theories[100,102,103] for the smectic phase.

Throughout this paper, we have in particular shed light on planar grain boundaries which split into two tetratic disclination lines. Our insight will thus be useful for the interpretation of future computational,[104,105] theoretical,[99–104,106] and experimental[79,98,107–109] research on confined smectic structures in three dimensions. To this end, our topological picture can be extended to study more complex geometries and topologies in 3d, *e.g.*, by observing $q = -1/4$ tetratic defects, which, in analogy to the 2d case, should emerge at junction points of defect networks in confinements that promote multiple domains[80] or close to concave regions of the system boundary.[79] Of interest may also be the investigation of the connection of orientational defects to positional defects, such as dislocations and focal conic domains. In nematic systems, it is widely accepted that the dynamical properties of a defect are influenced by the respective topological charge.[1,20,66–68,110] Therefore, understanding the role of smectic orientational defects, *i.e.*, grain boundaries analyzed as a connected pair of tetratic defects, in nonequilibrium is also of particular importance for understanding, *e.g.*, nucleation processes[111–114] and the dynamics[115] of smectics, as well as active liquid crystal systems,[18–21] which might also exhibit smectic order.

Conflicts of interest

There are no conflicts to declare.

Appendix A: tetratic order parameter in three dimensions

In this appendix, we provide an appropriate definition of the tetratic order parameter to characterize the topological fine structure in smectic systems of uniaxial rods.

1. Definition

In general, a system of N uniaxial particles can be microscopically described by a distribution function $f(\hat{\mathbf{u}})$ that reads

$$f(\hat{\mathbf{u}}) = \frac{1}{N}\sum_{k=1}^{N}\delta(\theta-\theta_k)\delta(\phi-\phi_k), \tag{A1}$$

where $\hat{\mathbf{u}} = (\sin\theta\cos\phi,\ \sin\theta\sin\phi,\ \cos\theta)^{\mathrm{T}}$ is the orientation vector. Such a function can be expanded as[116]

$$f(\hat{\mathbf{u}}) = \sum_{l=0}^{\infty}\sum_{i_1,\ldots,i_l=1}^{3} f^{(3\mathrm{d})}_{i_1\cdots i_l} u_{i_1}\cdots u_{i_l}, \tag{A2}$$

where u_i is the i-th element of the orientation vector and the expansion coefficients are given by[116]

$$f^{(3\mathrm{d})}_{i_1\cdots i_l} = \frac{2l+1}{4\pi}\int_{S^2}\mathrm{d}\Omega f(\hat{\mathbf{u}})\mathcal{P}^{(3\mathrm{d})}_{i_1\cdots i_l} \tag{A3}$$

with the tensor Legendre polynomials $\mathcal{P}^{(3\mathrm{d})}_{i_1\cdots i_l}$. An expansion of the form (A2) is also possible in a 2d system, in this case $\hat{\mathbf{u}}$ is a 2d vector depending on just one angle and the expression (A3) is slightly modified (see ref. 116). The second-order contribution $f^{(3\mathrm{d})}_{i_1\cdots i_2}$ is the nematic tensor. (In the main text (eqn (5)), we have, as is common, defined it with a different normalization that corresponds to multiplying the one resulting from eqn (A3) by $4\pi/5$.) An interesting mathematical property of the Cartesian expansion (A2) is that it is orderwise equivalent to the spherical multipole expansion

$$f(\theta,\phi) = \sum_{l=0}^{\infty}\sum_{m=-l}^{l} f_{lm}Y_{lm}(\theta,\phi) \tag{A4}$$

with the spherical harmonics Y_{lm} and the expansion coefficients

$$f_{lm} = \int_{S^2}\mathrm{d}\Omega f(\theta,\phi)\,Y^*_{lm}(\theta,\phi), \tag{A5}$$

where * denotes a complex conjugation.[116,117]

We are now looking for an order parameter that identifies configurations as ordered if the rods are either parallel or orthogonal to each other. In the 2d case, this can be simply done by superimposing tetratic order,[80] *i.e.*, fourfold rotational symmetry. Mathematically, this corresponds to measuring defects not in the nematic order-parameter field, corresponding to the second-order term in the 2d version of eqn (A2), but in the fourth-order contribution. This suggests that the desired order parameter can be constructed from the fourth-order term ($l = 4$) in eqn (A2) also in the 3d case. Since the Cartesian order parameter at fourth order has 81 components of which, due to symmetry and tracelessness, only 9 are independent, it is more convenient to work with the expansion coefficients of the angular expansion (A4) instead.

From eqn (A1) and (A5) we would then get the order parameters

$$f_{4m} = \frac{1}{N}\sum_{k=1}^{N} Y^*_{4m}(\theta_k,\phi_k) \tag{A6}$$

of order $l = 4$. The values of these order parameters (A6) depend, however, on the choice of the coordinate system. We now make use of the fact that the quantity

$$I_l = \sum_{m=-l}^{l}|\langle Y_{lm}\rangle|^2 \tag{A7}$$

with the average $\langle Y_{lm}\rangle$ is an invariant of the spherical

harmonics[88] (*i.e.*, it takes the same value for all choices of the coordinate system). This fact has been exploited in the study of bonding in liquids[88,118,119] or orientational order in liquid crystals.[120] Consequently, we should consider I_4 instead of f_{4m}.

Finally, we also need to take into account that the order parameter constructed from the invariants I_l should (a) be normalized – this can simply be ensured by multiplying it by an appropriate prefactor – and (b) not distinguish between parallel and orthogonal rods. Unfortunately, the invariant I_4 gives a larger value for parallel than for orthogonal configurations. To correct for this, we exploit the fact that the invariant I_2 measures nematic order,[120,121] such that it is large for parallel configurations. Hence, our generalized order parameter should be proportional to $I_4 - \beta I_2$, where β is a suitable prefactor. We have found an appropriate choice to be $\beta = 3/4$. Thus, we arrive at the tetratic order parameter

$$\mathcal{T} = \frac{16\pi}{21N^2}\left|\sum_{m=-4}^{4}\left|\sum_{k=1}^{N} Y_{4m}(\theta_k,\phi_k)\right|^2 - \frac{3}{4}\sum_{m=-2}^{2}\left|\sum_{k=1}^{N} Y_{2m}(\theta_k,\phi_k)\right|^2\right| \tag{A8}$$

stated in eqn (8). The prefactor ensures a proper normalization. Moreover, we use absolute values to ensure that $\mathcal{T}$ is always positive. We have tested a range of possible configurations and found that $I_4 - \beta I_2 < 0$ is measured only for isotropic systems with $|I_4 - \beta I_2| \ll 1$ (probably due to numerical fluctuations). This is reinforced by the notion that I_2 measures nematic order and systems with high nematic order result in $\mathcal{T} \approx 1$.

5.2 Examples

To get an exemplary system that should be perfectly ordered by our definition, consider three orthogonal particles with orientations $(\theta_1, \phi_1) = (\pi/2, 0)$, $(\theta_2, \phi_2) = (\pi, 0)$ and $(\theta_3, \phi_3) = (\pi/2, \pi/2)$. We find

$$\mathcal{T} = \frac{16\pi}{21\cdot 3^2}\left|\sum_{m=-4}^{4}\left|Y_{4m}\left(\frac{\pi}{2},0\right) + Y_{4m}(\pi,0) + Y_{4m}\left(\frac{\pi}{2},\frac{\pi}{2}\right)\right|^2 - \frac{3}{4}\sum_{m=-2}^{2}\left|Y_{2m}\left(\frac{\pi}{2},0\right) + Y_{2m}(\pi,0) + Y_{2m}\left(\frac{\pi}{2},\frac{\pi}{2}\right)\right|^2\right| = 1, \tag{A9}$$

as required. Similarly, for three parallel particles with orientations $(\theta_1, \phi_1) = (\theta_2, \phi_2) = (\theta_3, \phi_3) = (\pi/2, 0)$, we get

$$\mathcal{T} = \frac{16\pi}{21\cdot 3^2}\left|\sum_{m=-4}^{4}\left|3Y_{4m}\left(\frac{\pi}{2},0\right)\right|^2 - \frac{3}{4}\sum_{m=-2}^{2}\left|3Y_{2m}\left(\frac{\pi}{2},0\right)\right|^2\right| = 1. \tag{A10}$$

Finally, we flip the orientation of one particle by π to show that this leaves the order parameter invariant, implying that it is apolar. We find

$$\mathcal{T} = \frac{16\pi}{21\cdot 3^2}\left|\sum_{m=-4}^{4}\left|2Y_{4m}\left(\frac{\pi}{2},0\right) + Y_{4m}\left(\frac{\pi}{2},\pi\right)\right|^2 - \frac{3}{4}\sum_{m=-2}^{2}\left|2Y_{2m}\left(\frac{\pi}{2},0\right) + Y_{2m}\left(\frac{\pi}{2},\pi\right)\right|^2\right| = 1, \tag{A11}$$

such that eqn (A8) constitutes a solid basis for exploring tetratic order phenomena in three dimensions.

Appendix B: taller cylinders

The height h of a spherical cap is limited by the full sphere with $h = 2R$, but the respective height of a cylindrical cavity can, in principle, be chosen arbitrarily large. While in the main text, we focus on heights of the cylinder which are also possible in the cap geometry, we discuss in this appendix the behavior of the same liquid crystal systems confined to taller cylinders up to a height $h = 15L$ (*i.e.*, up to $N \approx 1.1 \times 10^4$ particles). Our results are shown in Fig. 7.

The snapshot in Fig. 7A depicts a system in a cylinder of height $h = 14L$. It is clearly visible that, along the entire mantle surface, the rods are aligned with the main axis of the cylinder. The structure at both the top and bottom layer in the cylinder (visible in the upper and lower picture, respectively, shown from the same, azimuthal viewing angle) still resembles a bridge state, which for the shorter cylindrical cavities was found to persist throughout the whole system. However, the two bridging domains have a different in-plane orientation, indicating that the structures at the top and bottom are independent.

Fig. 7B shows the orientational distribution $g_2(r, z)$ (defined by eqn (14)) sampled as average over five simulation snapshots from systems with $h = 14L$. Here, the independence of the two horizontal layers of rods at the top and bottom of the cavity becomes apparent, since throughout the majority of the system the rods are vertical. More specifically, contrasting this observation to Fig. 5B1, we notice that here the signal indicating a vertical orientation percolates throughout several horizontal slices, while for shorter cylinders the signal indicating the horizontal orientation percolates from top to bottom. Taking a closer look at the distribution for the tall cylinder, we observe that the vertical regime is slightly perturbed by horizontal stripes in the field at a distance corresponding to the smectic layer spacing. These dips correspond to the occasional occurrence of horizontal rods between the layers,[122] as is also visible in the snapshot in Fig. 7A.

Fig. 7C shows the 3d tetratic order parameter $\mathcal{T}$ as well as the standard nematic order parameter $\mathcal{S}$ (see Section 2.2) for a range $h \in [0.3L, 15L]$ of cylinder heights as an extension of Fig. 6. As the behavior for extremely shallow cavities has been discussed in detail in Section 3.2, we focus here on larger values of h. It is clearly visible from Fig. 7C that $\mathcal{S}$ has a minimum at

View Article Online
Paper PCCP

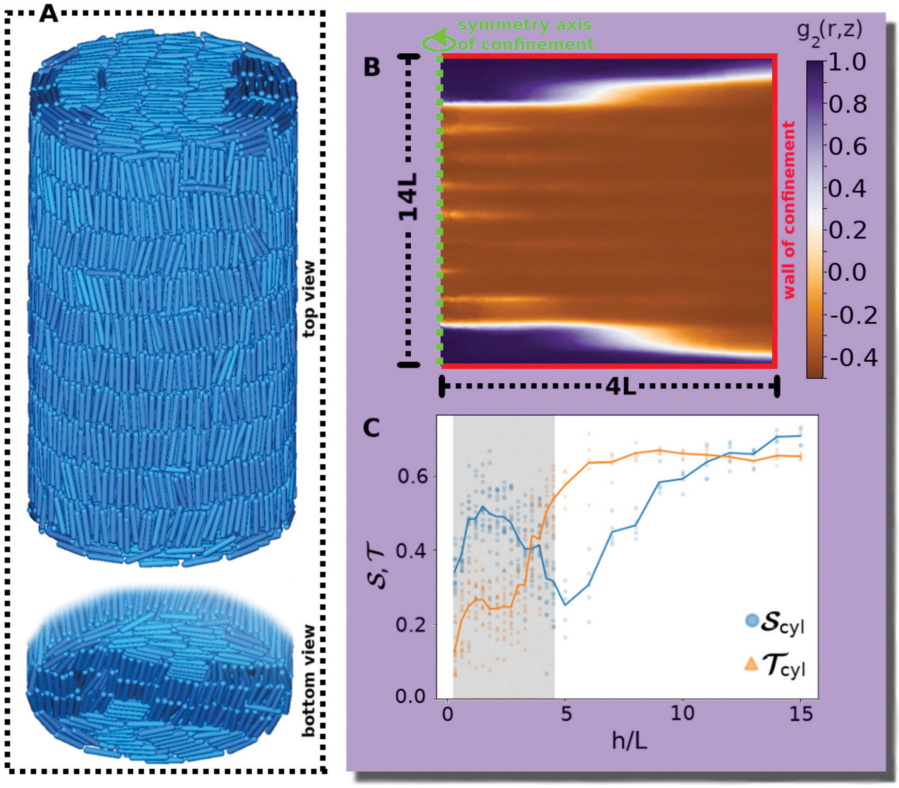

Fig. 7 Properties of smectic liquid crystals confined to cylinders of diameter $2R = 8L$ as shown in the main text but with taller heights h. (A) Representative snapshot for $h = 14L$ from a bird's eye view, as in Fig. 3A1. The picture below shows the bottom side of the same system, from the same azimuthal viewing angle. (B) Correlation function $g_2(r, z)$ (defined by eqn (14)) of the orientations at a certain position with the orientations projected into the horizontal plane for $h = 14L$, as in Fig. 5. Here, the field is generated as average over five simulation runs. (C) Nematic and tetratic order parameters $\mathcal{S}$ and $\mathcal{T}$ (see Section 2.2) with additional data for $h \in [5L, 15L]$, taken from five simulation runs. The gray background indicates the interval $h \in [0.3L, 4.5L]$ which includes the data from Fig. 6.

$h \approx 5L$, which reflects the transition from a structure with the majority of rods aligning horizontally along the top and bottom plates for short cylinders to a structure with the majority of rods aligning vertically along the cylinder mantle for tall cylinders. In the latter case, two additional grain boundaries between horizontal and vertical rods emerge close to the two ends of the cylinder, decreasing the global nematic order. When further increasing $h \gtrsim 5L$, the nematic order parameter $\mathcal{S}$ increases again until eventually reaching a plateau when the fraction of the horizontal rods and the corresponding defects become negligible. In stark contrast, the value of the tetratic order parameter $\mathcal{T}$ is not affected by the relative size of the interface between horizontal and vertical domains, such that there is no minimum around $h \approx 5L$. Instead, as soon as the vertical rods become relevant, $\mathcal{T}$ increases monotonously with increasing cylinder height h and plateaus already at $h \approx 6L$, since the tetratic defects (*cf.* Fig. 3C1) are only located in the horizontal layers.

Acknowledgements

We thank Arjun Yodh and Alice Rolf for helpful discussions. This work is funded by the Deutsche Forschungsgemeinschaft (DFG, German Research Foundation) – VO 899/19-2; WI 4170/3-1; LO 418/20-2. M. t. V. thanks the Studienstiftung des deutschen Volkes for financial support.

References

1 N. D. Mermin, *Rev. Mod. Phys.*, 1979, **51**, 591.
2 T. W.-B. Kibble, *J. Phys. A*, 1976, **9**, 1387.
3 T. Shinjo, T. Okuno, R. Hassdorf, K. Shigeto and T. Ono, *Science*, 2000, **289**, 930.
4 C. Phatak, A. K. Petford-Long and O. Heinonen, *Phys. Rev. Lett.*, 2012, **108**, 067205.
5 L. Lu, J. D. Joannopoulos and M. Soljačić, *Nat. Photonics*, 2014, **8**, 821.

6 A. Moor, A. F. Volkov and K. B. Efetov, *Phys. Rev. B*, 2014, **90**, 224512.
7 A. Tan, J. Li, A. Scholl, E. Arenholz, A. T. Young, Q. Li, C. Hwang and Z. Q. Qiu, *Phys. Rev. B*, 2016, **94**, 014433.
8 G. Yi and B. D. Youn, *Struct. Multidiscip. Optim.*, 2016, **54**, 1315.
9 A. O. Sorokin, *Phys. Rev. B*, 2017, **95**, 094408.
10 Y. Liu, Z. Wang, T. Sato, M. Hohenadler, C. Wang, W. Guo and F. F. Assaad, *Nat. Commun.*, 2019, **10**, 2658.
11 X. Lu, R. Fei, L. Zhu and L. Yang, *Nat. Commun.*, 2020, **11**, 4724.
12 C. Wang, C.-H. Chang, A. Herklotz, C. Chen, F. Ganss, U. Kentsch, D. Chen, X. Gao, Y.-J. Zeng and O. Hellwig, *et al.*, *Adv. Electron. Mater.*, 2020, **6**, 2000184.
13 P.-G. De Gennes and J. Prost, *The physics of liquid crystals*, Oxford University Press, Oxford, UK, 1993.
14 M. C. Marchetti, J.-F. Joanny, S. Ramaswamy, T. B. Liverpool, J. Prost, M. Rao and R. A. Simha, *Rev. Mod. Phys.*, 2013, **85**, 1143.
15 C. E. Fowler, W. Shenton, G. Stubbs and S. Mann, *Adv. Mater.*, 2001, **13**, 1266.
16 Z. Reich, E. J. Wachtel and A. Minsky, *Science*, 1994, **264**, 1460.
17 I. W. Hamley, *Soft Matter*, 2010, **6**, 1863.
18 L. Giomi, *Phys. Rev. X*, 2015, **5**, 031003.
19 S. J. DeCamp, G. S. Redner, A. Baskaran, M. F. Hagan and Z. Dogic, *Nat. Mater.*, 2015, **14**, 1110.
20 A. J. Tan, E. Roberts, S. A. Smith, U. A. Olvera, J. Arteaga, S. Fortini, K. A. Mitchell and L. S. Hirst, *Nat. Phys.*, 2019, **15**, 1033.
21 S. Shankar, A. Souslov, M. J. Bowick, M. C. Marchetti and V. Vitelli, 2020, arXiv:2010.00364.
22 K. Beppu, Z. Izri, J. Gohya, K. Eto, M. Ichikawa and Y. T. Maeda, *Soft Matter*, 2017, **13**, 5038.
23 A. Sokolov, I. S. Aranson, J. O. Kessler and R. E. Goldstein, *Phys. Rev. Lett.*, 2007, **98**, 158102.
24 H. H. Wensink, J. Dunkel, S. Heidenreich, K. Drescher, R. E. Goldstein, H. Löwen and J. M. Yeomans, *Proc. Natl. Acad. Sci. U. S. A.*, 2012, **109**, 14308.
25 J. Dunkel, S. Heidenreich, K. Drescher, H. H. Wensink, M. Bär and R. E. Goldstein, *Phys. Rev. Lett.*, 2013, **110**, 228102.
26 F. J. Ndlec, T. Surrey, A. C. Maggs and S. Leibler, *Nature*, 1997, **389**, 305.
27 V. Schaller, C. Weber, C. Semmrich, E. Frey and A. R. Bausch, *Nature*, 2010, **467**, 73.
28 S. J. Hall, C. S. Wardle and D. N. MacLennan, *Mar. Biol.*, 1986, **91**, 143.
29 N. Abaid and M. Porfiri, *J. R. Soc., Interface*, 2010, **7**, 1441.
30 M. Dijkstra, R. van Roij and R. Evans, *Phys. Rev. E*, 2001, **63**, 051703.
31 P. E. Brumby, H. H. Wensink, A. J. Haslam and G. Jackson, *Langmuir*, 2017, **33**, 11754.
32 E. Basurto, P. Gurin, S. Varga and G. Odriozola, *Phys. Rev. Res.*, 2020, **2**, 013356.
33 C. Chiccoli, P. Pasini, F. Semeria and C. Zannoni, *Mol. Cryst. Liq. Cryst.*, 1992, **221**, 19.
34 O. D. Lavrentovich, *Liq. Cryst.*, 1998, **24**, 117.
35 Y.-K. Kim, S. V. Shiyanovskii and O. D. Lavrentovich, *J. Condens. Matter Phys.*, 2013, **25**, 404202.
36 P. Prinsen and P. van der Schoot, *Phys. Rev. E*, 2003, **68**, 021701.
37 Y. Trukhina, S. Jungblut, P. van der Schoot and T. Schilling, *J. Chem. Phys.*, 2009, **130**, 164513.
38 Y. Trukhina and T. Schilling, *Phys. Rev. E*, 2008, **77**, 011701.
39 D. de las Heras, E. Velasco and L. Mederos, *Phys. Rev. E*, 2009, **79**, 061703.
40 O. J. Dammone, I. Zacharoudiou, R. P.-A. Dullens, J. M. Yeomans, M. P. Lettinga and D. G.-A. L. Aarts, *Phys. Rev. Lett.*, 2012, **109**, 108303.
41 O. V. Manyuhina, K. B. Lawlor, M. C. Marchetti and M. J. Bowick, *Soft Matter*, 2015, **11**, 6099.
42 A. Majumdar and A. Lewis, *Liq. Cryst.*, 2016, **43**, 2332.
43 A. H. Lewis, I. Garlea, J. Alvarado, O. J. Dammone, P. D. Howell, A. Majumdar, B. M. Mulder, M. Lettinga, G. H. Koenderink and D. G.-A. L. Aarts, *Soft Matter*, 2014, **10**, 7865.
44 I. C. Gârlea, P. Mulder, J. Alvarado, O. J. Dammone, D. G.-A. L. Aarts, M. P. Lettinga, G. H. Koenderink and B. M. Mulder, *Nat. Commun.*, 2016, **7**, 12112.
45 A. Daz-De Armas, M. Maza-Cuello, Y. Martnez-Ratón and E. Velasco, *Phys. Rev. Res.*, 2020, **2**, 033436.
46 X. Yao and J. Z.-Y. Chen, *Phys. Rev. E*, 2020, **101**, 062706.
47 X. Yao, H. Zhang and J. Z.-Y. Chen, *Phys. Rev. E*, 2018, **97**, 052707.
48 X. Yao, L. Zhang and J. Z.-Y. Chen, *Phys. Rev. E*, 2022, **105**, 044704.
49 P. Poulin, V. Cabuil and D. A. Weitz, *Phys. Rev. Lett.*, 1997, **79**, 4862.
50 R. W. Ruhwandl and E. M. Terentjev, *Phys. Rev. E*, 1997, **56**, 5561.
51 D. Andrienko, G. Germano and M. P. Allen, *Phys. Rev. E*, 2001, **63**, 041701.
52 H. Stark, *Phys. Rep.*, 2001, **351**, 387.
53 S. Čopar, T. Porenta, V. S.-R. Jampani, I. Muševič and S. Žumer, *Soft Matter*, 2012, **8**, 8595.
54 J. M. Ilnytskyi, A. Trokhymchuk and M. Schoen, *J. Chem. Phys.*, 2014, **141**, 114903.
55 S. Püschel-Schlotthauer, V. Meiwes Turrión, C. K. Hall, M. G. Mazza and M. Schoen, *Langmuir*, 2017, **33**, 2222.
56 K. Chen, O. J. Gebhardt, R. Devendra, G. Drazer, R. D. Kamien, D. H. Reich and R. L. Leheny, *Soft Matter*, 2018, **14**, 83.
57 K. H. Kil, A. Yethiraj and J. S. Kim, *Phys. Rev. E*, 2020, **101**, 032705.
58 B. Loewe and T. N. Shendruk, *New J. Phys.*, 2022, **24**, 012001.
59 J. Dzubiella, M. Schmidt and H. Löwen, *Phys. Rev. E*, 2000, **62**, 5081.
60 E. Allahyarov, A. Voigt and H. Löwen, *Soft Matter*, 2017, **13**, 8120.
61 F. C. Keber, E. Loiseau, T. Sanchez, S. J. DeCamp, L. Giomi, M. J. Bowick, M. C. Marchetti, Z. Dogic and A. R. Bausch, *Science*, 2014, **345**, 1135.

62 S. Kralj, R. Rosso and E. G. Virga, *Soft Matter*, 2011, **7**, 670.
63 I. Nitschke, M. Nestler, S. Praetorius, H. Löwen and A. Voigt, *Proc. R. Soc. A*, 2018, **474**, 20170686.
64 M. Nestler, I. Nitschke, H. Löwen and A. Voigt, *Soft Matter*, 2020, **16**, 4032.
65 I. Nitschke, S. Reuther and A. Voigt, *Proc. R. Soc. A*, 2020, **476**, 20200313.
66 A. J. Vromans and L. Giomi, *Soft Matter*, 2016, **12**, 6490.
67 K. Harth and R. Stannarius, *Front. Phys.*, 2020, **8**, 112.
68 G. Tóth, C. Denniston and J. M. Yeomans, *Phys. Rev. Lett.*, 2002, **88**, 105504.
69 G. P. Alexander, B. G.-g Chen, E. A. Matsumoto and R. D. Kamien, *Rev. Mod. Phys.*, 2012, **84**, 497.
70 M. Kléman, *Rep. Prog. Phys.*, 1989, **52**, 555.
71 R. B. Meyer, B. Stebler and S. T. Lagerwall, *Phys. Rev. Lett.*, 1978, **41**, 1393.
72 P. Chen and C.-Y. D. Lu, *J. Phys. Soc. Jpn.*, 2011, **80**, 094802.
73 C. Zhang, A. M. Grubb, A. J. Seed, P. Sampson, A. Jákli and O. D. Lavrentovich, *Phys. Rev. Lett.*, 2015, **115**, 087801.
74 R. D. Kamien and R. A. Mosna, *New J. Phys.*, 2016, **18**, 053012.
75 J. P. Bramble, S. D. Evans, J. R. Henderson, T. J. Atherton and N. J. Smith, *Liq. Cryst.*, 2007, **34**, 1137.
76 Y. H. Kim, D. K. Yoon, M.-C. Choi, H. S. Jeong, M. W. Kim, O. D. Lavrentovich and H.-T. Jung, *Langmuir*, 2009, **25**, 1685.
77 D. B. Liarte, M. Bierbaum, R. A. Mosna, R. D. Kamien and J. P. Sethna, *Phys. Rev. Lett.*, 2016, **116**, 147802.
78 M. Kléman and O. D. Lavrentovich, *Eur. Phys. J. E*, 2000, **2**, 47.
79 R. Wittmann, L. B.-G. Cortes, H. Löwen and D. G.-A. L. Aarts, *Nat. Commun.*, 2021, **12**, 623.
80 P. A. Monderkamp, R. Wittmann, L. B.-G. Cortes, D. G.-A. L. Aarts, F. Smallenburg and H. Löwen, *Phys. Rev. Lett.*, 2021, **127**, 198001.
81 S. Afghah, R. L.-B. Selinger and J. V. Selinger, *Liq. Cryst.*, 2018, **45**, 2022.
82 C. Vega and S. Lago, *Comput. Chem.*, 1994, **18**, 55.
83 H. C. Andersen, D. Chandler and J. D. Weeks, *J. Chem. Phys.*, 1972, **56**, 3812.
84 N. Metropolis, A. W. Rosenbluth, M. N. Rosenbluth, A. H. Teller and E. Teller, *J. Chem. Phys.*, 1953, **21**, 1087.
85 M. Kleman and O. D. Lavrentovich, *Soft Matter Physics – An Introduction*, Springer, New York, NY, 2003.
86 M. A. Bates and D. Frenkel, *J. Chem. Phys.*, 2000, **112**, 10034.
87 K. Zhao, C. Harrison, D. Huse, W. B. Russel and P. M. Chaikin, *Phys. Rev. E*, 2007, **76**, 040401.
88 P. J. Steinhardt, D. R. Nelson and M. Ronchetti, *Phys. Rev. B*, 1983, **28**, 784.
89 J. A.-C. Veerman and D. Frenkel, *Phys. Rev. A*, 1992, **45**, 5632.
90 P. D. Duncan, M. Dennison, A. J. Masters and M. R. Wilson, *Phys. Rev. E*, 2009, **79**, 031702.
91 M. J. Bowick and L. Giomi, *Adv. Phys.*, 2009, **58**, 449.
92 F. C. Frank, *Discuss. Faraday Soc.*, 1958, **25**, 19.
93 B. G.-g Chen, G. P. Alexander and R. D. Kamien, *Proc. Natl. Acad. Sci. U. S. A.*, 2009, **106**, 15577.
94 T. Machon, H. Aharoni, Y. Hu and R. D. Kamien, *Commun. Math. Phys.*, 2019, **372**, 525.
95 R. Pindak, C. Y. Young, R. B. Meyer and N. A. Clark, *Phys. Rev. Lett.*, 1980, **45**, 1193.
96 H.-R. Trebin, *Adv. Phys.*, 1982, **31**, 195.
97 T. Geigenfeind, S. Rosenzweig, M. Schmidt and D. de las Heras, *J. Chem. Phys.*, 2015, **142**, 174701.
98 L. B.-G. Cortes, Y. Gao, R. P.-A. Dullens and D. G.-A. L. Aarts, *J. Phys.: Condens. Matter*, 2017, **29**, 064003.
99 R. Wittmann, M. Marechal and K. Mecke, *J. Chem. Phys.*, 2014, **141**, 064103.
100 R. Wittmann, M. Marechal and K. Mecke, *J. Phys.: Condens. Matter*, 2016, **28**, 244003.
101 R. Wittmann, M. Marechal and K. Mecke, *Phys. Rev. E*, 2015, **91**, 052501.
102 J. Xia, S. MacLachlan, T. J. Atherton and P. E. Farrell, *Phys. Rev. Lett.*, 2021, **126**, 177801.
103 J. Paget, M. G. Mazza, A. J. Archer and T. N. Shendruk, 2022, arXiv:2201.09019.
104 M. Marechal, S. Dussi and M. Dijkstra, *J. Chem. Phys.*, 2017, **146**, 124905.
105 M. Chiappini, E. Grelet and M. Dijkstra, *Phys. Rev. Lett.*, 2020, **124**, 087801.
106 D. de las Heras, E. Velasco and L. Mederos, *Phys. Rev. E*, 2006, **74**, 011709.
107 W. Wang, G. Lieser and G. Wegner, *Liq. Cryst.*, 1993, **15**, 1.
108 T. Lopez-Leon, A. Fernandez-Nieves, M. Nobili and C. Blanc, *J. Phys.: Condens. Matter*, 2012, **24**, 284122.
109 A. Repula and E. Grelet, *Phys. Rev. Lett.*, 2018, **121**, 097801.
110 G. P. Crawford and S. Zumer, *Liquid crystals in complex geometries: formed by polymer and porous networks*, CRC Press, Boca Raton, Florida, USA, 1996.
111 H. Maeda and Y. Maeda, *Phys. Rev. Lett.*, 2003, **90**, 018303.
112 T. Schilling and D. Frenkel, *Phys. Rev. Lett.*, 2004, **92**, 085505.
113 R. Ni, S. Belli, R. van Roij and M. Dijkstra, *Phys. Rev. Lett.*, 2010, **105**, 088302.
114 A. Cuetos, E. Sanz and M. Dijkstra, *Faraday Discuss.*, 2010, **144**, 253.
115 E. Grelet, M. P. Lettinga, M. Bier, R. van Roij and P. van der Schoot, *J. Phys.: Condens. Matter*, 2008, **20**, 494213.
116 M. te Vrugt and R. Wittkowski, *AIP Adv.*, 2020, **10**, 035106.
117 M. te Vrugt and R. Wittkowski, *Ann. Phys.*, 2020, **532**, 2000266.
118 W. Lechner and C. Dellago, *J. Chem. Phys.*, 2008, **129**, 114707.
119 H. Tanaka, *Eur. Phys. J. E*, 2012, **35**, 113.
120 B. S. John, C. Juhlin and F. A. Escobedo, *J. Chem. Phys.*, 2008, **128**, 044909.
121 R. Blaak, D. Frenkel and B. M. Mulder, *J. Chem. Phys.*, 1999, **110**, 11652.
122 R. van Roij, P. Bolhuis, B. Mulder and D. Frenkel, *Phys. Rev. E*, 1995, **52**, R1277.

P3 Smectic structures in button-like confinements: experiment and theory

Published as ArXiv-preprint and reproduced from

R. Wittmann, P. A. Monderkamp, J. Xia, L. B. G. Cortes, I. Grobas, P. E. Farrell, D. G. A. L. Aarts and H. Löwen
Smectic structures in button-like confinements: experiment and theory,
arXiv:2303.01425 (2023),

Digital Object Identifier (DOI): `https://doi.org/10.48550/arXiv.2303.01425`

Statement of contribution

All authors contributed equally to the conceptualisation of the project.
L. B. G. Cortes and I. Grobas performed the experiments. J. Xia and P. E. Farrell performed the Q-tensor theory and designed Fig. 5.
R. Wittmann performed the DFT and provided the first complete draft of the main text.
I performed the simulations, designed the figures and performed the visualisation of the experimental and simulation data (with the exception of Fig. 5).
Funding and overseeing was provided by D. G. A. L. Aarts, P. E. Farrell and H. Löwen.
Specific funding information regarding individual authors, e.g., funding for oneselve, is stated in the end of the main manuscript.
All authors contributed text associated with their respective expertise in paper and appendix and contributed to the finalisation of the manuscript.

P3.1 Paper and appendix: Smectic structures in button-like confinements: experiment and theory

Smectic structures in button-like confinements: experiment and theory

René Wittmann,[1,*] Paul A. Monderkamp,[1] Jingmin Xia,[2,†] Louis B. G. Cortes,[3,4] Iago Grobas,[4] Patrick E. Farrell,[5] Dirk G. A. L. Aarts,[4,‡] and Hartmut Löwen[1,§]

[1] *Institut für Theoretische Physik II: Weiche Materie, Heinrich-Heine-Universität Düsseldorf, Germany*
[2] *College of Meteorology and Oceanography, National University of Defense Technology, China*
[3] *School of Applied and Engineering Physics, Cornell University, Ithaca, NY, USA*
[4] *Physical and Theoretical Chemistry Laboratory, University of Oxford, United Kingdom*
[5] *Mathematical Institute, University of Oxford, United Kingdom*

(Dated: March 3, 2023)

Liquid crystals can self-organize into a layered smectic phase. While in bulk the smectic layers are typically straight forming a lamellar pattern, external confinement may drastically distort the layers due to the boundary conditions imposed on the orientational director field. Resolving this distortion leads to complex structures with topological defects. Here, we explore the configurations adopted by two-dimensional smectic liquid crystals of rod-like particles in complex confinements characterized by a button-like structure with two internal boundaries (inclusions): a two-holed disk and a double annulus. The topology of the confinement generates new structures which we classify as generalized laminar and generalized Shubnikov states. To explore these configurations, we combine particle-resolved experiments on colloidal rods with three complementary theoretical approaches: Monte-Carlo simulation, first-principles density functional theory and phenomenological **Q**-tensor modeling. This yields a consistent and comprehensive description of the structural details. In particular, we characterize a nontrivial tilt angle between the direction of the layers and symmetry axes of the confinement.

I. INTRODUCTION

Liquid crystals [1, 2] have proven to be an important tool in the investigation of various topological phenomena. In nematic liquid crystals, topological defects reflect the frustrated orientational order due to, e.g., confining geometries [3–11], active dynamics [12–16] or a combination of both [17–19]. This diversity of defects and formation pathways has led to extensive research attention devoted to understanding and accurately modeling the emerging topological defect structures [20–26].

In recent years, there has been an increasing interest in layered liquid crystals [27] and, in particular, smectic phases [28–32], which possess both orientational order and a periodic modulation of the center-of-mass density in the form of layers. This development owes to progress in (i) advances in experiments [33–46], (ii) continuum modeling [47–50] and (iii) first-principles theory [51–53], complemented by (iv) topological insight [54–57] reinforced by (v) simulating particle-resolved defect structures [58–61]. Despite these advances, there remains a gap between theoretical approaches (of all kinds) and experiments for smectic liquid crystals.

In this paper, we bring four complementary approaches together to understand the structure of colloidal smectics, confined to two-dimensional domains with a complex topology involving two holes. We use particle-resolved colloidal experiments on silica rods [44], Monte-Carlo simulations of a hard-rod model [59], microscopic density functional theory (DFT) for hard rods [53] and a recent continuum **Q**-tensor model extending the Landau–de Gennes theory for nematics [49]. These methods not only yield consistent predictions but also allow us to tackle the problems from different viewpoints.

In particular, we investigate responses of the system to both changes of the confining geometry and variation of interaction parameters. This allows us to systematically explore the ranges of stability of different topological states as well as different alignment phenomena and structures in the absence of a continuous rotational symmetry. To this end, we provide details on the confining geometries, methods and topological classification scheme in Sec. II, before discussing our results in Sec. III. After summarizing our observations, we conclude in Sec. IV.

II. CONFINED SMECTIC STATES

Our goal is to identify the structure and topology of the smectic states emerging in various two-dimensional confinements. The complexity of a confining domain can be both of explicit geometrical origin, related to the curvature of the walls, or of topological origin. The latter can be quantified by the Euler characteristic χ, which in two dimensions counts the number of connected components minus the number of holes, irrespective of the particular geometric shape of the domain. In the following, we elaborate on the relevant geometrical parameters (Sec. II A), describe how we resolve smectic structures in experiments and three theoretical approaches (Sec. II B) and provide details on the topological analysis (Sec. II C).

* rene.wittmann@hhu.de
† jingmin.xia@nudt.edu.cn
‡ dirk.aarts@chem.ox.ac.uk
§ Hartmut.Loewen@uni-duesseldorf.de

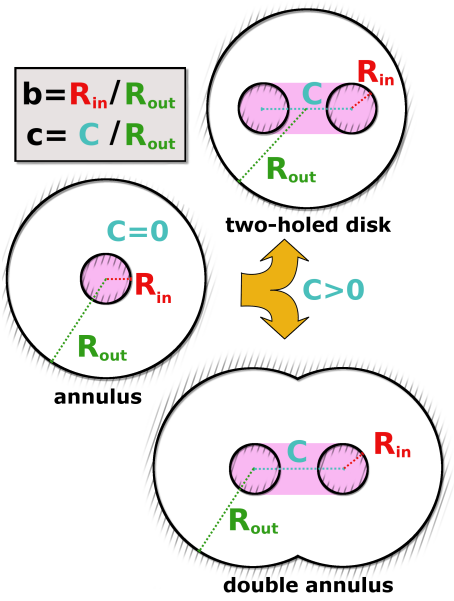

FIG. 1. Schematic depiction of the button-like confining geometries investigated in this work generalizing an annulus (middle) with inclusion size ratio $b = R_{\text{in}}/R_{\text{out}}$, where R_{out} is the radius of the outer confining wall and R_{in} is the radius of the circular wall in the interior, called inclusion [62]. Here, we consider two inclusions at distance C, introducing the inclusion distance ratio $c = C/R_{\text{out}}$. In detail, we define the two-holed-disk geometry (top), where the outer wall is always circular, and the double-annulus geometry (bottom), where the outer wall is defined via two intersecting circles at the same distance C. The outer radius R_{out} is kept at a fixed value throughout the manuscript, which corresponds to about five smectic layers. Further details are provided in Sec. II A.

A. Button-like confinements

As confining domains, we consider two generalizations of an annular geometry (central drawing in Fig. 1). This allows us to compare against solutions characterized for an annulus in previous work [62]. An annulus is composed of a large circle of radius $R_{\text{out}} > 0$ with a single circular hole (inclusion) of radius $R_{\text{in}} < R_{\text{out}}$ in the center. This topology has an Euler characteristic $\chi = 0$, which allows for a structure free of orientational topological defects (Shubnikov state). Depending on the particular geometry, this structure competes, among others, with an undeformed structure (laminar state), which comes at the cost of the formation of grain boundaries, i.e., defects in both orientational and positional order [62].

The central geometrical parameter which determines the stability of a structure emerging in annular geometry is the inclusion size ratio $b = R_{\text{in}}/R_{\text{out}}$. For each of our two related geometries, further specified below, we add a second inclusion of the same inclusion size ratio b and introduce the geometrical parameter $C = cR_{\text{out}}$, which denotes the distance between the centers of the two inclusions. In general, for small enough relative distance $c \leq 2b$ the inclusions intersect, resulting in a distorted annulus with an effectively stretched inclusion ($\chi = 0$), while for larger distances c, there are two separated holes such that the Euler characteristic equals $\chi = -1$.

First, we consider the two-holed-disk geometry (top drawing in Fig. 1), made of a single outer circle of radius R_{out}, and two inclusions whose centers are shifted away from each other in opposite directions with the mutual distance C, such that the distance to the center of the outer disk is $C/2$ in each case. Regarding the region accessible to the particles, the shortest distance between outer and inner walls varies upon circling along the outer wall. Note that, for extreme distances $c \geq 2 - 2b$, the inclusions are in contact with the outer wall, such that the geometry becomes simply connected again ($\chi = 1$).

Second, we consider the double-annulus geometry (bottom drawing in Fig. 1), composed of two outer circles, which are shifted alongside the two inner circles, such that each pair of inner and outer circles has the same center with a mutual distance of C. Each point of the outer confining wall thus has the same shortest distance $(1 - b)R_{\text{out}}$ to one of the inclusions.

To summarize, each geometry in Fig. 1 is fully determined by three parameters: the inclusion size ratio b, the inclusion distance ratio c and the total size of the confining domain specified by the radius R_{out} of the outer wall. Throughout the manuscript, we keep $R_{\text{out}} \approx 5\lambda$ fixed, where λ is the layer spacing of the smectic.

B. Complementary methods

Next we briefly introduce our methods to generate two-dimensional smectic states in extreme confinement and describe how to interpret the final smectic structures depicted in Fig. 2. In general, smectic order is characterized by positional order of the particle centers in equidistant layers and orientational order along a director at a constant angle to these layers. Confinement induces frustration of this preferred alignment in the form of deformations or discontinuities of the layers and/or the director field. The complementary use of our different approaches, allows us to optimally exploit their advantages when it comes to understanding the driving forces behind the formation, the stability range and the topology of the emerging structures. Further details on each method are provided in Appendix A.

Our experiments exploit the sedimentation equilibrium of silica rods in an aqueous solution, as described in Appendix A 1. The particle-resolved optical micrographs, displayed in the first row of Fig. 2, are then taken from the bottom, where the rods settle within tailor-made

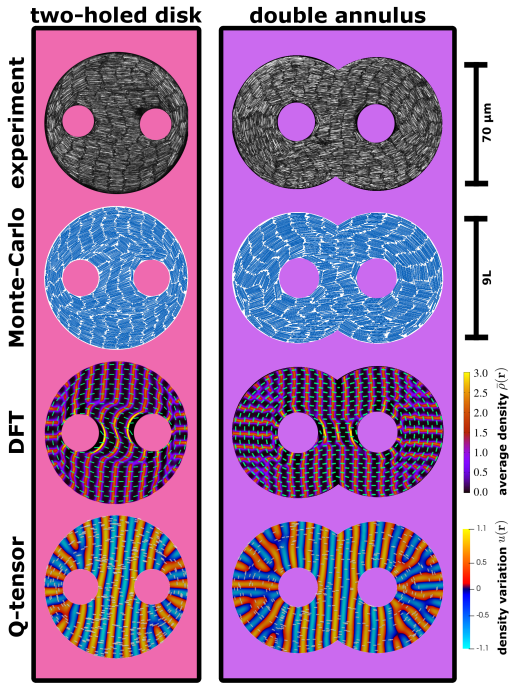

FIG. 2. Example structures in the two confining geometries shown in Fig. 1 with two inclusions. The left and right columns depict the two-holed-disk geometry for $b \approx 0.25$ and $c \approx 1.0$ and the double-annulus geometry for $b \approx 0.3$ and $c \approx 1.2$, respectively. In both geometries we show (from top to bottom) typical particle configurations in colloidal experiments, Monte-Carlo simulations of rod-like particles, density profiles and director fields from hard-rod density functional theory (DFT) and **Q**-tensor theory with suitably adapted parameters (see text).

cavities. These quasi-two-dimensional smectic structures can then be analyzed by direct optical inspection or reading out individual particle coordinates and orientations from processed images.

We also perform Monte-Carlo simulations on confined systems of rods modeled as hard discorectangles in the canonical ensemble, as described in Appendix A 2. The simulation snapshots, as displayed in the second row of Fig. 2, can be analyzed in the same manner as those from the experiments, while this particle-resolved numerical method leaves us in full control of the particle shape, number density and geometrical parameters. This allows us to gather a large amount of statistics for any prescribed geometry. From that we can further locate the grain boundaries by sampling a local version (cf. Fig. 9) of the two-dimensional orientational order parameter $S(\mathbf{r}) = |\langle \exp(i2\phi(\mathbf{r})) \rangle|$, where ϕ denotes the orientation angle of the individual rods within a local environment around the position $\mathbf{r}$.

On the theory side, we employ classical density functional theory (DFT) [63] for hard discorectangles, as described in Appendix A 3. In DFT, all structural information is comprised within the number density $\rho(\mathbf{r}, \phi)$ found by minimizing an appropriate functional $\Omega[\rho]$. This central quantity reflects the probability of finding a particle with the center-of-mass position $\mathbf{r}$ and its long axis oriented in a direction given by the angle ϕ. The typical density profiles, as displayed in the third row of Fig. 2, indicate both the smectic layers by a color plot of the local density (averaged over all orientations) and the director by green bars. In the employed version of DFT [53, 62] based on fundamental measure theory [64, 65] the interactions are treated on a microscopic level through the geometry of individual particles, such that the density profiles reflect the particle dimensions. As DFT is founded in statistical mechanics, no additional averaging is required and the most stable state can be identified among multiple solutions from the minimal value of the corresponding free energy.

Furthermore, we study a recent phenomenonlogical model for smectic layering, based on an extension of Landau–de Gennes theory to smectics, as described in Appendix A 4. It minimizes a total free energy $\mathcal{J}(u, \mathbf{Q})$ of the local density perturbation $u(\mathbf{r})$ for smectic phases and a tensorial order parameter $\mathbf{Q}(\mathbf{r})$ encoding the orientational order. As displayed in the fourth row of Fig. 2, typical profiles of the smectic density variation u exhibit maxima (light yellow) and minima (light blue) which both can be interpreted as the smectic layers, while the orientational director field (gray rods) corresponds to the eigenvector of tensor $\mathbf{Q}$ with the largest eigenvalue. In this smectic **Q**-tensor theory, the interactions are implicitly described through a range of phenomenological parameters. To connect to our other approaches, we consider two of these parameters as free variables: the elasticity parameter K of the director field and the anchoring parameter w, which indicates the strength of tangential alignment of directors at the outer wall. As the latter depends on curvature, the alignment at the inner wall is accordingly weaker (see Appendix A 4 for further details). When choosing $K = 0.5$ and $w = 5$ (two-holed disk) or $K = 1$ and $w = 10$ (double annulus) we find convincing agreement with our other methods in Fig. 2.

C. Topological classification

The hard rods described in our particle-based approaches favorably align parallel to the system walls. This externally imposed boundary condition competes with the intrinsic smectic structure favoring defect-free, undeformed, parallel and equidistant layers. The resulting (stable or metastable) equilibrium structure are thus governed by a balance between elastic deformations and topological defects. The type, location and shape of the

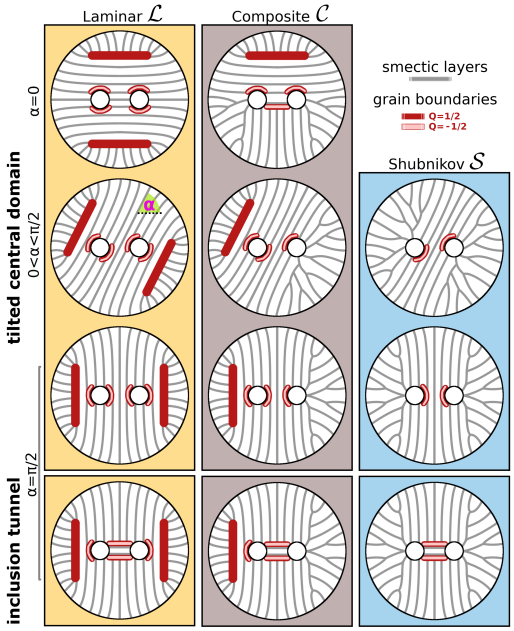

FIG. 3. Illustrative overview of topological structures. The rows show different realizations of generalized laminar ($\mathcal{L}$, two $+1/2$ and four $-1/2$ charges), composite ($\mathcal{C}$, one $+1/2$ and three $-1/2$ charges) and generalized Shubnikov ($\mathcal{S}$, two $-1/2$ charges) states. The first three rows display the structures with a continuous central domain which is tilted by the angle α relative to the axis that connects the two inclusion centers, as annotated (the definition of α is included in the first illustration of the second row). The fourth row displays the structures for $\alpha = \pi/2$ with the central domain interrupted by a few layers spanning between the two inclusions, which we refer to as inclusion tunnel. The illustrations depict the typical appearance of these generalized states in the two-holed-disk geometry (where we also speak of dual laminar and stretched Shubnikov states), but the same general classification also holds for the double-annulus geometry. Further details are provided in Sec. II C.

emerging topological defects provides a convenient way to classify and distinguish between the observed smectic states, as illustrated in Fig. 3. [59, 62]. In smectics, we typically observe spatially extended grain boundaries or virtual boundary defects (misalignment of rods at the wall), whose orientational frustration can be quantified by a topological charge Q in analogy to nematic disclinations [59, 60]. The Poincaré–Hopf theorem gives rise to a fundamental law of charge conservation for two-dimensional smectic structures: the total sum of topological charges $\sum Q = \chi$ in a confined system must equal the confining domain's Euler characteristic χ. The two main types of grain boundaries relevant in our study possess a $Q = +1/2$ or a $Q = -1/2$ topological charge, associated with a clockwise and counterclockwise rotation of the director field around the defect, respectively. In both cases, the main rotation occurs at the end points of the grain boundaries, which can then be identified as point-like tetratic defects of quarter-integer magnitude [59].

As a first step of our topological analysis, we focus on the structural properties on the largest scale and ignore the details in the region between the two inclusions. By doing so, we can classify the overall smectic states in the same spirit as in an annular geometry [62], i.e., by considering an effective geometry with Euler characteristic $\chi_{\text{eff}} = 0$, obtained by formally replacing the two inclusions with a single inclusion given by their convex hull (indicated by the magenta shaded areas in Fig. 1). On this level, we can classify solutions into (i) generalized laminar states, with two $Q = +1/2$ defects close to the outer wall and two $Q = -1/2$ defects at the effective inclusion, (ii) generalized composite states, combining features of both (one $Q = +1/2$, one $Q = -1/2$ defect and edge dislocations), or (iii) generalized Shubnikov states, with no topological charges but edge dislocations of the layers, as sketched in the different columns of Fig. 3. Due to the particular appearance of these states in the two-holed-disk geometry, we also speak of dual laminar and stretched Shubnikov states in this case.

As a second step, we account for the broken continuous rotational symmetry for a nonzero inclusion distance $c > 0$. We introduce the tilt angle $\alpha \in [0, \pi/2]$ of the central domain with respect to the axis that connects the two inclusion centers (cf. the second row in Fig. 3) as an additional structural quantifier. The rows of Fig. 3 depict the different states for $\alpha = 0$ (layers parallel to the connecting axis), an intermediate value of α, and $\alpha = \pi/2$ (layers perpendicular to the connecting axis).

The third step of our topological analysis concerns the fine structure between the inclusions, i.e., the location and shape of the two additional $Q = -1/2$ defects required by the charge conservation to match the overall Euler characteristic $\chi = -1$ in the presence of two holes. In general, there are two possibilities. First, the layers between the inclusions can align with the adjacent layers outside to become part of a larger domain, comparing the first three rows in Fig. 3. In this case, the two $Q = -1/2$ defects are directly located at the inclusions. Second, if $\alpha \gtrsim \pi/4$, it is also possible that the two inclusions are connected by one or more isolated smectic layers, such that the rods in the central region fulfill the parallel wall anchoring condition. However, this inclusion tunnel then interrupts the central domain, compare the last row in Fig. 3, which results in two grain boundaries with $Q = -1/2$, parallel to the line connecting the inclusions. Note that for $\alpha \lesssim \pi/4$, the anchoring condition can be fulfilled without forming an inclusion tunnel, i.e., when the layers connecting the inclusions are part of the defect-free central domain.

We comment that the stretched Shubnikov state in the two-holed-disk geometry cannot be realized for small tilt

angles. When decreasing the tilt angle α of a structure below $\alpha \lesssim \pi/4$, the central domain eventually fulfills the first criterion for an inclusion tunnel (layers connecting the inclusions), comparing with the generalized laminar state in the top-right illustration of Fig. 3 for $\alpha = 0$. In turn, a generalized Shubnikov state is only possible if the second criterion for an inclusion tunnel is also fulfilled, i.e., that there exists a larger domain outside the convex hull of the inclusions which has a tilt angle $\alpha \gtrsim \pi/4$ and is separated from the inclusion tunnel by two grain boundaries, comparing with the bottom-right illustration of Fig. 3 for $\alpha = \pi/2$. Combining these two structures, the composite state depicted in Fig. 3 for $\alpha = 0$ constitutes a particular example with two domains of comparable size.

III. RESULTS

A. Two-holed disk

We focus first on the two-holed-disk geometry. As in the annulus, the circular shape of the outer confining wall remains invariant for all choices of the geometrical parameters b and c, where an annular geometry is recovered for $c = 0$. To quantify the emerging structures in full detail, we proceed stepwise. First, in Sec. III A 1, we study the transition between the generalized laminar and Shubnikov states, focusing only on the smectic structures outside the convex hull of the two inclusions. Then, we use these insights to explain our general observations in experiments and Monte-Carlo simulations in Sec. III A 2 before quantifying the two structural aspects indicated in Fig. 3. In particular, we study the tilt angle α of the central smectic domain in Sec. III A 3 and investigate the locations of the topological defects in the region between the inclusions in Sec. III A 4.

1. *Theoretical laminar-Shubnikov transition*

We start by systematically mapping out a simple state diagram using DFT, which gives us full control over the structures we wish to compare. In particular, to understand the general structural response upon varying both b and c, we focus on (dual) laminar and (stretched) Shubnikov states, as specified in Sec. II C. Moreover, we restrict ourselves to (fairly) axially symmetric structures, i.e., we impose the two extreme tilt angles $\alpha = 0$ or $\alpha = \pi/2$ in the laminar case and just $\alpha = \pi/2$ in the Shubnikov case.

Our results are compiled in Fig. 4. We find that the laminar state is destabilized in favor of the Shubnikov state upon increasing the inclusion size ratio b, as in the special case $c = 0$ of an annulus [62]. The laminar state is also destabilized upon increasing the spacing c between the inclusions for a fixed value of b. This

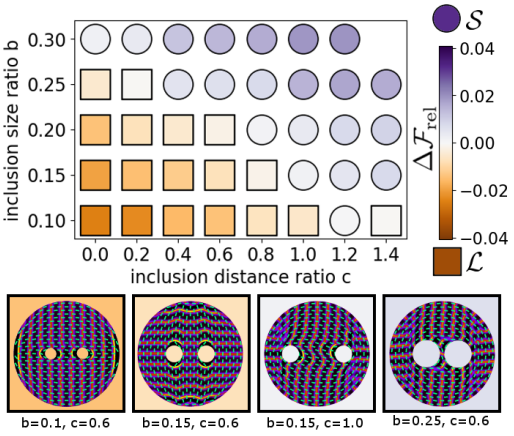

FIG. 4. DFT state diagram in the two-holed-disk geometry indicating the stable laminar (square symbols) or Shubnikov (round symbols) states for different inclusion distance ratios c and inclusion size ratios b. The data for $c = 0$, indicating the special case of annular confinement, are taken from Ref. [62]. The color denotes the relative free energy difference $\Delta\mathcal{F}_{\rm rel} := (\mathcal{F}_0^{(\mathcal{L})} - \mathcal{F}_0^{(\mathcal{S})})/\mathcal{F}_0$ between the optimal laminar ($\mathcal{L}$) and Shubnikov ($\mathcal{S}$) states, where $\mathcal{F}_0 := \min\{\mathcal{F}_0^{(\mathcal{L})}, \mathcal{F}_0^{(\mathcal{S})}\}$ is the free energy of the overall optimal state. For $b = 0.3$ and $c = 1.4$ the inclusions are in contact with the outer wall, such that no Shubnikov state can exist. The snapshots in the bottom panel depict four representative examples of optimal structures: laminar structures with tilt angles $\alpha = 0$ or $\alpha = \pi/2$ (intermediate values of α are examined below in Fig. 7) and Shubnikov structures without and with an inclusion tunnel.

behavior matches expectations, since the size of the effective inclusion increases when the two inclusions have a larger distance, such that Shubnikov structures, characterized by layers spanning from the inclusions to the outer wall, become generally more favorable. Since only the structure outside the convex hull of the inclusions is relevant for this first part of our discussion, it is not important whether or not the two inclusions are connected (topological details arising from disconnected inclusions at $c > 2b$ are discussed in Sec. III A 4). However, we stress that, as soon as $c \geq 2 - 2b$, the inclusions overlap with the outer confining wall, such that it is no longer possible to fulfill the criterion to identify a Shubnikov state (cf. the missing top-right state point in Fig. 4). In these extreme cases, the confining geometry is, once again, simply connected and only deformed variants of a bridge state (laminar state without negatively charged defects) [62] exist, which are not our main interest here. In the trivial bounding cases $c > 2 + 2b$ or $b = 0$ (not shown), the confinement simply reduces to a disk.

In general, the laminar-Shubnikov transition is driven by the tendency of the system to achieve an optimal bal-

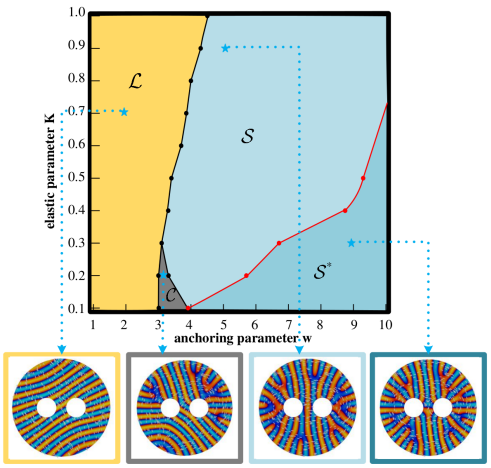

FIG. 5. State diagram from **Q**-tensor theory in the two-holed-disk geometry for different values of the elastic parameter K and the wall anchoring parameter w. The inclusion size ratio $b = 0.2$ and the inclusion distance ratio $c = 0.6$ are kept fixed. We distinguish between four different structures: laminar ($\mathcal{L}$), composite ($\mathcal{C}$), Shubnikov without ($\mathcal{S}$) and with an inclusion tunnel ($\mathcal{S}^*$). The bottom panel depicts one representative snapshot for each case (parameters according to the connected stars).

ance between satisfying the external constraints of the confining geometry (since the rods preferably align parallel to the wall) and maintaining the intrinsic smectic structure. This results in a trade-off between deformations, as dominant in the Shubnikov structures, and topological defects, governing the laminar structures.

To better characterize this competition, we employ the smectic **Q**-tensor theory to examine how the structural transitions can be induced by tuning the elastic behavior and the strength of the tangential wall alignment, determined by the parameters K and w, respectively. To this end, we fix the inclusion size ratio $b = 0.2$ and the inclusion distance ratio $c = 0.6$, so as to take values close to the laminar-Shubnikov transition predicted by DFT in Fig. 4. The state diagram from **Q**-tensor theory in Fig. 5 confirms the expectation that Shubnikov states are stabilized upon imposing stronger anchoring conditions (i.e., larger w) to minimize the number of defects. In particular, the observed laminar states are typically characterized by a single domain with the defects appearing through a misalignment at the walls (as also frequently observed in DFT). Moreover, we see that the laminar state is generally stabilized upon increasing K and thus the bending rigidity of the layers. For smaller values of $K < 0.3$, composite structures are also found and the laminar state becomes compatible with strongly deformed layers. Such highly elastic behavior is, however, rather atypical in the context of hard rods. These results demonstrate a reassuring consistency between the DFT and smectic **Q**-tensor results, even without extensive tuning of the other parameters of the **Q**-tensor model.

Returning to microscopic DFT structures, we can make more precise statements regarding the stability of the generalized laminar and Shubnikov states, by comparing the examples shown at the bottom of Fig. 4. First of all, both the number of layers in the central domain and their orientation in the optimal laminar state (under the symmetry constraints imposed so far) strongly depend on the geometrical parameters. This suggests that by allowing for different values of the tilt angle α we should find states with an even smaller free energy, which will be studied in Sec. III A 3. Second, and most importantly, we notice for $\alpha = \pi/2$ that the structural differences between states classified as laminar or Shubnikov become less pronounced upon increasing the inclusion distance c, due to the larger size of the central domain. This intuitively explains the destabilization of the laminar state for increasing c: the number of laminar layers between the inclusions and outer wall decreases, which brings the two defects closer to annihilation, while the extreme case of zero laminar layers eventually corresponds to a Shubnikov structure. Third, for $b = 0.1$, we even observe in Fig. 4 a particular example of a re-entrant stable laminar state at $c = 1.4$, in which the spacing between the inclusions and outer wall allows for all layers being parallel. Finally, we expect that, within a small range of parameters, there exists a stable intermediate composite state [62], as in the illustrations in the middle panel of Fig. 3.

2. *General particle-based observations*

In our colloidal experiments, we focus on a few selected sets of geometrical parameters. Qualitatively inspecting our snapshots for $b \approx 0.25$ and $0.6 < c < 1.2$, we arrive at the following general picture. We predominantly observe the Shubnikov state, in agreement with the DFT prediction. All of these Shubnikov structures possess large tilt angles $\alpha > \pi/4$ of the central domain. Recalling the discussion in Sec. II C, such an alignment allows for a larger number of straight layers in the central domain between the inclusions. Quite remarkably, however, only one of our 104 inspected structures depicts a nearly laminar state (see the second snapshot in Fig. 6), while only three of them can be clearly identified as composite states. In all these cases, the laminar parts of the structure possess a small tilt angle $\alpha < \pi/4$. To quantify the tilt-angle statistics, we measure in Fig. 6 the global orientational distribution of all rods, averaged over all cavities with comparable geometry. In accordance with the typical orientation α of the central domain, we find that the most frequent angles are close to $\pi/2$, where the exact location of this peak appears to depend on the inclusion distance.

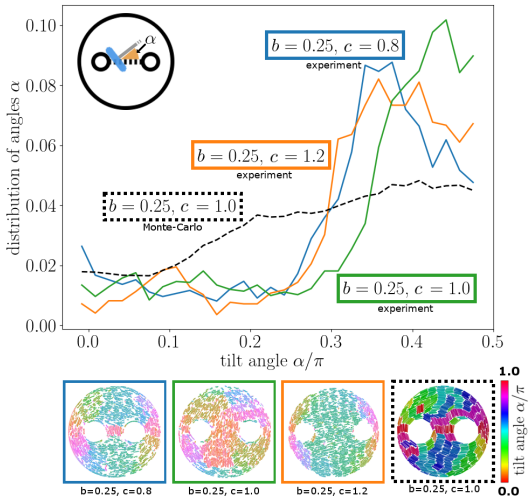

FIG. 6. Global orientational distribution in the two-holed-disk geometry for the inclusion size ratio $b = 0.25$. As illustrated at the top right, the relative frequency of individual rod orientations (blue) reflects the preferred tilt angle α of the layers (gray line) relative to the axis that connects the two inclusions (dotted line), see also Fig. 3. We compare experimental data for different inclusion distance ratios $c \approx 0.8$, $c \approx 1.0$ and $c \approx 1.2$, averaged over 21, 24 and 15 available structures, respectively, and Monte-Carlo data for $c = 1.0$, sampled from 1800 independent simulation runs. For symmetry reasons we map orientations with $\alpha > \pi/2$ onto $\pi - \alpha$ and only consider $0 \leq \alpha \leq \pi/2$. The bottom panel depicts one particular snapshot for each case, where the rods are colored according to their orientation.

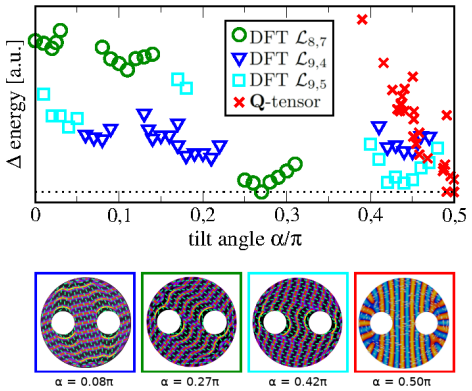

FIG. 7. Energy landscape for different structures depending on the tilt angle α of the central domain in the two-holed-disk geometry for the inclusion size ratio $b = 0.25$ and the inclusion distance ratio $c = 1.0$. According to the legend, we compare different laminar DFT structures $\mathcal{L}_{ab}$, where the indices a and b denote the number of layers in the central domain and perpendicular to it, respectively, and several minimizers of the energy functional from **Q**-tensor theory with $K = 1$ and $w = 5$. Exemplary snapshots are shown in the bottom panel. As only the energy difference is relevant for the stability, the vertical axes depicts the rescaled difference to the global minimum (indicated by the dotted line), calculated separately for DFT and **Q**-tensor results in arbitrary units [a.u.]. Since the minima for large angles α are generally deeper, it is more likely to find such structures, consistent with the observation in Fig. 6.

Overall, the suppression of the stability of laminar states, upon increasing the distance between the inclusions, appears to be even more pronounced in the experiments than predicted theoretically in Fig. 4. This observation can be explained by the typically lower number of parallel layers in the experiment compared to the most stable DFT solution [62] in combination with the preference of the rods to align in a central domain at large tilt angles. To understand this, consider, for instance, the experimental laminar structure depicted in Fig. 6 with $b = 0.25$ and $c = 1.0$. Now imagine, instead, the inclusions placed over the top and bottom grain boundary. This would both reduce the defect region and classify the structure as a Shubnikov state with a significantly increased tilt angle α, intuitively explaining our predominant observations of large tilt angles and Shubnikov structures.

Our Monte-Carlo simulations of hard rods carried out for $b = 0.25$ and $c = 1.0$ confirm the basic experimental observations that nearly all identified structures reflect stretched Shubnikov states and that large tilt angles are favored. We depict the global orientational distribution and the typical snapshot at the bottom-right of Fig. 6. Moreover, our particle-resolved simulations allow us to further explore smaller inclusion sizes than those realized experimentally (not shown). As expected from the discussion above, there is still a high probability to observe Shubnikov structures for $b = 0.1$, while the laminar state becomes dominant for $b = 0.05$.

3. *Orientation of the central domain*

Our experimental and Monte-Carlo results suggest that the assumption, made in Sec. III A 1 for DFT, of imposing smectic structures with the same symmetry as the confining geometry is not justified in general. While the orientational distribution in Fig. 6 generally suggests that large tilt angles $\alpha > \pi/4$ are most likely, we also notice that the maximum is not always located at the extreme value $\alpha = \pi/2$. Even more so, we expect that the geometrical constraints on laminar structures, arising from the competition of the preferred layer spacing with both the distance between the two inclusions and the distance from each inclusion to the outer wall, can be

efficiently relaxed by aligning the central domain along characteristic tilt angles. A first evidence for this prediction stems from the DFT results in Fig. 4, where the tilt angle of the optimal laminar structure (given the constraint to either $\alpha = 0$ or $\alpha = \pi/2$) strongly depends on the particular geometry (contrast the two depicted laminar structures).

To learn more about the preferred tilt angle, we compare in Fig. 7 the energy of different states as a function of α for a fixed geometry with $b = 0.25$ and $c = 1.0$. In the smectic **Q**-tensor theory, we only find solutions with large tilt angles $\alpha > 0.4\pi$ for the intrinsic parameters $K = 1$ and $w = 5$, which demonstrates the instability of structures with smaller α under these conditions. The corresponding free energy decreases with increasing tilt angle, such that the global minimum is found for $\alpha \simeq 0.5\pi$, which is in principal agreement with the statistics from experiment and Monte-Carlo simulation.

To systematically study the tilt-angle dependence in DFT, we restrict ourselves to laminar states. We choose three representative template structures with a well-defined numbers of layers both in the central domain and perpendicular to it (c.f. the example structures shown at the bottom of Fig. 7). By doing so, all structures generated by imposing different tilt angles remain comparable among each other. For the parameters $b = 0.25$ and $c = 1.0$, we find that structures with two layers interrupted by each inclusion are generally favorable. We further focus in each case on three typical ranges of the tilt angle, such that there are (with increasing α) three, two or one laminar layers between one inclusion and the outer wall, respectively. These values of α depend on whether the central point of the geometry is occupied by a layer (central domain with nine layers in total) or by the void space in between two layers (central domain with eight layers in total). The corresponding free energy landscapes shown in Fig. 7 reveal that the most stable structures correspond to the minima in the range of tilt angles with the largest values. This reflects the intuition that the two inclusions are preferably located close to (or even on) the edge of the central domain and not in its center, such that the extent of deformations of the central smectic layers is reduced. The existence of distinct local free energy minima in Fig. 7 explains the nonmonotonic and geometry-dependent experimental distributions in Fig. 6.

4. Fine structure between the inclusions

Having understood the large-scale layering behavior of the central domain, we now investigate structure inside the convex hull of the inclusions in more detail. For $c > 2b$, the two inclusions are disconnected and we anticipate two additional (compared to a single or two overlapping inclusions) topological defects with a negative charge. As generally described in Sec. II C, there are two possible scenarios, related to how the smectic layers between the inclusions align. The first possibility, which has been silently implied so far when discussing our large-scale results in the previous sections, is that the central domain and the layers between the inclusions align with each other, compare the first three rows of Fig. 3. To be more specific, we can conclude that the layers need to fill the space between the inclusions in an entropically convenient way is probably one of the main driving forces that determines the geometry-dependent tilt angle of the central domain as a whole.

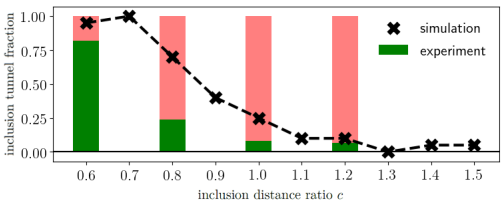

FIG. 8. Relative frequencies of structures with an inclusion tunnel (cf. the second row in Fig. 3) in the two-holed-disk geometry for the inclusion size ratio $b = 0.25$. We compare experimental data (green bars) for different inclusion distance ratios $c \approx 0.6$, $c \approx 0.8$, $c \approx 1.0$ and $c \approx 1.2$, averaged over 44, 21, 24 and 15 available structures, respectively, and Monte-Carlo data (black crosses) averaged over 20 simulations for each selected c. The dotted line serves as a guide to the eye, illustrating how the fraction of inclusion tunnels decreases with increasing inclusion distance. Regarding the occurrence of structures with inclusion tunnel in DFT and **Q**-tensor theory, please refer to the bottom-right snapshot in Fig. 4 and the state diagram in Fig. 5, respectively.

The second possibility of alignment between the inclusions is an inclusion tunnel, compare the last row of Fig. 3. This structure is defined by one or more smectic layers spanning between the two inclusions, irrespective of the orientation of the central domain. The driving force behind the formation of an inclusion tunnel is the adherence to the preferred wall alignment which comes at the cost of a larger grain boundary within the system. This is nicely reflected by additionally differentiating in the state diagram from **Q**-tensor theory, as in Fig. 5, between Shubnikov states with and without an inclusion tunnel. It is apparent from the state diagram that structures with an inclusion tunnel stabilize upon increasing the anchoring parameter w and decreasing the elastic parameter K.

In our DFT study, we find that structures with the central domain interrupted by an inclusion tunnel are almost always less stable than comparable ones with a continuous central domain, for both laminar and Shubnikov structures alike. The fact that the central domain tends to tilt, renders such an inclusion tunnel even less favorable due to the general preference of hard rods to meet at a grain boundary with nearly perpendicular orientations, instead of an oblique alignment. An inclusion

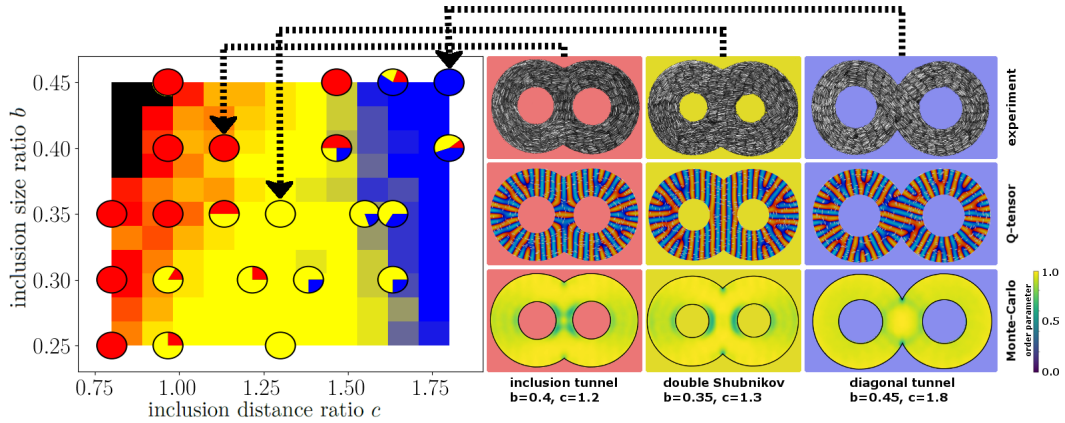

FIG. 9. Structures in the double-annulus geometry for different inclusion size ratios b and inclusion distance ratios c. While in the annular arcs we generally observe layering of the Shubnikov type for the parameters considered, we distinguish three states by the layer arrangement in the intersection region: inclusion tunnel (red), double-Shubnikov state (yellow) and diagonal tunnel (blue). Left panel: state diagram indicating the relative frequencies of the three structures between the two inclusions. The experimental and Monte-Carlo results are represented by pie charts and background pixels with proportional color mixing, respectively. For $c \lesssim 2b$ no rods fit in between the inclusions and there is no distinction (black pixels). Right panel: observed structures for three pairs of b and c corresponding to the state points indicated by the arrows. We depict experimental snapshots (top), solution profiles of the $\mathbf{Q}$-tensor model with for $K = 1.0$ and $w = 10$ (middle) and the orientational order parameter $S(\mathbf{r})$ averaged over 10^3 independent Monte-Carlo simulation runs per parameter pair, revealing the typical location of the topological defects through the darker shades (bottom).

tunnel only becomes energetically favorable for extremely small distances between the surfaces of the two inclusions, of about one rod length or less, as e.g. for $b = 0.25$ and $c = 0.6$, compare the fourth structure shown at the bottom of Fig. 4.

In practice, however, it is much more likely to observe these inclusion tunnels as a result of the equilibration protocol. More specifically, in our experiments and Monte-Carlo simulations, the growth of an inclusion tunnel can be triggered by small domains aligning with the inclusion at an early stage. Hence, such structures are observed with a noticeable probability, even for relatively large c, as verified in Fig. 8.

B. Double annulus

We have seen in Sec. III A that the inclusion distance ratio c and, therefore, the minimal distance from the inclusions to the outer wall is an important criterion which determines the globally observed state in the two-holed-disk geometry. The smectic structure between the inclusions then largely follows the alignment of the central domain, while inclusion tunnels are only rarely observed.

Now we focus on the double-annulus geometry, illustrated at the bottom of Fig. 1, for which a larger range $b < c < 2$ of inclusion distance ratios c can be examined without changing the Euler characteristic $\chi = -1$. Since the shortest distance from any point on the outer wall to one of the inclusions remains the same for all c, the smectic structure in the two annular arcs is largely determined by the inclusion size ratio b alone and can thus be well understood by taking cues from the state diagram in annular confinement [62]. This gives us a better control of how the central smectic layers in the intersection region of the two annular halves respond to changes of the inclusion distance compared to the single circular outer wall of the two-holed-disk geometry. We are thus primarily interested in the question of how the structure between the two inclusions of the double annulus is determined by the geometrical parameters b and c, as we focus on inclusion size ratios $b \geq 0.25$ which predominantly give rise to generalized Shubnikov structures in the annular arcs.

Our state diagram, compiled from experiments and particle-resolved Monte-Carlo simulations, is shown in the left panel of Fig. 9. Both methods consistently predict three different types of structures, shown in the right panel. First, for relatively large and nearby inclusions, we typically observe an inclusion tunnel, similar to the two-holed-disk geometry (cf. Sec. III A 4). Second, for relatively small and distant inclusions, we typically observe a structure with a large central domain of vertical layers, which is similar to the $\alpha = \pi/2$ alignment in the two-holed-disk geometry (cf. Sec. III A 3). As mentioned in the previous paragraph this extreme tilt angle

is favored here due to the broken rotational symmetry and the non-convex shape of the outer wall. We refer to such a structure as the double Shubnikov state, as there are no grain boundaries (the two $Q = -1/2$ defects are mostly due to misalignment at the inclusions). Third, for relatively large and distant inclusions, we typically observe a structure which is characterized by both a large tilted central domain and grain boundaries. The tilt angle is again roughly set by the geometry, such that the orientation of the rods follows an infinity symbol. This diagonal-tunnel state possesses no analogue in the two-holed-disk geometry. To corroborate these observations, we also evaluated our **Q**-tensor theory for representative pairs of parameters and find consistent minimizers, shown in the right panel of Fig. 9. Moreover, the exemplary double-Shubnikov structures shown in Fig. 3 using all four methods are in close agreement.

To further highlight the topological distinction between the three different structures observed in the double-annulus geometry, we additionally show in the right panel of Fig. 9 Monte-Carlo results for the local order parameter field $S(\mathbf{r})$, sampled as an average from 10^3 independent simulation runs. Due to the averaging, we obtain in each case a characteristic pattern, which possesses the same symmetry as the confinement. The inclusion tunnel is characterized by its orthogonal alignment relative to the nearby layers and therefore a large degree of orientational frustration between the inclusions. In the double Shubnikov state, the region between the inclusion largely aligns with the central domain and the orientational frustration is manifest only close to the inclusions (usually due to small domains of a few rods). Finally, for the diagonal tunnel, it is clearly visible that the grain boundaries are located at the edges of the central crossing of the annular arcs.

IV. SUMMARY AND CONCLUSIONS

In this work, we investigate smectic states, confined to complex geometries, illustrated in Fig. 1, with two circular inclusions (interior boundaries) by means of colloidal experiments, Monte-Carlo simulations, density functional theory (DFT) and smectic **Q**-tensor theory. Our four approaches consistently predict the main structural features, as exemplified in Fig. 2. All observed and expected structures are compiled in Fig. 3.

For large inclusions (or strong wall anchoring), the layers arrange into a generalized Shubnikov state, characterized by an overall perpendicular alignment of layers (or parallel alignment of rod-like particles) at the outer wall, which minimizes the number of topological defects. This is observed in both the two-holed-disk geometry (see the circular data points in Fig. 4 and the bottom-right and central regions (both shades of blue) in Fig. 5), where a stretched Shubnikov state also stabilizes for increasing inclusion distance, and the double-annulus geometry (see all data in Fig. 9). On the contrary, for small inclusions (or weak wall anchoring), the layers arrange into a generalized laminar state characterized by two $Q = -1/2$ defects at either of the two inclusions and two $Q = +1/2$ defects close to the outer wall. This is explicitly observed in the two-holed-disk geometry (see the quadratic data points in Fig. 4 and the leftmost region (yellow) in Fig. 5) but we expect the same upon further decreasing the inclusion size the double-annulus geometry.

If the two inclusions are sufficiently close to each other, we observe an inclusion tunnel in both the two-holed-disk geometry (see the bottom-right structure in Fig. 4, dark blue color in Fig. 5 and the statistics in Fig. 8) and the double-annulus geometry (see the data with red color in Fig. 9). This structure forms an isolated domain between the two inclusions and two grain boundaries, irrespective of whether global state. More distant inclusions allow for the layers to align in a larger central domain at the cost of misalignment at the inclusions. In fact, in the two-holed-disk geometry, this relative alignment of the central layers to the axis connecting the two inclusions is characterized by large tilt angles $\alpha \simeq \pi/2$ (see Figs. 6 and 7). In the double-annulus geometry, we further distinguish between two cases (identified here for generalized Shubnikov states). The double Shubnikov structure possesses a large central domain which extends over all four ends of the geometry's central junction at a fixed tilt angle $\alpha \approx \pi/2$ (see the data with yellow color in Fig. 9), while for even larger inclusion distances, we observe a diagonal tunnel, characterized by two grain boundaries at two opposing ends of the central junction and a tilt angle $0 < \alpha < \pi/2$ dictated by the geometry (see the data with yellow color in Fig. 9).

Our study represents a first step towards the study of liquid crystals confined to topologically highly complex environments such as random porous media [66–69] or arrays of obstacles [68]. Our complementary approaches can, in principle, be applied to any kind of confinement [24, 59, 70, 71]. This applies in particular also to systems in three dimensions to which our experimental, computational and theoretical methods, as well as, our topological concepts can be generalized [49, 52, 60]. Another generalization is to proceed towards more complex particle shapes and interactions such as hard polygons [69, 72], non-convex [73–77], or chiral particles [61, 78–84]. Finally it bears mentioning that many bacteria have rod-like shapes [85–88] and are living on two-dimensional substrates, where they can be easily be put in confinement [89, 90]. Bacterial colonies can approach high densities, where smectic layering is expected [91–93], such that our work may have important consequences for the structure in dense biofilms.

ACKNOWLEDGMENTS

RW and HL acknowledge support by the Deutsche Forschungsgemeinschaft (DFG) through the SPP 2265, under grant numbers WI 5527/1-1 (RW) and LO 418/25-

1 (HL). The work of JX is supported by the National Natural Science Foundation of China (No. 12201636) and the Research Fund of National University of Defense Technology [grant number ZK22-37]. The work of PEF is supported by the Engineering and Physical Sciences Research Council [grant numbers EP/R029423/1 and EP/W026163/1]. PEF and RW acknowledge the support of the Banff International Research Station (workshop 22w5159).

Appendix A: Details on the methods

1. Experiment

The experimental methods follow from our previous work [44, 62]. In short, home-synthesized silica rods [94] suspended in a 1mM NaCl water solution form sedimentation-diffusion equilibrium into a cylinder-shaped reservoir glued to a glass coverslip (see Fig. 1a in Ref. [62]). Confinement cavities, as shown in the first row of Fig. 2, are printed on the coverslip using polydimethylsiloxane (PDMS) mold and Norland Optical Adhesive glue. PDMS molds are made using standard soft lithography technique.

Particles have average effective length of 5.3μm, aspect ratio of 10.6 and gravitational length of 0.8μm. After insertion they start forming a concentration gradient along the direction of gravity. At the bottom, inside the cavities, we successively observe the formation of isotropic, nematic and finally smectic phases. The total amount of particles is chosen such that there is no crystalline state. The smectic structures are left to equilibrate for at least 12 hours.

Experimental snapshots capture the rods in direct vicinity of the bottom wall of the cavity that, paired with gravity, imposes a quasi-two dimensional confinement. We record images by mean of confocal microscopy with a Zeiss LSM Exciter 5 microscope and a 63x Zeiss Plan Apo Chromat objective. We collect scattered light to form images as this batch of rods is not fluorescent.

A custom python script is used to segment single rods and detect position and orientation (Wolfram Mathematica [62] and python scripts [60] are already available). The specific python script used to process the snapshots of Fig. 6 is provided along with an experimental snapshot as supplementary material.

2. Monte-Carlo simulations

With the help of canonical Monte-Carlo simulations we generate equilibrium states for liquid crystals composed of hard rods at bulk smectic area fraction $\eta_2 = 0.725$. The rods are modeled as discorectangles with aspect ratio $p = L/D = 16.5$, where L denotes the length and D the width of the particles. The k^{th} rod is parametrized by a line segment $\mathbf{a}_k = \mathbf{r}_k + \alpha_k \hat{\mathbf{u}}_k$, with position $\mathbf{r}_k$, normalized orientation $\hat{\mathbf{u}}_k$ and $|\alpha_k| < L/2$. All points within the area of the rod are characterized by $\{\mathbf{x} \in \mathbb{R}^2 | \, \|\mathbf{x} - \mathbf{a}_k\| \leq D/2\}$ such that the standard hard-core repulsion between a pair of rods i, j can be defined by

$$U(\mathbf{r}_i, \mathbf{r}_j, \hat{\mathbf{u}}_i, \hat{\mathbf{u}}_j) = \begin{cases} \infty & \text{for } d_{i,j} \leq D\,, \\ 0 & \text{for } d_{i,j} > D\,, \end{cases} \tag{A1}$$

where

$$d_{i,j} = \min_{|\alpha,\beta| < \frac{L}{2}} \|\mathbf{r}_i + \alpha\hat{\mathbf{u}}_i - (\mathbf{r}_j + \beta\hat{\mathbf{u}}_j)\| \tag{A2}$$

corresponds to the smallest distance between the opposing line segments [95].

The interaction of the rods with the walls is modeled by considering the rods as three virtual point particles at $\mathbf{r}_k + \gamma\hat{\mathbf{u}}_k$, $\gamma \in \{-L/2, 0, L/2\}$. The wall potential reads as

$$V(x) = \begin{cases} \Phi(x_0) + \Phi'(x_0)(x - x_0) & \text{for } x \leq x_0\,, \\ \Phi(x) & \text{for } x_0 > x\,. \end{cases} \tag{A3}$$

Here, $|x|$ denotes the minimal perpendicular distance from either of the two points to the wall and $x > 0$ corresponds to the inside of the cavity. The cut-off point, below which $V(x)$ is linear, is chosen as $x_0 = 0.5D$. For $\Phi(x)$, we choose the standard 12-6-Weeks-Chandler-Andersen-potential [96]

$$\Phi(x) = \begin{cases} 4\epsilon\left[\left(\frac{D}{x}\right)^{12} - \left(\frac{D}{x}\right)^{6}\right] + \epsilon & \text{for } x \leq 2^{\frac{1}{6}}D\,, \\ 0 & \text{for } x > 2^{\frac{1}{6}}D \end{cases} \tag{A4}$$

with $\epsilon = 10k_{\text{B}}T$, with the Boltzmann constant k_{B} and temperature T. The potential landscapes to model the two-holed-disk and double-annulus geometries can be expressed as combination of circular well and obstacles. The outer radius of the cavity is chosen as $R_{\text{out}} = 6L$.

To obtain the equilibrated configurations, we initialize the system at a dilute area fraction $\eta_0 = 0.01$. We subsequently compress the system, by rescaling the cavity, at a compression rate of $\Delta\eta_1 = 3.50 \times 10^{-7}$ per MC cycle to an intermediate area fraction just below the bulk isotropic-nematic phase transition. In a second stage, we compress the system with $\Delta\eta_1 = 7.33 \times 10^{-8}$ per MC cycle to the final area fraction $\eta_2 = 0.725$. The area fraction is given by the fraction of the sum of the individual volumes of the rods V_{rod} to the total volume of the cavity V_{cav}. Since the final area fraction and the final volume are fixed variables, by the geometric parameters b, c (see Fig. 1) and R_{out} in terms of the particle size, the particle number N remains a free parameter that is determined at the start of the simulation via the relation

$$\eta = \frac{NV_{\text{rod}}}{V_{\text{cav}}} = \frac{N}{V_{\text{cav}}}\left(\frac{\pi D^2}{4} + DL\right). \tag{A5}$$

The typical values for N we investigate are on the scale of several thousand. Typical snapshots in the two geometries are shown in the second row of Fig. 2.

3. Density functional theory (DFT)

Classical density functional theory DFT [63] allows us to predict the structure of anisotropic fluids in an external potential $V_{\text{ext}}(\mathbf{r},\phi)$ by calculating the equilibrium density profile $\rho(\mathbf{r},\phi)$ from a variational principle, where $\mathbf{r}$ denotes the center-of-mass position and ϕ the particle orientation. This is achieved by minimizing the grand potential functional

$$\Omega[\rho] = \mathcal{F}[\rho] + \int \mathrm{d}\mathbf{r} \int_0^{2\pi} \frac{\mathrm{d}\phi}{2\pi}\, \rho(\mathbf{r},\phi)(V_{\text{ext}}(\mathbf{r},\phi) - \mu)\,, \quad \text{(A6)}$$

at given chemical potential μ by iterating the Euler-Lagrange equation $\delta\Omega[\rho]/\delta\rho(\mathbf{r},\phi) = 0$, where $\mathcal{F}[\rho]$ is the intrinsic Helmholtz free energy functional. The solution density profile $\rho(\mathbf{r},\phi)$ for a given initial guess is given by a local minimum of the grand potential Ω. Here, we minimize under the constraint of a fixed total particle number $\int \mathrm{d}\mathbf{r} \int_0^{2\pi} \frac{\mathrm{d}\phi}{2\pi}\, \rho(\mathbf{r},\phi)$, to obtain local minima of the Helmholtz free energy $\mathcal{F}$.

For an explicit calculation, we need to specify the Helmholtz free energy functional $\mathcal{F}[\rho] = \mathcal{F}_{\text{id}}[\rho] + \mathcal{F}_{\text{ex}}[\rho]$, which is conveniently split into an exactly known ideal part

$$\beta\mathcal{F}_{\text{id}}[\rho] = \int \mathrm{d}\mathbf{r} \int_0^{2\pi} \frac{\mathrm{d}\phi}{2\pi}\, \rho(\mathbf{r},\phi)\left(\ln(\rho(\mathbf{r},\phi)\Lambda^2) - 1\right) \quad \text{(A7)}$$

and an excess part $\mathcal{F}_{\text{ex}}[\rho]$. The irrelevant thermal wave length Λ is set to unity the inverse temperature $\beta := (k_{\text{B}}T)^{-1}$ is just a scaling factor. The excess free energy is based on fundamental measure theory [64, 65, 97] for anisotropic hard particles in two dimensions [53, 62], expressing the functional $\mathcal{F}_{\text{ex}}[\rho]$ as a function of weighted densities

$$n_\nu(\mathbf{r}) = \int \mathrm{d}\mathbf{r}_1 \int_0^{2\pi} \frac{\mathrm{d}\phi}{2\pi}\, \rho(\mathbf{r}_1,\phi)\, \omega^{(\nu)}(\mathbf{r}-\mathbf{r}_1,\phi)\,. \quad \text{(A8)}$$

These are calculated by convolution of the density and the scalar, vectorial or tensorial one-body measures $\omega^{(\nu)}(\mathbf{r},\phi)$, which describe the geometry of the hard particles. The explicit expression for $\mathcal{F}_{\text{ex}}[\rho]$ makes use of a truncated and corrected expansion up to rank-two tensors, see Ref. [62] for further details.

In this study we focus on hard discorectangles with rectangular length L and circular diameter D at fixed aspect ratio $p = L/D = 10$. Throughout the manuscript, we consider structures with fixed area fraction $\eta = 0.65$, as defined in Eq. (A5). Typical density profiles in the two geometries are shown in the third row of Fig. 2, which displays the dimensionless total density

$$\bar{\rho}(\mathbf{r}) := \left(LD + \frac{D^2\pi}{4}\right) \int_0^{2\pi} \frac{\mathrm{d}\phi}{2\pi}\, \rho(\mathbf{r},\phi)\,. \quad \text{(A9)}$$

through a color coding and the local orientational director field (representing the locally preferred value of ϕ) through green arrows.

All structures are calculated by free minimization of the density functional on a spatial grid with resolution $\Delta x = \Delta y = 0.2$ and $N_\phi = 96$ orientational angles. Laminar structures are typically initialized by cutting out the inclusions from equilibrium structures in circular confinement. Then we can also smoothly change the inclusion size ratio b and/or the inclusion distance ratio c to different target values, while continuously minimizing the functional. To examine the stability of an inclusion tunnel, appropriate structures are superimposed and subsequently minimized for comparison. To generate comparable structures with different tilt angles for Fig. 7, we also start from two specific structures in circular confinement, possessing eight or nine parallel layers in the central domain. Then we cut out the two inclusions at typical angles α at which a regular layer structure is maintained and smoothly rotate the inclusions towards other target tilt angles, while continuously minimizing the functional. Shubnikov structures are initialized either by superimposing a perpendicular domain aligning with the inclusions on equilibrium laminar structures with $\alpha = \pi/2$ or from a random structure with circular orientational director [62]. After minimization of multiple structures for a given set of parameters, we compare the values of the free energy $\mathcal{F}[\rho]$ to determine the most stable state with minimal free energy.

4. Smectic Q-tensor theory

It is also possible to adapt continuum models to investigate the qualitative behavior of smectics. Recently, [49] proposes a new continuum model, solving for a real-valued smectic order parameter u, indicating the local density variation, and a tensor-valued nematic order parameter $\mathbf{Q}$. A detailed discussion about deriving continuum model can be found in [98].

Specifically, we use the two-dimensional version of the $\mathbf{Q}$-tensor model from [49] with the volumetric free energy:

$$\mathcal{J}_{\text{v}}(u,\mathbf{Q}) = \int_\Omega \Big(f_{\text{s}}(u) + B \left| \mathcal{D}^2 u + q^2 \left(\mathbf{Q} + \frac{\mathbf{I}_2}{2}\right) u \right|^2 + f_{\text{n}}(\mathbf{Q}, \nabla\mathbf{Q}) \Big), \quad \text{(A10)}$$

where

$$f_{\text{s}}(u) := \frac{a_1}{2}u^2 + \frac{a_2}{3}u^3 + \frac{a_3}{4}u^4, \quad \text{(A11)}$$

and

$$f_{\text{n}}(\mathbf{Q},\nabla\mathbf{Q}) := \frac{K}{2}|\nabla\mathbf{Q}|^2 - l\left(\mathrm{tr}(\mathbf{Q}^2)\right) + l\left(\mathrm{tr}(\mathbf{Q}^2)\right)^2. \quad \text{(A12)}$$

Here, K is the nematic elastic constant, l represents the nematic bulk parameter, $\mathbf{I}_2$ is the 2×2 identity matrix and a_1, a_2, a_3, B, q are given real parameters. We fix $a_1 = -5$, $a_2 = 0$, $a_3 = 5$, $B = 10^{-5}$, $q = 30$ and

$l = 2$, similar to the choice in Ref. [49]. In Eq. (A10), $\mathcal{D}^2$ denotes the Hessian operator, so that the associated Euler–Lagrange equation for u is a fourth-order partial differential equation. One can intuitively understand the free energy functional $\mathcal{J}$ as a combination of three contributions: the smectic bulk energy f_s, the coupling effect (B-term) between the nematic director and smectic layers and the nematic elastic and bulk energies f_n.

In extreme confinement, we cannot expect the hard rods to perfectly satisfy tangential wall anchoring, as represented by Dirichlet boundary conditions. Therefore, we weakly impose tangential boundary conditions on both inner boundaries (denoted as Γ_1 and Γ_2) and outer boundary Γ_outer by means of Rapini–Papoular surface anchoring. To this end, an additional anchoring energy is added to Eq. (A10), leading to the following total energy:

$$\mathcal{J}(u,\mathbf{Q}) = \mathcal{J}_\mathrm{v}(u,\mathbf{Q}) + \frac{w}{2}\Big(\int_{\Gamma_\mathrm{outer}} |Q - Q_\mathrm{outer}|^2 + a_\mathrm{r}\big(\int_{\Gamma_1} |Q-Q_1|^2 + \int_{\Gamma_2} |Q-Q_2|^2 \big)\Big) \quad \text{(A13)}$$

with the prescribed tangential configurations given by

$$Q_\mathrm{outer} = \begin{bmatrix} \frac{y^2}{x^2+y^2} - \frac{1}{2} & -\frac{xy}{x^2+y^2} \\ -\frac{xy}{x^2+y^2} & \frac{x^2}{x^2+y^2} - \frac{1}{2} \end{bmatrix}, \quad \text{(A14)}$$

$$Q_1 = \begin{bmatrix} \frac{y^2}{(x-c/2)^2+y^2} - \frac{1}{2} & -\frac{(x-c/2)y}{(x-c/2)^2+y^2} \\ -\frac{(x-c/2)y}{(x-c/2)^2+y^2} & \frac{(x-0.3)^2}{(x-c/2)^2+y^2} - \frac{1}{2} \end{bmatrix}, \quad \text{(A15)}$$

$$Q_2 = \begin{bmatrix} \frac{y^2}{(x+c/2)^2+y^2} - \frac{1}{2} & -\frac{(x+c/2)y}{(x+c/2)^2+y^2} \\ -\frac{(x+c/2)y}{(x+c/2)^2+y^2} & \frac{(x+c/2)^2}{(x+c/2)^2+y^2} - \frac{1}{2} \end{bmatrix}. \quad \text{(A16)}$$

Here, c is the inclusion distance ratio as defined in Fig. 1, w denotes the anchoring weight with larger values representing stronger anchoring and a_r accounts for the expected curvature dependence of surface anchoring. Specifically, the choice of a_r indicates different anchoring strength w on the outer and $a_\mathrm{r}w$ on the inner boundaries, which can affect the resulting final minimizer with the lowest energy. Accordingly, we have verified that a slightly weaker anchoring strength, $a_\mathrm{r} < 1$, on the inner boundary gives a better consistency with experimental results for the two-holed disk problem. Therefore, we take $a_\mathrm{r} = 0.7$ throughout the manuscript, except for Fig. 5, where the focus lies on illustrating the Laminar-Shubnikov transitions using the same anchoring strength variation on both boundaries for each w-continuation step and thus $a_\mathrm{r} = 1$ is taken for simplicity.

Due to the nonconvexity of $\mathcal{J}$, there typically exist multiple local minimizers. In our work we employ the deflation technique to discover them [99]; in all figures, we plot the minimizer with lowest energy found for different input parameters K and w (specified accordingly in the manuscript) of the energy functional in Eq. (A13). More details about the model and associated numerical methods can be found in Refs. [49, 100] and [98, Chapters 8-10]. Typical solution profiles in the two geometries are shown in the fourth row of Fig. 2.

[1] P.-G. De Gennes and J. Prost, *The physics of liquid crystals*, 83 (Oxford University Press, Oxford, United Kingdom, 1993).
[2] O. D. Lavrentovich, Liq. Cryst. **24**, 117 (1998).
[3] O. J. Dammone, I. Zacharoudiou, R. P. A. Dullens, J. M. Yeomans, M. P. Lettinga, and D. G. A. L. Aarts, Phys. Rev. Lett. **109**, 108303 (2012).
[4] O. V. Manyuhina, K. B. Lawlor, M. C. Marchetti, and M. J. Bowick, Soft Matter **11**, 6099 (2015).
[5] I. C. Gârlea, P. Mulder, J. Alvarado, O. J. Dammone, D. G. A. L. Aarts, M. P. Lettinga, G. H. Koenderink, and B. M. Mulder, Nat. Commun. **7**, 12112 (2016).
[6] L. Tran, M. O. Lavrentovich, D. A. Beller, N. Li, K. J. Stebe, and R. D. Kamien, Proc. Natl. Acad. Sci. U.S.A. **113**, 7106 (2016).
[7] Y. Han, A. Majumdar, and L. Zhang, SIAM J. Appl. Math. **80**, 1678 (2020).
[8] X. Yao and J. Z. Y. Chen, Phys. Rev. E **101**, 062706 (2020).
[9] X. Yao, L. Zhang, and J. Z. Chen, Phys. Rev. E **105**, 044704 (2022).
[10] K. Sentker, A. W. Zantop, M. Lippmann, T. Hofmann, O. H. Seeck, A. V. Kityk, A. Yildirim, A. Schönhals, M. G. Mazza, and P. Huber, Phys. Rev. Lett. **120**, 067801 (2018).
[11] R. Ienaga, K. Beppu, and Y. T. Maeda, arXiv preprint arXiv:2212.13756 (2022).
[12] X.-Q. Shi and Y.-Q. Ma, Nat. Commun. **4**, 3013 (2013).
[13] F. C. Keber, E. Loiseau, T. Sanchez, S. J. DeCamp, L. Giomi, M. J. Bowick, M. C. Marchetti, Z. Dogic, and A. R. Bausch, Science **345**, 1135 (2014).
[14] S. J. DeCamp, G. S. Redner, A. Baskaran, M. F. Hagan, and Z. Dogic, Nat. Mater. **14**, 1110 (2015).
[15] L. Giomi, Phys. Rev. X **5**, 031003 (2015).
[16] A. J. Tan, E. Roberts, S. A. Smith, U. A. Olvera, J. Arteaga, S. Fortini, K. A. Mitchell, and L. S. Hirst, Nat. Phys. **15**, 1033 (2019).
[17] T. N. Shendruk, A. Doostmohammadi, K. Thijssen, and J. M. Yeomans, Soft Matter **13**, 3853 (2017).
[18] J. Hardoüin, C. Doré, J. Laurent, T. Lopez-Leon, J. Ignés-Mullol, and F. Sagués, Nat. Commun. **13**, 6675 (2022).
[19] Z.-F. Huang, H. Löwen, and A. Voigt, Commun. Phys. **5**, 294 (2022).

[20] N. D. Mermin, Rev. Mod. Phys. **51**, 591 (1979).
[21] G. Tóth, C. Denniston, and J. M. Yeomans, Phys. Rev. Lett. **88**, 105504 (2002).
[22] R. A. Mosna, D. A. Beller, and R. D. Kamien, Phys. Rev. E **86**, 011707 (2012).
[23] G. P. Alexander, B. G.-g. Chen, E. A. Matsumoto, and R. D. Kamien, Rev. Mod. Phys. **84**, 497 (2012).
[24] Y.-K. Kim, S. V. Shiyanovskii, and O. D. Lavrentovich, J. Condens. Matter Phys. **25**, 404202 (2013).
[25] A. J. Vromans and L. Giomi, Soft Matter **12**, 6490 (2016).
[26] X. Tang and J. V. Selinger, Soft Matter **13**, 5481 (2017).
[27] T. Guin, M. J. Settle, B. A. Kowalski, A. D. Auguste, R. V. Beblo, G. W. Reich, and T. J. White, Nat. Commun. **9**, 2531 (2018).
[28] D. B. Liarte, M. Bierbaum, R. A. Mosna, R. D. Kamien, and J. P. Sethna, Phys. Rev. Lett. **116**, 147802 (2016).
[29] H. Aharoni, T. Machon, and R. Kamien, Phys. Rev. Lett. **118**, 257801 (2017).
[30] L. Radzihovsky, Phys. Rev. Lett. **125**, 267601 (2020).
[31] J. Paget, U. Alberti, M. G. Mazza., A. J. Archer, and T. N. Shendruk, J. Phys. A: Math. Theor. **55**, 354001 (2022).
[32] B. Zappone and E. Lacaze, Liq. Cryst. Rev. **0**, 1 (2022).
[33] S.-P. Do, A. Missaoui, A. Coati, D. Coursault, H. Jeridi, A. Resta, N. Goubet, M. M. Wojcik, A. Choux, S. Royer, E. Briand, B. Donnio, J. L. Gallani, B. Pansu, E. Lhuillier, Y. Garreau, D. Babonneau, M. Goldmann, D. Constantin, B. Gallas, B. Croset, and E. Lacaze, Nano Lett. **20**, 1598 (2020).
[34] B. Zappone, A. E. Mamuk, I. Gryn, V. Arima, A. Zizzari, R. Bartolino, E. Lacaze, and R. Petschek, Proc. Natl. Acad. Sci. U.S.A. **117**, 17643 (2020).
[35] M. A. Gharbi, I. B. Liu, Y. Luo, F. Serra, N. D. Bade, H.-N. Kim, Y. Xia, R. D. Kamien, S. Yang, and K. J. Stebe, Langmuir **31**, 11135 (2015).
[36] F. Serra, M. A. Gharbi, Y. Luo, I. B. Liu, N. D. Bade, R. D. Kamien, S. Yang, and K. J. Stebe, Adv. Opt. Mater. **3**, 1287 (2015).
[37] J. Jeong and M. W. Kim, Phys. Rev. Lett. **108**, 207802 (2012).
[38] R. S. Preusse, E. R. George, S. A. Aghvami, T. M. Otchy, and M. A. Gharbi, Soft Matter **16**, 8352 (2020).
[39] M. A. Gharbi, D. A. Beller, N. Sharifi-Mood, R. Gupta, R. D. Kamien, S. Yang, and K. J. Stebe, Langmuir **34**, 2006 (2018).
[40] T. Lopez-Leon and A. Fernandez-Nieves, Colloid Polym. Sci. **289**, 345 (2011).
[41] S. M. Hare, B. Lunsford-Poe, M. Kim, and F. Serra, Materials **13**, 3761 (2020).
[42] M.-J. Gim, D. A. Beller, and D. K. Yoon, Nat. Commun. **8**, 15453 (2017).
[43] A. Kuijk, D. V. Byelov, A. V. Petukhov, A. Van Blaaderen, and A. Imhof, Faraday Discuss. **159**, 181 (2012).
[44] L. B. G. Cortes, Y. Gao, R. P. A. Dullens, and D. G. A. L. Aarts, J. Phys. Condens. Matter **29**, 064003 (2017).
[45] M. González-Pinto, F. Borondo, Y. Martínez-Ratón, and E. Velasco, Soft Matter **13**, 2571 (2017).
[46] A. Díaz-De Armas, M. Maza-Cuello, Y. Martínez-Ratón, and E. Velasco, Phys. Rev. Research **2**, 033436 (2020).
[47] M. Y. Pevnyi, J. V. Selinger, and T. J. Sluckin, Phys. Rev. E **90**, 032507 (2014).
[48] J. M. Ball and S. J. Bedford, Mol. Cryst. Liq. Cryst. **612**, 1 (2015).
[49] J. Xia, S. MacLachlan, T. J. Atherton, and P. E. Farrell, Phys. Rev. Lett. **126**, 177801 (2021).
[50] J. Paget, M. G. Mazza, A. J. Archer, and T. N. Shendruk, arXiv preprint arXiv:2201.09019 (2022).
[51] R. Wittmann, M. Marechal, and K. Mecke, J. Chem. Phys. **141**, 064103 (2014).
[52] R. Wittmann, M. Marechal, and K. Mecke, J. Phys. Condens. Matter **28**, 244003 (2016).
[53] R. Wittmann, C. E. Sitta, F. Smallenburg, and H. Löwen, J. Chem. Phys. **147**, 134908 (2017).
[54] B. G.-g. Chen, G. P. Alexander, and R. D. Kamien, Proc. Natl. Acad. Sci. U.S.A. **106**, 15577 (2009).
[55] R. D. Kamien and R. A. Mosna, New J. Phys. **18**, 053012 (2016).
[56] H. Aharoni, T. Machon, and R. D. Kamien, Phys. Rev. Lett. **118**, 257801 (2017).
[57] T. Machon, H. Aharoni, Y. Hu, and R. D. Kamien, Commun. Math. Phys. **372**, 525 (2019).
[58] R. E. Webster, N. J. Mottram, and D. J. Cleaver, Phys. Rev. E **68**, 021706 (2003).
[59] P. A. Monderkamp, R. Wittmann, L. B. G. Cortes, D. G. A. L. Aarts, F. Smallenburg, and H. Löwen, Phys. Rev. Lett. **127**, 198001 (2021).
[60] P. A. Monderkamp, R. Wittmann, M. te Vrugt, A. Voigt, R. Wittkowski, and H. Löwen, Phys. Chem. Chem. Phys. **24**, 15691 (2022).
[61] P. A. Monderkamp, R. S. Windisch, R. Wittmann, and H. Löwen, arXiv preprint arXiv:2301.09541 (2023).
[62] R. Wittmann, L. B. G. Cortes, H. Löwen, and D. G. A. L. Aarts, Nat. Commun. **12**, 623 (2021).
[63] R. Evans, Adv. Phys. **28**, 143 (1979).
[64] Y. Rosenfeld, Phys. Rev. Lett. **63**, 980 (1989).
[65] R. Roth, J. Phys. Condens. Matter **22**, 063102 (2010).
[66] R. Guégan, D. Morineau, C. Loverdo, W. Béziel, and M. Guendouz, Phys. Rev. E **73**, 011707 (2006).
[67] C. Scholz, F. Wirner, J. Götz, U. Rüde, G. E. Schröder-Turk, K. Mecke, and C. Bechinger, Phys. Rev. Lett. **109**, 264504 (2012).
[68] K. Chen, O. J. Gebhardt, R. Devendra, G. Drazer, R. D. Kamien, D. H. Reich, and R. L. Leheny, Soft Matter **14**, 83 (2018).
[69] C. Avendaño, G. Jackson, E. A. Müller, and F. A. Escobedo, Proc. Natl. Acad. Sci. U.S.A. **113**, 9699 (2016).
[70] T. Geigenfeind, S. Rosenzweig, M. Schmidt, and D. de las Heras, J. Chem. Phys. **142**, 174701 (2015).
[71] I. C. Gârlea, O. Dammone, J. Alvarado, V. Notenboom, Y. Jia, G. H. Koenderink, D. G. A. L. Aarts, M. P. Lettinga, and B. M. Mulder, Sci. Rep. **9**, 20391 (2019).
[72] A. P. Gantapara, W. Qi, and M. Dijkstra, Soft Matter **11**, 8684 (2015).
[73] C. J. Hernandez and T. G. Mason, J. Phys. Chem. C **111**, 4477 (2007).
[74] T. Niori, T. Sekine, J. Watanabe, T. Furukawa, and H. Takezoe, J. Mater. Chem. **6**, 1231 (1996).
[75] G. Heppke, D. Parghi, and H. Sawade, Liq. Cryst. **27**, 313 (2000).
[76] T. J. Dingemans and E. T. Samulski, Liq. Cryst. **27**, 131 (2000).
[77] M. B. Ros, J. L. Serrano, M. R. de La Fuente, and C. L. Folcia, J. Mater. Chem. **15**, 5093 (2005).
[78] R. D. Kamien and J. V. Selinger, J. Phys. Condens.

Matter **13**, R1 (2001).
[79] A. B. Harris, R. D. Kamien, and T. C. Lubensky, Phys. Rev. Lett. **78**, 1476 (1997).
[80] A. B. Harris, R. D. Kamien, and T. C. Lubensky, Rev. Mod. Phys. **71**, 1745 (1999).
[81] J. Pollard, G. Posnjak, S. Čopar, I. Muševič, and G. P. Alexander, Phys. Rev. X **9**, 021004 (2019).
[82] R. B. Meyer, Mol. Cryst. Liq. **40**, 33 (1977).
[83] I. Dierking, Sym. **6**, 444 (2014).
[84] C. Hoell and H. Löwen, J. Chem. Phys. **144**, 174901 (2016).
[85] H. H. Wensink, J. Dunkel, S. Heidenreich, K. Drescher, R. E. Goldstein, H. Löwen, and J. M. Yeomans, Proc. Natl. Acad. Sci. U.S.A. **109**, 14308 (2012).
[86] S. van Teeffelen and L. D. Renner, F1000Research **7**, 241 (2018).
[87] R. J. Allen and B. Waclaw, Rep. Prog. Phys. **82**, 016601 (2018).
[88] R. Wittmann, G. Nguyen, H. Löwen, A. Sengupta, and F. J. Schwarzendahl, arXiv preprint arXiv:2212.10101 (2022).
[89] D. Volfson, S. Cookson, J. Hasty, and L. S. Tsimring, Proc. Natl. Acad. Sci. U.S.A. **105**, 15346 (2008).
[90] H. Wioland, F. G. Woodhouse, J. Dunkel, J. O. Kessler, and R. E. Goldstein, Phys. Rev. Lett. **110**, 268102 (2013).
[91] D. Boyer, W. Mather, O. Mondragón-Palomino, S. Orozco-Fuentes, T. Danino, J. Hasty, and L. S. Tsimring, Phys. Biol. **8**, 026008 (2011).
[92] Z. You, D. J. G. Pearce, A. Sengupta, and L. Giomi, Phys. Rev. X **8**, 031065 (2018).
[93] B. Langeslay and G. Juarez, arXiv preprint arXiv:2212.00233 (2022).
[94] A. Kuijk, A. Van Blaaderen, and A. Imhof, J. Am. Chem. Soc. **133**, 2346 (2011).
[95] C. Vega and S. Lago, Comput. Chem. **18**, 55 (1994).
[96] H. C. Andersen, D. Chandler, and J. D. Weeks, J. Chem. Phys. **56**, 3812 (1972).
[97] R. Roth, K. Mecke, and M. Oettel, J. Chem. Phys. **136**, 081101 (2012).
[98] J. Xia, *Computational and Analytical Aspects of Energy Minimisation Problems in Cholesteric, Ferronematic and Smectic Liquid Crystals*, Ph.d thesis, University of Oxford (2021).
[99] P. E. Farrell, Á. Birkisson, and S. W. Funke, SIAM J. Sci. Comput. **37**, A2026 (2015).
[100] J. Xia and P. E. Farrell, accepted by ESAIM: Math. Model. Numer. Anal. arXiv:2110.06479 (2022).

P4 Network topology of interlocked chiral particles

Published as ArXiv-preprint and reproduced from

P. A. Monderkamp, R. S. Windisch, R. Wittmann and H. Löwen,
Network topology of interlocked chiral particles,
accepted for publication at J. Chem. Phys.,
arXiv:2301.09541 (2023),

Digital Object Identifier (DOI): `https://arxiv.org/abs/2301.09541`

Statement of contribution

All authors contributed equally to the conceptualisation of the project. R. Windisch and I developed the simulation code and the software for analysis.
I performed numerical simulations, designed the figures and wrote the original draft.
All authors contributed text associated with their respective expertise in paper and appendix and contributed to the finalisation of the manuscript.
Funding and overseeing was provided by H. Löwen. More details on all contributions can be found in the author declarations of the main body of the manuscript.

P4.1 Paper and appendix: Network topology of interlocked chiral particles

Network topology of interlocked chiral particles

Paul A. Monderkamp,[1,*] Rika S. Windisch,[1] René Wittmann,[1] and Hartmut Löwen[1]

[1] *Institut für Theoretische Physik II: Weiche Materie, Heinrich-Heine-Universität Düsseldorf, 40225 Düsseldorf, Germany*

Self-assembly of chiral particles with an L-shape is explored by Monte-Carlo computer simulations in two spatial dimensions. For sufficiently high packing densities in confinement, a carpet-like texture emerges due to the interlocking of L-shaped particles, resembling a distorted smectic liquid crystalline layer pattern. From the positions of either of the two axes of the particles, two different types of layers can be extracted, which form distinct but complementary entangled networks. These coarse-grained network structures are then analyzed from a topological point of view. We propose a global charge conservation law by using an analogy to uniaxial smectics and show that the individual network topology can be steered by both confinement and particle geometry. Our topological analysis provides a general classification framework for applications to other intertwined dual networks.

I. INTRODUCTION

The response of any liquid crystal to external constraints, such as confinement, intricately depends on the density but crucially also on the geometry of the particles. In fluids of uniaxial rod-like particles, for instance, the particles tend to align at intermediate densities, forming a so-called nematic phase. At the same time, the rods favor certain alignments with confining walls, such that the material becomes continuously deformed, to balance the competition between these two factors [1–4]. Upon increasing packing fraction, the liquid crystal tends to transition into a smectic phase, where the particles additionally stack into layers. Consequently, confinement typically leads to a fragmentation into several domains, separated by grain boundaries [5–8]. Advances in the synthesis of molecular and colloidal liquid crystals, enables the study of systems with increasing geometrical complexity of the particles. Non-convex particles such as polygonal rings, banana-shaped particles and *colloidal alphabet soups* allow for geometric interlocking, increasing the rigidity of the material [9–14]. In particular, particles with a characteristic chiral shape can exhibit interlocking at high densities providing an ideal playground for a wealth of interesting ordered structures [15–21].

In this work, we study the topology of smectic-like layers for interlocked chiral particles under the influence of confinement (see Fig. 1). To this end, with the aid of Monte-Carlo simulations, we generate systems of particles with the chiral shape of the letter L (see Fig. 2), which are confined to circular and annular cavities. We observe the emergence of highly complex structures through the interlocking of the chiral, non-convex particles (see Fig. 1.**(a)**). In particular, both particle axes display a tendency for layering, while the competition between these two rigidly connected building blocks prevents the formation of regular layered patterns found in ordinary smectics. Each layer associated with one axis of the L-shaped particles can be interpreted as a network such that the whole confined liquid crystal can be understood as an interwoven structure of two coexisting species of networks (see Fig. 1.**(b)**). We

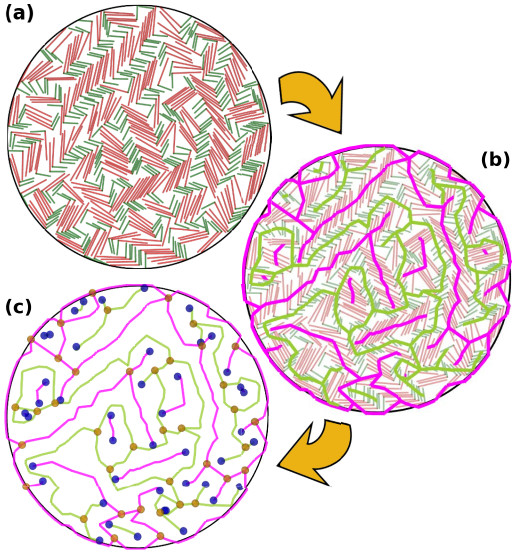

FIG. 1. Circularly confined L-particles on different levels of coarse-graining according to the yellow arrows. **(a)**: Simulation snapshot. The long axis of the L is colored in red, the short axis in green. **(b)**: The coarse-grained layer structures of both axes are visualized (long axis layers: magenta, short axis layers: green). **(c)**: Further coarse-grained structures with their vertices (dots). We assign the vertices a topological charge q, according to the number of adjacent edges (blue: $q > 0$, yellow $q < 0$). The number of these charges q serves the quantification of disorder in the confined systems.

* paul.monderkamp@hhu.de

analyze the topology of the systems by only considering these coarse-grained networks and assigning an index to the vertices, depending on the number of adjacent edges (see Fig. 1.(**c**)).

The algorithm for the extraction of these layers is designed to create an output analogous to the topological picture of conventional uniaxial smectics. There, topological charge conservation is guaranteed by explicitly considering smectic layers (density peaks) and so-called half-layers in between (density minima) as topological entities, that carry topological charge [22–25]. In that way, the indices of the vertices become topological, i.e., adhere to topological charge conservation in analogy to conventional electrodynamics, where the total charge, consisting of inside and boundary charge, adjusts to the topology of the confining container. In that way, the circle and the annulus yield different total topological charges, due to their different connectivity.

Moreover, we show that the structure of the individual networks can be largely steered by the particle shape. The vertical axis of the letter L is denoted as *leg*, while the horizontal axis is denoted as *foot*. In particular, the spatial distribution as well as the amount of inside topological charges depends delicately on the *foot* to *leg* ratio $p = L_\mathrm{f}/L_\mathrm{l}$ (see Fig. 2) of the L-shaped particle. Specifically, the total amount of charge within the interior depends non-monotonically on p.

Finally, We expect that our general topological treatment of the convoluted network structures is also of practical value as a classification framework for other systems, where intertwined dual network structures can be found, such as gyroid phases in celestial nuclear matter [26, 27], technical applications [28], blood vessels in living organisms or traffic networks [29, 30].

The paper is arranged as follows. In Sec. II A, we present our simulation protocol, while we elaborate on the graph-theoretical foundations of the network topology in Sec. II B. We present our results in Sec. III, before we conclude in Sec. IV.

II. METHODS

A. Simulations

We perform canonical Monte-Carlo simulations for particles that have the shape of the letter L (see Fig. 2). We confine the particles to two-dimensional spherical and annular cavities. The particles are modeled as a pair of rigidly connected almost hard discorectangles with equal diameters D, and core lengths L_f, L_l, expressed in units of D. Throughout this work, we vary $p = L_\mathrm{f}/L_\mathrm{l}$, while $L_\mathrm{f} + L_\mathrm{l} = 28D$ stays constant. The interactions of the L-shaped particles are conveniently specified through

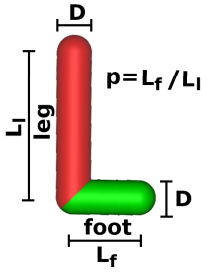

FIG. 2. Schematic of the particles with the shape of the letter L as considered in this work. The lengths of the two axes are referred to as L_f (foot of the letter L, green) and L_l (leg of the letter L, red), respectively. The ratio of the axes is denoted by $p = L_\mathrm{f}/L_\mathrm{l}$.

those of the individual rod-like building blocks.

For any two rods, i and j, not constituting to the same L-particle, with positions $\mathbf{r}_i$, $\mathbf{r}_j$ and orientations $\hat{\mathbf{u}}_i$ and $\hat{\mathbf{u}}_j$, the pair potential is defined as harmonic repulsion

$$U_{i,j}(\mathbf{r}_i, \mathbf{r}_j, \hat{\mathbf{u}}_i, \hat{\mathbf{u}}_j) = \begin{cases} U_0(\tau)(D - d_{ij})^2 & d_{ij} < D \\ 0 & d_{ij} \geq D, \end{cases} \quad (1)$$

$$d_{i,j} = \min_{|\alpha,\beta|<\frac{L}{2}} \|\mathbf{r}_i + \alpha\hat{\mathbf{u}}_i - (\mathbf{r}_j + \beta\hat{\mathbf{u}}_j)\|\,, \quad (2)$$

with $\alpha, \beta \in [-L/2, L/2]$, with L in $\{L_\mathrm{f}, L_\mathrm{l}\}$ defines the overlap [31] and $U_0(\tau)$ is the interaction coefficient, which is linearly increasing as a function of the simulation progress $\tau \in [0, 1]$, i.e., fraction of completed total of 10^6 MC-cycles. $U_0(\tau = 1)$ is chosen as $10^3 k_\mathrm{B}T$ to mimic almost hard repulsion in the equilibrated system.

We model the wall interaction by representing the rods as three virtual point-like particles sitting at the ends, and middle of the k-th rod $\mathbf{r}_\lambda = \mathbf{r}_k + \lambda\hat{\mathbf{u}}_k$, with $\lambda \in \{-L/2, 0, L/2\}$. The interaction potential

$$V(x) = \begin{cases} V_0\,(\tau)\; x^2 & \text{for } \mathbf{r}_\lambda \text{ outside,} \\ 0 & \text{for } \mathbf{r}_\lambda \text{ inside the cavity} \end{cases} \quad (3)$$

with the walls is once again harmonic, where x denotes the closest distance of $\mathbf{r}_\lambda$ to the inside of the respective cavity. Similarly to U_0, V_0 is linearly increased as a function of the completed Monte-Carlo cycles $\tau \in [0, 1]$ up to as $10^3 k_\mathrm{B}T$ to mimic hard walls. We simulate the systems at packing fractions $\eta_1 = N a_\mathrm{L}/a_\mathrm{cav} = 0.4$ and 0.6, with the area of a single L-shaped particle a_L and the area of the cavity a_cav. The radii of the confinements are typically in the range $4L \lesssim R \lesssim 50L$. Correspondingly, typical particle numbers N are between several hundreds and several thousands. In the annular confinement, we keep the width of the annular

ring constant ($\Delta R \approx 1.83 L_\mathrm{l}$), while we vary the inner radius (R_in) and outer radius ($R_\mathrm{in} + \Delta R$).

We follow a compression protocol, where we randomly initialize the system at a low volume fraction $\eta_0 = 0.1\eta_1$. Each MC-cycle consists of a trial displacement or rotation of each particle. The acceptance probability $P = \min(1, \exp(-\Delta U / k_\mathrm{B}T))$, for any trial move, is given by the Metropolis criterion from the difference ΔU of the energies (see Eqs. (1) and (3)) in the system before and after trial [32]. Over the course of the simulation, we gradually rescale the positions of the walls and particles to increase η according to

$$\eta(\tau) = \eta(\tau) = (\eta_1 - \eta_0)\tau^{\frac{1}{3}} + \eta_0 \tag{4}$$

until the volume fraction $\eta_1 = 0.4$ is reached. This type of decelerating compression aids the equilibration speed, since the system is quickly compressed in the dilute stage, while being allowed to undergo a larger fraction of MC-cycles in the regime, where self-assembly of the ordered structures is expected (for more details on the protocol, see Appendix A).

B. Network topological charge analysis

As illustrated in Fig. 2, we denote the vertical (red) axis by *leg* which we distinguish from the horizontal *foot* (green) axis by presuming a parallel wall alignment of the *leg* (see Appendix B for more details). As visible in Fig. 1, each ensemble of smectic-like layers associated with either *foot* or *leg* (perceived as individual rods) forms convoluted networks and correspondingly can be analyzed with the help of mathematical graph theory.

Each network consists of a set of vertices . Those vertices are connected via a set of edge lines [33, 34]. As known from the treatment of the topology of layers in conventional smectics [22–25], a charge conservation follows, if the species of networks alternate. In other words, between any two smectic layers has to be a density minimum, i.e., a half-layer. Accordingly, our graph generation is designed, such that empty loops are contracted into a single vertex (see Appendix B). Therefore, we only observe the occurrence of loops (see Fig. 1), that each envelop a simply connected graph (without loops) of the other species. This is schematically visualized in Fig. 3.**(a)**. More seldom, multiple loops of alternating species are nestled into each other, with a simply connected graph in the middle. To characterize this behavior in general, we assign a topological network charge to any vertex in the network as

$$q = 1 - \frac{\not{d}}{2} \tag{5}$$

with the degree $\not{d}$, i.e., the adjacent number of edges. Note, that this definition of the network charges is analogous to the layer topological charges, typically considered in smectic liquid crystals, where the edge lines represent smectic layers (see Appendix C). As such, the total charge of a network species reads as

$$Q_a = \sum_{\substack{\text{vertices} \\ \text{in } a}} q \tag{6}$$

with $a \in \{\mathrm{f}, \mathrm{l}\}$, standing for *foot* and *leg*. where $Q_\mathrm{f} + Q_\mathrm{l}$ is a conserved quantity.

The total charge of a network is only determined by its connectivity and not by the total number of vertices. As visible from Fig. 3.**(b)**, adding a dangling end to a previously existing network, is a charge neutral operation. Consequently, any simply connected network, carries the charge of a single isolated vertex $q = 1$. Only the addition of loops, i.e., adding an edge between two existing vertices, decreases the net charge by 1. This

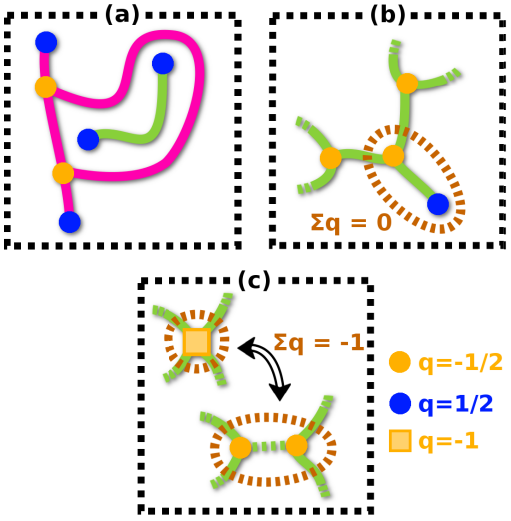

FIG. 3. Schematic of the network topological model (see Eq. (5)). **(a)**: Serving charge conservation, our algorithm is designed such that there can not be empty loops. As such, any loop contains a network of the respective other species. The total network topological charge in the system is conserved under this condition, since the charges of a loop and a simply connected network cancel. **(b)**: The total charge q, within any area of a single network, is calculated from the number of in-/outgoing edges through the boundary, inserted into Eq. (5). Dangling ends, such as within the dashed circle, are charge neutral. Vertices with two adjacent edges, carry no charge, and are therefore not explicitly labeled. Non charge-neutral operations are *(i)* adding loops ($\Delta q = -1$) or (ii) new networks ($\Delta q = +1$) adds to the total charge within the system. **(c)**: A vertex with four outgoing edges ($\not{d} = 4$, $q = -1$ see Eq. 5) can be understood as two infinitesimally close vertices with $\not{d} = 3$, $q = -1/2$, respectively.

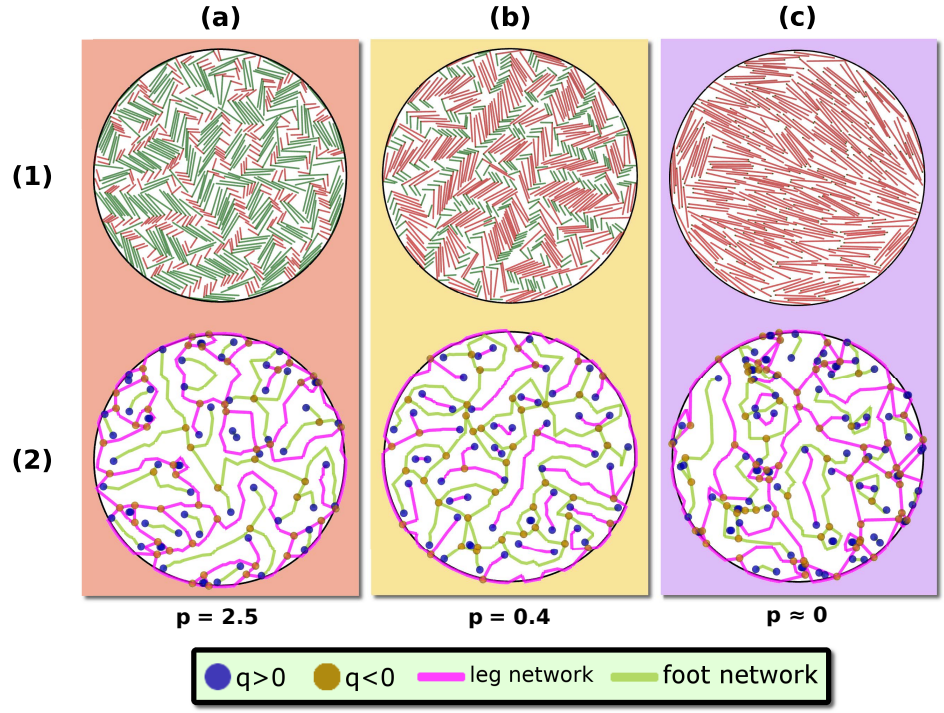

FIG. 4. Results of three independent simulation runs for L-shaped particles confined to spherical cavities with packing fraction $\eta = 0.4$ and **(a)**: $p = 0.4$, **(b)**: $p = 2.5$ and the hard-rod limit **(c)**: $p \approx 0$. The upper row **(1)** displays particle snapshots superimposed with the layer networks of both species (see sec. II B). The lower row **(2)** shows the isolated networks. The negative network charges are indicated in brown, while the positive are shown in blue. In all cases, the boundary charges are assigned to the magenta *leg*-network. Therefore the inside charge of the *foot*-species, matches the respective total charge ($Q_{\mathrm{f}}^{(\mathrm{in})} = Q_{\mathrm{f}}$), which is not true for the *leg*-species ($Q_{\mathrm{l}}^{(\mathrm{in})} \neq Q_{\mathrm{l}}$). Accordingly (a) and (b) correspond to a color swap, only in the inside of the cavity. The total network charge in the system $Q_{\mathrm{f}} + Q_{\mathrm{l}}$ matches the Euler characteristic of the confinement $\chi = 1$.

network topological charge can only be conserved, if every loop coincides with a simply connected (loop-less) network, e.g., at its center.

This definition of the charge is consistent, such that the charge within any area, can be calculated from the number of in-/outgoing edges, similar to Gauss's law in classical electrodynamics (see Fig. 3.**(c)**). Any vertex of higher degree can be viewed as a composition of merged $q = -1/2$ charges. Vertices with $\not{d} = 2$ carry no charge, and can be therefore, together with the edges, viewed as constituting the layers, in between the rest of the charges. Respecting these properties of the network charge, our algorithm which generates the final networks (see Appendix B) is designed to systematically eliminate vertices, such that the final network structure, as shown in Fig. 1.**(c)**, both illustrates the network connectivity and allows us to properly determine the total charges Q_{f} and Q_{l}.

Typically, considering the conservation of topological charges in confined geometries, e.g., orientational topological defects in nematically ordered fluids [7, 35], requires the identification of boundary defects on the system walls if no global alignment condition is obeyed. Due to the invariance of the total charge within the cavity $Q = Q_{\mathrm{f}} + Q_{\mathrm{l}}$ (determined by the topology of the confining domain), we have the liberty to assign the outer walls of the confinement to any of the two network species. In the following, without loss of generality, we choose to assign the boundary defects to the layer network of the *leg*, generating the boundary charge $Q_{\mathrm{l}}^{(\mathrm{b})}$. We will denote the inside network charges, i.e., charges without explicit inclusion of boundary charge, as $Q_{\mathrm{f}}^{(\mathrm{in})}$ and $Q_{\mathrm{l}}^{(\mathrm{in})}$. As de-

tailed in Sec. III, the total sum

$$Q_{\mathrm{f}}^{(\mathrm{in})} + Q_{\mathrm{l}}^{(\mathrm{in})} = Q - Q_{\mathrm{l}}^{(\mathrm{b})} \tag{7}$$

is not conserved. Still, these quantities contain structural information about the confined state. Through our choice of assigning the boundary charges to the *leg*-network, clearly $Q_{\mathrm{f}}^{(\mathrm{in})} = Q_{\mathrm{f}}$ but $Q_{\mathrm{l}}^{(\mathrm{in})} \neq Q_{\mathrm{l}} = Q_{\mathrm{l}}^{(\mathrm{in})} + Q_{\mathrm{l}}^{(\mathrm{b})}$.

III. RESULTS

A. Circular confinement

For circular cavities, we show simulation results for systems of L-shaped particles, with three different ratios of axes lengths p in Fig. 4. at packing fraction $\eta = 0.4$. In Fig. 4.**(a1)** a typical snapshot, for $p = 2.5$, is depicted. The particles locally interlock, while the longer *foot*-axes display a strong tendency for alignment, leading to elongated clusters. Global orientational ordering, however, is not visible, such as would be expected from, e.g., a conventional smectic liquid crystal. Through the interlocking, the shorter *leg*-axes fill the spaces in between. Below, in Fig. 4.**(a2)**, we show the corresponding graph network, resulting from our analysis of the layers. The elongated *foot*-clusters are represented in Fig. 4.**(a2)** by the green network. The *leg*-network is depicted in magenta. The relative higher stiffness of the wider *foot*-layers results in a favoring of longer simply-connected networks, each contained in a loop of a single large magenta *leg*-network. This results in the presence of majorly negative defects (indicated in brown), due to the loops. Conversely, every separated component of the *foot*-network contains a charge $\sum q = 1$. As elaborated in Sec. II B, this results in a total network charge within the system of $Q = 1$. Similarly, Fig. 4.**(b)** shows a simulation snapshot for the inverse length ratio $p = 0.4$. Accordingly, the behavior of the networks within the interior of the confinement, visible in Fig. 4.**(b2)** is analogous to the former case with inverted species. The assignment of the boundary charges remains with the *leg*-network, as in Fig. 4.**(a)**. As the total charge is invariant of our choice of this alignment condition, the inclusion of the boundary charges still retains total network charge within the confined system as $Q = 1$. Finally, Fig. 4.**(c)** shows a simulation snapshot, where $p \approx 0$, i.e., hard rods. The confined system resides in a state, where global orientational ordering is present. Through the lack of interlocking, no strong indications of layers are visible, as expected from the unconfined nematic bulk phase which is stable at the chosen packing fraction $\eta = 0.4$ [36, 37]. Nevertheless, the network analysis can still be used to quantify the global topology. Naturally, the total charge is still conserved as $Q = 1$.

In Fig. 5.**(a)** we show the inside charges $Q_{\mathrm{f}}^{(\mathrm{in})}$ and

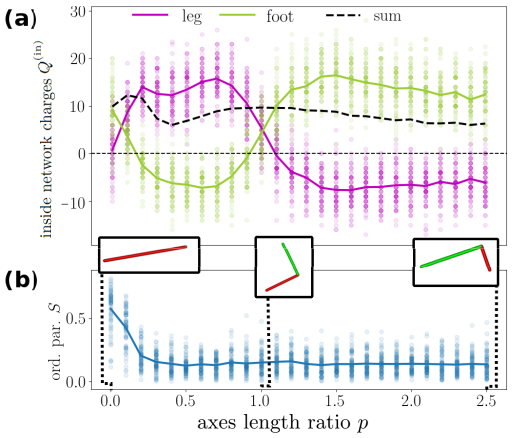

FIG. 5. Simulation results of liquid crystals composed of L-shaped particles for a range of different length ratios p of both particle axes, illustrating a topological transition in the networks at $p = 1$, where the chirality of the particles flips. **(a)**: Inside charges $Q_{\mathrm{f}}^{(\mathrm{in})}$ (green), $Q_{\mathrm{l}}^{(\mathrm{in})}$ (magenta) and sum $Q_{\mathrm{f}}^{(\mathrm{in})} + Q_{\mathrm{l}}^{(\mathrm{in})}$ (dashed black) **(b)**: Global orientational order parameter S. We observe, that at each point of the horizontal axes, the respective longer axis network has a positive charge, and the shorter axis network a negative charge. Above approximately 0.2, the systems reside in interlocked layered states without global orientational order. Below 0.2, the systems converge against conventional nematic order. The results are shown at packing fraction $\eta = 0.4$ .The lines correspond to averages over 75 simulations per p.

$Q_{\mathrm{l}}^{(\mathrm{in})}$ of both network species as well as their sum, i.e., the total charge without the inclusion of boundary charges, as a function of p. Additionally, along the same horizontal axis, in Fig. 5.**(b)**, we show the global orientational order parameter $S = |\langle \exp(i2\phi) \rangle|$, where $\langle ... \rangle$ denotes an average over all particles. The data shown in both figures can be roughly divided into three characteristic regions along the horizontal axis, namely $p > 1$ (cf. Fig. 4.**(a)**), $0.2 \lesssim p < 1$ (cf. Fig. 4.**(b)**, as well as $p \lesssim 0.2$ (cf. Fig. 4.**(c)**). In the case $p > 1$, the simply-connected, but isolated *foot*-layers (green) result in positive inside charge. At the same time, the single large *leg*-network with loops results in negative charges (magenta). Analogously, the same holds true in the regime $0.2 \lesssim p < 1$, only with inverted network species. Therefore, the signs of $Q_{\mathrm{f}}^{(\mathrm{in})}$ and $Q_{\mathrm{l}}^{(\mathrm{in})}$ are flipped. For $p \lesssim 0.2$, the shapes of the particles are approaching the hard-rod limit. The absence of an entropic contribution from the interlocking mechanism of the L-shaped particles, allows the liquid crystal to undergo a transition into a nematic state with global orientational ordering. Correspondingly, Fig. 5.**(b)** shows

an increased orientational order parameter S. In the transition regime, complicated packing effects dominate the system, causing non-trivial behavior in $Q_{\mathrm{f}}^{(\mathrm{in})}$ and $Q_{\mathrm{l}}^{(\mathrm{in})}$. We observe that the first peak in $Q_{\mathrm{l}}^{(\mathrm{in})}$ decreases for larger systems, where the interior of the confinement is less influenced by the system boundaries (not shown). We therefore infer, that the behavior in Fig. 5 stems from the extreme influence exerted by the confinement. Due to the symmetry of the particles, all the observables are symmetric around 1, i.e., $S(p) = S(1/p)$, as well as $Q_{\mathrm{l}}^{(\mathrm{in})}(p) = Q_{\mathrm{f}}^{(\mathrm{in})}(1/p)$ (see Appendix D). Naturally, the total charges Q_{f} and Q_{l} do not adhere to this symmetry, which is broken by the assignment of the boundary charges to the *leg*-network.

In general, the total inside charge $Q_{\mathrm{f}}^{(\mathrm{in})} + Q_{\mathrm{l}}^{(\mathrm{in})}$ within the cavity, i.e., the sum of all network charges in Fig. 5 is constantly greater than zero. This is consistent with our observation, of the presence of isolated networks within the inside, without the existence of empty loops. Moreover, including the boundary to the *leg*-network does by construction only add negative defects, i.e., $Q_{\mathrm{l}}^{(\mathrm{b})} < 0$, compare, e.g., Fig. 4.**(2)**. Taking a closer look at the behavior of $Q_{\mathrm{f}}^{(\mathrm{in})} + Q_{\mathrm{l}}^{(\mathrm{in})}$ in Fig. 5.**(a)**, we notice two local maxima. The first one at $p \approx 0.1$ coincides with the onset of global orientational order, i.e., close to the transition between confined nematic and interlocked layer states. The second one is located around $p = 1$, i.e., where neither network dominates the structure, such that the mutual interruption of the layering of the two building blocks is most pronounced. We thus conclude that the total inside charge $Q_{\mathrm{f}}^{(\mathrm{in})} + Q_{\mathrm{l}}^{(\mathrm{in})}$ provides a useful measure for disorder in interlocked or frustrated systems.

B. Annular confinement

One of the important characteristics of a topological conservation law within a confined liquid crystal system is the relevance of the topology of the confining container [38, 39]. To further explore this, we introduce a confining domain with annular shape, that possesses Euler characteristic $\chi = 0$. In Fig. 6.**(a)**, a corresponding particle snapshot is shown ($R_{\mathrm{in}} = 4L_{\mathrm{l}}$, $\Delta R \approx 1.83L_{\mathrm{l}}$, $\eta = 0.6$, $p = 0.1$). Through the high packing fraction and the relatively long *leg*-axes (red), the particles show a visible tendency to reside in locally parallel layers, where the long axes of the particles are parallel align with the outer walls. At the same time, the protruding *foot*-axes (green) cause a relative shift of neighboring particles, resulting in a characteristic smectic-C-like shape, where the particles are tilted with respect to the layers. The associated network structure is visible in Fig. 6.**(b)**. As in the previous section, the boundary charges are assigned to the *leg*-network. Each smectic block of particles results in an isolated simply connected *foot*-network, wrapped into a loop of the large *leg*-network. The inner confinement walls cause an additional empty loop. As a result, all charges sum up to the Euler characteristic of an annulus $\chi = Q = 0$.

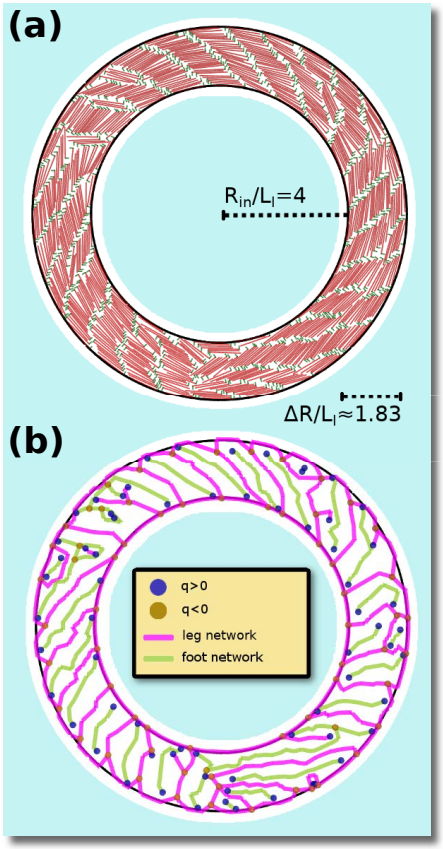

FIG. 6. Simulation results for a system of L-shaped particles in annular confinement. **(a)**: The system resides in a smectic-C-like state, where due to the interlocking, the layer director is at an angle to the local orientation. **(b)**: The network structure roughly shows one *foot*-network per smectic layer. The boundary charges are assigned to the *leg*-network, therefore the network charge is conserved. Through the empty loop on the inner wall, the total network charge matches the Euler characteristic $\chi = 0$ of the confinement. Packing fraction and axes length ratio are $\eta = 0.6$ and $p = 0.1$.

The previous results are for systems with relatively small particle numbers $N = 320$. We make this particular choice to illustrate the network charges on the particle-resolved level. Naturally, all of the above holds true also for larger systems. In Fig. 7, we present

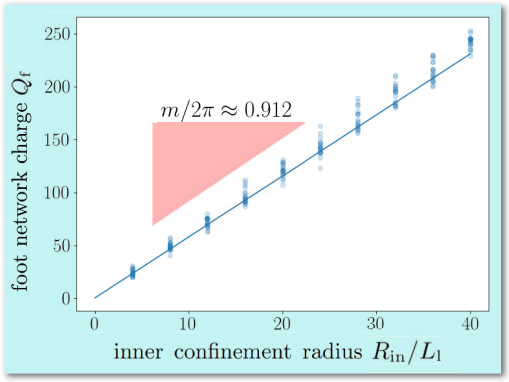

FIG. 7. Network topological charge of the *foot*-species $Q_\mathrm{f} = -Q_\mathrm{l}$ within annular confinement as a function of the inner radius R_in. Packing fraction and particle dimensions match Fig. 6. We show results of 20 simulations per considered R_in and a linear fit. The slope of the line m divided by 2π is approximately one, confirming that there is slightly less than one charge per particle length around the perimeter. This represents, as expected, one smectic-like layer per particle length (cf. Fig. 6).

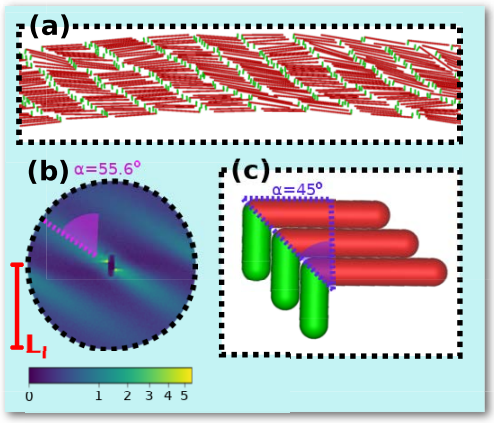

FIG. 8. Simulation results in annuli with large inner radii $R_\mathrm{in} = 40L_\mathrm{l}$. The other simulation parameters match Fig. 6. **(a)**: Excerpt from a simulation snapshot. The tilt angle of the layers with respect to the walls of the annular ring is clearly visible. **(b)**: Annular pair distribution function $g_\circ(\mathbf{r})$ between the positions of the *foot*-particles (green) in the xy-plane up to a radial distance of L_l (cf. Eq. (8)). The slanted peaks represent the slanted *foot*-layers in (a). The angle relative to the horizontal is equal to $\approx 34.4°$. **(c)**: schematic of L-particles in close packing. For $D_\mathrm{foot} = D_\mathrm{leg} = D$, the optimal tilt angles of the layers is equal to 45° (vertical and horizontal sides of the right triangle in the figure have to be equal). The deviation in the measured angle in (b) possibly stems from complex entropic interactions of the layer species at lower packing fraction.

the total topological charge $Q_\mathrm{f} = Q_\mathrm{f}^{(\mathrm{in})} = -Q_\mathrm{l}$ of the *foot*-species as a function of the inner radius R_in of the annular confinement, while keeping the width of the annulus $\Delta R = 1.83L_\mathrm{l}$ constant. Since the boundary charges are assigned to the *leg*-network, the total charge Q_f coincides with the inside charge $Q_\mathrm{f}^{(\mathrm{in})}$. Each depicted point represents an individual simulation. As visible in the plot, the data points lie fairly accurately on a straight line, indicated by a linear fit with slope $m = 0.912 \times 2\pi$. More specifically, there is slightly less than one positive charge per particle length along the inner circumference of the annulus. This is consistent with the observations made in Fig. 6, where each particle layer forms a new network. Since any particle layer has a width, which is slightly larger than L_l, $m/(2\pi)$ is slightly smaller than one.

To further investigate the origin of the smectic-C-like tilted layers for these L-shaped particles, additional results are presented in Fig. 8. In conventional hard-rod smectics, confined to annular cavities, the layers typically align with the outer walls, while the direction of the layer is typically in radial direction of the confinement, i.e., orthogonal to the walls [2, 5]. Here, we observe layers which are tilted with respect to the radial direction. This is nicely visible in Fig. 6 and Fig. 8.**(a)**. The latter shows an excerpt from a simulation in an annulus with inner radius $R_\mathrm{in} = 40L_\mathrm{l}$. We see similar tilt angles in both snapshots, irrespective of the large difference in curvature of the respective confinement walls. In order to show the local structure within the annular ring, we introduce the two-dimensional annular pair distribution function

$$g_\circ(\mathbf{r}) = \frac{1}{N\rho}\left\langle \sum_{\substack{i,j=1 \\ i\neq j}}^{N} \delta(\mathbf{r} - \overline{\overline{\mathbf{R}}}\cdot(\mathbf{r}_i - \mathbf{r}_j)) \right\rangle . \qquad (8)$$

This is obtained via the matrix

$$\overline{\overline{\mathbf{R}}} = \overline{\overline{\mathbf{R}}}(\phi_i) = \begin{pmatrix} \cos(\pi/2-\phi_i) & -\sin(\pi/2-\phi_i) \\ \sin(\pi/2-\phi_i) & \cos(\pi/2-\phi_i) \end{pmatrix}, \qquad (9)$$

where ϕ_i is the polar angle of the position $\mathbf{r}_i$ of the i-th particle with respect to the annulus center. Here, N and ρ are the global particle numbers and densities, respectively, and $\delta(\mathbf{r})$ denotes the delta-distribution. The physical interpretation of $g_\circ(\mathbf{r})$ is a distribution function of rotated relative vectors. The data to obtain $g_\circ(\mathbf{r})$ are sampled from 20 independent simulation runs. We compute $g_\circ(\mathbf{r})$ for the positions of the green *foot*-particles, as depicted in Fig. 8.**(b)**. In the depiction, the horizontal axis denotes the tangential direction of the annular

walls. The center of the diagram shows an anisotropic depletion zone around the particles, resulting from the almost hard repulsion. Furthermore, slanted density peaks are visible, representing the tilted layers within the annular ring. These peaks form an approximate angle of $\alpha = 55.6°$ with the radial direction. In Fig. 8.**(c)**, it is illustrated that for identical width of the particle axes ($D_{\text{foot}} = D_{\text{leg}} = D$), an angle of $\alpha = 45°$ leads to efficient packing at extreme packing fractions. At lower packing fractions, however, this would lead to a drastic decrease of the free length out of the layer, parallel to the longer *leg*-particles. More specifically, the measured angle can be understood as a result of two competing entropic factors: *(i)* the aforementioned free length along the *leg* orientation, which tends to increase the tilt angle relative to the radial direction, and *(ii)* the systems tendency to reside in a smectic-like layered structure perpendicular to the *leg* orientation, due to the high density, which tends to decrease the tilt angle (as presumably, the layered structure breaks apart for $\alpha \to \pi/2$).

IV. CONCLUSION

In this work, we present a formalism for the analysis of the topology of liquid crystals with chiral particle shapes, which give rise to irregular defect structures in confinement. This approach is based on the consideration of the entangled network structure formed by the respective axes positions. In order to analyze the structures with two layer species, we generate networks utilizing Delaunay triangulations and identify topological charges, from the degrees (number of adjacent edges) of the network vertices. This procedure leans on the concept of layers and half-layers that characterize the topology in conventional smectics [22, 23], as, e.g., formed by uniaxial hard rods. Like these previous applications, our study relies on coexisting but disjoint network species, which as a whole adhere to a common topological conservation law, where the sum of the respective topological charges in a confined system equals the Euler characteristic χ of the finite container. However, there are two crucial differences. *(i)* In our study, both network species explicitly refer to an axis of the particles. In contrast, in conventional smectics, one layer species represents the density minima in between the particle layers. *(ii)* Our approach is based on the analysis of the layer network structure on the particle-resolved level, while the observation of conventional smectic point defects (see Appendix C) typically happens on much larger length scales and was hitherto majorly employed in approaches that describe the coarse-grained smectic layer structure [22–25, 40, 41]. Moreover, we exemplify that the bare inside charges serve as a useful quantifier of disorder.

We use this framework of network topology to analyze the structure of liquid crystals composed of particles with the shape of the letter L, confined to circular ($\chi = 1$) and annular ($\chi = 0$) cavities. These are generated via the use of canonical Monte-Carlo simulation. We find that the global inside charges of the two network species intricately depend on both the local particle symmetries and the global degree of order. We observe a variety of remarkable states at different packing fractions and L-axes lengths: at intermediate densities, the particles prefer interlocking with suppression of global orientational order, when both axes of the L-shape have comparable sizes. Otherwise the system tends towards a conventional nematic state [1, 36, 42]. At high packing fractions in the annulus, the particles arrange in more rigid layers, which resembles a smectic-*C* structure. In regards to the latter, we present additional simulation for annuli with large radii elucidating the origin of the tilt angle of the layers.

Based on this insight, we expect that the formalism used throughout this work can positively contribute to a variety of future endeavors. In particular we expect, that it will be useful in the interpretation of future computational, theoretical and experimental studies of systems with complicated particle shapes [43–51]. Even though we introduce this method as a tool for the investigation of relatively complex chiral particles, we also suspect that it will be insightful to apply it to hard-rod fluids, since the network analysis can be readily applied to visualize the half-layers in conventional smectics. We expect it to provide also insight, applied in the analysis of gyroid phases in systems of particles without chirality [52, 53]. This will possibly be a powerful tool in understanding the emergent topological structures [54–56]. Recent years have also seen an increased interest in non-equilibrium systems, where the individual particles consume energy from their surrounding to propel themselves [57–60]. It has been shown, that in these systems, the orientational defects have dynamical properties, which in turn depend on the respective topological charges [61–63]. It seems therefore very reasonable to assume, that network topological charges will carry interesting dynamical properties in collectively moving L-shaped or other chiral swimmers [64–67].

ACKNOWLEDGEMENTS

The authors would like to thank Michael te Vrugt and Raphael Wittkowski for stimulating discussions. This work is funded by the Deutsche Forschungsgemeinschaft (DFG, German Research Foundation) – LO 418/20-2.

AUTHOR DECLARATIONS

Conflict of Interest

The authors have no conflicts to disclose.

Author contributions

Paul A. Monderkamp: Conceptualization (equal); Data Curation (lead); Formal Analysis (lead); Methodology (equal); Project Administration (equal); Software (equal); Supervision (equal); Validation (lead); Visualization (lead); Writing/Original Draft Preparation (lead); Writing/Review & Editing (equal); **Rika S. Windisch**: Conceptualization (equal); Data Curation (supporting); Formal Analysis (supporting); Methodology (equal); Project Administration (supporting); Software (equal); **René Wittmann**: Conceptualization (equal); Formal Analysis (supporting); Funding Acquisition (supporting); Methodology (equal); Project Administration (equal); Supervision (equal); Writing/Review & Editing (equal); **Hartmut Löwen**: Conceptualization (equal); Funding Acquisition (lead); Methodology (equal); Project Administration (equal); Resources (lead); Supervision (equal); Writing/Review & Editing (equal);

Data availability

The data that support the findings of this study are available from the corresponding author upon reasonable request.

Appendix A: Details on the equilibration protocol

In the main manuscript, the simulation results are generated with the help of a canonical Monte-Carlo simulation, as described in Sec. II A. The fundamental goal of the procedure is to find a configuration at a relatively high packing fraction which reflects the equilibrium state. Since it is practically impossible to obtain a randomized configuration at the target packing fraction (since guessing a configuration which fits into the cavity corresponds to guessing the final simulation result), the systems are initialized several orders of magnitude below the target packing fraction. They are subsequently compressed with a decelerating compression rate (cf. Eq. (4)). Additionally, the interaction constant U_0 (cf. Eq. (1)) between the particles and the wall interaction constant V_0 (cf. Eq. (3)) are linearly increased as a function of the fraction of completed Monte-Carlo cycles $\tau \in [0, 1]$. The initial softness of the interactions helps the particles heal-out overlaps, which may occur in the beginning of the simulation due to random initialization. At the end of the simulation, U_0 and V_0 are $10^3 k_\mathrm{B}T$. We find that the τ-dependence of these constants becomes less relevant, as the simulation progresses, since the particles effectively feature hard repulsion at a certain point. This positively contributes to the equilibration.

To obtain configurations, which reflect the equilibrium configuration, without explicitly evaluating free energies, the equilibration is performed slowly enough, such that two assumptions can be made about the transient configurations over the course of the simulation. *(i)*: The system is ergodic (samples the whole configuration space), in the stage of self-assembly, such that the system configuration space at higher densities is also sampled fairly over independent different simulation runs. *(ii)*: The compression of the system and increase of the interaction strengths occurs slowly enough, that the system can equilibrate faster than the parameters change, such that the final configuration reflects a state close to equilibrium.

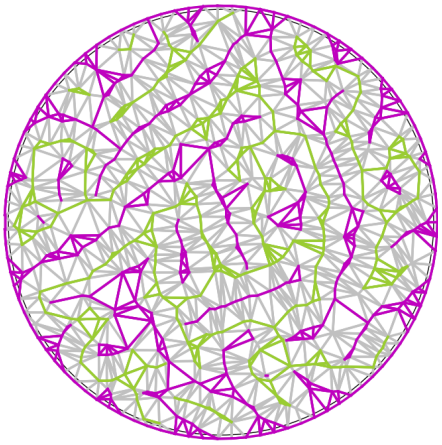

FIG. 9. Delaunay triangulation of the union of all coordinate positions of both axes of all L-shaped particles, used as a base point for the generation of the graphs networks, considered in this manuscript. The corresponding particle snapshot is shown in Fig. 1. The edges, connecting the *foot*-positions are colored in green, while the edges, connecting the *leg*-axes are colored magenta. Grey edges connect *foot*- and *leg*-vertices. In order to obtain lines, representing the layer structure of the respective axes, the gray edges are deleted, and the remaining colored networks are transformed into simple lines.

Below, we show additional simulation results, which aim to support both assumptions. The simulations are performed as described in Sec. II A with axis length ratio $p = 1$ and fraction $\eta_1 = 0.4$ inserted into the formula for compression (Eq. (4)). But instead of equilibrating up to $\eta_1 = 0.4$, the compression and increase of the interaction constants are stopped at the half-point of the simulation $\tau = 1/2$. This value coincides with $\eta \approx 0.32$ (cf. Eq. (4)) Subsequently, the simulation runs at constant parameters for the second half to illustrate the change of the system without compression at intermediate densities.

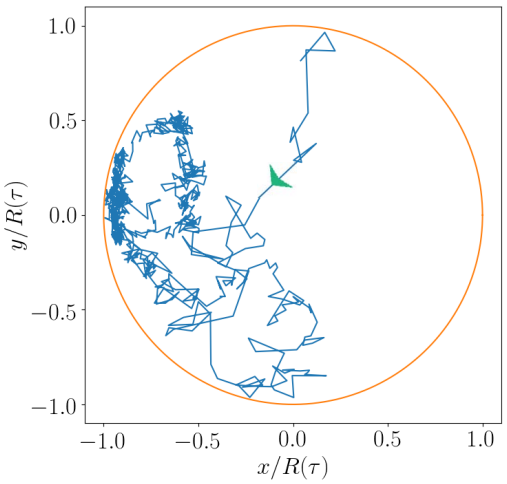

FIG. 10. Trajectory of a single particle within a Monte-Carlo simulation, where the compression and change of interaction constants is stopped at half the number of total Monte-Carlo cycles $\tau = 1/2$. The simulation starts as described in Sec. II A, but runs with constant parameters after $\tau = 1/2$. The displayed particle positions are rescaled with the radius of the confinement, i.e. the depicted trajectory shows $\mathbf{r}(\tau)/R(\tau)$. The green arrow denotes the direction of motion within the trajectory. Note that the trajectory reflects Monte-Carlo displacement (contrary to a standard equation of motion). The relatively unconstrained motion suggests, that the system is in principle able to occupy all configurations. The particle also samples the whole orientation space (not shown).

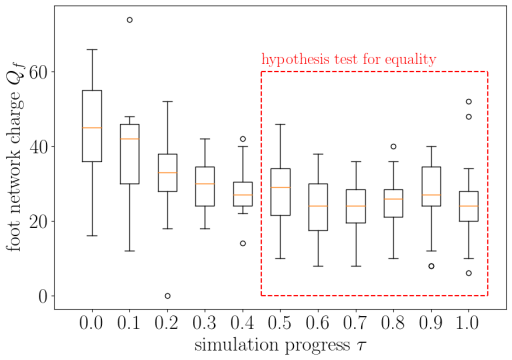

FIG. 11. Total network charge of the *foot*-network as a function of simulation progress τ, i.e., the fraction of completed Monte-Carlo cycles. The compression and adjustment of interaction constants is stopped at the half-way point, after which the simulation runs at constant parameters. We pick six instances of simulation progress at which we average Q_f. Those averages are denoted $\overline{Q}_f$ (see red box). We perform a hypothesis test for equality of all six $\overline{Q}_f$, via a one-way F-test. We find an F-value of approximately 0.70 and a p-value of approximately 0.62. We view this as indication, that the system at $\tau = 1/2$ already reflects an equilibrium configuration well.

1. Ergodicity

Here, we support the assumption, that the simulation protocol samples the configuration space ergodically at intermediate densities. This is to guarantee that the configuration space at higher densities is sampled fairly across many simulations. To this end, we show the trajectory of the *leg*-axis of a single particle over the course of the simulation in Fig. 10. The displayed positions are rescaled with radius of the confinement $R(\tau)$ ($R(\tau)^2 \propto 1/\eta(\tau)^{1/2}$, cf. Eq. (4)). As such, the figure shows $\mathbf{r}(\tau)/R(\tau)$. The fact that the particle moves throughout the whole cavity strongly suggests, that the entire configuration space is sampled fairly, since the particles can freely rearrange at intermediate densities, and therefore the system is not hindered from occupying specific configurations. Note that not every single particle has to be able to traverse the whole cavity, since they can be considered physically indistinguishable in terms of the states. We consider this numerical indication, that the system arrests into a high-density state, which is close to the equilibrium and independent of the initialization.

2. Slow compression

In a simulation protocol, such as described in Sec. II A, one needs to guarantee, that the final configuration reflects/is close to a true equilibrium configuration. In practice, this corresponds to the execution of the protocol slowly enough, such that the system does not get quenched into an unfavorable kinetically arrested state. In particular, we execute the protocol slowly enough, that all configurations throughout the simulation (beyond the initial fast compression given by Eq. (4)) reflect a state close to equilibrium for any instance of parameters across the simulation.

To reinforce this claim, we show simulation results in this section, where we stop the compression and increase of the interaction constants, U_0 and V_0, after half the number of Monte-Carlo cycles is completed ($\tau = 1/2$). More specifically, we start the simulation with the same equilibration protocol as described in Sec. II A. We abruptly terminate the change of parameters at $\tau = 1/2$. We continue the Monte-Carlo simulation at constant parameters and show that the *foot*-network charge Q_f does not significantly change afterwards. We do this, to illustrate, that the system is close to equilibrium throughout the simulation. In Fig. 11, we show distributions of Q_f over 20 independent simulations as a function of simulation progress τ (completed number of Monte-Carlo cycles). We denote the average value of Q_f for a constant τ by $\overline{Q}_f$. We test whether the $\overline{Q}_f$ vary significantly af-

ter stopping the compression at $\tau = 1/2$. To this end, we set up a hypothesis test for the equality of all values with $\tau \geq 1/2$ [68] (the conditions for the hypothesis test: equal variance, approximate normality, independence, were checked). The null hypothesis is given by H_0: "All measured $\overline{\mathcal{Q}}_f(\tau \geq 1/2)$ do not differ significantly" i.e., the true average Q_f from all possible configurations, which can theoretically be obtained in simulation, is constant. The alternate hypothesis is H_α: "At least one pair is not equal.". If the alternate hypothesis is true, we have to assume that the $\overline{\mathcal{Q}}_f(\tau \geq 1/2)$ vary significantly, and so the simulation has not reached near-equilibrium. Through a one-way F-test [69], we find $F \approx 0.70$ and a p-value of 0.62. The value F denotes the variance between $\overline{\mathcal{Q}}_f$ for different τ divided by the variance for a constant τ. The p-value indicates that a distribution of $\overline{\mathcal{Q}}_f$ with such a variance, or more, is expected to occur with probability $p = 0.62$. We conclude, that given this data, the null hypothesis H_0 can not be rejected with any reasonable significance level. We furthermore infer that, in combination with the absence of a clear up- or downwards trend after $\tau = 1/2$, we have reason to believe, that the observables do not change after stopping compression. This can be considered indication, that at $\tau = 1/2$, the system resides in a state which reflects equilibrium well.

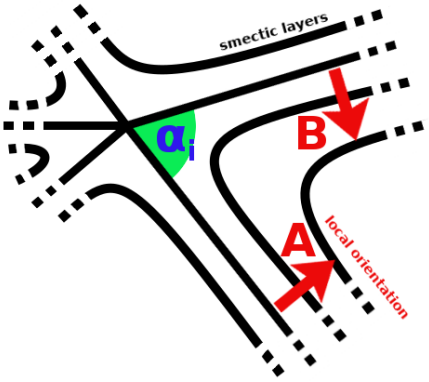

FIG. 12. Schematic of an orientational topological defect in a smectic liquid crystal. The defect is a point, where the local orientation $\hat{\mathbf{n}}(\mathbf{r})$, typically orthogonal to the smectic layers, indicated as black lines, is ill-defined. The rotation $\Delta\phi_i$ from **A** to **B** is equal to $\alpha_i - \pi$. Therefore the total rotation Φ is equal to $\sum_i^n \Delta\phi_i = 2\pi(1 - n/2)$, with the number of outgoing layers n. The topological charge is equal to $\Phi/2\pi = 1 - n/2$, in analogy to Eq. (5).

Appendix B: Network generation

The networks, considered in this work, are generated by considering the Delaunay triangulation [70] of the union of the geometrical centers of both axes of the L-shaped particles (see Fig. 9, corresponding to the particle snapshot in Fig. 1.**(a)**). The emerging network is disconnected into the two network species, by deleting edges between opposing foot and leg vertices (Fig. 9, gray). Furthermore, to obtain a physical picture of these two intertwined networks as a pair of smectic-like layers with a topological charge conservation, we require two further systematic modifications. Firstly, we assign the boundary to the *leg*-network. This corresponds to assuming that the *leg* of the particles align preferably parallel with the wall, while other local configurations are interpreted as a defect. Such a presumed uniform alignment rule stands at the basis of any topological conservation law in confinement. Secondly, to ensure that the final networks represent global layer structures, we transform the triangular meshes into simple lines through merging vertices that form empty triangles (without changing the hierarchy between the two networks). Thereby we delete any empty loops which are not compatible with the concept of alternating layers required for topological charge conservation. This is in accordance with the layer and half-layer picture of conventional smectics and can be readily applied to uniaxial rods by considering the limit $L_l = 0$. The final network, after applying this protocol to Fig. 9, is shown in Fig. 1.**(c)**.

Appendix C: Analogy to topological charges in smectics

The network topological charges, introduced in Sec. II B share a close relation with the orientational topological charges, typically considered in smectic liquid crystals [71–73]. In this manuscript, we assign a network topological charge $q = 1 - d/2$ to any vertex in the observed network via its degree d (see Eq. (5)). Similarly, topological charges of defects in smectic systems can be understood in terms of adjacent layers [22, 23].

Orientational topological defects in liquid crystals, that display local alignment of the molecules, can be understood as singular locations in space, where the local orientation $\hat{\mathbf{n}}(\mathbf{r})$ undergoes a discontinuous jump and is therefore ill-defined. In smectic systems, where the particles additionally arrange in layers, this can happen across grain boundaries in two and three dimensions, or across points in two dimensions. A schematic of a two-dimensional point defect is depicted in Fig. 12. Smectic layers are represented by black lines. In this particular example, five layers meet in a singular point. Around this point, the layers, and thus $\hat{\mathbf{n}}(\mathbf{r})$, typically at a constant angle to the layers, are continuously bent. The

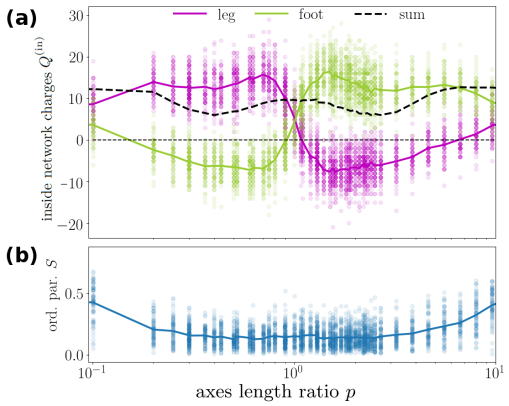

FIG. 13. Simulation results of liquid crystals composed of L-shaped particles for a range of different length ratios p of both particle axes as Fig. 5 in the main text. Through the logarithmic scaling of the horizontal axis, the symmetry around $p = 1$ becomes apparent.

strength of the defect is characterized by the total rotation of $\hat{\mathbf{n}}(\mathbf{r})$ traversing the defect in counterclockwise direction. Consider one wedge of the rotation $\mathbf{A} \to \mathbf{B}$ between two layers at an angle α_i: The rotation angle is equal to $\Delta\phi_i = \alpha_i - \pi$. Consequently, the total rotation around the defect is equal to

$$\Phi = \sum_i^n \Delta\phi_i = 2\pi(1 - n/2), \tag{C1}$$

with the number of outgoing layers n. The topological charge of the defect is defined by $\Phi/2\pi$ resulting in Eq. (5), with the vertex degree $\not{d}$ identified with n.

Appendix D: Larger axes length ratios

We denote the conventionally short (length L_f) horizontal axis of the letter L by *foot* and the conventionally long (length L_l) vertical axis by *leg*. The length ratio p of the axes can in practice vary between 0 and ∞. If the symmetry between the two axes is not broken, e.g., by assignment of boundary charges to any of the two corresponding network species, the physical observables should generally be symmetric around $p = 1$. This is confirmed in Fig. 13, where **(a)** the inside network charges and **(b)** the global orientational order parameter S are depicted. The figure features the simulation data depicted in Fig. 5 supplemented with simulation data for larger p. In particular, we verify that $S(p) = S(1/p)$, as well as $Q_\mathrm{l}^{(\mathrm{in})}(p) = Q_\mathrm{f}^{(\mathrm{in})}(1/p)$, i.e., the symmetry around $p = 1$ is clearly visible.

[1] X. Yao, H. Zhang, and J. Z. Chen, Phys. Rev. E **97**, 052707 (2018).
[2] X. Yao and J. Z. Y. Chen, Phys. Rev. E **101**, 062706 (2020).
[3] A. H. Lewis, I. Garlea, J. Alvarado, O. J. Dammone, P. D. Howell, A. Majumdar, B. M. Mulder, M. Lettinga, G. H. Koenderink, and D. G. A. L. Aarts, Soft Matter **10**, 7865 (2014).
[4] T. Geigenfeind, S. Rosenzweig, M. Schmidt, and D. de las Heras, J. Chem. Phys. **142**, 174701 (2015).
[5] R. Wittmann, L. B. G. Cortes, H. Löwen, and D. G. A. L. Aarts, Nat. Commun. **12**, 623 (2021).
[6] E. Basurto, P. Gurin, S. Varga, and G. Odriozola, Phys. Rev. Research **2**, 013356 (2020).
[7] P. A. Monderkamp, R. Wittmann, L. B. G. Cortes, D. G. A. L. Aarts, F. Smallenburg, and H. Löwen, Phys. Rev. Lett. **127**, 198001 (2021).
[8] P. A. Monderkamp, R. Wittmann, M. Te Vrugt, A. Voigt, R. Wittkowski, and H. Löwen, PCCP **24**, 15691 (2022).
[9] C. Avendaño, G. Jackson, E. A. Müller, and F. A. Escobedo, PNAS **113**, 9699 (2016).
[10] C. J. Hernandez and T. G. Mason, J. Phys. Chem. C **111**, 4477 (2007).
[11] T. Niori, T. Sekine, J. Watanabe, T. Furukawa, and H. Takezoe, J. Mater. Chem. **6**, 1231 (1996).
[12] G. Heppke, D. Parghi, and H. Sawade, Liq. Cryst. **27**, 313 (2000).
[13] T. J. Dingemans and E. T. Samulski, Liq. Cryst. **27**, 131 (2000).
[14] M. B. Ros, J. L. Serrano, M. R. de La Fuente, and C. L. Folcia, J. Mater. Chem. **15**, 5093 (2005).
[15] R. D. Kamien and J. V. Selinger, Journal of Physics: Condensed Matter **13**, R1 (2001).
[16] A. B. Harris, R. D. Kamien, and T. C. Lubensky, Phys. Rev. Lett. **78**, 1476 (1997).
[17] A. B. Harris, R. D. Kamien, and T. C. Lubensky, Rev. Mod. Phys. **71**, 1745 (1999).
[18] J. Pollard, G. Posnjak, S. Čopar, I. Muševič, and G. P. Alexander, Phys. Rev. X **9**, 021004 (2019).
[19] R. B. Meyer, Mol. Cryst. Liq. **40**, 33 (1977).
[20] I. Dierking, Sym. **6**, 444 (2014).
[21] C. Hoell and H. Löwen, J. Chem. Phys. **144**, 174901 (2016).
[22] T. Machon, H. Aharoni, Y. Hu, and R. D. Kamien, Commun. Math. Phys. **372**, 525 (2019).
[23] H. Aharoni, T. Machon, and R. D. Kamien, Phys. Rev. Lett. **118**, 257801 (2017).
[24] D. A. Beller, T. Machon, S. Čopar, D. M. Sussman, G. P. Alexander, R. D. Kamien, and R. A. Mosna, Phys. Rev. X **4**, 031050 (2014).

[25] B. J. Hocking, H. S. Ansell, R. D. Kamien, and T. Machon, Proc. R. Soc. **478**, 20210725 (2022).
[26] B. Schütrumpf, M. A. Klatt, K. Iida, G. E. Schröder-Turk, J. A. Maruhn, K. Mecke, and P.-G. Reinhard, Phys. Rev. C **91**, 025801 (2015).
[27] K. Nakazato, K. Oyamatsu, and S. Yamada, Phys. Rev. Lett. **103**, 132501 (2009).
[28] E. J. Crossland, M. Kamperman, M. Nedelcu, C. Ducati, U. Wiesner, D.-M. Smilgies, G. E. Toombes, M. A. Hillmyer, S. Ludwigs, U. Steiner, et al., Nano Lett. **9**, 2807 (2009).
[29] M. Barthélemy and A. Flammini, JSTAT **2006**, L07002 (2006).
[30] M. Papageorgiou, TRANSPORT RES B-METH **24**, 471 (1990).
[31] C. Vega and S. Lago, Comput. Chem. **18**, 55 (1994).
[32] N. Metropolis, A. W. Rosenbluth, M. N. Rosenbluth, A. H. Teller, and E. Teller, J. Chem. Phys. **21**, 1087 (1953).
[33] L. Euler, Novi Comment. Acad. Sci. I. Petropolitanae **4**, 109 (1758).
[34] J. Alama, Formaliz. Math. **16**, 7 (2008).
[35] Y.-K. Kim, S. V. Shiyanovskii, and O. D. Lavrentovich, J. Condens. Matter Phys. **25**, 404202 (2013).
[36] M. A. Bates and D. Frenkel, J. Chem. Phys. **112**, 10034 (2000).
[37] P. Bolhuis and D. Frenkel, J. Chem. Phys. **106**, 666 (1997).
[38] W. Fulton, *Algebraic Topology - A First Course* (Springer-Verlag, 1995).
[39] G. P. Alexander, B. G.-g. Chen, E. A. Matsumoto, and R. D. Kamien, Rev. Mod. Phys. **84**, 497 (2012).
[40] R. Stannarius and K. Harth, Phys. Rev. Lett. **117**, 157801 (2016).
[41] K. Harth and R. Stannarius, Front. Phys. **8**, 112 (2020).
[42] X. Yao, L. Zhang, and J. Z. Y. Chen, arXiv:2112.07889 (2021).
[43] Y. Martínez-Ratón and E. Velasco, Phys. Fluids **34**, 037110 (2022).
[44] K. Zhao, C. Harrison, D. Huse, W. Russel, and P. Chaikin, Phys. Rev. E **76**, 040401 (2007).
[45] K. Zhao, R. Bruinsma, and T. G. Mason, Nat. Commun. **3**, 801 (2012).
[46] C. Avendaño and F. A. Escobedo, COCIS **30**, 62 (2017).
[47] F. Barmes, M. Ricci, C. Zannoni, and D. Cleaver, Phys. Rev. E **68**, 021708 (2003).
[48] D. J. Kraft, R. Wittkowski, B. Ten Hagen, K. V. Edmond, D. J. Pine, and H. Löwen, Phys. Rev. E **88**, 050301 (2013).
[49] Y. Yuan, A. Martinez, B. Senyuk, M. Tasinkevych, and I. I. Smalyukh, Nat. Mater **17**, 71 (2018).
[50] C. P. Lapointe, T. G. Mason, and I. I. Smalyukh, Science **326**, 1083 (2009).
[51] D. Zerrouki, J. Baudry, D. Pine, P. Chaikin, and J. Bibette, Nature **455**, 380 (2008).
[52] P. W. Schönhöfer, L. J. Ellison, M. Marechal, D. J. Cleaver, and G. E. Schröder-Turk, Interface Focus **7**, 20160161 (2017).
[53] P. W. Schönhöfer, D. J. Cleaver, and G. E. Schröder-Turk, J. Phys. D **51**, 464003 (2018).
[54] J. P. Bramble, S. D. Evans, J. R. Henderson, T. J. Atherton, and N. J. Smith, Liq. Cryst. **34**, 1137 (2007).
[55] Y. H. Kim, D. K. Yoon, M.-C. Choi, H. S. Jeong, M. W. Kim, O. D. Lavrentovich, and H.-T. Jung, Langmuir **25**, 1685 (2009).
[56] D. B. Liarte, M. Bierbaum, R. A. Mosna, R. D. Kamien, and J. P. Sethna, Phys. Rev. Lett. **116**, 147802 (2016).
[57] A. J. Tan, E. Roberts, S. A. Smith, U. A. Olvera, J. Arteaga, S. Fortini, K. A. Mitchell, and L. S. Hirst, Nat. Phys. **15**, 1033 (2019).
[58] B. Loewe and T. N. Shendruk, arXiv:2111.07364 (2021).
[59] L. Giomi, Phys. Rev. X **5**, 031003 (2015).
[60] M. Bär, R. Großmann, S. Heidenreich, and F. Peruani, Annu. Rev. Condens. Matter Phys. **11**, 441 (2020).
[61] S. J. DeCamp, G. S. Redner, A. Baskaran, M. F. Hagan, and Z. Dogic, Nat. Mater. **14**, 1110 (2015).
[62] G. Tóth, C. Denniston, and J. M. Yeomans, Phys. Rev. Lett. **88**, 105504 (2002).
[63] Z.-F. Huang, H. Löwen, and A. Voigt, Commun. Phys. **5**, 294 (2022).
[64] R. J. Hernández, F. J. Sevilla, A. Mazzulla, P. Pagliusi, N. Pellizzi, and G. Cipparrone, Soft Matter **16**, 7704 (2020).
[65] F. Kümmel, B. Ten Hagen, R. Wittkowski, I. Buttinoni, R. Eichhorn, G. Volpe, H. Löwen, and C. Bechinger, Phys. Rev. Lett. **110**, 198302 (2013).
[66] L. Caprini and U. M. B. Marconi, Soft Matter **15**, 2627 (2019).
[67] H. Löwen, EPJ ST **225**, 2319 (2016).
[68] R. G. Miller Jr, *Beyond ANOVA: basics of applied statistics* (CRC press, 1997).
[69] P. Virtanen, R. Gommers, T. E. Oliphant, M. Haberland, T. Reddy, D. Cournapeau, E. Burovski, P. Peterson, W. Weckesser, J. Bright, et al., Nat. Methods **17**, 261 (2020).
[70] F. Aurenhammer, R. Klein, and D.-T. Lee, *Voronoi diagrams and Delaunay triangulations* (World Scientific Publishing Company, 2013).
[71] R. D. Kamien and R. A. Mosna, New J. Phys. **18**, 053012 (2016).
[72] B. G.-g. Chen, G. P. Alexander, and R. D. Kamien, Proc. Natl. Acad. Sci. U.S.A. **106**, 15577 (2009).
[73] M. V. Kurik and O. Lavrentovich, Phys.-Uspekhi **31**, 196 (1988).

P5 Active particles using reinforcement learning to navigate in complex motility landscapes

Published under the gold open access model and reproduced from

P. A. Monderkamp, F. J. Schwarzendahl, M. A. Klatt and H. Löwen,
Active particles using reinforcement learning to navigate in complex motility landscapes,
MLST, 3, 045024 (2022),

with permission from the Institute of Physics (IOP).

Digital Object Identifier (DOI): `https://doi.org//10.1088/2632-2153/aca7b0`

Statement of contribution

F. J. Schwarzendahl, H. Löwen, and I developed the reinforcement learning model. M. A. Klatt and I developed the functional form for the learning environment. I performed the numerical simulations, designed the figures. F. J. Schwarzendahl and I wrote the original draft.
Funding and overseeing was provided by H. Löwen. All authors contributed text associated with their respective expertise in paper and supplementary material and contributed to the finalisation of the manuscript.

P5.1 Paper: Active particles using reinforcement learning to navigate in complex motility landscapes

Machine Learning: Science and Technology

Active particles using reinforcement learning to navigate in complex motility landscapes

IOP Publishing Mach. Learn.: Sci. Technol. 3 (2022) 045024 https://doi.org/10.1088/2632-2153/aca7b0

MACHINE LEARNING
Science and Technology

OPEN ACCESS

RECEIVED
7 September 2022

REVISED
11 November 2022

ACCEPTED FOR PUBLICATION
30 November 2022

PUBLISHED
16 December 2022

PAPER

Active particles using reinforcement learning to navigate in complex motility landscapes

Paul A Monderkamp*, Fabian Jan Schwarzendahl, Michael A Klatt and Hartmut Löwen

Institut für Theoretische Physik II: Weiche Materie, Heinrich-Heine-Universität Düsseldorf, Universitätsstraße 1, 40225 Düsseldorf, Germany

* Author to whom any correspondence should be addressed.

E-mail: paul.monderkamp@hhu.de

Keywords: active Brownian particles, reinforcement learning, active matter, soft condensed matter, active colloids, Q-learning

Supplementary material for this article is available online

Abstract

As the length scales of the smallest technology continue to advance beyond the micron scale it becomes increasingly important to equip robotic components with the means for intelligent and autonomous decision making with limited information. With the help of a tabular Q-learning algorithm, we design a model for training a microswimmer, to navigate quickly through an environment given by various different scalar motility fields, while receiving a limited amount of local information. We compare the performances of the microswimmer, defined via time of first passage to a target, with performances of suitable reference cases. We show that the strategy obtained with our reinforcement learning model indeed represents an efficient navigation strategy, that outperforms the reference cases. By confronting the swimmer with a variety of unfamiliar environments after the finalised training, we show that the obtained strategy generalises to different classes of random fields.

1. Introduction

Technological advances in producing micron sized swimmers and robots give hope for applications to minimal invasive medicine [1]. The possibilities reach from targeted drug delivery, over material removal in minimal invasive surgery, to telemetric applications where microrobots transmit information that is otherwise hard to obtain. In all of these examples, microrobots need to find a specific target, e.g. the location to which a drug needs to be delivered, or an infected piece of tissue that needs to be surgically extracted. In order to find these targets, usually only local information about the surrounding environment of the robot is given. The robots might need to travel through a complex network of veines or pass through mucus, which makes navigation challenging. Hence, smart navigation strategies for microswimmers need to be found. Here, we develop intelligent strategies, that utilise only limited local information, for microswimmers in a complex motility field by employing reinforcement machine learning techniques.

Recently, machine learning techniques have been applied to active and soft matter systems [2–4]. Specifically, artificial microswimmers, which have been studied intensely [5], might be used for technological applications such as decontamination of polluted water [6], or minimal invasive surgery [1, 7–9]. Active particles have been taught to navigate in different environments, for example optimal paths in force fields [10–12] or flow [13–16] have been computed. Related to the latter, gliders have learned to navigate in a turbulent flow [17, 18] and microswimmers learned a complex flow field [19–24]. In experiments, reinforcement learning has been applied to microswimmers [25] and artificial visual perception has been given to active colloids [26].

The motility of active particles is strongly influenced by the surrounding medium [27], and in particular, viscous landscapes have been studied [28–33], giving rise to viscotaxis. Furthermore, active particles can be steered with an orientation dependent motility [34].

IOP Publishing Mach. Learn.: Sci. Technol. 3 (2022) 045024 P A Monderkamp et al

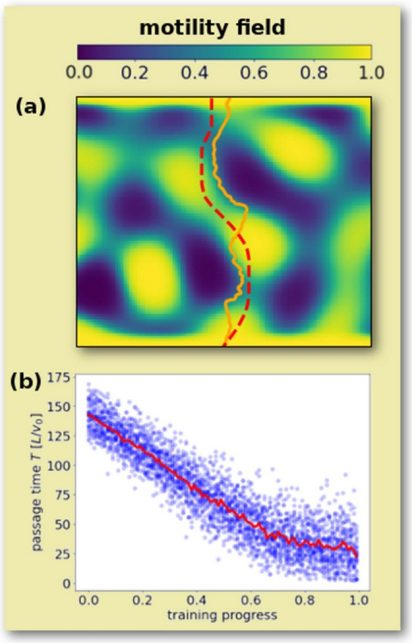

Figure 1. Training an ABP to navigate, with limited local information, through a complex random environment given by a scalar motility field. (a) Typical trajectory after the finalised training procedure (solid orange line) and optimal trajectory obtained with the help of *Dijkstras (shortest path) algorithm* (dashed red line). (b) Average passage time through the simulation box (from bottom to top) at each percent of the training procedure (red line), sampled from 30 independent training procedures. Each blue dot denotes an average over 10^4 trajectories.

In this paper, we teach an active particle that has only local information about its environment to navigate through a complex motility field. A reinforcement learning technique (Q-learning, see section 2.2) that requires a limited amount of data storage is used, making it usable for real life applications. Over the training time, the Q-learning active Brownian particle (QABP) learns to solve different realisations of a random environment, with increasing success (figure 1(b)). At the end of training, the particle outperforms a simple active Brownian particle (ABP), and comes close to the globally optimal path (figure 1(a)) with only local information. Furthermore, once the particle has learned a strategy, we place it in qualitatively different environments, in which it still finds an almost optimal path.

2. Methods

2.1. Equations of motion

We model the swimmer as an overdamped ABP in two dimensions with position $\mathbf{r}(t)$ and orientation $\hat{\mathbf{u}}(t) = (\cos\phi(t), \sin\phi(t))$. It exerts a space-dependent self-propulsion velocity $v_0\mu(\mathbf{r})$ along its orientation. $\mu(\mathbf{r}) \in (0, 1]$ represents the motility field around the particle, such that the particle velocity is bound between 0 and the self-propulsion velocity v_0. In order to perform intelligent navigation, the QABP is capable of either rotating itself with an angular velocity $\omega_Q(\mathbf{r}(t), t) = \pm\,\omega_0$ in either direction or retaining it is orientation such that $\omega_Q(\mathbf{r}(t), t) = 0$. Accordingly, the equations of motion are

$$\dot{\mathbf{r}}(t) = v_0\mu(\boldsymbol{r}(t))\hat{\mathbf{u}}(t), \tag{1}$$

$$\dot{\phi}(t) = \omega_Q(\boldsymbol{r}(t), t) + \sqrt{2D_r}\xi, \tag{2}$$

where ξ represents Gaussian white noise exerted from the solvent environment on the orientation of the particle, with $\langle\xi(t)\rangle = 0$ and $\langle\xi(t)\xi(t')\rangle = \delta(t - t')$.

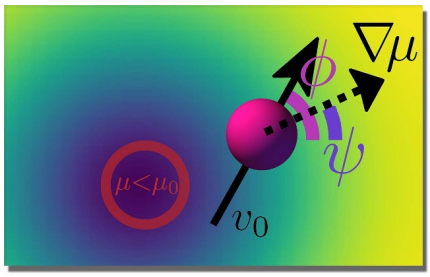

Figure 2. Schematic of the local information, that the QABP receives for the decision making. The swimmer knows the discretised polar angle of its own orientation $\hat{\mathbf{u}} = (\cos(\phi), \sin(\phi))$, and the polar angle ψ of the local gradient $\nabla\mu$ of the motility field. Further, it has information about low motility zones, defined by $\mu < \mu_0$, as indicated by the red circle.

The swimmer moves within a box of side lengths $L_x = 100 v_0 \tau_Q$ and $L_y = 85 v_0 \tau_Q$, where τ_Q denotes the characteristic time scale of an intelligent decision (see section 2.2). The reinforcement learning problem is defined by navigating as quickly as possible from the bottom hard wall to the top hard wall of the box. Depending on the specific model of $\mu(\mathbf{r})$, either reflecting or periodic boundary conditions in horizontal direction are used. The QABP and the reference case of the ABP start their trajectories at $\mathbf{r}(t=0) = (0.5L_x, 0)$, oriented upwards ($\hat{\mathbf{u}}(t=0) = (0,1)$). The swimmers are trained in a motility field that is generated with a Gaussian random wave model (GRW), with wave vectors $\boldsymbol{k}_n$ of wavelength $\|\mathbf{k}_n\| = 20/L_y$ (for details see supplementary material section 1). The GRW gives isotropic non-periodic random waves, a typical example is shown figure 1(a). A remarkable property of this model is an optimal suppression of density fluctuations above a certain wavelength, a property known as stealthy hyperuniformity [35–38]. The use of stealthy hyperuniform models as randomly generated motility fields has the advantage that the formation of large clusters of low motility zones is suppressed. This typically results in the presence of several global paths through the environment without an imminent danger of getting stuck in a dead end at a non-convex low motility zone, which greatly facilitates the learning of the QABP.

2.2. Q-learning algorithm

To enable swimmer navigation within the simulated physical environment, a tabular Q-learning algorithm [39] is superimposed on the Brownian dynamics simulation, giving the QABP the ability for self rotation through the torque expressed by ω_Q. Such an algorithm is characterised by a matrix table $\mathcal{Q}$, which encompasses the strategy and learned experience by the active agent. This matrix functions as a decision matrix, where the rows represent all possible discrete states, in which the swimmer can reside and the columns represent all possible discrete actions. At any time t of action, the swimmer checks its current state i, and performs the action A_i corresponding to the highest value within row i of the matrix:

$$A_i = \arg\max_j \mathcal{Q}_{ij}(t). \tag{3}$$

In our model, the swimmer has information (see figure 2) about its own orientation $\phi(t)$ and the polar angle $\psi(\mathbf{r}(t))$ of the local gradient of the motility field $\nabla\mu(\mathbf{r}(t))$. Furthermore, it knows whether $\mu(\mathbf{r}(t))$ is above or below a threshold value $\mu_0 = 0.25$ (see supplementary material section 4).

The orientational dynamics of the QABP (see equation (2)) are approximated by run and tumble dynamics, where the swimmer tumbles in each integration time step $t_n = n\Delta t$ with a probability $P_{\text{tumble}} = 2D_r\Delta t/(\Delta\phi)^2$, where $\Delta\phi = 2\pi/M_\phi$. The local gradient direction and swimmer orientation are discretised on the unit circle with $M_\phi = M_\psi = 12$ (see supplementary material section 3). All possible combinations of discrete orientations and gradient directions as well as the binary information about the velocity form the complete state space of the Q-learning algorithm. With a given periodicity $\tau_Q = 10\Delta t$, the swimmer takes action, by rotating itself in either direction by $\Delta\phi$, or not rotating, depending on the decision matrix $\mathcal{Q}$. This rotation defines an effective angular velocity $\omega_0 = \Delta\phi/\tau_Q = 2\pi/(N_\phi \tau_Q)$.

In order to obtain a decision matrix, which represents a good strategy for navigating through the complex environment given by $\mu(\mathbf{r})$, $\mathcal{Q}$ is optimised over the course of $N_{epi} = 10^6$ episodes, i.e. trajectories. Before the training procedure, $\mathcal{Q}$ is initialised with zero values. For each episode in the learning phase, the trajectory of the swimmer is simulated until it either reaches the top of the box, swims into a region with

$\mu < 0.5\mu_0 = 0.125$ or the travel time surpasses an upper bound $T_{\max}$, obtained by 100 times the time of a comparable optimal trajectory, obtained with *Dijkstra's algorithm* (see supplementary material section 2). To obtain a navigation strategy, as general as possible, 10^3 realisations of the random environment are used over of $N_{epi} = 10^6$ episodes. The results are sampled, with the trained QABP, on 10^3 new environments.

During training, when an action j is performed, the QABP transitions from state i to i'. Then $\mathcal{Q}$ is updated, following the update formula

$$\mathcal{Q}_{ij}^{new} = \mathcal{Q}_{ij} + \alpha\left(R + \gamma \max_k(Q_{i'k}) - \mathcal{Q}_{ij}\right). \tag{4}$$

Here, $\alpha, \gamma \in [0,1]$ denote hyperparameters of the learning algorithm and R denotes the sum of the specific numeric rewards, that the active agent obtained through performing the current action j. The learning rate α is initialised at 10^{-4} and linearly decreases to 10^{-5} at the end of the training, reinforcing the reliability of $\mathcal{Q}$ with proceeding learning. The term $\gamma \max_j(Q_{i'j})$ incorporates the highest entry in a row from the following state into the current $\mathcal{Q}_{ij}$, estimating the future reward. Since a reasonably different behaviour in neighbouring states is expected across the swimmers state space, $\gamma = 0.3$ is used. During training an ϵ-greedy policy is used. Here, random actions are chosen with probability $\epsilon = 1$ at the beginning of training, then during training ϵ is decreased linearly to 0 such that equation (3) is used for any decision at the end of training (see supplementary material section 5).

In order to navigate efficiently the swimmer is rewarded once it reaches the top of the simulation box. Further, it is punished when it enters a low motility region, or if its displacement is very small (for reward details supplementary material section 4.).

3. Results

To give an intuition on the development of the strategy, three characteristic trajectories from different stages of the learning process are shown in figure 3. For visual reference, each panel additionally shows a globally optimal trajectory obtained via *Dijkstra's algorithm*. In figure 3(a) we show a trajectory from an episode early in the training procedure. Since the QABP has yet to learn about its environment, the probability ϵ to perform a random rotation in either direction is close to 1. Accordingly, the trajectory is similar to that of a common ABP. Due to the indecisiveness of the QABP at this explorative stage, the episode terminates eventually by entering a low motility zone.

Figure 3(b) depicts a trajectory from an episode halfway through the training procedure. The corresponding probability to perform random actions ϵ is approximately 0.45. The trajectory shows randomness, through rotational diffusion as well as random active rotation. Despite the fact that more than half of the actions are randomly chosen, it is visible, how the QABP displays noticeable competence of avoiding the regions with $\mu \ll 1$ to reach the finish line. Finally, the trajectory in figure 3(c) shows the dynamics of the QABP after the learning procedure when $\epsilon = 0$. The QABP swims decisively in vertical direction, such that the trajectory exhibits little dents, thereby maneuvering around the low motility zone in its path.

3.1. Quantitative performance

Optimising the navigation through the environment, given by the motility field $\mu(\mathbf{r})$, relies on the balancing between two opposing principles: minimising the length of the path while simultaneously maximising the instantaneous velocity $v_0\mu(\mathbf{r})$ [40, 41]. Formally, this problem is solved by the solution that minimises the following functional

$$T[\mathbf{c}] = \int_{\mathbf{c}_0}^{\mathbf{c}_1} \frac{\|\dot{\boldsymbol{c}}(t)\|}{v_0\mu(\mathbf{c}(t))}\mathrm{d}t, \tag{5}$$

which is the passage time T from the starting point $\mathbf{c}_0$ to any point on the finish line $\mathbf{c}_1$. Here, $\boldsymbol{c}(t)$ is a curve through the environment, parameterised by t. A convenient figure of merit for the performance of the swimmer along any trajectory $\mathbf{r}(t)$ is defined as

$$\frac{v_y}{v_0} := \frac{L_y}{T[\mathbf{r}(t)]v_0}. \tag{6}$$

This quantity is in the interval $(0,1]$ for any trajectory. After each independent training procedure, the resulting $\mathcal{Q}$ is tested in 10^3 trajectories on every independent realisation $\mu(\mathbf{r})$ respectively. Performance data

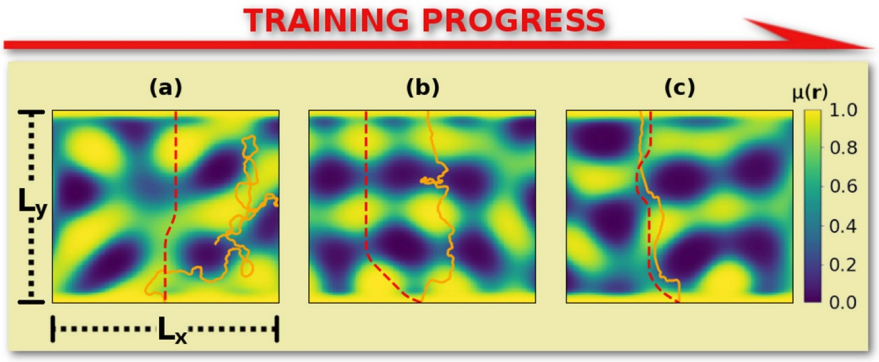

Figure 3. Three typical trajectories (orange solid lines) in three motility fields $\mu(\mathbf{r})$ over the course of the training procedure of the QABP. The particle's objective is to cross the box from bottom to top as fast as possible. The environments are generated with the help of modified isotropic Gaussian random waves. The probablities to perform random actions are (a) $\epsilon = 1.0$, (b) $\epsilon \approx 0.58$, (c) $\epsilon \approx 0$. The red dashed line highlight the optimal trajectories obtained with *Dijkstras algorithm* (see supplementary material section 2). Motility fields are generated as modified isotropic Gaussian random waves and in the horizontal direction reflecting boundary conditions are employed.

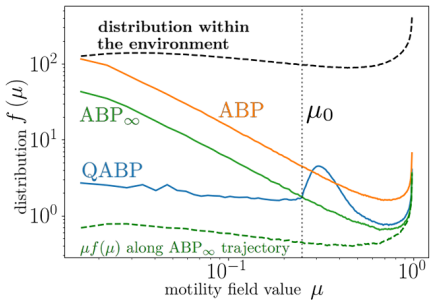

Figure 4. Distributions of scalar values $\mu(\mathbf{r}(t)) = \|\dot{\mathbf{r}}\|/v_0$ along trajectories with $\langle\mu\rangle \approx 0.557$ and $\mathcal{P}_{\text{rot}} \approx 46$, sampled from 15 simulations with 1000 trajectories each. The lines indicate ABP (solid orange), straight trajectory, i.e. ABP_∞ (solid green), and intelligent swimmer (QABP, solid blue). The dashed black line shows the distribution of the $\mu(\mathbf{r})$-values within the environment, averaged from 1000 independent $\mu(\mathbf{r})$. The dashed green line corresponds to $\mu f(\mu)$ of the ABP_∞ trajectory. The dotted vertical line denotes the velocity state threshold $\mu_0 = 0.25$.

was additionally gathered from multiple independent training procedures for each set a parameters. The general performance of the resulting strategy, encoded in $\mathcal{Q}$, is determined by averaging over the 10^3 trajectories, giving $\langle v_y \rangle / v_0$. The performance will depend on the average motility $\langle\mu\rangle$ and the rotational Péclet number, which is defined as

$$\mathcal{P}_{\text{rot}} = (\Delta\phi)^2 / 2D_{\text{rot}}\tau_Q \tag{7}$$

comparing the typical time scale of the rotational diffusion to that of the intelligent active rotation.

The total passage time T (see equation (5)) can be calculated from the non-normalised distribution of velocities $f(\mu)$, sampled with a time step of τ_Q, along a given trajectory as

$$T = \tau_Q \int_0^1 f(\mu) d\mu. \tag{8}$$

To quantify the behaviour of the individual swimmers, the frequencies $f(\mu)$ of the scalar values of $\mu(\mathbf{r})$ are shown in figure 4. The data is averaged from 15 independent simulation runs with 10^3 trajectories each. Additionally $\mu f(\mu)$ is shown for the ABP, for a straight line (i.e. an ABP in the limit of vanishing diffusion denoted by ABP_∞), and for the distribution of function values $\mu(\mathbf{r})$ within the environment, averaged from 10^3 independent motility fields. More specifically, the distribution of the ABP_∞ trajectory (green solid line)

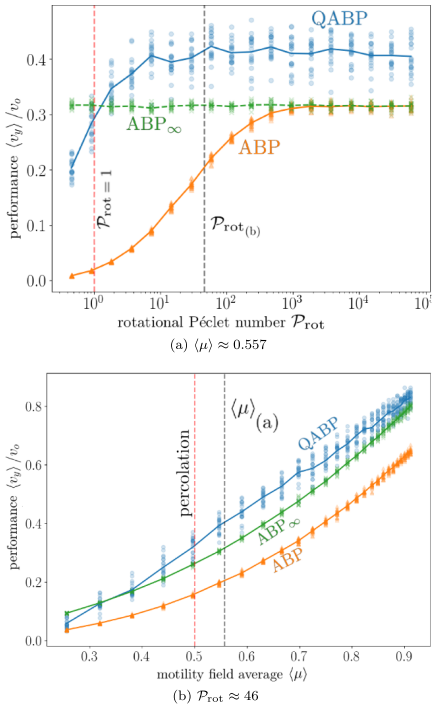

Figure 5. Performances $\langle v_y \rangle / v_0$ of the QABP as well as an ABP and a particle swimming in a straight line without diffusion (ABP_∞) as reference swimmers. The scattered data data points indicate a simulation with 10^3 trajectories each. The solid lines denote the averages over the respective ten data points per parameter set. (a) shows the performance for varying rotational Péclet number $\mathcal{P}_{\mathrm{rot}}$ and (b) for varying environment $\langle \mu \rangle$.

counts the frequencies of function values of $\mu(\mathbf{r})$ along a vertical line, sampled in time. Due to the longer retention time at slower velocities, we obtain the distribution in space, sampled at constant distances, as $\mu f(\mu)$. Since the data is averaged over 1.5×10^4 different environments, the corresponding $\mu f(\mu)$ (green dashed line) is proportional to the distribution of the values in the total field (black dashed line). On the other hand, the ABP_∞ reflects the limit of the ABP, for vanishing diffusion. As visible in the plot, the respective curves are proportional to each other, emphasising that the performances of the ABP is tangible through consideration of the motility field alone. Observing the QABP case, it is visible that the distribution in the lower velocities is approximately constant and lies orders of magnitude below both ABP cases. Instead, $f(\mu)$ displays a significant peak above the velocity state threshold indicated by the vertical line at $\mu_0 = 0.25$. This exemplifies how the navigation strategy of the QABP relies on circumvention of the low motility zones, through higher motility regions, thereby elongating the trajectory, but saving time through the faster swimming.

The performances $\langle v_y \rangle / v_0$ of the QABP, and the two reference cases (ABP, ABP_∞) are shown as a function of $\mathcal{P}_{\mathrm{rot}}$ in figure 5(a), where $\langle \mu \rangle \approx 0.557$ is chosen. For large $\mathcal{P}_{\mathrm{rot}}$, the $\langle v_y \rangle / v_0$ of the ABP approaches the performance of the ABP_∞. More specifically, the ABP is bounded by the ABP_∞, and $\langle v_y \rangle / v_0$ is monotonous in $\mathcal{P}_{\mathrm{rot}}$. For small $\mathcal{P}_{\mathrm{rot}}$, the performance of the ABP approaches 0. For almost the whole parameter range the QABP is faster than both reference cases. Additionally $\langle v_y \rangle / v_0$ seems to be independent from $\mathcal{P}_{\mathrm{rot}}$ for $\mathcal{P}_{\mathrm{rot}} \gtrsim 1$. This demonstrates the QABP's ability to steer against the kicks from rotational diffusion. Only for $\mathcal{P}_{\mathrm{rot}} \lesssim 1$, the QABP loses its ability to correct for rotational noise, and hence the performance declines with decreasing values of $\mathcal{P}_{\mathrm{rot}}$. Figure 5(b) shows the respective performances as a function the environment parameter $\langle \mu \rangle$ for a constant $\mathcal{P}_{\mathrm{rot}} \approx 46$. For all three cases, $\langle v_y \rangle / v_0$ increases with μ. Once again, the QABP surpasses the ABP across all $\langle \mu \rangle$, and the ABP_∞ for most of the shown parameter range. For $\langle \mu \rangle \approx 1$, the performances $\langle v_y \rangle / v_0$ of both QABP and ABP_∞ approach 1, since the optimal trajectory becomes a straight line. For $\langle \mu \rangle = 0.5$, the motility field $\mu(\mathbf{r})$ displays a percolation transition of

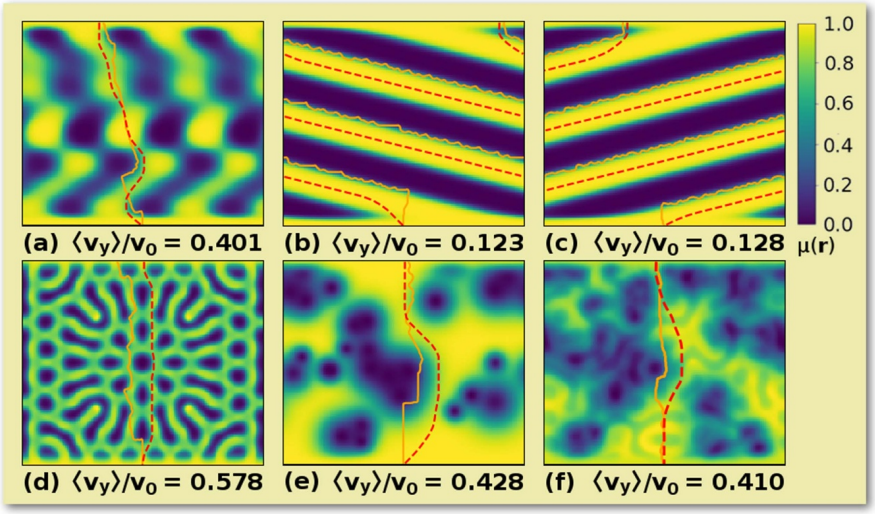

Figure 6. Trajectories of QABPs, trained in non-periodic Gaussian random wave environments (see figure 3), placed in unknown environments, after the finalised learning process ($\mathcal{P}_{\text{rot}} \approx 46$, $\langle\mu\rangle \approx 0.557$). The globally optimised trajectories, generated with the help of *Dijkstra's algorithm*, are shown as dashed red lines. The motility fields $\mu(\mathbf{r})$ are generated with the help of (a) Gaussian random waves (see. Supplemental Material section 1) periodic in horizontal direction, (b), (c) Gaussian random waves periodic in both Carthesian directions, (d) Gray–Scott model for reaction-diffusion (e) 30 Gauss peaks scattered randomly across the simulation box and (f) Eight Gauss peaks scattered randomly across the simulation box, superimposed with solutions to the randomly initialised Gray–Scott model.

the low motility zones, and therefore the Q-learning model of avoiding low motility zones becomes less viable. It is visible in the figure, however, that the QABP surpasses the ABP_∞ down to $\langle\mu\rangle \approx 0.35$.

3.2. Generalisation to unfamiliar environments

In order to demonstrate the generality of the learned strategy, i.e. to show that the final result $\mathcal{Q}$ of the learning process transcends the specific implementation of our learning environment, we test the QABP's ability to navigate in other motility fields that represent different types of long- and short-order order in space. More specifically, the swimmer is first trained on the previously used non-periodic Gaussian random fields with reflecting boundary conditions. After the learning procedure is finalised, the swimmer is placed in the respective unfamiliar environment.

A selection of the emerging trajectories ($\mathcal{P}_{\text{rot}} \approx 46$) is shown in figure 6. All fields are generated such that $\langle\mu\rangle \approx 0.557$. Additionally, a performance $\langle v_y\rangle / v_0$ is given averaged from ten independent training procedures with 10^3 trajectories each. For all fields, the QABP outperforms the references cases and displays performances reasonably close to the globally optimal solutions (the exact numerical values of the different performances can be found in the supplementary material section 9).

3.2.1. Directional patterns

The first instance in figure 6(a) displays an environment that is periodic in horizontal direction. The horizontal components of the random wave vectors fulfill $|\mathbf{k}_n \cdot \hat{\mathbf{e}}_x| = 6\pi/L$. The absolute value of the vertical components $|\mathbf{k}_n \cdot \hat{\mathbf{e}}_y|$ are randomised uniformly in $[0, 12\pi/L]$. The QABP visually displays competence of maneuvering through the new environment. Furthermore, $\langle v_y\rangle / v_0$ shows similar values as presented for the same parameters ($\mathcal{P}_{\text{rot}} \approx 46$, $\langle\mu\rangle \approx 0.557$) in section 3.1. This likely stems from the similarity of the wave vectors $\mathbf{k}_n$ and the resulting characteristic length scales in the environments $\mu(\mathbf{r})$.

Figures 6(b) and (c) show trajectories through periodic Gaussian random fields with $\mathbf{k}_n \cdot \hat{\mathbf{e}}_x = 2\pi/L$ and $\mathbf{k}_n \cdot \hat{\mathbf{e}}_y = \pm 8\pi/L$, respectively. It is visible through the global solutions, that the optimal paths are obtained by avoiding the low motility stripes through the periodicity of the box, persistently swimming in the same slanted direction. The performance of both environments with opposite parity are approximately equal. We thereby show, that the machine learning model is on average not subject to unexpected symmetry breaking.

Furthermore, the swimmers exhibit a significant tendency to slide across the boundary of the low motility zones. This behaviour exemplifies the strategy of the QABP to avoid motilities below a certain threshold rather than optimising the instantaneous velocity at all times.

3.2.2. Gray-Scott field

Figure 6(d) shows an environment obtained through integration of the Gray–Scott equations for reaction-diffusion [42, 43] (see supplementary material section 1.A). The typical length scales of the low motility zones obtained through this model are drastically smaller, than the previous examples. Furthermore, due to the entirely different algorithm, the functional form at the edges of the low motility zones is different. Despite these drastic differences to the original training data, the QABP displays the capability of efficiently maneuvering through the environment.

3.2.3. Strongly clustering patterns

All of the previously shown examples of scalar fields are based on hyperuniform models with suppressed density fluctuations. Next, we show that after training, the QABP also successfully navigates in random motility fields with strong heterogeneities (based on non-hyperuniform models).

Figure 6(e) shows an environment, which is generated by scattering 30 points $\mathbf{q}_k$ uniformly in the simulation box, and assigning each a characteristic randomly chosen length scale κ_k. Explicitly, the motility field is given by

$$\mu(\mathbf{r}) = \prod_{k=1}^{30} \left[1 - \exp\left(\frac{\|\mathbf{r} - \mathbf{q}_k\|^2}{{\kappa_k}^2} \right) \right], \tag{9}$$

with periodic boundary conditions. The environment in figure 6(e) displays several clusters of peaks. Nevertheless, we observe that the QABP finds a quick path through the environment by evading low motility zones of any size (for which it was efficiently trained in the stealthy hyperuniform GRW).

Finally, figure 6(f) shows a trajectory through a motility field that is given by a sum of equation (9) and a randomly initialised solution to the Gray–Scott model with amplitude 0.1 (see supplementary material section 1.A). This approach yields a motility field, with large low motility zones throughout the environment, overlaid with a more regular perturbation, that causes local gradients, which drastically influence local information. Even though, not having learned about the local structure, our results show, that the QABP noticeably interacts with the respective local gradients only at low swimming velocities. This result emphasises the significance of the inclusion of the swimming velocity in the QABPs state space.

4. Conclusions

In this work, we used a reinforcement learning algorithm to teach a microswimmer (QABP) to navigate through complex environments, given by scalar motility fields, that determine the local swimming velocity of the particle. Brownian dynamics simulations were used to investigate the dynamics of the QABP in this two-dimensional physical environment. To enable smart navigation, a tabular Q-learning algorithm was superimposed. The swimmer receives the ability to perform deterministic rotations, while only receiving local information about its environment.

First, modified Gaussian random waves were employed as motility fields. Two reference cases of an ABP and a particle swimming in a straight line (ABP_∞) were simulated and it was shown that the time of first passage of the ABP to a given target can be inferred from the motility field. The performance, i.e. the speed of finding the target, of the ABP, is bounded by the ABP_∞, as the limit of low diffusion. We demonstrate, that our intelligent QABP outperforms both the ABP and ABP_∞. To demonstrate the applicability of the resulting strategy, we test the ability of the QABP to solve different environments, generated with various algorithms, though only having learned the Gaussian random wave environment. The swimmers display competence of maneuvering through all the displayed examples of motility fields and again outperforms the ABP and ABP_∞. Our stealthy hyperuniform model provides a random yet relatively homogeneous environment that is well suited for the initial training of the QABP. In our observation, QABP provides competitive results in non-hyperuniform fields unseen during the training phase. Furthermore, due to the translational symmetries of our scalar random fields, we expect that the strategy, which has been learned in the training on relatively small box sizes, can automatically be transferred to applications, which feature meaningfully large environments.

Throughout this paper, we lay emphasis on the fact, that the final decision matrix only requires the microswimmer to know little local information about its environment. This will be of particular relevance to future microrobotic applications, where individual autonomous agents rarely possess the ability to capture

information about the whole environment at once, and the amount of data storage is dictated by the size of the technical components. Future studies of this local algorithm can be extended to more complex problems such as the inclusion of hydrodynamic force fields, or more general vectorial fields. [13, 16]. The explicit inclusion of cargo uptake and delivery [44, 45], as well as the consumption of fuel, into the machine learning model, may be of interest to medical applications [1]. Swimming strategies, which combine a deterministic approach to the decision making, such as through our reinforcement learning, with undeterministic approaches, e.g. random actions (cf figure 3(b)), may yield insight as models for biological microswimmers, that are motivated, for instance by the search for nutrients.

Data availability statement

The data that support the findings of this study are available upon reasonable request from the authors.

Acknowledgment

The authors like to thank Jens Grauer for sharing his machine learning expertise and methodic advice. Without his impactful feeback, this paper would not exist in the current form. This work was supported by the German Research Foundation (DFG) within project LO 418/25-1.

Conflict of Interest declaration

The authors declare, that there are no conflicts of interest to disclose.

ORCID iDs

Paul A Monderkamp https://orcid.org/0000-0001-5244-1586
Fabian Jan Schwarzendahl https://orcid.org/0000-0002-5779-3772
Michael A Klatt https://orcid.org/0000-0002-1029-5960
Hartmut Löwen https://orcid.org/0000-0001-5376-8062

References

[1] Nelson B J, Kaliakatsos I K and Abbott J J 2010 *Annu. Rev. Biomed. Eng.* **12** 55
[2] Cichos F, Gustavsson K, Mehlig B and Volpe G 2020 *Nat. Mach. Intell.* **2** 94
[3] Clegg P S 2021 *Soft Matter* **17** 3991
[4] Falk M J, Alizadehyazdi V, Jaeger H and Murugan A 2021 *Phys. Rev. Res.* **3** 033291
[5] Bechinger C, Di Leonardo R, Löwen H, Reichhardt C, Volpe G and Volpe G 2016 *Rev. Mod. Phys.* **88** 045006
[6] Gao W and Wang J 2014 *ACS Nano* **8** 3170
[7] Abdelmohsen L K, Peng F, Tu Y and Wilson D A 2014 *J. Mater. Chem.* B **2** 2395
[8] Patra D, Sengupta S, Duan W, Zhang H, Pavlick R and Sen A 2013 *Nanoscale* **5** 1273
[9] You M, Chen C, Xu L, Mou F and Guan J 2018 *Acc. Chem. Res.* **51** 3006
[10] Schneider E and Stark H 2019 *Europhys. Lett.* **127** 64003
[11] Yang Y and Bevan M A 2018 *ACS Nano* **12** 10712
[12] La H M, Lim R and Sheng W 2014 *IEEE Trans. Control Syst. Technol.* **23** 52
[13] Liebchen B and Löwen H 2019 *Europhys. Lett.* **127** 34003
[14] Daddi-Moussa-Ider A, Löwen H and Liebchen B 2021 *Commun. Phys.* **4** 1
[15] Zanovello L, Caraglio M, Franosch T and Faccioli P 2021 *Phys. Rev. Lett.* **126** 018001
[16] Nasiri M and Liebchen B 2022 *New J. Phys.* **24** 073042
[17] Reddy G, Celani A, Sejnowski T J and Vergassola M 2016 *Proc. Natl Acad. Sci.* **113** E4877
[18] Reddy G, Wong-Ng J, Celani A, Sejnowski T J and Vergassola M 2018 *Nature* **562** 236
[19] Colabrese S, Gustavsson K, Celani A and Biferale L 2017 *Phys. Rev. Lett.* **118** 158004
[20] Colabrese S, Gustavsson K, Celani A and Biferale L 2018 *Phys. Rev. Fluids* **3** 084301
[21] Gustavsson K, Biferale L, Celani A and Colabrese S 2017 *Eur. Phys. J.* E **40** 110
[22] Alageshan J K, Verma A K, Bec J and Pandit R 2020 *Phys. Rev.* E **101** 043110
[23] Qiu J, Huang W, Xu C and Zhao L 2020 *Sci. China Phys. Mech. Astron.* **63** 284711
[24] Biferale L, Bonaccorso F, Buzzicotti M, Clark P Leoni Di and Gustavsson K 2019 *Chaos* **29** 103138
[25] Muiños-Landin S, Fischer A, Holubec V and Cichos F 2021 *Sci. Robot.* **6** eabd9285
[26] Lavergne F A, Wendehenne H, Bäuerle T and Bechinger C 2019 *Science* **364** 70
[27] Breoni D, Schmiedeberg M and Löwen H 2020 *Phys. Rev.* E **102** 062604
[28] Datt C and Elfring G J 2019 *Phys. Rev. Lett.* **123** 158006
[29] Liebchen B, Monderkamp P, ten Hagen B and Löwen H 2018 *Phys. Rev. Lett.* **120** 208002
[30] Daniels M J, Longland J M and Gilbart J 1980 *Microbiology* **118** 429
[31] Kaiser G and Doetsch R 1975 *Nature* **255** 656
[32] Petrino M G and Doetsch R 1978 *Microbiology* **109** 113
[33] Takabe K, Tahara H, Islam M S, Affroze S, Kudo S and Nakamura S 2017 *Microbiology* **163** 153
[34] Sprenger A R, Fernandez-Rodriguez M A, Alvarez L, Isa L, Wittkowski R and Löwen H 2020 *Langmuir* **36** 7066

[35] Torquato S 2018 *Phys. Rep.* **745** 1–95
[36] Ma Z and Torquato S 2017 *J. Appl. Phys.* **121** 244904
[37] Chen Y, Britton W A and Dal Negro L 2021 *Opt. Lett.* **46** 5360
[38] Klatt M A, Hörmann M and Mecke K 2022 *J. Stat. Mech.: Theory Exp.* **2022** 043301
[39] Sutton R S and Barto A G 2018 *Reinforcement Learning: An Introduction* (Cambridge, MA: MIT Press)
[40] Louste C and Liégeois A 2000 *JINT* **27** 99
[41] Reynoso-Mora P, Chen W and Tomizuka M 2016 *Optim. Control Appl. Methods* **37** 1263
[42] McGough J S and Riley K 2004 *Nonlinear Anal. Real World Appl.* **5** 105
[43] Gray P and Scott S K 1990 *Chemical Oscillations and Instabilities: Non-Linear Chemical Kinetics* (Oxford: Clarendon)
[44] Ma X, Hahn K and Sanchez S 2015 *J. Am. Chem. Soc.* **137** 4976
[45] Demirörs A F, Akan M T, Poloni E and Studart A R 2018 *Soft Matter* **14** 4741

P5.2 Supplementary material: Active particles using reinforcement learning to navigate in complex motility landscapes

Supplementary Material: Active particles using reinforcement learning to navigate in complex motility landscapes

Paul A. Monderkamp
Institut für Theoretische Physik II: Weiche Materie, Heinrich-Heine-Universität Düsseldorf, Universitätsstraße 1, 40225 Düsseldorf, Germany
E-mail: paul.monderkamp@hhu.de

Fabian Jan Schwarzendahl
Institut für Theoretische Physik II: Weiche Materie, Heinrich-Heine-Universität Düsseldorf, Universitätsstraße 1, 40225 Düsseldorf, Germany

Michael A. Klatt
Institut für Theoretische Physik II: Weiche Materie, Heinrich-Heine-Universität Düsseldorf, Universitätsstraße 1, 40225 Düsseldorf, Germany

Hartmut Löwen
Institut für Theoretische Physik II: Weiche Materie, Heinrich-Heine-Universität Düsseldorf, Universitätsstraße 1, 40225 Düsseldorf, Germany
November 2021

1. Learning environments

We train the swimmer in a Gaussian random wave model (GRW). To construct an appropriate motility field, we use a sinusoidal function

$$g(\mathbf{r}) = \sum_{n=1}^{M} \cos\left(\mathbf{k}_n \mathbf{r} + \eta_n\right), \tag{1}$$

where the $\mathbf{k}_n$ and random wave vectors with $\|\mathbf{k}_n\| = 20/L$, drawn from an isotropic probability distribution and the η_n are random phases, uniformly distributed in $[0, 2\pi)$. M denotes the number of superposed harmonic waves. We pick $M = 100$, which is sufficient to obtain peaks with the shape of Gaussian bell curves. The motility field $\mu(\mathbf{r})_{GRW}$ is obtained from $g(\mathbf{r})$ via

$$\mu(\mathbf{r})_{GRW} = \frac{1}{1 + \exp\left(\lambda\left[0.5 - [\tilde{g}(\mathbf{r})]^{\nu}\right]\right)}, \tag{2}$$

where $\tilde{g}(\mathbf{r})$ is obtained from $g(\mathbf{r})$ via renormalising to the interval $[0, 1]$. We vary the exponent ν, in order to shift the whole function towards 0 or 1, and therefore control the average function value $\langle\mu\rangle$, by which the difficulty of a given field is characterised. Here, $\langle\mu\rangle$ denotes the average over space and independent realisations of the field $\mu(\mathbf{r})$. With the help of the outside sigmoid function, with the parameter $\lambda = 10$, $\mu(\mathbf{r})_{GRW}$ is pushed away from 0.5 towards 0 and 1. This modification is performed to obtain a continuous field, where the majority of the space is occupied by either low motility regions or high motility regions. One example is shown in Fig. 1.**(a) (main text)**. Furthermore, the final $\mu(\mathbf{r})$ is modified with appropriate sigmoid functions of the y-coordinate, to avoid low motility zones on the starting- or finish line. To test the versatility of the machine learning model, different methods for the generation of the motility field $\mu(\mathbf{r})$ are employed (see Sec.3B (main text)).

1.1. Gray-Scott model for field generation

The Gray-Scott model for reaction diffusion through integration of the Gray-Scott model for reaction-diffusion [1, 2] can be used to generate fields, that can be used as motility fields $\mu(\mathbf{r})$. The equations model the time evolution of two scalar fields, that diffuse and interact with each other through the dynamics prescribed be the equations

$$\frac{\partial u}{\partial t} = D_u \nabla^2 u + uv^2 + f(1-u), \tag{3}$$

$$\frac{\partial v}{\partial t} = D_v \nabla^2 v + uv^2 - (f+k)v. \tag{4}$$

In Fig. 6 **(d)** (main text), we use a single solution, that fulfills $\langle\mu\rangle \approx 0.557$, generated with the parameters with $D_u = 0.2$, $D_v = 0.1$, $f = 0.0545$, $k = 0.06125$. u and v are initialised to 0.5 and 0.25 within a square of side length $L/5$ in the middle of the simulation box, respectively. Random Gray-Scott fields, as used in Fig. 6 **(f)**

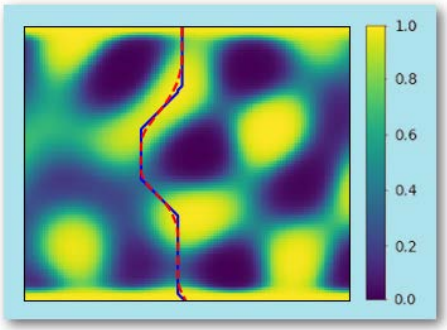

Figure 1: Trajectories approximating the globally optimal trajectory obtained with *Dijkstra's algorithm*. **Blue solid curve**: Trajectory obtained after employing *Dijkstra's algorithm* on a discrete square grid in the simulation box, using local swimming time (Eq. (5)) as grid distances. **Red dashed curve**: Approximation to the globally optimal trajectory, obtained after heuristic optimisation with a Monte-Carlo approach, using continuous trajectory nodes.

(main text), can be generated for this choice of parameters, for instance, by initialising each node of the u-mesh to a random number in $[0, 1]$ and the each node on the v-mesh to a random number in $[0, 0.5]$. The fields are discretised on a quadratic mesh of size 150×150. We solve the equations via an explicit forward Euler scheme in time, where we integrate for 10^4 time-steps with $\Delta t = 1$, with periodic boundary conditions. Finally, after appropriate renormalisation, we use the resulting $v(\mathbf{r})$ as motility field $\mu(\mathbf{r})$.

2. Augmented Dijkstra's algorithm

In order to obtain a visual reference for the ability of the swimmer to find a reasonable path through the environment, as well as having a quantitative benchmark for the difficulty of any environment $\mu(\mathbf{r})$, we perform a global optimisation scheme with the help of *Dijkstra's (shortest path) algorithm* [3]. E.W. Dijkstra initially conceptualised this algorithm for finding the shortest distance between two given nodes in a discrete network. A slightly more modern version, assumes an origin node and calculates the shortest distance from each node to the origin node.

In our version, we start with a network, where the positions of the nodes fall on the grid positions of the discretised motility field. We assign the node, closest to the designated starting position of the swimmer as origin node. The neighbours of the network are vertical, horizontal and diagonal next neighbours within the square grid. In accordance to the standard procedure of *Dijkstra's algorithm*, we initialise the total distances of all nodes to the starting node to ∞, except itself. We update all total distances iteratively by evaluating the distances to all next neighbours, starting from

the origin node, visiting each node once. The network distance $d_{i,j}$ between a pair of neighbouring grid nodes i, j at $\mathbf{r}_i$,$\mathbf{r}_j$ we define by the Euclidian distance divided by the mean local swimmer velocity

$$d_{i,j} = \frac{2\,\|\mathbf{r}_i - \mathbf{r}_j\|}{v_0(\mu(\mathbf{r}_i) + \mu(\mathbf{r}_j))}. \tag{5}$$

Minimising with respect to the sum of the instantaneous swimming times $\sum_k d_{k,k+1}$, in a trajectory, yields an approximation to the solution of the functional, given in Eq. (5) (main text), for any point in the simulation box $\mathbf{r}_1$ and the starting point $\mathbf{r}_0$ assuming the constraint, that the swimmer may only turn by angles that are multiples of $\pi/4$. We choose as destination node, the node on the finish line, with the shortest distance to the origin node. Over the execution of *Dijkstra's algorithm*, we save for each node the ancestor node, from which the shortest distance is obtained, such that we can backtrace optimal trajectories to the origin node in this step (see Fig. 1, blue solid line).

In a second step, we augment the search for an optimal trajectory with a Monte-Carlo optimisation, to accommodate for the lack for continuous angles. More specifically, we perform 1000 Monte-Carlo cycles in which we displace the individual nodes to optimise for the total travel time along the trajectory. We accept a trial displacement only, if it decreases the total travel time. This heuristic supplementation results in smoother curves, and slightly reduces the total travel time (see. Fig. 1, red dashed line).

In practice, we use this optimal first passage time as quantitative measure of the difficulty for the swimmer to maneuver through environments for a given set of parameters. More specifically, in the beginning of each training procedure, we use the current environment parameters, to generate a set of typical environments and solve it with the protocol described above. We multiply the obtained average first passage time with 100 and use this as a termination criterion $T_{\max}$ for the individual episodes. We have found that this value of all the simulated environments typically corresponds to $10^{-3} \lesssim v_y/v_0 \lesssim 10^{-2}$.

3. Angular discretisation M_ϕ

To investigate the influence of the discretisation of the orientation angles M_ϕ, on the overall performance of the algorithm, we here present results for different values than the one used in the main manuscript ($M_\phi = 12$). We generated additional simulation results with the physical parameters used throughout the majority of the main manuscript, i.e., with rotational Peclét number $\mathcal{P}_{\text{rot}} \approx 46$ (see main manuscript Eq. (7)) and average value of the Gaussian random wave based motility fields $\langle\mu\rangle \approx 0.557$ (see Sec. 1). Fig. 2.**(a)** shows a typical trajectory for the QABP with $M_\phi = 24$. Qualitatively, the trajectory looks similar to the trajectories with $M_\phi = 12$ presented in the main manuscript. We have additionally gathered performance data from 10^3 trajectories from ten independent simulations. The resulting performance $\langle v_y\rangle/v_0 \approx 40.5$ is very

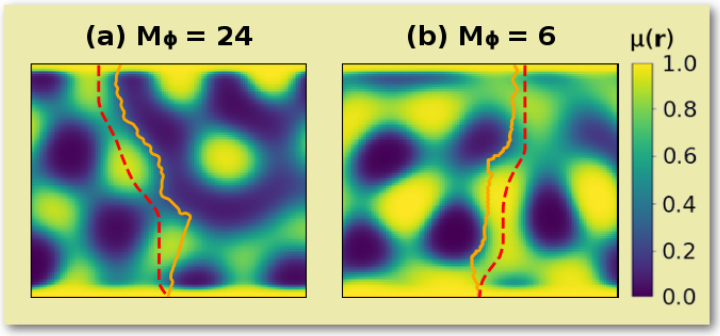

Figure 2: Trajectories of QABP with different angular discretisations **(a)** $M_\phi = 24$ and **(b)** $M_\phi = 6$ ($M_\phi = 12$ in the main manuscript). The results are simulated at rotational Peclét number $\mathcal{P}_{\text{rot}} \approx 46$ (see main manuscript Eq. (7)) within fields $\mu(\mathbf{r})$ with $\langle\mu\rangle \approx 0.557$. As visible from the shape of the trajectory, the reinforcement learning algorithm converges quickly in M_ϕ. For $M_\phi = 24$, the performance $\langle v_y\rangle / v_0 \approx 40.5$ is very similar to that with $M_\phi = 12$. Crucially, the performance of the QABP with $M_\phi = 6$, $\langle v_y\rangle / v_0 \approx 35.4$, is still very close even though, due to the discretisation of the allowed swimming directions, the QABP is not allowed to swim directly towards the target in the upwards vertical direction (see zig-zag pattern in the trajectory close to the finish line in **(b)**).

similar to the case with $M_\phi = 12$ (cf. performance Figs. 5.**(a)** and Figs. 5.**(b)** in the main manuscript). Importantly, the algorithm performs similarly well even for the case, where the discretisation is as coarse as $M_\phi = 6$. For this value, the allowed swimming directions $k \times 2\pi/M_\phi$, $k \in \{0, 1, ..., M_\phi - 1\}$ do not include the vertical direction, which is prominently visible in the zig-zag pattern close to the finish line in Fig. 2.**(b)**. Nevertheless, the QABP is able to perform well with $\langle v_y\rangle / v_0 \approx 35.4$.

4. Velocity state threshold μ_0

In our reinforcement learning model, the QABP receives information about its own instantaneous velocity $v_0\mu(\mathbf{r})$ in form of a binary discretisation. The state space of the agent encodes the information, whether the current $\mu(\mathbf{r})$ is either above or below a threshold value μ_0. As visible from the large peak just above μ_0 in the velocity distribution of the QABP in Fig. 4 (main text), this threshold value directly determines the regions in the environment, that the swimmer aims to evade. Consequently, μ_0 directly influences the performance $\langle v_y\rangle / v_0$ of the swimmer (see Eq. (6) (main text)).

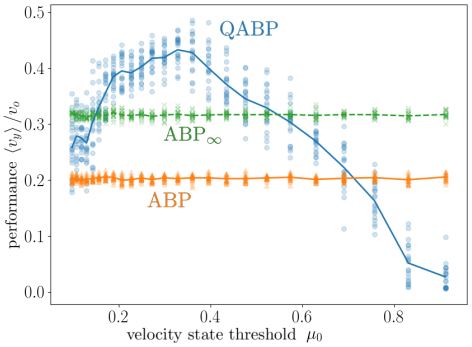

Figure 3: Performances $\langle v_y \rangle / v_0$ of the QABP as a function of the velocity state threshold μ_0 at $\mathcal{P}_{\text{rot}} \approx 46$. The environments are generated with the help of as Gaussian random waves (see. Sec. 1) with $\langle \mu \rangle \approx 0.557$. The scattered data data points indicate a simulation with 10^3 trajectories each. The solid lines denote the averages over the respective ten data points per parameter set. For reference, the figure shows the respective performances of ABP and ABP$_\infty$, which swims in a straight line.

It is reasonable to expect, that a variable threshold for the velocity discretisation, thus creating a possibility for the swimmers to adjust better to their surroundings, can substantially increase the performance. A concrete implementation, which retains the local quality of the algorithm might be to allow the swimmer to collect and store information about the previously encountered scalar field values of $\mu(\mathbf{r})$, which in turn would increase the swimmers capabilities, but also increase the required storage space (cf. SM Sec. 7). In the interest of keeping the model as simple as possible, we opt for a constant choice of μ_0.

We show $\langle v_y \rangle / v_0$ as a function of μ_0 in Fig. 3 at $\mathcal{P}_{\text{rot}} \approx 46$. The environments are generated with the help of Gaussian random waves (see. Sec. 1) with $\langle \mu \rangle \approx 0.557$. Even though independent of μ_0, we show the performance of an active Brownian particle (ABP) and a particle swimming along a straight line trajectory (ABP$_\infty$) for reference.

As expected, the performance $\langle v_y \rangle / v_0$ as a function of μ_0 shows non-monotonic behaviour. For $\mu_0 \ll 1$, the lowest velocity, that the particle tolerates increases, hence $\langle v_y \rangle / v_0$ increases. In the limit $\mu_0 = 1$, the QABP considers the whole environment as low motility to avoid and the algorithm ceases to function. As a result, for larger μ_0, the relative differences between the instantaneous swimming velocities decrease in importance. Instead, the free space to maneuver dominates. In between the two competing limits, there is an optimal μ_0 at approximately 0.3 for this choice of environment and $\langle \mu \rangle$. In the training of the QABP, we choose $\mu_0 = 0.25$.

5. Reward for QABP

To impel a net upward motion of the swimmer, the last action is rewarded with $R_f = 100$ if the swimmer reaches the top of the box. To disincentivise the motion through low motility zones, an action is punished with $R_\mu = -0.5$, if it coincides with the termination of the episode due to entering a low motility region $\mu < 0.125$.

Maneuvering with only local information in randomly generated fields almost inevitably leads to the encounter of dead end situations, depending on the difficulty of the environment, i.e. $\langle\mu\rangle$. In these cases, given only the two aforementioned rewards R_f, R_μ, the swimmers trajectory coils up, and the swimmer is almost stuck in place. We suppress this issue, by introducing a third reward, which aims to incentivise the QABP towards trajectories with higher persistence. To this end, the swimmer memorises 100 of its own local position, over a time of $100\tau_Q$. The swimmer measures its displacement with respect to the average of its saved positions.

In almost all trajectories, where the swimmer does not get stuck, the respective displacement lies around 1.0. On the contrary, when it does get stuck, the displacement is close to 0. Therefore we introduce an additional punishment. If the displacement above falls below a value 0.5, the current action is punished by $R_p = -0.4$. In general, the choice of this threshold value depends on the typical length scale of the environment. Here, employing a general threshold value sufficiently enhances the performance of the QABP across all simulated parameters.

6. ϵ-greedy policy

In every episode, the swimmer is given a random probability ϵ, with which random actions are performed. Otherwise it uses $\mathcal{Q}$ as basis for decision. In episode 1, ϵ is initialised as 1 and linearly decreases until episode 10^3, after which another 1000 episodes are performed at $\epsilon = 0$, each in a new environment. At $\epsilon = 0$ the training procedure is considered to be finalised, $\mathcal{Q}$ to be converged, and the corresponding results are sampled. While sampling, the trajectories upon entering low motility zones are not terminated. If the swimmer surpasses the upper bound $T_{\max}$, the trajectory is terminated and the first passage time is considered to be equal to ∞. This protocol of a decreasing ϵ takes into consideration the initial ignorance of the swimmer about his environment, and therefore the swimmer relies on random exploration. As the training proceeds, the decision matrix $\mathcal{Q}$ becomes gradually more reliable, and the swimmer targets the $\mathcal{Q}$ entries which are more likely to be the locally correct choices.

7. Data storage

The total amount of data storage that is needed for the decision matrix (Q-matrix) in our model necessitates $12 \times 12 \times 2 \times 3 = 864$ floating point numbers. The additional amount of data that is needed for the displacement reward R_p incorporates 200 floating

Landscape structure	QABP	Dijkstra's	ABP_∞	ABP
standard GRW-based	$0.405 \pm 3\times10^{-2}$	$0.698 \pm 3\times10^{-2}$	$0.320 \pm 6\times10^{-2}$	$0.204 \pm 6\times10^{-2}$
periodic GRW-based [6.(a)]	$0.401 \pm 3\times10^{-2}$	$0.675 \pm 3\times10^{-2}$	$0.273 \pm 5\times10^{-3}$	$0.170 \pm 5\times10^{-3}$
slanted left [6.(b)]	$0.123 \pm 1\times10^{-2}$	$0.678 \pm 6\times10^{-2}$	$0.042 \pm 4\times10^{-5}$	$0.011 \pm 3\times10^{-4}$
slanted right [6.(c)]	$0.128 \pm 7\times10^{-3}$	$0.720 \pm 6\times10^{-2}$	$0.042 \pm 3\times10^{-5}$	$0.011 \pm 3\times10^{-4}$
Gray-Scott [6.(d)]	$0.578 \pm 4\times10^{-2}$	$0.709 \pm 5\times10^{-2}$	0.102 ± 0.00	$0.186 \pm 5\times10^{-3}$
randomly scattered [6.(e)]	$0.428 \pm 3\times10^{-2}$	$0.686 \pm 4\times10^{-2}$	$0.302 \pm 6\times10^{-3}$	$0.194 \pm 4\times10^{-3}$
GS & scattered [6.(f)]	$0.410 \pm 2\times10^{-2}$	$0.670 \pm 8\times10^{-2}$	$0.372 \pm 5\times10^{-3}$	$0.245 \pm 3\times10^{-3}$

Table 1: Performances $\langle v_y \rangle / v_0$ (and respective standard deviations) of different trajectories within the environments, and the same physical parameters, as presented in Fig. 6 in the main manuscript. Presented are the performances of all methods used in the main text: the QABP, the trajectory obtained with Dijkstra's algorithm, ABP_∞ and ABP. The different environments pose challenges of varying difficulty to the different swimmers. The trajectory obtained with Dijkstra's algorithm stays relatively constant.

point numbers for the hundred positions in two-dimensional space. The latter 200 floating point numbers can be ommited in practical applications, by employing a finalised decision matrix $\mathcal{Q}$ obtained, e.g., in our computer simulation.

8. Computational cost of the simulation

The simulation code is written in standard python, where all of the calculations are done within the algebraic framework given by the *numpy* library [4] without any external machine learning specific libraries. Additionally, large fractions of the code was just-in-time compiled with the help of *numba* [5], reaching computation speeds that are competitive against precompiled code in languages such as *C/C++*.

Much of the development and testing was done on a single computer, with an INTEL(R) CORE(TM) i5-4460 with a clock speed of 3.2 GHz, where the code ran purely in python without parallelisation and took around 20 minutes per independent training procedure, including the rendering and output of around 50 pictures.

Two significant parameters that determine the runtime of the simulation are the number of episodes of N_{epi} and the average function value of the motility field $\langle \mu \rangle$. In our experience, the time of execution of the learning protocol scales approximately as $T_{\text{exec}} \propto N_{epi}^1$. Secondly, since the average velocity of the particle is determined by $\langle \mu \rangle$, we expect that $T_{\text{exec}} \propto \langle \mu \rangle^{-1}$, which is coherent with our observations.

9. Performances of different trajectories within different environments

In Fig. 6 of the main manuscript, we present a range of simulation results, where we train the QABP on a standard Gaussian random wave based (GRW) environment (see Sec. 1), and after completion of the learning phase, place it into different environments,

which were unknown until after the training. Each of the six panels **(a-f)** in Fig. 6 corresponds to a different protocol/algorithm of generating environments. In Fig. 6 we give the performances $\langle v_y \rangle / v_0$ of the QABP for the different environments to draw a quantitative comparison of the swimmers capabilities in different unknown environments.

In Tab. 1 in this section, we present the performances for the trajectories of QABP, the optimal trajectory, calculated with *Dijkstra's algorithm* (cf. Sec. 2), as well as the performances of the straight line trajectory (ABP_∞) and an active Brownian particle (ABP). The data is gathered from ten simulation runs per data paint with 10^3 trajectories each, at the same parameters as in Fig. 6 of the main manuscript ($\mathcal{P}_{\mathrm{rot}} \approx 46$, $\langle \mu \rangle \approx 0.557$). The performance $\langle v_y \rangle / v_0$ of the optimal trajectory is fairly uniform at approximately 0.7, across all environments. Despite this, the performances of the QABP vary in the different fields. This illustrates the relative difficulty of the different environments, due to their different local structures, for the QABP with only local information.

As an example, we consider the slanted environments **(b,c)**. Here, the swimmer continuously attempts to swim upwards, sliding across the lower boundaries of the slanted low motility zones, because it has learned in the training on the GRW based environments, that this is a profitable strategy. This keeps its velocity permanently drastically reduced at $v \approx \mu_0 v_0 = 0.25 v_0$. Instead, training on these environments immediately, the swimmer incorporates this structure into his learned experience, and will utilise this during performance testing.

Note that for our Gray-Scott model, the standard deviation of $\langle v_y \rangle / v_0$ of the ABP_∞ is zero, since the environment is solved from the same initial conditions every time, and the trajectory is deterministic.

[1] McGough J S and Riley K 2004 *Nonlinear Anal. Real World Appl.* **5** 105–121
[2] Gray P and Scott S K 1990 *Chemical oscillations and instabilities: non-linear chemical kinetics* (Clarendon Press, Oxford)
[3] Dijkstra E W *et al.* 1959 *Numerische Mathematik* **1** 269–271
[4] Harris C R, Millman K J, Van Der Walt S J, Gommers R, Virtanen P, Cournapeau D, Wieser E, Taylor J, Berg S, Smith N J *et al.* 2020 *Nature* **585** 357–362
[5] Lam S K, Pitrou A and Seibert S 2015 Numba: A llvm-based python jit compiler *Proceedings of the Second Workshop on the LLVM Compiler Infrastructure in HPC* pp 1–6

P6 Statistics of carrier-cargo complexes

Published as ArXiv-preprint and reproduced from

R. Wittmann, P. A. Monderkamp and H. Löwen
Statistics of carrier-cargo complexes,
arXiv:2303.04005 (2023),

Digital Object Identifier (DOI): `https://doi.org/10.48550/arXiv.2303.04005`

Statement of contribution

The project was conceptualised by R. Wittmann and H. Löwen. I fulfilled a supportive role in the conceptualisation. R. Wittmann performed the derivation of the equations via DFT and provided the first complete draft of the main text. I numerically solved the equations, yielded by the DFT. I performed the simulations, designed the figures and performed the visualisation of the theoretical and simulation data. Funding and overseeing was provided by H. Löwen. All authors contributed text associated with their respective expertise in paper and appendix and contributed to the finalisation of the manuscript.

P6.1 Paper and appendix: Statistics of carrier-cargo complexes

Statistics of carrier-cargo complexes

René Wittmann,[1,*] Paul A. Monderkamp,[1] and Hartmut Löwen[1]

[1] *Institut für Theoretische Physik II: Weiche Materie, Heinrich-Heine-Universität Düsseldorf, 40225 Düsseldorf, Germany*

(Dated: March 8, 2023)

We explore the statistics of assembling soft-matter building blocks to investigate the uptake and encapsulation of cargo particles by carriers engulfing their load. While the such carrier-cargo complexes are important for many applications out of equilibrium, such as drug delivery and synthetic cell encapsulation, we uncover here the basic statistical physics in minimal hard-core-like models for particle uptake. Introducing an exactly solvable equilibrium model in one dimension, we demonstrate that the formation of carrier-cargo complexes can be largely tuned by both the cargo concentration and the carriers' interior size. These findings are intuitively explained by interpreting the internal free space (partition function) of the cargo inside a carrier as its engulfment strength, which can be mapped to an external control parameter (chemical potential) of an additional effective particle species. Such a mapping can be generally applied to account for attractive interactions, multiple cargo uptake and various carrier or cargo species. Within this effective equilibrium picture, we then suggest to employ effective non-Boltzmann occupation laws to describe the statistics of non-equilibrium particle uptake on the coarse-grained level. As a particular example, we put forward a Bose-Einstein-like phase transition associated with polydisperse carrier properties.

I. INTRODUCTION

When two or more soft-matter building blocks are combined, self-organization can lead to novel hierarchical structures with unusual material properties [1–10]. One archetypal problem is a mesoscopic carrier particle that swallows or uptakes smaller cargo particles to build a carrier-cargo complex. These superstructures can occur in quite diverse situations ranging from greenhouse gases stored in porous liquids [11, 12] over adsorbed or encapsulated drugs which need to be delivered to a target [13–18] to molecules or nanoparticles that penetrate through the membrane of synthetic and living cells [19–25] or bacteria engulfed by phagocytes [26, 27]. Complex assemblies on a larger scale involve colloidal particles that are embedded within, e.g., droplets [28–31] or vesicles [32–35], or dock at surfaces [36–39].

Despite this plethora of realizations of particle uptake or encapsulation, the collective properties of larger assemblies of such interacting particles have not yet been systematically explored. Even with simple pair interactions, the statistics of carrier-cargo mixtures has barely been considered from the angle of classical statistical mechanics. This is most likely due to the intrinsic complexity of internal degrees of freedom, needed for a basic description of particles which are swallowed (or ejected again) and thus continuously change their role from freely floating to loaded cargo. Therefore there is a principal need for minimal models which provide insight into the composition and structure of such carrier-cargo mixtures.

Here, we develop a controlled setting, which allows us to classify the occupation statistics of different carrier-cargo mixtures and predict their structural properties within a first-principles framework of statistical mechanics. First, we devise a basic model involving hollow carriers with excluded-volume interactions to exemplify that the emerging complexes of carriers occupied by cargo can be efficiently considered as individual species. This equilibrium picture allows us relate the occupation probability (or engulfment strength) directly to the partition functions of confined cargo particles. Second, in view of the variety of the soft matter zoo or applications in biology, we interpret the individual engulfment strength as a coarse-grained quantity that should take into account processes at the carrier membrane. Third, we postulate effective non-equilibrium occupation laws for uptake of multiple carriers and show that these can lead to intriguing collective effects, as exemplified by identifying a Bose-Einstein condensation outside the quantum world [40–42].

The paper is arranged as follows. We first introduce our excluded-volume model in Sec. II and outline a general rigorous mapping to an effective system, which allows for an exact solution in one dimension. This mapping is then applied in Sec. III to determine different properties of carrier-cargo mixtures, where we also show that our theoretical treatment leads to highly accurate predictions in higher dimensions. Moreover, we elaborate on the role of attractive or soft interactions and propose the relevance for applications to non-equilibrium particle uptake on a coarse-grained level. We then conclude in Sec. IV.

II. THEORETICAL TREATMENT

A. Excluded-volume model

The ingredients of our minimal model in d spatial dimensions are illustrated in Fig. 1. We consider two fundamental types of particles: carriers, which offer internal storage space, and cargo, which can occupy this space.

* Rene.Wittmann@hhu.de

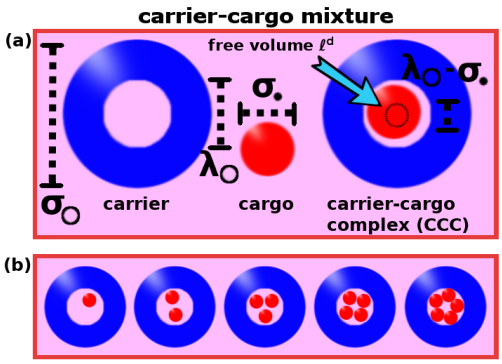

FIG. 1. Hard-body model for complex-forming carrier-cargo mixtures. (a) A hollow carrier (blue) and a smaller cargo (red) with annotated size parameters as basic building blocks. The d-dimensional free volume ℓ^d (black circle) available to the center of the loaded cargo drives the formation of a carrier-cargo complex (CCC). For $\lambda_\bigcirc - \sigma_\bullet < \sigma_\bullet$ there exists only one possible CCC. (b) A carrier with larger interior ($\lambda_\bigcirc - \sigma_\bullet > \sigma_\bullet$) can hold more than one cargo and thus different CCCs can form, illustrated here for occupation numbers $\nu = 1, \ldots, 5$.

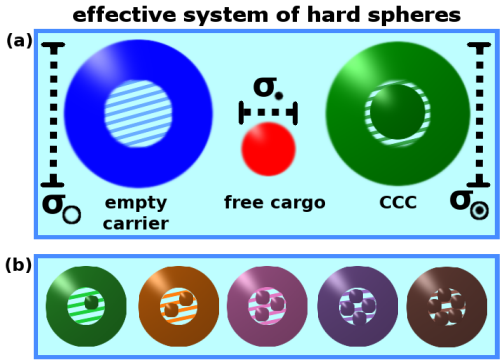

FIG. 2. Effective description of the carrier-cargo mixtures depicted in Fig. 1 as d-dimensional hard spheres. Each CCC consisting of one carrier and exactly ν cargo particles is associated with an effective species. All CCCs have the same physical properties, i.e., the same diameter $\sigma_{\circledcirc} \equiv \sigma_\bigcirc$, as the carriers (indicated by the shaded interior). The internal degrees of freedom due to carrier occupation are mapped onto the effective chemical potential(s) (a) $\mu_{\circledcirc}$, defined in Eq. (10), or (b) μ_ν, defined in Eq. (25), of the CCCs. The empty carriers and free cargo have the chemical potentials $\mu_\bigcirc$ and $\mu_\bullet$, respectively.

A carrier whose internal degrees of freedom are explored by cargo, represents a carrier-cargo complex (CCC). All particles are radially symmetric and interact solely via their excluded volume. The carriers have diameter $\sigma_\bigcirc$ and posses a void space of diameter $\lambda_\bigcirc$ in their interior. The diameter of the cargo is denoted by $\sigma_\bullet$. While particles of the same species $i \in \{\bigcirc, \bullet\}$ interact with each other as d-dimensional hard spheres with the potential

$$U_{ii}(r) = \begin{cases} 0 & \text{for } r \geq \sigma_i \,, \\ \infty & \text{else} \,, \end{cases} \tag{1}$$

the interaction between a cargo and a carrier is given by

$$U_{\bullet\bigcirc}(r) = U_{\bigcirc\bullet}(r) = \begin{cases} 0 & \text{for } r < (\lambda_\bigcirc - \sigma_\bullet)/2 \,, \\ 0 & \text{for } r \geq (\sigma_\bigcirc + \sigma_\bullet)/2 \,, \\ \infty & \text{else} \,, \end{cases} \tag{2}$$

where r is the center-to-center distance between a pair of particles.

As illustrated in Fig. 1a, there exists a single possible CCC, representing a carrier holding exactly one cargo, if $\sigma_\bullet < \lambda_\bigcirc < 2\sigma_\bullet$. For carriers with larger interiors, multiple CCCs can form, see Fig. 1b. We will outline below, that the driving force of CCC formation is generally related to the standard Boltzmann statistics for a system of cargo particles in a cavity with the shape of the interior of the carrier. Hence, the carrier occupation in our hard-body model is limited by close packing. Our model is evaluated via Monte-Carlo simulation in the canonical ensemble with M carriers and N cargo particles, as described in appendix A, and, in the following, by statistical calculations in the grand canonical ensemble, where $\mu_\bigcirc$ and $\mu_\bullet$ denote the chemical potentials of the two particle species.

B. Exact solution in one dimension

To demonstrate step by step how to treat the general problem of CCC formation in an elegant way through effective chemical potentials, we first consider the most intuitive model for a carrier-cargo mixture in which the carriers can hold at most one cargo. We further focus for the moment on one spatial dimension where it is exactly solvable. For this setup, we define the free length

$$\ell := \lambda_\bigcirc - \sigma_\bullet \tag{3}$$

of one loaded cargo within a carrier, such that $\ell < \sigma_\bullet$. Note that also the case with $\lambda_\bigcirc > 2\sigma_\bullet$, allowing for multiple carrier occupation, is exactly solvable in one dimension, but for clarity of the following presentation, we will discuss this scenario later in Sec. II C.

1. *Canonical partition function*

As a first step we provide the exact canonical partition function Z_{MN} of the carrier-cargo mixture. The standard partition function $\mathcal{Z}^{(L)}_{N_1,N_2,\ldots,N_K}(\sigma_1, \sigma_2, \ldots, \sigma_K)$ of a

K-component hard rod mixture in a system of length L, consisting of N_i particles of length σ_i for species $i = 1, \ldots, K$, in is stated in appendix B as a reference. Denoting by $C \leq \min(M, N)$ the number of CCCs (the carrier particles which are occupied by a cargo particle), we find

$$Z_{MN} = \sum_{C=0}^{\min(M,N)} \mathcal{Z}^{(L)}_{M,N-C}(\sigma_\bigcirc, \sigma_\bullet) \frac{\ell^C}{\Lambda^C C!} \frac{M!}{(M-C)!}, \tag{4}$$

where Λ is the thermal wave length. Each term in this sum corresponds to a number $N - C$ of free cargo particles interacting with the M carriers as hard rods, while a multiplicative factor accounts for the occupation statistics of the C bounded cargo particles within the CCCs.

Substituting $\mathcal{Z}^{(L)}_{M,N}$ into Eq. (4) we get

$$Z_{MN} = \sum_{C=0}^{\min(M,N)} \frac{(L - M\sigma_\bigcirc - (N-C)\sigma_\bullet)^{(M+N-C)}\, \ell^C}{\Lambda^{M+N}(M-C)!(N-C)!C!}. \tag{5}$$

Although the sum over C cannot be explicitly calculated, this result suggests an alternative interpretation of the binary carrier-cargo mixture as an effective three-component mixture, illustrated in Fig. 2, with the species denoted as empty carriers, free cargo and occupied carriers, i.e., CCCs. As shown in appendix C, this becomes clear by expressing Eq. (5) solely in terms of the partition functions $\mathcal{Z}^{(L)}_{M-C,N-C,C}(\sigma_\bigcirc, \sigma_\bullet, \sigma_\bigcirc)$ and $\mathcal{Z}_1^{(\lambda_\bigcirc)}(\sigma_\bullet) = \ell/\Lambda$.

2. *Grand canonical partition function*

The interpretation of the CCCs as members of a third particle species with ℓ being an intrinsic control parameter, becomes more transparent when switching to the grand-canonical picture. The exact grand canonical partition function

$$\Xi = \sum_{M=0}^{\infty} \sum_{N=0}^{\infty} \sum_{C=0}^{\min(M,N)} \frac{z_\bigcirc^M z_\bullet^N \ell^C}{(M-C)!(N-C)!C!} \times (L - M\sigma_\bigcirc - (N-C)\sigma_\bullet)^{(M+N-C)} \tag{6}$$

of the carrier-cargo mixture can be determined from weighting Eq. (5) with the fugacities $z_i := e^{\beta\mu_i}/\Lambda$ of species $i \in \{\bigcirc, \bullet\}$, where μ_i are the respective chemical potentials and $\beta = (k_\mathrm{B}T)^{-1}$ is the inverse of the temperature T with Boltzmann's constant k_B. Recognizing the identity

$$\sum_{M=0}^{\infty} \sum_{N=0}^{\infty} \sum_{C=0}^{\min(M,N)} = \sum_{C=0}^{\infty} \sum_{M=C}^{\infty} \sum_{N=C}^{\infty} \tag{7}$$

for the infinite series and shifting the indices through the substitutions $M \to A + C$ and $N \to B + C$, Eq. (6) can be further evaluated as

$$\Xi = \sum_{A=0}^{\infty} \sum_{B=0}^{\infty} \sum_{C=0}^{\infty} \frac{z_\bigcirc^A z_\bullet^B (z_\bigcirc z_\bullet \ell)^C}{A!B!C!} \times (L - A\sigma_\bigcirc - B\sigma_\bullet - C\sigma_\bigcirc)^{(A+B+C)}, \tag{8}$$

where we have introduced the diameter $\sigma_\bigcirc \equiv \sigma_\bigcirc$ of the CCCs for later convenience.

3. *Exact mapping onto an effective ternary mixture*

Defining the effective fugacity

$$z_\bigcirc := \ell z_\bigcirc z_\bullet \tag{9}$$

associated with the third species of CCCs, we have established a proper mapping of the two-component carrier-cargo mixture onto a three-component mixture, illustrated in Fig. 2, of three (reacting) species: empty carriers, controlled by the chemical potential $\mu_\bigcirc$, free cargo, controlled by the chemical potential $\mu_\bullet$, and CCCs composed of one carrier and one cargo, with the effective chemical potential

$$\mu_\bigcirc := k_\mathrm{B}T \ln(\ell/\Lambda) + \mu_\bigcirc + \mu_\bullet. \tag{10}$$

The interpretation of this mapping is, that the average number of CCCs is determined by both the two external particle reservoirs, represented by $\mu_\bigcirc$ and $\mu_\bullet$ of the carrier-cargo mixture, and the internal degrees of freedom, represented by the free length ℓ explored by the cargo upon occupying a carrier.

While the sums in Eq. (8) can be explicitly carried out, we refrain here from doing so. Instead, we emphasize that, as soon as an effective fugacity (9) or chemical potential (10) is specified, the properties of the mixture can be explicitly evaluated using the vast toolbox from liquid-state theory [43]. This fundamental mapping holds even if the grand-canonical partition function cannot be exactly determined and will be generalized later to multiple cargo loading. In fact, to (approximately) describe a general interacting system, it is sufficient to know the combinatorics of the CCC formation to specify $z_\bigcirc$ and thus $\mu_\bigcirc$, as explored in more detail in appendix D.

In this manuscript, we make use of the framework of classical density functional theory (DFT) [44] introduced in appendix E In the special case of one-dimensional hard rods, considered so far, we can thus obtain the exact statistics by evaluating the Percus functional [45, 46] for a mixture of empty carriers of length $\sigma_\bigcirc$, free cargo of length $\sigma_\bullet$ and CCCs of the same length $\sigma_\bigcirc \equiv \sigma_\bigcirc$ as the carriers.

4. Number densities

Focusing on a spatially homogeneous system, we can gain general insight into the carrier-cargo mixture from Eq. (8). Introducing the homogeneous density operators $\hat{\rho}_X = \frac{X}{L}$, where $X \in \{M, N, A, B, C\}$ represents the number of particles in the different (effective) species, the probabilities of aggregation of the carrier and cargo into a CCC can be determined from the ensemble average (grand-canonical trace) $\langle \hat{\rho}_X \rangle$ of $\hat{\rho}_X$. Specifically, the total densities $\rho^{\mathrm{t}}_{\bigcirc} := \langle \hat{\rho}_M \rangle$ of all carriers and $\rho^{\mathrm{t}}_{\bullet} := \langle \hat{\rho}_N \rangle$ of all cargo particles in the carrier-cargo mixture can be calculated from Eq. (6) and the densities $\rho_{\bigcirc} := \langle \hat{\rho}_A \rangle$ of empty carriers, $\rho_{\bullet} := \langle \hat{\rho}_B \rangle$ of free cargo and $\rho_{\textcircled{\bullet}} := \langle \hat{\rho}_C \rangle$ of CCCs follow from Eq. (8).

Performing the same manipulations which were used to derive Eq. (8) from Eq. (6), it is easy to show that

$$\rho^{\mathrm{t}}_{\bigcirc} = \rho_{\bigcirc} + \rho_{\textcircled{\bullet}} \quad \text{and} \quad \rho^{\mathrm{t}}_{\bullet} = \rho_{\bullet} + \rho_{\textcircled{\bullet}} \tag{11}$$

These relations hold for any kind of interactions between the particles and also for a spatially inhomogeneous system. It is thus generally possible to recover information on the physical system from an effective DFT calculation based on the mapping in Eq. (10).

Moreover, if one is only interested in ratios of the (homogeneous) densities, it suffices to know the respective fugacities. For example, the fraction $\rho_{\textcircled{\bullet}}/\rho^{\mathrm{t}}_{\bigcirc}$ of CCCs, indicating the percentage of occupied carriers, follows as $\rho_{\textcircled{\bullet}}/\rho^{\mathrm{t}}_{\bigcirc} = z_{\textcircled{\bullet}}/z^{\mathrm{t}}_{\bigcirc}$. A concise discussion can be found in appendix D.

5. Pair distributions

To extract structural information on the carrier-cargo mixture from a standard calculation in the effective system, the relation, Eq. (11), between the number densities can also be generalized to pair distribution functions, which indicate the probability to find two particles of a certain species at distance $x = |x_1 - x_2|$. This can be achieved by use of the additivity of the two-body densities while taking into account that a CCC represents both a carrier and a cargo with blurred position.

As further explained in appendix F, it is possible to express the pair distributions $g^{\mathrm{t}}_{ij}(x)$ with $i, j \in \{\bigcirc, \bullet\}$ of the physical carrier-cargo mixture in terms of the (exactly known [47]) effective pair distributions $g_{ij}(x)$ with $i, j \in \{\bigcirc, \bullet, \textcircled{\bullet}\}$ of a three-component hard-rod mixture as

$$g^{\mathrm{t}}_{\bigcirc\bigcirc} = g_{\bigcirc\bigcirc}\,, \tag{12}$$

$$g^{\mathrm{t}}_{\bullet\bullet} = \frac{\rho^2_{\bullet} g_{\bullet\bullet} + \rho_{\bullet}\rho_{\textcircled{\bullet}} \left(g^{(\mathrm{b})}_{\bullet\textcircled{\bullet}} + g^{(\mathrm{b})}_{\textcircled{\bullet}\bullet} \right) + \rho^2_{\textcircled{\bullet}} g^{(\mathrm{bb})}_{\textcircled{\bullet}\textcircled{\bullet}}}{(\rho^{\mathrm{t}}_{\bullet})^2}\,, \tag{13}$$

$$g^{\mathrm{t}}_{\bigcirc\bullet} = \frac{\rho_{\bigcirc}\rho_{\bullet} g_{\bigcirc\bullet} + \rho_{\bigcirc}\rho_{\textcircled{\bullet}} g^{(\mathrm{b})}_{\bigcirc\textcircled{\bullet}} + \rho_{\bullet}\rho_{\textcircled{\bullet}} g_{\textcircled{\bullet}\bullet} + G^{(\mathrm{b})}_{\textcircled{\bullet}\textcircled{\bullet}}}{\rho^{\mathrm{t}}_{\bigcirc}\rho^{\mathrm{t}}_{\bullet}}\,, \tag{14}$$

$$g^{\mathrm{t}}_{\bullet\bigcirc} = g^{\mathrm{t}}_{\bigcirc\bullet}\,. \tag{15}$$

Here, the functions

$$g^{(\mathrm{b})}_{\textcircled{\bullet}l} := \frac{1}{\ell} \int \mathrm{d}x' \Theta(\ell/2 - |x_1 - x'|) g_{\textcircled{\bullet}l}(|x' - x_2|) = g^{(\mathrm{b})}_{l\textcircled{\bullet}}\,, \tag{16}$$

$$g^{(\mathrm{bb})}_{\textcircled{\bullet}\textcircled{\bullet}} := \frac{1}{\ell^2} \int \mathrm{d}x' \int \mathrm{d}x'' \Theta(\ell/2 - |x_2 - x''|) \times g_{\textcircled{\bullet}\textcircled{\bullet}}(|x' - x''|) \Theta(\ell/2 - |x_1 - x'|) \tag{17}$$

with $l \in \{\bigcirc, \bullet, \textcircled{\bullet}\}$ denote the blurred effective distributions and

$$G^{(\mathrm{b})}_{\textcircled{\bullet}\textcircled{\bullet}} := \frac{\rho_{\textcircled{\bullet}}}{\ell} \Theta(\ell/2 - |x_2 - x_1|) + \rho^2_{\textcircled{\bullet}} g^{(\mathrm{b})}_{\textcircled{\bullet}\textcircled{\bullet}}(|x_1 - x_2|) \tag{18}$$

denotes the blurred effective two-body density of two CCCs extended by a blurred self contribution.

C. Combinatorics of general particle complexes

As a next step, we extend our treatment (10) to general d-dimensional mixtures of κ different particle species, representing different types of both carriers and cargo. To this end, let us recall from Sec. II B 3 that it is sufficient to consider ideal point-like particles which only interact by forming complexes and establish the mapping for such a system. The notion of carrier and cargo particles then follows by assigning appropriate interactions in the effective system. In a more abstract manner, we can in general simply speak of free particles which can join to form a complex particle with internal degrees of freedom. This allows for further applications, for example, in the context of aggregation or clustering. In what follows, we continue using the term CCC when referring to any kind of effective complex particle.

1. General properties of a CCC

In a general mixture of κ components, the total number k of possible CCCs depends on both κ and the particular occupation statistics of the carriers determined by the physical interactions in the system. To establish the underlying combinatorics, let us denote the particle number, chemical potential and fugacity of species $i = 1, \ldots, \kappa$ as N_i, μ_i and $z_i = e^{\beta\mu_i}/\Lambda^d$, respectively. Now suppose a generic CCC of effective species $\nu = 1, \ldots, k$ is made up from joining in total $X_\nu = \sum_i x^{(i)}_\nu$ building blocks, where the $x^{(i)}_\nu$ denote the numbers of particles of species i contributing to that particular type of CCC.

Such a CCC has d external configurational degrees of freedom, associated with its spatial coordinates. The remaining $(X_\nu - 1)d$ internal configurational degrees of freedom act as a statistical weight for the aggregation and are specified by the underlying model. For example, in our hard-body model for carrier-cargo mixtures, we discuss in Sec. II D 3 that these correspond to the free volume available for the loaded cargo particles (or their canonical partition function for more general interactions). Therefore,

we choose for each ν an effective length scale ℓ_ν counting the number of states associated with one internal degree of freedom. In other words, the occupation parameters ℓ_ν follow from an occupation law of the carriers, which for equilibrium carrier-cargo mixtures always obeys standard Boltzmann statistics. More general occupation laws are suggested and discussed in Sec. III B 5.

2. Exact mapping onto a general effective mixture

In generalization of Eq. (9), the occurrence of general CCCs of species ν can be understood in terms of the effective fugacity

$$z_{\bullcirc}^{(\nu)} := \ell_\nu^{(X_\nu-1)d} \prod_i^\kappa z_i^{x_\nu^{(i)}}, \tag{19}$$

as we show below in Sec. II C 3. Upon expressing z_i and $z_{\bullcirc}^{(\nu)}$ in terms of μ_i and $\mu_{\bullcirc}^{(\nu)} = k_\mathrm{B}T \ln\left(z_{\bullcirc}^{(\nu)}\Lambda^d\right)$, respectively, we find the effective chemical potentials

$$\mu_{\bullcirc}^{(\nu)} := k_\mathrm{B}T(X_\nu - 1)\, d\, \ln(\ell_\nu/\Lambda) + \sum_{i=1}^\kappa x_\nu^{(i)}\mu_i\,. \tag{20}$$

This comprehensive combination law (20) can be utilized to describe any conceivable soft-matter system involving particle uptake or other types of bonding mechanisms in terms of $\kappa + k$ effective components.

3. General ideal partition functions

To derive Eq. (19), we consider point particles in a d-dimensional box of length L. For $\nu = 1, \ldots, k$ let us denote by C_ν the number of CCCs of species ν that are present in a specific (allowed) configuration. Then there are in total $C^{(i)} = \sum_{\nu=1}^k C_\nu x_\nu^{(i)}$ particles of species i which contribute to any CCC, such that $N_i - C^{(i)}$ particles of that species remain free (or empty). The condition that $N_i - C^{(i)} \geq 0$ for all i sets an upper bound to the numbers C_ν of CCCs in a given composition.

Now, taking the analogy to the considerations outlined in Sec. II B 1, we can write the canonical partition function from Eq. (C1) as

$$Z^{(\mathrm{id})}_{N_1,N_2,\ldots,N_\kappa} = \sum_{\{C_\nu\}}^{\{N_i - C^{(i)} \geq 0\}} \mathcal{Z}^{(L)}_{N_1-C^{(1)},\ldots,N_\kappa-C^{(\kappa)},C_1,\ldots,C_k} \times \prod_{\nu=1}^k \left(\frac{\ell_\nu^{(X_\nu-1)}}{\Lambda}\right)^{dC_\nu}, \tag{21}$$

where the sum counts all sets of admissible numbers $\{C_\nu\}$ of CCCs such that the numbers $\{N_i - C^{(i)}\}$ of free particles are non-negative for all species.

Again, switching to the grand-canonical picture allows us to remove the interdependence of the sums. Subsequently introducing $A_i := N_i - C^{(i)}$, we find the ideal grand-canonical partition function

$$\begin{aligned}\Xi^{(\mathrm{id})} &= \sum_{AC} \prod_{i=1}^\kappa \frac{(L^d z_i)^{A_i}}{A_i!} \prod_{\nu=1}^k \frac{(L^d z_{\bullcirc}^{(\nu)})^{C_\nu}}{C_\nu!} \\ &= \exp\left(\sum_{i=1}^\kappa L^d z_i + \sum_{\nu=1}^k L^d z_{\bullcirc}^{(\nu)}\right).\end{aligned} \tag{22}$$

with $\sum_{AC} \equiv \sum_{A_1=0}^\infty \cdots \sum_{A_\kappa=0}^\infty \sum_{C_1=0}^\infty \cdots \sum_{C_k=0}^\infty$ and the effective fugacities $z_{\bullcirc}^{(\nu)}$ from Eq. (20). Such an effective $\kappa + k$-component mixture can then be equipped with physical interactions and evaluated accordingly.

4. Number densities for general complexes

As discussed in Sec. II B 4, the composition of the effective mixture can be studied by calculating the ensemble average of the density operators $\{\hat{\rho}_X\}$, where X now represents $\{N_i\}$, $\{N_i - C^{(i)}\}$ and $\{C_\nu\}$. It follows that the respective total number densities $\{\rho_i^\mathrm{t}\}$ of particles of species i, the number densities $\{\rho_i\}$ of free particles of species i (which are not bound in a CCC) and the number densities $\{\rho_{\bullcirc}^{(\nu)}\}$ of CCCs of species ν are related by

$$\rho_i^\mathrm{t} = \rho_i + \sum_{\nu=1}^k x_\nu^{(i)} \rho_{\bullcirc}^{(\nu)}, \quad i \in \{1, \ldots, \kappa\}. \tag{23}$$

In generalization of Eq. (11), the contribution of the CCCs to the total densities is weighted by the number $x_\nu^{(i)}$ of a single CCC's ingredients of species i.

D. Combinatorics of carrier-cargo mixtures

To apply the general combinatorics established in Sec. II C to carrier-cargo mixtures with $\kappa = 2$ components, such that $i \in \{1, 2\}$, which is equivalent to $i \in \{\circ, \bullet\}$ in our pictorial notation introduced in Sec. II A. Thus, a CCC of index $\nu = 1, \ldots, k$ consists of $x_\nu^{(1)} = 1$ carrier and $x_\nu^{(2)} = \nu$ cargo particles, which makes in total $X_\nu = 1 + \nu$ building blocks. Below, we elaborate how our general results can be applied to this case. Moreover, we discuss in appendix G a more general mixtures involving $\kappa - 1$ carrier species.

1. Fugacities and number densities

Upon inserting $\kappa = 2$, $x_\nu^{(1)} = 1$ and $x_\nu^{(2)} = \nu$ into Eq. (19) and we get the effective fugacities

$$z_{\bullcirc}^{(\nu)} = z_\circ (\ell_\nu^d z_\bullet)^\nu, \tag{24}$$

such that we further recover $z_{\textcircled{\bullet}}^{(1)} \simeq z_{\textcircled{\bullet}}$ from Eq. (9) in the special case $k = 1$ with $\ell_1 \simeq \ell$ for $d = 1$. Similarly, the effective chemical potentials from Eq. (20) become

$$\mu_{\textcircled{\bullet}}^{(\nu)} = k_{\mathrm{B}}T\nu\, d\, \ln(\ell_\nu/\Lambda) + \mu_{\bigcirc} + \nu\, \mu_{\bullet} \tag{25}$$

in accordance with Eq. (10).

Accordingly, the relations in Eq. (23) for the number densities become

$$\rho_{\bigcirc}^{\mathrm{t}} = \rho_{\bigcirc} + \sum_{\nu=1}^{k} \rho_{\textcircled{\bullet}}^{(\nu)}\,, \quad \rho_{\bullet}^{\mathrm{t}} = \rho_{\bullet} + \sum_{\nu=1}^{k} \nu\rho_{\textcircled{\bullet}}^{(\nu)}\,, \tag{26}$$

where again recover Eq. (11) for $k = 1$ with $\rho_{\textcircled{\bullet}}^{(1)} \simeq \rho_{\textcircled{\bullet}}$. Depending on the system of interest, it may be quite cumbersome to determine all $\rho_{\textcircled{\bullet}}^{(\nu)}$ in Eq. (26). It may further prove insightful to explicitly evaluate the sums and we discuss below a convenient way to do so.

2. Total number densities of CCCs and loaded cargo

To keep the following discussion general, we formally take the limit $k \to \infty$, noting that $\rho_{\textcircled{\bullet}}^{(\nu)} = 0$ if there exists no CCC that contains ν cargo particles, i.e., if there is no free space, $\ell_\nu = 0$, to place ν cargo particles inside a carrier. We can thus define the total number density

$$\rho_{\textcircled{\bullet}} := \sum_{\nu=1}^{\infty} \rho_{\textcircled{\bullet}}^{(\nu)} \tag{27}$$

of all CCCs (irrespective of their species) in a way that is consistent with the definition of $\rho_{\textcircled{\bullet}}$ in Sec. II B 4 for $k = 1$. Moreover, we define

$$\rho_{\circledast} := \sum_{\nu=1}^{\infty} \nu\rho_{\textcircled{\bullet}}^{(\nu)} \tag{28}$$

as the total number density of loaded cargo, which scales with the average occupation number of a single CCC and is, in general, different from the total number density of CCCs, specifically $\rho_{\circledast} \leq \rho_{\textcircled{\bullet}}$. To further express these total number densities we make use of the relations as exemplified in appendix D.

First, we define the appropriate effective fugacity

$$z_{\textcircled{\bullet}} := \sum_{\nu=1}^{\infty} z_{\textcircled{\bullet}}^{(\nu)} = z_{\bigcirc} \sum_{\nu=1}^{\infty} (\ell_\nu^d z_{\bullet})^\nu \tag{29}$$

of a generalized CCC by adding up the individual contributions from Eq. (24). Hence, all CCCs with the same physical length $\sigma_{\bigcirc}$ can be treated as a single species with number density $\rho_{\textcircled{\bullet}}$, i.e., we may merely distinguish between an empty and a nonempty carrier.

Second, we define $z_{\bigcirc}^{\mathrm{t}} = z_{\bigcirc} + z_{\textcircled{\bullet}}$ and use the scaling relations

$$\frac{\rho_{\bigcirc}^{\mathrm{t}}}{z_{\bigcirc}^{\mathrm{t}}} = \frac{\rho_{\bigcirc}}{z_{\bigcirc}} = \frac{\rho_{\textcircled{\bullet}}^{(\nu)}}{z_{\textcircled{\bullet}}^{(\nu)}} = \frac{\rho_{\textcircled{\bullet}}}{z_{\textcircled{\bullet}}} \tag{30}$$

to determine the generalized CCC fraction $\rho_{\textcircled{\bullet}}/\rho_{\bigcirc}^{\mathrm{t}}$, as

$$\frac{\rho_{\textcircled{\bullet}}}{\rho_{\bigcirc}^{\mathrm{t}}} = \frac{z_{\textcircled{\bullet}}}{z_{\bigcirc}^{\mathrm{t}}} = \frac{-1 + \sum_{\nu=0}^{\infty} (\ell_\nu^d z_{\bullet})^\nu}{\sum_{\nu=0}^{\infty} (\ell_\nu^d z_{\bullet})^\nu}\,. \tag{31}$$

and the loaded-cargo fraction $\rho_{\textcircled{\bullet}}/\rho_{\bigcirc}^{\mathrm{t}}$, i.e., the number of loaded cargo per carrier, as

$$\frac{\rho_{\circledast}}{\rho_{\bigcirc}^{\mathrm{t}}} = \frac{\sum_{\nu=1}^{\infty} \nu\, z_{\textcircled{\bullet}}^{(\nu)}}{z_{\bigcirc}^{\mathrm{t}}} = \frac{\sum_{\nu=0}^{\infty} \nu (\ell_\nu^d z_{\bullet})^\nu}{\sum_{\nu=0}^{\infty} (\ell_\nu^d z_{\bullet})^\nu}\,. \tag{32}$$

We stress that these ratios are independent of the specific interparticle interactions. What is left to be done is to specify all ℓ_ν for $\nu = 1, \ldots, k$ and then evaluate Eqs. (31) and (32) as the fundamental characteristics of the carrier-cargo mixture.

3. Boltzmann occupation law in equilibrium

As exemplified in Sec. II B 1 and appendix C for one-dimensional excluded volume interactions allowing only for a single type, the canonical partition function Z_{MN} of a general carrier-cargo mixture can be expressed as an appropriate combination of auxiliary partition functions. In particular, upon properly deriving Eq. (21) with $\kappa = 2$ and $X_\nu - 1 = \nu$, the terms

$$\left(\frac{\ell_\nu}{\Lambda}\right)^{\nu d} = \mathcal{Z}_\nu^{(\mathcal{I}_{\bigcirc})}(\mathcal{B}_{\bullet})\,, \quad \nu = 1, 2, \ldots \tag{33}$$

emerge when accounting for a configuration in which ν cargo particles with a certain shape (denoted by $\mathcal{B}_{\bullet}$) are confined to a carrier with a certain interior shape (denoted by $\mathcal{I}_{\bigcirc}$). The weight of all possible configurations is given by the canonical partition function $\mathcal{Z}_\nu^{(\mathcal{I}_{\bigcirc})}(\mathcal{B}_{\bullet})$. Hence, through Eq. (33), all occupation parameters ℓ_ν characterizing the formation of CCCs in our equilibrium model have an explicit interpretation in terms of Boltzmann statistics and we say that the carrier occupation follows a Boltzmann law. We substantiate this general result by providing three relevant examples.

For spherically symmetric hard bodies in d dimensions with $\sigma_{\bullet} < \lambda_{\bigcirc} < 2\sigma_{\bullet}$, as illustrated in Fig. 1a, ℓ_1^d represents the spherical free volume with the diameter $\ell = \lambda_{\bigcirc} - \sigma_{\bullet}$ given in Eq. (3), while all other occupation parameters are zero. Hence we have

$$\ell_1 = \frac{\ell\sqrt{\pi}}{2} \left(\Gamma\left(\frac{d}{2} + 1\right)\right)^{-\frac{1}{d}}\,,$$
$$\ell_\nu = 0\,, \quad \nu > 1 \tag{34}$$

with the gamma function Γ. Together with Eq. (24), we have fully recovered the result of Sec. II B in the special case $d = 1$, where we have $\ell_1 = \ell$.

Next we consider in our excluded-volume model the case of carriers which can hold at most k cargo particles,

as illustrated in Fig. 1b. Specifically for $d = 1$ this corresponds to particles with $k\sigma_\bullet < \lambda_\bigcirc < (k+1)\sigma_\bullet$, such that

$$\ell_\nu^\nu = \frac{(\lambda_\bigcirc - \nu\sigma_\bullet)^\nu}{\nu!} = \frac{(\ell - (\nu-1)\sigma_\bullet)^\nu}{\nu!} \qquad \nu \le k\,,$$
$$\ell_\nu^\nu = 0 \qquad \nu > k\,. \tag{35}$$

Together with Eq. (24) and an appropriate treatment of interactions, these occupation parameters allow for an exact description of this one-dimensional carrier-cargo mixture, where Eq. (34) is recovered for $k = 1$.

We conclude by discussing the particularly simple case of non-interacting cargo with $\sigma_\bullet = 0$, sticking to $d = 1$ for simplicity. Due to the absence of interactions in the occupied carrier, we formally have $k \to \infty$ with all occupation parameters

$$\ell_\nu = \frac{\ell}{(\nu!)^{\frac{1}{\nu}}} \tag{36}$$

depending on a single length scale $\ell = \ell_1 = \lambda_\bigcirc$. In this case, the expressions from Eqs. (29), (31) and (32) can be considerably simplified to

$$z_\textcircled{\bullet} = z_\bigcirc \left(e^{\ell z_\bullet} - 1\right)\,, \quad \frac{\rho_\textcircled{\bullet}}{\rho_\bigcirc^{\mathrm{t}}} = 1 - e^{-\ell z_\bullet}\,, \quad \frac{\rho_\circledast}{\rho_\bigcirc^{\mathrm{t}}} = \ell z_\bullet\,, \tag{37}$$

where we have used $\sum_{\nu=0}^\infty (\ell z_\bullet)^\nu/\nu! = e^{\ell z_\bullet}$ and $\sum_{\nu=1}^\infty (\ell z_\bullet)^\nu/(\nu-1)! = \ell z_\bullet e^{\ell z_\bullet}$. We notice that the CCC fraction exponentially approaches the limiting value $\rho_\textcircled{\bullet}/\rho_\bigcirc^{\mathrm{t}} \to 1$, i.e., a system in which all carriers are occupied, when taking the limit $z_\bullet \to \infty$.

III. EVALUATION OF THE MODEL

A. Results for hard bodies

To illustrate the results of our theoretical treatment from Sec. II, we study the effective mixture within classical density functional theory (DFT), as described in appendix E. This amounts to solving a system of $\kappa + k$ coupled algebraic equation (one for each component of the effective system). While our treatment based on Fundamental Measure Theory (FMT) [48–50] is exact in one spatial dimension [45, 46], there exists no exact theory for interacting systems in higher spatial dimensions. Hence, we also compare our results to Monte-Carlo simulations as described in appendix A.

Specifically, we study the composition, given by the fraction $\rho_\textcircled{\bullet}/\rho_\bigcirc^{\mathrm{t}}$ or $\rho_\textcircled{\bullet}^{(\nu)}/\rho_\bigcirc^{\mathrm{t}}$ of all CCCs or CCCs of species ν, respectively, among the carriers, as introduced in Secs. II B 4 and II D 2, and the structure, characterized by the pair distribution g_{ij}^{t} in the physical carrier-cargo mixture, as discussed in Sec. II B 5.

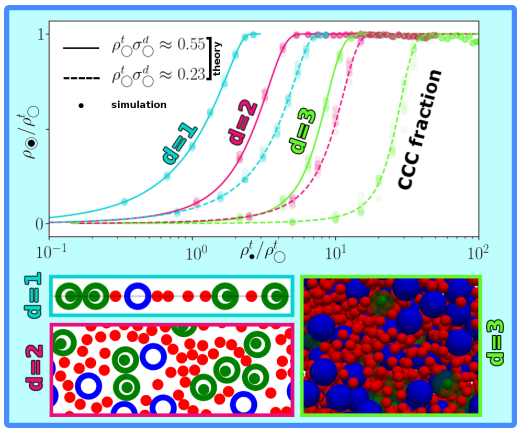

FIG. 3. Composition of a carrier-cargo mixture, cf. Fig. 1a, with $\sigma_\bullet = 0.4\sigma_\bigcirc$ and $\lambda_\bigcirc = 0.6\sigma_\bigcirc$ determined using density functional theory (lines) and Monte-Carlo simulation (symbols). We show the CCC fraction $\rho_\textcircled{\bullet}/\rho_\bigcirc^{\mathrm{t}}$, indicating the percentage of occupied carriers, as a function of the total cargo density $\rho_\bullet^{\mathrm{t}}$ for different total carrier densities $\rho_\bigcirc^{\mathrm{t}}$ (as labeled). As illustrated in Fig. 2, our theory describes an effective system with an additional CCC species, compare Eq. (10). Below we show excerpts of typical simulation snapshots in which the CCCs are detected and colored in green, according to the scheme in Fig. 2a. The frames provide the color code for our results in $d = 1, 2, 3$ dimensions, where the one-dimensional system is illustrated as two-dimensional particles whose centers are confined to a line.

1. *Single-cargo uptake without interactions*

For a mixture of interacting particles, it is not possible to determine an explicit solution for the CCC fraction $\rho_\textcircled{\bullet}/\rho_\bigcirc^{\mathrm{t}}$ as a function of the total number densities $\rho_\bigcirc^{\mathrm{t}}$ of the carriers and $\rho_\bullet^{\mathrm{t}}$ of the cargo, even if a carrier can hold no more that a single cargo. Thus, before discussing these results, we consider a simplified model of a point-like carrier-cargo mixture with $\sigma_\bigcirc = \sigma_\bullet = \sigma_\textcircled{\bullet} = 0$. However, we still assume a positive interior length scale $\ell_1 > 0$ of the carrier, such that the only interaction is by cargo uptake, see Sec. III B 2 or Sec. III B 5 for possible interpretations of such a scenario.

In this particular case, the CCC fraction follows in the desired closed form

$$\frac{\rho_\textcircled{\bullet}}{\rho_\bigcirc^{\mathrm{t}}} = \frac{1 + \mathcal{L}(1+\mathcal{R}) - \sqrt{1 + 2\mathcal{L}(1+\mathcal{R}) + \mathcal{L}^2(1-\mathcal{R})^2}}{2\mathcal{L}} \tag{38}$$

as the explicit solution of the three equations given by the two relations in Eq. (11) and $\rho_\textcircled{\bullet} := \ell_1^d \rho_\bigcirc \rho_\bullet$, which follows from Eq. (24) with $\nu = 1$ upon identifying the fugacities as number densities in the absence of effective

interactions. Here, the dimensionless parameters are the weighted interior volume $\mathcal{L} := \ell_1^d \rho^{\mathrm{t}}_{\bigcirc}$, where ℓ_1 is specified in d spatial dimensions by Eq. (34), and the cargo-to-carrier ratio $\mathcal{R} := \rho^{\mathrm{t}}_{\bullet}/\rho^{\mathrm{t}}_{\bigcirc}$.

From Eq. (38) we can directly infer the basic behavior and qualitatively understand the composition of carrier-cargo mixtures. Specifically, the CCC fraction is a positive and monotone increasing function of both parameters $\mathcal{L}$ and $\mathcal{R}$, which vanishes for either $\mathcal{L} = 0$ or $\mathcal{R} = 0$. In the limit $\mathcal{L} \to \infty$ of an infinitely large available space inside the carrier, we obtain $\rho_{\textcircled{\bullet}}/\rho^{\mathrm{t}}_{\bigcirc} \to \min(\mathcal{R}, 1)$, i.e., all cargo particles are engulfed by a carrier, while not all carriers are occupied for small cargo-to-carrier ratio $\mathcal{R} < 1$. In turn, for an infinite number of available cargo particles, $\mathcal{R} \to \infty$, all carriers are occupied, $\rho_{\textcircled{\bullet}}/\rho^{\mathrm{t}}_{\bigcirc} \to 1$. This nicely confirms the intuition that the number of CCCs in the system increases upon increasing either the free space in the interior of the carriers or the total number of cargo in the system. However, the approximation in terms of non-interacting particles does not provide any insight into the structure of carrier-cargo mixtures.

2. *Single-cargo uptake in d dimensions*

In our excluded-volume model, the behavior of a carrier-cargo mixture is governed by the competition between the overall gain of external free volume and the individual building blocks' sacrifice of entropy upon forming a CCC. To gain further insight, we first discuss the statistical properties associated with carriers that can hold no more that a single cargo particle. The CCC fraction $\rho_{\textcircled{\bullet}}/\rho^{\mathrm{t}}_{\bigcirc}$ is shown in Fig. 3 as a function of the cargo-to-carrier ratio $\rho^{\mathrm{t}}_{\bullet}/\rho^{\mathrm{t}}_{\bigcirc}$. Also in spatial dimensions $d > 1$, the results from our approximate DFT treatment relying on state-of-the art fundamental measure theory are in excellent agreement with the Monte-Carlo data.

Specifically, we predict in Fig. 3 that the fraction $\rho_{\textcircled{\bullet}}/\rho^{\mathrm{t}}_{\bigcirc}$ of CCCs gradually increases with increasing cargo-to-carrier ratio $\rho^{\mathrm{t}}_{\bullet}/\rho^{\mathrm{t}}_{\bigcirc}$ in any of the three considered spatial dimensions. The same holds true when increasing the absolute number density $\rho^{\mathrm{t}}_{\bigcirc}$ of all carriers while keeping $\rho^{\mathrm{t}}_{\bullet}/\rho^{\mathrm{t}}_{\bigcirc}$ fixed, since an enhanced CCC formation balances the increase of global packing. These results are qualitatively consistent with the analytical prediction in Eq. (38) for increasing $\mathcal{R}$ at constant $\mathcal{L}$ or vice versa. Likewise, an increasing CCC fraction is observed for an increasing internal size $\ell = \lambda_{\bigcirc} - \sigma_{\bullet} <$ of the carrier (not shown), until multiple cargo uptake occurs for $\ell > \sigma_{\bullet}$ (see Sec. III A 3).

Increasing the dimensionality of the system at fixed number densities, the onset of the CCC formation in Fig. 3 shifts to higher cargo-to-carrier ratios. This can be attributed on the one hand to the decreased packing efficiency of hard-sphere systems for larger d, such that cargo can also occupy the voids between the carriers, thereby lowering the external drive towards CCC formation. On the other hand, also the internal drive towards CCC formation is lowered for larger d, as the free volume ℓ_1^d of the carrier decreases relatively to $\sigma^d_{\bigcirc}$, compare Eq. (34). Hence, also this dimensional aspect is qualitatively captured by Eq. (38).

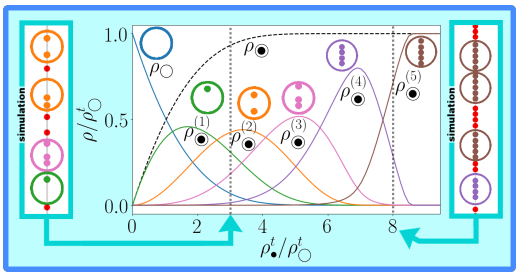

FIG. 4. Composition of a carrier-cargo mixture ($\kappa = 2$) with multiple carrier occupation ($k = 5$), cf. Fig. 1b, for $d = 1$. Different from Fig. 3, we consider here $\rho^{\mathrm{t}}_{\bigcirc}\sigma_{\bigcirc} = 0.25$ and the size parameters $\sigma_{\bullet} = \sigma_{\bigcirc}/6$ and $\lambda_{\bigcirc} = 11\sigma_{\bigcirc}/12$, such that up to $k = 5$ cargo particles fit into one carrier. The exact theoretical fraction of empty carriers, $\rho_{\bigcirc}$, CCCs with $1 \le \nu \le 5$ cargo, $\rho^{(\nu)}_{\textcircled{\bullet}}$, and total CCCs, $\rho_{\textcircled{\bullet}} = \sum_{\nu=1}^{5} \rho^{(\nu)}_{\textcircled{\bullet}}$, are shown as labeled, using the same coloring as in Fig. 2b. The two boxes at the sides display typical excerpts from simulation snapshots, illustrated as in Fig. 3, which reflect the plotted CCC fractions at the densities indicated by the teal arrows and dotted vertical lines.

3. *Multiple-cargo uptake in one dimension*

Turning to systems with carriers that offer more space to their cargo, we predict specifically for $d = 1$ the exact density $\rho^{(\nu)}_{\textcircled{\bullet}}$ of each CCC representing $\nu = 1, \ldots, k$ loaded cargo particles and the exact density $\rho_{\textcircled{\bullet}}$ of all CCCs according to Eq. (27). The corresponding CCC fractions are shown in Fig. 4 for a maximal carrier load $k = 5$. In this case, we see that the balance between internal and external entropical forces results in subsequent peaks of the different CCC fractions located at a higher total cargo density for larger ν. The simulation snapshots in Fig. 4 illustrate these percentages at the selected cargo-to-carrier ratios. Due to the larger interior size of the carriers, compared to those in Sec. III A 2 with $k = 1$, the total CCC fraction $\rho_{\textcircled{\bullet}}/\rho^{\mathrm{t}}_{\bigcirc}$ of non-empty carriers increases more rapidly than in Fig. 3 for a comparable density.

4. *Exact structure for one-dimensional single-cargo uptake*

The possibility of spherical cargo to occupy the interior of hollow carriers is accompanied by structural changes of the carrier-cargo mixture compared to an ordinary hard-sphere mixture described by the effective system. We

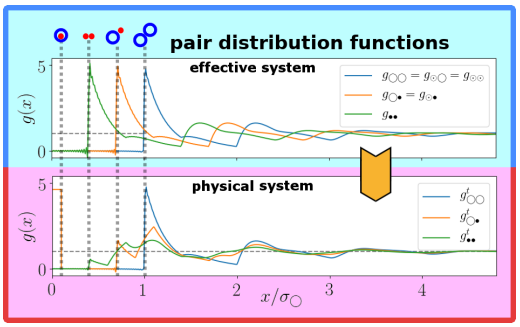

FIG. 5. Structure of the $d = 1$ dimensional carrier-cargo mixture from Fig. 3 with $\sigma_\bullet = 0.4\sigma_\bigcirc$ and $\lambda_\bigcirc = 0.6\sigma_\bigcirc$. We show exact results obtained using density functional theory for the pair distribution functions at the densities $\rho^{\mathrm{t}}_\bullet\sigma_\bigcirc = 0.625$ and $\rho^{\mathrm{t}}_\bigcirc\sigma_\bigcirc = 0.72$. The distributions for an effective hard-rod mixture (top) can be recombined to obtain the structure of the physical carrier-cargo mixture (bottom) according to Eqs. (12) to (15). By providing a direct measurement via Monte-Carlo simulation in appendix A, this result is exactly confirmed. The lengths associated with the drawn characteristic two-particle configurations are highlighted by vertical lines.

illustrate the deeper connection between these two systems by discussing the exact pair distributions for the one-dimensional particles considered in Sec. III A 2. This can be conveniently achieved by reconstructing the distributions $g^{\mathrm{t}}_{ij}(x)$ with $i, j \in \{\bigcirc, \bullet\}$ of the physical carrier-cargo mixture from the effective DFT results $g_{ij}(x)$ with $i, j \in \{\bigcirc, \bullet, \circledcirc\}$ according to Eqs. (12) to (15).

While Fig. 5 illustrates the basic relation $g^{\mathrm{t}}_{\bigcirc\bigcirc} = g_{\bigcirc\bigcirc}$, it also shows that $g^{\mathrm{t}}_{\bigcirc\bullet}$ possesses as a remarkable signature of CCC formation a strong signal for short distances. Moreover, $g^{\mathrm{t}}_{\bigcirc\bullet}$ exhibits two (additional) and $g^{\mathrm{t}}_{\bullet\bullet}$ even three main peaks, associated with those of a binary hard-sphere mixture. The broadening of the peaks related to cargo within CCCs is apparent, as most clearly visible for $g^{\mathrm{t}}_{\bullet\bullet}$ at the distance corresponding to two CCCs at contact.

B. Further applications

In Sec. III A we have presented the main observations, derived in Sec. II, for our binary carrier-cargo mixture with excluded volume interactions in equilibrium. Our central theoretical result, the combination law in Eq. (19) or Eq. (20), is however, more versatile. This general relation between the internal degrees of freedom and an effective external particle reservoir is exact for all interactions which allows to make a clear distinction between the interior and the exterior of the carrier.

Our model also offers the flexibility for investigating more complex interactions between the occurring (effective) species. We can therefore formally assign an individual interaction to each CCC species which may be distinct from that of the carrier species and interpret the ℓ_ν as generalized parameters for controlling the carrier occupation. In the remainder of this section, we will further elaborate on selected aspects related to these points.

1. *Interpretation of the model*

The driving force of a generic carrier to engulf its cargo may have different physical, chemical or biological origins, e.g., resulting from entropic, energetic, active or even intelligent mechanisms. Based on phenomenological intuition, a basic model for CCC formation should account for two internal properties: (i) an engulfment strength, which quantifies the individual uptake probability and (ii) a corresponding occupation law governing multiple cargo uptake. In our model, both properties are comprised within the parameters ℓ_ν entering in Eq. (24) or Eq. (25), which carry microscopic information.

In our simple hard-body model, introduced in Sec. II A the engulfment strength ℓ_1, associated with the first cargo loaded, is given explicitly by its available d-dimensional free volume, compare Eq. (34). The engulfment strength ℓ_ν, associated with the ν-th cargo loaded, is generally reduced (or even zero), since the occupation law is based on Boltzmann statistics, compare Eq. (35). Even for non-interacting particles, there is still an effective repulsion of the cargo within the carrier upon multiple uptake due to the factor $1/(\nu!)$ in Eq. (36). Due to this indistinguishability, the tendency towards cargo uptake depends on number of cargo already engulfed, which is a signature of the equilibrium nature of our model.

2. *Attraction-enhanced engulfment strength*

While hitherto we have exclusively used typical lengths ℓ_ν to quantify cargo uptake, we stress that our model is not limited to excluded-volume interactions. As demonstrated by Eq. (33), the engulfment strength is rather associated with dimensionless partition functions of the confined cargo. Thus an equally valid interpretation of engulfment strength is possible in terms of the binding energies

$$E_\nu := -k_{\mathrm{B}}Td\ln(\ell_\nu/\Lambda)\,. \tag{39}$$

In general, we can describe cargo uptake, that is governed by a combination of soft interactions and available space inside vesicles, while both driving forces can then be commonly quantified by either ℓ_ν or E_ν.

Since attraction mechanisms are expected to play an important role in the process of cargo uptake, we propose

the modified carrier-cargo interaction potential

$$U_{\bullet\bigcirc}(r) = U_{\bigcirc\bullet}(r) = \begin{cases} -a & \text{for } r < (\lambda_{\bigcirc} - \sigma_{\bullet})/2\,, \\ 0 & \text{for } r \geq (\sigma_{\bigcirc} + \sigma_{\bullet})/2\,, \\ \infty & \text{else} \end{cases} \quad (40)$$

as a basic example, which extends Eq. (2) by introducing the attraction parameter $a \geq 0$. Apparently, upon evaluating Eq. (33), there is an additional Boltzmann factor $\exp(\beta a/d)$, which enhances the engulfment strengths ℓ_ν according to setting $\ell_\nu \to \ell_\nu \exp(\beta a/d)$. Therefore, a carrier-cargo mixture interacting according to Eq. (40) remains exactly solvable in one spatial dimension.

This generalized consideration shows that the use of the parameters ℓ_ν (which have the dimensions of length) is not limited to describe excluded-volume interactions, but allows for a quite general description of engulfment strength. In particular, the value of ℓ_ν can exceed the dimensions of the carrier. Also with this interpretation, the parameters ℓ_ν rigorously derive from a microscopic model, as specified here through Eq. (40), which imposes a Boltzmann occupation law.

3. *Soft interactions and membranes*

In many practical applications, cargo uptake is governed by soft interactions with a carrier membrane, which controls the encapsulation (and release) of particles. Within our model, the interaction between a cargo and a carrier can be most generally described as

$$U_{\bullet\bigcirc}(r) = U_{\bigcirc\bullet}(r) = \begin{cases} U_{\text{out}}(r) & \text{for } r \geq \sigma_{\bigcirc}/2\,, \\ U_{\text{in}}(r) & \text{else}\,, \end{cases} \quad (41)$$

where $\sigma_{\bigcirc}/2$ is the radius of the carrier membrane and the potentials $U_{\text{in}}(r)$ and $U_{\text{out}}(r)$ act inside and outside this membrane, respectively. Then the engulfment strengths can be determined from $U_{\text{in}}(r)$ for $r < \sigma_{\bigcirc}/2$, while $U_{\text{out}}(r)$ describes the interaction of the CCC. The effective interaction of the CCC should then be assumed to have hard core for $r < \sigma_{\bigcirc}/2$.

A soft carrier model can thus be conveniently devised by choosing only bounded potentials in Eq. (41) and relating the carrier radius $\sigma_{\bigcirc}/2$ to a potential maximum. However, the resulting effective treatment neglects direct cargo-cargo interactions through the carrier membrane, which cannot be accounted for in the picture described above. Despite such an approximation, the resulting parameters ℓ_ν describing the engulfment strengths in an effective system are still related to a microscopic model, as specified here through Eq. (41), and thus obey a Boltzmann occupation law.

4. *Coarse-grained engulfment strength*

In biological carrier-cargo systems, the complexity of physical processes that happen at the carrier membrane goes beyond refined equilibrium models based on soft potentials. For example, a proper description should take into account adhesive forces, bending rigidity, surface tension or signaling. Moreover, there exist mechanisms, such as the digestion of encapsulated cargo, which prevent its release. This can apparently break detailed balance, an important underlying principle of equilibrium physics.

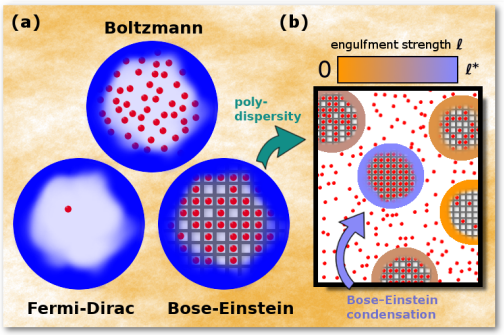

FIG. 6. Empirical applications of our model. (a) Different occupation laws can emerge on a coarse-grained level when Boltzmann law (top) is effectively broken out of equilibrium. Taking cues from quantum statistics, we conceive *Fermi-Dirac occupation* (left) if a carrier is designed to engulf no more than a single cargo, while *Bose-Einstein occupation* (right) formally corresponds to distinguishable cargo storage, illustrated here by drawing multiple compartments, each characterized by the same engulfment strength ℓ. (b) Polydispersity of the engulfment strength ℓ (indicated by the particle colors) can result in a Bose-Einstein condensation of cargo on the carriers with the maximal value $\ell = \ell^*$ (blue).

Microscopic models, which accurately reflect all microscopic properties of such processes are often difficult to handle. As an approximate alternative, our treatment allows to effectively model various (non-equilibrium) driving forces for cargo uptake by directly choosing appropriate values of the occupation parameters ℓ_ν. For applying such a coarse-grained equilibrium picture, we stress that systems in nature often suggest occupation laws that are not of the Boltzmann type.

5. *Coarse-grained occupation laws*

Having elaborated that the fundamental Boltzmann law of particle uptake may be broken for general carrier-cargo mixtures, we suggest the possibility to use non-Boltzmann occupation laws for modeling non-equilibrium driving forces of cargo uptake, such as conscious sensing, active chasing or digestion mechanisms. To discuss the basic implications, we assume that typical cargo can be much smaller than the carriers and consider again an ide-

alized system with non-interacting cargo in $d = 1$ dimensions. Recalling the results in Eq. (37) obtained with the ideal Boltzmann occupation law from Eq. (36), we propose and compare two examples, inspired by quantum statistics, compare the illustration in Fig. 6a.

A carrier that closes down after taking up a single cargo particle constitutes the Soft-Matter analogy to Pauli exclusion. This Fermi-Dirac occupation law is defined by $\ell_1 = \ell$ and $\ell_\nu = 0$ for $\nu > 1$, as in Eq. (34) but with ℓ being completely unrelated to any particle dimension or other interactions. In this case, the expressions from Eqs. (29), (31) and (32) can simply be calculated by truncating all sums after $\nu = 1$, which yields

$$z_{\textcircled{\bullet}} = z_{\bigcirc} \ell z_\bullet \,, \quad \frac{\rho_{\textcircled{\bullet}}}{\rho^{\mathrm{t}}_{\bigcirc}} = \frac{\ell z_\bullet}{1+\ell z_\bullet} \,, \quad \frac{\rho_{\circledast}}{\rho^{\mathrm{t}}_{\bigcirc}} = \frac{\ell z_\bullet}{1+\ell z_\bullet} \,. \tag{42}$$

In contrast to Boltzmann occupation, the limit $\rho_{\textcircled{\bullet}}/\rho^{\mathrm{t}}_{\bigcirc} \to 1$ for $z_\bullet \to \infty$ is approached algebraically as a function of $z_\bullet$.

If a carrier can store all cargo particles independently, or, more generally, if the effective engulfment strength does not depend on the number of cargo already engulfed by the carrier, there is effectively no repulsion at all between the engulfed non-interacting cargo particles, as if each of them is stored in an individual compartment of size ℓ. This reflects the behavior of effectively distinguishable particles (for example due to instant digestion), which is governed by a Bose-Einstein occupation law which is defined as

$$\ell_\nu = \ell \,, \quad \nu = 1, 2, \ldots \tag{43}$$

and yields

$$z_{\textcircled{\bullet}} = z_{\bigcirc} \frac{\ell z_\bullet}{1-\ell z_\bullet} \,, \quad \frac{\rho_{\textcircled{\bullet}}}{\rho^{\mathrm{t}}_{\bigcirc}} = \ell z_\bullet \,, \quad \frac{\rho_{\circledast}}{\rho^{\mathrm{t}}_{\bigcirc}} = \frac{\ell z_\bullet}{1-\ell z_\bullet} \tag{44}$$

with the restriction to $\ell z_\bullet < 1$. Here we have used the identities $\sum_{\nu=0}^{\infty} (\ell z_\bullet)^\nu = \frac{1}{1-\ell z_\bullet}$ and $\sum_{\nu=1}^{\infty} \nu (\ell z_\bullet)^\nu = \frac{z_\bullet \ell}{(1-\ell z_\bullet)^2}$ for the case $\ell z_\bullet < 1$ and silently omitted including the step function $\Theta(1 - \ell z_\bullet)$ in these formulas. For larger $\ell z_\bullet > 1$ the above quantities are ill-defined, as both the effective fugacity and the loaded-cargo fraction diverge for $\ell z_\bullet \to 1$. The CCC fraction approaches the limiting value $\rho_{\textcircled{\bullet}}/\rho^{\mathrm{t}}_{\bigcirc} \to 1$ already at the finite value $z_\bullet \to \ell^{-1}$ of the fugacity of the cargo particles.

Comparing the different scenarios (37) (42) (44), it can be shown that Fermi-Dirac (Bose-Einstein) occupation yields the smallest (largest) values of both $\rho_{\textcircled{\bullet}}$ and $\rho_{\circledast}$ and the weakest (strongest) increase of the CCC fraction, $\rho_{\textcircled{\bullet}}/\rho^{\mathrm{t}}_{\bigcirc}$ as a function of $\rho^{\mathrm{t}}_\bullet$. One intriguing result is that, in each case, the number of loaded cargo per carrier, $\rho_{\circledast}/\rho^{\mathrm{t}}_{\bigcirc}$, takes the same functional form as the average occupation number of a certain energy level in quantum statistics.

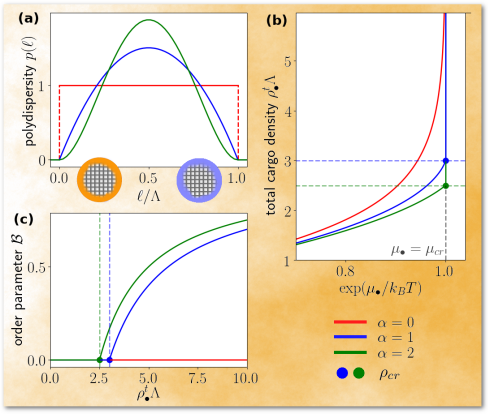

FIG. 7. Bose-Einstein condensation for carriers with polydispersity $p(\ell) \propto \ell^\alpha(\ell^* - \ell)^\alpha$ in the engulfment strength $0 \le \ell \le \ell^* = \Lambda$ for representative exponents $\alpha = 0, 1, 2$ (colors as labeled) and the total carrier density $\bar{\rho}^{\mathrm{t}}_{\bigcirc}\Lambda = 1$. a) Normalized distributions $p(\ell)$ with illustrations of the resulting average occupation by cargo, cf. Fig. 1c., b) The total cargo density $\rho^{\mathrm{t}}_\bullet$ increases with the chemical potential $\mu_\bullet$. At $\mu_\bullet = \mu_{\mathrm{cr}}$ (vertical line) $\rho^{\mathrm{t}}_\bullet$ diverges if $\alpha \le 1$ and reaches the finite critical value ρ_{cr} (bullets) otherwise. c) Order parameter $\mathcal{B}$ (Eq. (51)) of the Bose-Einstein condensation, i.e., fraction of cargo on carriers with largest engulfment strength ℓ^*, as a function of $\rho^{\mathrm{t}}_\bullet$.

C. Bose-Einstein condensation with polydispersity

To demonstrate the collective effects that can arise from a certain coarse-grained treatment of non-equilibrium cargo uptake, we further investigate the implications of assuming a Bose-Einstein occupation law according to Eq. (43). Here, we additionally consider a polydisperse mixture of carriers, each with a characteristic engulfment strength $0 \le \ell \le \ell^*$. Then, as illustrated in Fig. 6b, a Bose-Einstein condensation of the cargo can occur on the carriers with the strongest drive to engulf their cargo, represented by $\ell = \ell^*$. The conditions for this phase transition are elaborated below and exemplified in Fig. 7.

The following considerations are independent of the interactions between the particles. However, our working hypothesis assumes that cargo particles become distinguishable and non-interacting upon being engulfed, e.g., as an effective picture for being gradually digested.

1. *Polydisperse carriers*

To consider a mixture of different carrier species i, the definitions in Sec. II D 2 can be easily generalized, as performed in appendix G. In particular, engulfment strength

$\ell^{[i]}$, and thus the resulting densities of (empty) carriers, CCCs and loaded cargo now additionally depend on the carrier species i. Here, we are specifically interested in the total number density $\rho_{\circledast}^{[i]}$ of cargo loaded on carriers of species i under Bose-Einstein occupation, which we can express from the result in Eq. (44) as

$$\rho_{\circledast}^{[i]} = \frac{\ell^{[i]} z_\bullet}{1-\ell^{[i]} z_\bullet}\, \rho_{\bigcirc}^{([i],\mathrm{t})} \tag{45}$$

with the restriction to $\ell^{[i]} z_\bullet < 1$.

For a mixture of carriers with polydisperse engulfment strengths ℓ the quantities of interest become continuous functions of ℓ. As input, we suppose that the total number density $\rho_{\bigcirc}^{\mathrm{t}}(\ell) = \bar{\rho}_{\bigcirc}^{\mathrm{t}} p(\ell)$ of carriers is distributed according to a known normalized function $p(\ell)$, which vanishes beyond a maximal size ℓ^*, see Fig. 7a for three examples considered here. The total number density $\bar{\rho}_{\bigcirc}^{\mathrm{t}} = \int_0^{\ell^*} \mathrm{d}\ell\, \rho_{\bigcirc}^{\mathrm{t}}(\ell)/\ell^*$ of all carriers follows by integration (and we write here $\bar{\rho}_{\bigcirc}^{\mathrm{t}}$ instead of $\rho_{\bigcirc}^{\mathrm{t}}$ to indicate the averaging involved). With the knowledge of $p(\ell)$, we can take the continuum limit of Eq. (45) to express the total number density $\rho_{\circledast}(\ell)$ of cargo loaded on carriers of engulfment strength ℓ under Bose-Einstein occupation as

$$\rho_{\circledast}(\ell) = \bar{\rho}_{\bigcirc}^{\mathrm{t}}\, p(\ell)\, \frac{\ell z_\bullet}{1-\ell z_\bullet} \tag{46}$$

with the restriction $\ell z_\bullet < 1$.

Then, the total number of carriers is given by

$$\rho_\bullet^{\mathrm{t}} = \rho_\bullet + \frac{\bar{\rho}_{\bigcirc}^{\mathrm{t}}}{\ell^*} \int_0^{\ell^*} \mathrm{d}\ell\, p(\ell)\, \frac{z_\bullet \ell}{1-\ell z_\bullet}\, \Theta(1-\ell z_\bullet)\,, \tag{47}$$

where $\Theta(1-\ell z_\bullet)$ denotes the Heaviside step function. Note that, since the particular expression for $\rho_{\circledast}(\ell)$ in Eq. (46) diverges for $\ell z_\bullet \to 1$ and $p(\ell$ is chosen such that $\ell \le \ell^*$, the expression in Eq. (47) is only valid for $\ell z_\bullet < 1$. Exploiting the mathematical analogy to quantum statistics [51], we show next how to identify a Bose-Einstein condensation in our model, where $p(\ell)$ takes the role of the density of states.

2. Bose-Einstein order parameter

Regarding the denominator in Eq. (46), we recognize that the fugacity $z_\bullet$ has an upper bound given by the condition $\ell^* z_\bullet < 1$, which defines the critical fugacity $z_{\mathrm{cr}} := 1/\ell^*$ (or the critical chemical potential $\mu_{\mathrm{cr}} := -k_{\mathrm{B}} T \ln(\ell^*/\Lambda)$). Despite this divergence, setting $\ell^* z_\bullet = 1$ is allowed if the limit $z_\bullet \to z_{\mathrm{cr}}$ of Eq. (47) exists, i.e., if the critical density

$$\rho_{\mathrm{cr}} := \lim_{z_\bullet \to z_{\mathrm{cr}}} \rho_\bullet^{\mathrm{t}} \tag{48}$$

has a finite value. In this case, a further increase of the total number density $\rho_\bullet^{\mathrm{t}}$ of loaded cargo is only possible by loading the largest carrier, i.e., by increasing the number density $\rho_{\circledast}(\ell^*)$ at constant $z_\bullet = z_{\mathrm{cr}}$. While, for $z_\bullet < z_{\mathrm{cr}}$, the expression

$$\rho_{\circledast}(\ell^*) = \bar{\rho}_{\bigcirc}^{\mathrm{t}}\, p(\ell^*)\, \frac{z_\bullet \ell^*}{1-\ell^* z_\bullet} \tag{49}$$

holds, such that the contribution to ρ_{cr} is infinitesimal, the value of $\rho_{\circledast}(\ell^*)$ may become finite as the denominator approaches zero for $z_\bullet \to z_{\mathrm{cr}}$.

In a system with a finite ρ_{cr}, defined in Eq. (48), the total number density $\rho_\bullet^{\mathrm{t}}$ must account for the explicit contribution of $\rho_{\circledast}(\ell^*)$. The according generalization of Eq. (47) yields

$$\rho_\bullet^{\mathrm{t}} = z_\bullet + \rho_{\circledast}(\ell^*) + \frac{\bar{\rho}_{\bigcirc}^{\mathrm{t}}}{\ell^*} \int_0^{\ell^*} \mathrm{d}\ell\, \frac{z_\bullet \ell}{1-\ell z_\bullet}\, p(\ell)\, \Theta(1-\ell z_\bullet)\,. \tag{50}$$

Then, we find that the fraction of cargo particles occupying the largest carrier is given by

$$\mathcal{B} := \frac{\rho_{\circledast}(\ell^*)}{\rho_\bullet^{\mathrm{t}}} = \begin{cases} 0 & \text{if } z_\bullet < z_{\mathrm{cr}}\,, \\ 1 - \frac{\rho_{\mathrm{cr}}}{\rho_\bullet^{\mathrm{t}}} & \text{if } z_\bullet = z_{\mathrm{cr}}\,. \end{cases} \tag{51}$$

This ratio constitutes the order parameter of a density-driven Bose-Einstein condensation [51] into a state with a macroscopic occupation of a single carrier species with engulfment strength ℓ^* for $\rho_\bullet^{\mathrm{t}} > \rho_{\mathrm{cr}}$.

3. Illustration and discussion

To illustrate the conditions for a Bose-Einstein condensation in a polydisperse carrier-cargo mixture, we discuss, as a particular example, a system in which all cargo particles (not only those engulfed by a carrier) are non-interacting. This allows us to express the critical density from Eq. (48) in the closed form

$$\rho_{\mathrm{cr}} = \frac{1}{\ell^*} + \lim_{z_\bullet \to z_{\mathrm{cr}}} \frac{\bar{\rho}_{\bigcirc}^{\mathrm{t}}}{\ell^*} \int_0^{\ell^*} \mathrm{d}\ell\, \frac{z_\bullet \ell}{1-\ell z_\bullet}\, p(\ell)\, \Theta(1-\ell z_\bullet)\,, \tag{52}$$

where we have replaced the number density $\rho_\bullet \to z_\bullet$ by the corresponding fugacity, which equals ℓ^* in the limit taken.

To evaluate the integral in the second term of Eq. (52) we consider a family of normalized distribution functions

$$p(\ell) \propto \left(-\left(\ell - \frac{\ell^*}{2}\right)^2 + \frac{{\ell^*}^2}{4} \right)^\alpha = \ell^\alpha (\ell^* - \ell)^\alpha\,, \tag{53}$$

given by an inverse parabola exponentiated by α. The form of $p(\ell)$ is shown in Fig. 7a for $\alpha = 0, 1, 2$. For $\alpha > 0$, we have $p(\ell^*) = 0$ and the scaling for $\ell \to \ell^*$ is given by

$$p(\ell) \propto (\ell^* - \ell)^\alpha + \mathcal{O}\left((\ell^* - \ell)^{\alpha+1}\right)\,. \tag{54}$$

Then ρ_{cr} can be explicitly calculated as a function of α and we find that it takes a finite value (blue and green

dots in Fig. 7b and c) if $\alpha > 0$, while it diverges logarithmically for $\alpha = 0$.

As shown in Fig. 7b, there are two possibilities for the behavior of the total number density $\rho_\bullet^\mathrm{t}$ of cargo particles, depending on the exponent α of $p(\ell)$ as $\ell \to \ell^*$ and thus on the critical density ρ_cr. First, if ρ_cr diverges, all carriers take up an infinitesimal fraction of cargo particles for $z_\bullet < z_\mathrm{cr}$ and no phase transition occurs. Second, if ρ_cr remains finite, then $\rho_\bullet^\mathrm{t}$ can be increased indefinitely at constant critical fugacity $z_\bullet = z_\mathrm{cr}$ by loading further cargo particles on the carriers with largest engulfment strength ℓ^*. As a consequence, a Bose-Einstein condensation occurs at $\rho_\bullet^\mathrm{t} = \rho_\mathrm{cr}$ towards a state with a macroscopic number of cargo occupying the carriers with $\ell = \ell^*$.

For $z_\bullet < z_\mathrm{cr}$, the behavior of $\rho_\bullet^\mathrm{t}$ as a function of $z_\bullet$ is given by either Eq. (47) or Eq. (50), since $\rho_\circledast(\ell^*) = 0$. Therefore, the order parameter $\mathcal{B}$ in Eq. (51) remains zero. However, when $\rho_\bullet^\mathrm{t} = \rho_\mathrm{cr}$ is exceeded for $z_\bullet = z_\mathrm{cr}$, we have $\rho_\circledast(\ell^*) > 0$, Hence, the value of $\mathcal{B}$ increases continuously as a function of $\rho_\bullet^\mathrm{t}$ in the new phase. This behavior is illustrated in Fig. 7c.

We conclude that there is no Bose-Einstein condensation for a constant distribution of engulfment strengths in a certain interval, while the formation of a Bose-Einstein condensate is facilitated for mixtures of carriers with an increasingly weaker polydispersity (such that $p(\ell)$ has a smaller variance). This observation is analogous to Bose-Einstein condensation in quantum statistics, where the density of states of a three dimensional ideal Bose gas has the exponent $1/2$ and gives rise to a phase transition, in contrast to the exponents 0 and $-1/2$ in two and one dimensions, respectively. Finally, we stress that the crucial technical difference between a classical system and quantum statistics is that, in the present case, the momenta of the particles are thermalized and represented by the thermal wave length Λ. Thus, following the discussion in Sec. III B 2, the respective energy levels $E := -k_\mathrm{B}T \ln(\ell/\Lambda)$ are provided by a configurational quantity modeling the non-equilibrium drive of the carriers to engulf their cargo. Moreover, the spatial dimension (taken here as $d = 1$) would only enter here as a trivial factor.

IV. CONCLUSIONS

In this work, we have introduced a combination law (20) that illustrates that the internal degrees of freedom associated with the formation of soft-matter complexes can be exactly mapped onto effective chemical potentials, which allow to describe such complexes as an independent particle species. We demonstrated the validity of our approach for carrier-cargo mixtures through exactly matching simulation results for a one-dimensional hard-rod model, where the formation of CCCs is purely driven by entropic free-volume effects. Then we argued that non-Boltzmann occupation laws provide a coarse-grained description of non-equilibrium particle uptake, as exemplified by recognizing a Bose-Einstein condensation for a polydisperse carrier model.

The versatility of our approach can be exploited when accounting for emergent properties of the assembled complexes that are distinct from their building blocks. While the present application to carrier-mixtures involves CCCs whose external length is strictly set by the carrier, we can also account for a shape change upon cargo uptake. Likewise, by appropriately adapting the interactions, it is possible to describe various types of aggregates [52] such as dimers formed by lock and key colloids [53–56], colloidal molecules [7, 57–61] or building blocks of systems with entropic bonds [62–64]. Exploiting the full potential of modern fundamental-measure density functional theory [48–50, 65, 66] the statistical treatment of such anisotropic interactions or inhomogeneities induced by external stimuli is within reach.

Another important application of our model would be a dynamical description of particle uptake, which can be achieved in two ways. The first possibility is via direct computer simulation of the dynamics. This requires, however, soft models for the carrier membrane as discussed in Sec. III B 3. The second possibility amounts to a direct application of our effective picture through an extension [67, 68] of dynamical density functional theory [69–71] in which appropriate reaction rates should be determined from the equilibrium statistics. Such dynamical approaches could also be used to explicitly study more complex carrier-cargo mixtures involving self-propelled building blocks [33–36, 61, 72–75] or emerging active motion of the assembled complex [31, 37, 39, 76–78].

A critical open question which could stimulate future efforts concerns the experimental realization of cargo uptake and release in equilibrium soft-matter systems, e.g., involving colloidal carriers or lipid vesicles. Further experimental challenges will be to discover or train functional carriers [79] whose non-equilibrium driving force for cargo uptake is not limited to Boltzmann occupation or develop intelligent micromachines [80] which learn to collect their cargo as programmed.

ACKNOWLEDGMENTS

The authors would like to thank Michael te Vrugt, Roland Roth, Daniel Borgis, Laura Alvarez and Philipp Maass for stimulating discussions and valuable suggestions. RW and HL acknowledge support by the Deutsche Forschungsgemeinschaft (DFG) through the SPP 2265, under grant numbers WI 5527/1-1 (RW) and LO 418/25-1 (HL).

Appendix A: Monte-Carlo simulation

To corroborate our analytic treatment, we perform canonical Monte-Carlo simulation of bulk systems of

M carriers and N cargo particles, realized via periodic boundary conditions, in $d = 1, 2, 3$ dimensions. The total particle number $M + N = 2000$ is always fixed, while we vary the ratio $N/M = \rho^{\mathrm{t}}_{\bullet}/\rho^{\mathrm{t}}_{\bigcirc}$ of cargo to carrier particles between independent simulation runs. The input densities $\rho^{\mathrm{t}}_{\bullet}$ and $\rho^{\mathrm{t}}_{\bigcirc}$ are determined by the final size of the simulation box. The overlap criterion between a pair of particles is given by Eqs. (1) and (2). We perform 10^6 Monte Carlo cycles, each consisting of $M + N$ trial moves. In each trial move, one of the particles is displaced by a distance vector $\Delta\mathbf{r}$, whose components Δr_i with $i = 1, \ldots, d$ are independent random numbers drawn from a uniform distribution in the interval $[-\Delta_{\max}, \Delta_{\max}]$. Any trial move is accepted with probability $P = \min(1, \exp(-\Delta U/k_{\mathrm{B}}T))$ [81], i.e, overlap free trial moves are accepted, while overlapping trial moves are rejected. Over the course of the simulation, the value of $\Delta_{\max}$ is adjusted such that acceptance ratio remains close to 0.3.

We obtain the particle configurations at high densities by following a compression protocol. We randomly initialize the system at low number densities $\rho^{\mathrm{t}}_{\bullet} + \rho^{\mathrm{t}}_{\bigcirc} = 5\times10^{-3}/\sigma_{\bigcirc}$. Over the course of the simulation, we gradually rescale all coordinate axes $x_i, i \in \{1, 2, 3\}$, such that $x_i \propto \tau^{-1/(3d)}$, where d is the number of spatial dimensions, effectively increasing all total densities within the system as $\rho^{\mathrm{t}}_{\bullet} \propto \rho^{\mathrm{t}}_{\bigcirc} \propto \tau^{1/3}$. Here, $\tau \in [0, 1]$ denotes the simulation progress, i.e., the number of completed Monte-Carlo cycles. This type of decelerating compression aids the equilibration speed, since the system is quickly compressed in the density regime where the particles are expected to rarely come in contact, while being allowed to undergo a larger fraction of Monte Carlo cycles at higher densities.

Exemplary simulation data is shown as dots in Fig. 2a of the main manuscript. In addition, Fig. 8 shows the pair distribution functions in one dimension for $\rho^{\mathrm{t}}_{\bullet}\sigma_{\bigcirc} = 0.625$ and $\rho^{\mathrm{t}}_{\bigcirc}\sigma_{\bigcirc} = 0.72$. Additionally, corresponding results are shown, obtained from the average over 200 simulation runs (dashed red). As visible, the theoretical graphs (blue, cf. Fig. 2b of the main manuscript), calculated as described in Sec. II B 5, agree with the simulation results to an excellent degree.

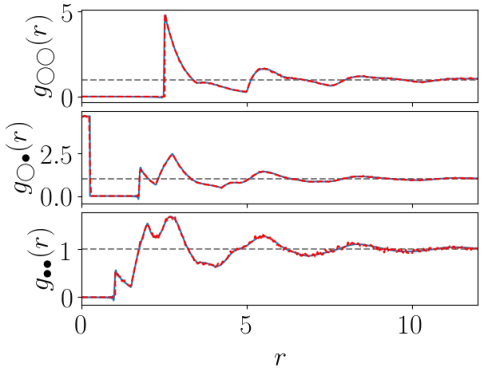

FIG. 8. Theoretical pair distribution functions (blue) in $d = 1$ dimension for $\rho^{\mathrm{t}}_{\bullet}\sigma_{\bigcirc} = 0.625$ and $\rho^{\mathrm{t}}_{\bigcirc}\sigma_{\bigcirc} = 0.72$, as shown at the bottom of Fig. 5. The respective pair distribution functions obtained from simulation (dashed red) show excellent agreement.

Appendix B: Canonical partition function of a hard-rod mixture in one dimension

To aid the discussion in Sec. II B 1, we state here the exact canonical partition function

$$\mathcal{Z}^{(L)}_{N_1,N_2,\ldots,N_K}(\sigma_1, \sigma_2, \ldots, \sigma_K) = \prod_{i=1}^{K} \frac{1}{N_i!\Lambda^{N_i}} \left(L - \sum_{j=1}^{K} N_j\sigma_j\right)^{N_i} \Theta\left(L - \sum_{j=1}^{K} N_j\sigma_j\right) \tag{B1}$$

a K-component mixture of hard rods (one-dimensional hard spheres or Tonks gas). Specifically, N_i denote the particle numbers of each species $i \in \{1, 2, \ldots, K\}$ confined in a one-dimensional interval of length L, while we ignore the trivial dependence on the temperature T through the thermal wavelength Λ. For later convenience, we further write $\mathcal{Z}^{(L)}_{N_1,N_2,\ldots,N_K}$ as a function of the particle lengths σ_i of each species, while the explicit dependence on the particle numbers and the system length is written as a subscript and a superscript, respectively. The Heaviside function $\Theta(x)$ merely ensures that the system is below close packing for the given particle numbers and is silently omitted elsewhere to ease the notation.

Appendix C: Canonical partition function of the carrier-cargo mixture

To better understand the notion of our system consisting of M carriers and N cargo as an effective three-component mixture, we rewrite Eq. (5) in the less intuitive but more instructive form

$$Z_{MN} = \sum_{C=0}^{\min(M,N)} \mathcal{Z}^{(L)}_{M-C,N-C,C}(\sigma_{\bigcirc}, \sigma_{\bullet}, \sigma_{\bigcirc}) \left(\mathcal{Z}_1^{(\lambda_{\bigcirc})}(\sigma_{\bullet})\right)^C , \tag{C1}$$

which contains no factorial expressions. In the second equality, we made use of the fact that the free length

$$\ell \equiv \Lambda\mathcal{Z}_1^{(\lambda_{\bigcirc})}(\sigma_{\bullet}) . \tag{C2}$$

accessible to a cargo particle within a CCC, as defined in Eq. (3), can be explicitly interpreted as the canonical partition function of single particle, i.e., Eq. (B1) with $K = 1$ and $N_1 = 1$. Therefore, we see that the total partition

function Z_{MN} of our carrier-cargo mixture can be perceived as sum over products of different partition functions: $\mathcal{Z}^{(L)}_{M-C,N-C,C}$ represents the external interactions and $\mathcal{Z}_1^{(\lambda_\bigcirc)}$ denotes the internal occupation statistics of a single CCC. By external interaction we generally mean the physical interactions between the particles excluding the possibility to engulf one another, which here is the hard-core repulsion of diameters $\sigma_\bigcirc$ and $\sigma_\bullet$. In other words, we have demonstrated that an occupied carrier represents a third species of size $\sigma_{\bigcirc\!\!\bullet} := \sigma_\bigcirc$ which additionally possesses internal degrees of freedom. We can therefore speak of an effective mixture of $A := M - C$ empty carriers, $B := N - C$ free cargo particles and C CCCs (occupied carriers).

Appendix D: Relation between fugacities and homogeneous number densities

In Eq. (8) we have derived the grand partition function for an effective ternary system representing the carrier-cargo mixture. To prepare for the effective treatment of more general mixtures, it is instructive to discuss an even simpler mapping. In fact, since empty carriers have the same length $\sigma_\bigcirc \equiv \sigma_{\bigcirc\!\!\bullet}$ as the corresponding CCCs, a two-species picture is sufficient if one is only interested in information contained in $\rho^{\mathrm{t}}_\bigcirc$. To see this, we recast Eq. (8) as

$$\Xi = \sum_{M=0}^{\infty}\sum_{B=0}^{\infty} \frac{(z_\bigcirc + z_{\bigcirc\!\!\bullet})^M z_\bullet^B}{M!B!} \left(L - M\sigma_\bigcirc - B\sigma_\bullet\right)^{(M+B)} \tag{D1}$$

by undoing the substitution $M \to A + C$ and rearranging the sums to obtain a binomial series. In such a two-species mixture, the carrier species (with no distinction of empty or occupied) can be interpreted to be coupled to a single effective particle reservoir with an enhanced fugacity $z^{\mathrm{t}}_\bigcirc := z_\bigcirc + z_{\bigcirc\!\!\bullet}$ also accounting for the internal degrees of freedom. Thus, Eq. (D1) illustrates the additivity $\rho^{\mathrm{t}}_\bigcirc = \rho_\bigcirc + \rho_{\bigcirc\!\!\bullet}$ of the effective densities in Eq. (11) directly by the additivity of the corresponding fugacities.

More generally, as long as the interactions $\sigma_\bigcirc = \sigma_{\bigcirc\!\!\bullet}$ between two (or more) species are the same, one finds the following scaling relation between densities and fugacities:

$$\frac{\rho^{\mathrm{t}}_\bigcirc}{z^{\mathrm{t}}_\bigcirc} = \frac{\rho_\bigcirc}{z_\bigcirc} = \frac{\rho_{\bigcirc\!\!\bullet}}{z_{\bigcirc\!\!\bullet}}\,. \tag{D2}$$

We thus see that the fraction $\rho_{\bigcirc\!\!\bullet}/\rho^{\mathrm{t}}_\bigcirc$ of CCCs (the number of carriers occupied by a cargo divided by the total number of carriers) can be determined solely from the corresponding fugacities for any interaction between the particles as $\rho_{\bigcirc\!\!\bullet}/\rho^{\mathrm{t}}_\bigcirc = z_{\bigcirc\!\!\bullet}/z^{\mathrm{t}}_\bigcirc$. To determine the CCC fraction as an explicit function of total carrier and cargo density, as, e.g., in Fig. 3, further calculations are necessary.

The above relations between (effective) fugacities and number densities become most apparent in an effective system without interactions, i.e., when setting $\sigma_\bigcirc = \sigma_\bullet = \sigma_{\bigcirc\!\!\bullet} = 0$. In this ideal case, indicated by the superscript (id), the homogeneous number densities $\rho^{(\mathrm{id})}_\bigcirc = z_\bigcirc$ and $\rho^{(\mathrm{id})}_{\bigcirc\!\!\bullet} = z_{\bigcirc\!\!\bullet}$ are explicitly given by the corresponding fugacities. Moreover, without (external) interactions, it is easy to see from either Eq. (8) or Eq. (D1) that the grand partition function can be explicitly written in the closed form

$$\Xi^{(\mathrm{id})} = e^{L(z_\bigcirc + z_\bullet + z_{\bigcirc\!\!\bullet})}\,. \tag{D3}$$

This result underlines that the combinatorics underlying the generic definition, Eq. (10), of the effective fugacity $z_{\bigcirc\!\!\bullet}$, is independent of the explicit interactions.

For practical reasons, considering two species with fugacities $z^{\mathrm{t}}_\bigcirc$ and $z_\bullet$ in Eq. (D1) is not very helpful, since the information on the distribution $\rho_{\bigcirc\!\!\bullet}$ of CCCs and thus also the total density $\rho^{\mathrm{t}}_\bullet$ of cargo particles is not available, as it requires knowing both $\rho_\bigcirc$ and $\rho^{\mathrm{t}}_\bigcirc$. As such, it is in general more appropriate to work with Eq. (8) and to distinguish between physically indistinguishable particles (empty carriers and CCCs) in our effective system. Then, $\rho^{\mathrm{t}}_\bullet$ can be determined from the auxiliary relation $\rho^{\mathrm{t}}_\bullet = \rho_\bullet + \rho_{\bigcirc\!\!\bullet}$ in Eq. (11). However, it is not possible to derive $\rho^{\mathrm{t}}_\bullet$ in the spirit of Eq. (D1), i.e., directly from the statistics underlying Ξ. This is because loaded cargo does not contribute to external interactions. In other words, the total packing fraction $\eta^{\mathrm{t}}_\bigcirc := \rho^{\mathrm{t}}_\bigcirc\sigma_\bigcirc = \rho_\bigcirc\sigma_\bigcirc + \rho_{\bigcirc\!\!\bullet}\sigma_\bigcirc$ of carriers is not affected by the number of CCCs and follows the addition law, Eq. (11), of number densities, while only the free cargo particles contribute to the total packing fraction $\eta^{\mathrm{t}}_\bullet := \rho_\bullet\sigma_\bullet \neq \rho^{\mathrm{t}}_\bullet\sigma_\bullet$.

Appendix E: Classical Density Functional Theory (DFT)

Here we provide a compact introduction to classical density functional theory (DFT) [43, 44], a powerful toolbox to determine the configuration and structure of interacting fluid mixtures. First, in Sec. E 1, we introduce the DFT framework for general inhomogeneous fluid mixtures and explain how to determine the homogeneous number densities in our effective description of carrier-cargo mixtures. Second, in Sec. E 2, we explain how to determine the effective pair distribution functions and from those recover the exact expressions for the physical carrier-cargo mixture in one spatial dimension.

1. Composition of a mixture from DFT

Consider in general a fluid mixture of K different components in the external one-body potentials $V^{(i)}_{\mathrm{ext}}(\mathbf{r})$ acting on the particles of species $i \in \{1, 2, \ldots, K\}$.

Then, the corresponding (inhomogeneous) number densities $\rho_i(\mathbf{r})$ in equilibrium can be obtained from solving the Euler-Lagrange equations

$$\frac{\delta\Omega[\{\rho_i\}]}{\delta\rho_i(\mathbf{r})} = 0\,, \tag{E1}$$

where $\Omega[\{\rho_i\}]$ is a density functional which becomes minimal when the equilibrium solutions are inserted. This minimal value of the functional corresponds to the grand potential $\beta\Omega = -\ln\Xi$ of the system. Hence, we can recover the grand-canonical partition functions Ξ calculated in the main text (or appropriate generalizations to arbitrary external fields). As a prerequisite, we need to know the proper functional.

The general form of the density functional reads

$$\Omega[\{\rho_i\}] = \Omega^{(\mathrm{id})}[\{\rho_i\}] + \mathcal{F}_{\mathrm{ex}}[\{\rho_i\}]\,, \tag{E2}$$

where the excess (over ideal gas) free energy $\mathcal{F}_{\mathrm{ex}}$ describes the interactions between the particles and the exactly known functional $\Omega^{(\mathrm{id})}$ for an ideal gas of point-like particles in an externally applied potential $V_{\mathrm{ext}}^{(i)}(\mathbf{r})$ reads

$$\beta\Omega^{(\mathrm{id})} = \sum_{i=1}^{K}\int \mathrm{d}\mathbf{r}\,\rho_i(\mathbf{r})\left(\ln\left(\frac{\rho_i(\mathbf{r}}{z_i}\right) - 1 + \beta V_{\mathrm{ext}}^{(i)}(\mathbf{r})\right) \tag{E3}$$

in d spatial dimensions, recalling the definitions $\beta = (k_{\mathrm{B}}T)^{-1}$ of the inverse temperature and $z_i := \exp(\beta\mu_i)/\Lambda^d$ of the fugacities.

For the hard-body interactions considered in this work, we employ fundamental measure theory (FMT) [48–50] for the excess free energy $\mathcal{F}_{\mathrm{ex}}$ which follows the same recipe in all spatial dimensions. Specifically, the FMT in one spatial dimension [45, 46], most commonly known as the Percus functional is exact. Here,

$$\beta\mathcal{F}_{\mathrm{ex}} = -\int \mathrm{d}x\, n_0(x)\ln(1-n_1(x)) \tag{E4}$$

follows as a function of the weighted densities

$$n_{0/1}(x) = \sum_{i=1}^{K}\int \mathrm{d}x_1\,\rho_i(x_1)\,\omega_i^{(0/1)}(x-x_1) \tag{E5}$$

which consist of convolution integrals of the densities and the weight functions

$$\begin{aligned}\omega_i^{(1)}(x) &= \Theta(\sigma_i/2-|x|)\,,\\ \omega_i^{(0)}(x) &= \frac{1}{2}(\delta(\sigma_i/2-x)+\delta(\sigma_i/2+x))\,,\end{aligned} \tag{E6}$$

where σ_i is the length of a hard rod of species i. These weight functions represent the geometry of particle i being local measures of the one-dimensional volume (rod length) and the surface area (characteristic function), respectively. In higher spatial dimensions, there exists a larger set of required weight functions.

For our calculations we consider homogeneous bulk systems with $V_{\mathrm{ext}}^{(i)}(\mathbf{r}) = 0$, such that the number densities ρ_i do not depend on the position $\mathbf{r}$. Then, the one-dimensional weighted densities simply read

$$n_0 = \sum_{i=1}^{K}\rho_i\,, \qquad n_1 = \sum_{i=1}^{K}\rho_i\sigma_i\,, \tag{E7}$$

such that the density functional $\Omega[\{\rho_i\}]$ turns into an explicit function of the number densities and the functional derivative in Eq. (E1) turns into a partial derivative. Thus, we only need to solve a set of algebraic equations to find the desired relation between the fugacities and densities. In one spatial dimension these are

$$\ln(\rho_i/z_i) = -\sum_{\nu=1}^{2}\frac{\partial\mathcal{F}_{\mathrm{ex}}}{\partial n_\nu}\frac{\partial n_\nu}{\partial\rho_i} = \ln(1-n_1) - \frac{n_0}{1-n_1}\sigma_i \tag{E8}$$

for $i = 1,\ldots,K$. In higher spatial dimensions, the structure is exactly the same but then the sum over ν must include the additional weighted densities.

To briefly connect to our previous statistical results, let us note that upon applying the variational scheme from Eq. (E1) to an ideal gas in an external field, with the functional from Eq. (E3), it is easy to show that the partition function reads

$$\Xi^{(\mathrm{id})} = \exp\left(\sum_{i=1}^{K}\left(\int \mathrm{d}\mathbf{r}\, e^{-\beta V_{\mathrm{ext}}^{(i)}(\mathbf{r})}\right) z_i\right)\,. \tag{E9}$$

In the absence of an external potential the integral must be replaced by the system volume $L^d = \int\mathrm{d}\mathbf{r}$. We have thus recovered Eq. (22) from our DFT formalism upon setting $K = k+\kappa$ and using the corresponding (effective) fugacities. Likewise, with interactions, we can also recover the exact result of Eq. (8) for the particular one-dimensional case, while the DFT calculation directly extends (in a good approximation) to higher spatial dimensions.

2. Structure of a mixture from DFT

Structural information on the system can be extracted from DFT by calculating functional derivatives of the excess free energy. In particular, the direct correlation functions $c_{ij}(r)$ of a fluid mixture with $i,j\in\{1,2,\ldots,K\}$ are defined as

$$c_{ij}(r=|\mathbf{r}_1-\mathbf{r}_2|) = -\frac{\delta^2\beta\mathcal{F}_{\mathrm{ex}}}{\delta\rho_i(\mathbf{r}_1)\delta\rho_j(\mathbf{r}_2)}\,. \tag{E10}$$

For a homogeneous system of hard rods, we find the exact direct correlation functions

$$c_{ij}(x) = -\frac{n_0}{(1-n_1)^2}\,W_{ij}^{(11)}(x) - \frac{1}{1-n_1}\,W_{ij}^{(10)}(x) \tag{E11}$$

from the Percus functional with the weighted densities given by Eq. (E7) and the functions

$$W_{ij}^{(11)}(x) = \min(\sigma_i,\sigma_j)\,\Theta(\Delta a - |x|) + (a_{ij} - |x|)\,\Theta(a_{ij} - |x|)\,\Theta(|x| - \Delta a)\,,$$
$$W_{ij}^{(10)}(x) = \Theta(a_{ij} - |x|)\,, \tag{E12}$$

where $a_{ij} := (\sigma_i + \sigma_j)/2$, $\Delta a := |\sigma_i - \sigma_j|/2$ and $\min(\sigma_i,\sigma_j)$ returns the smaller one of the two length. In general, $W_{ij}^{(\nu\mu)}$ can be calculated through convolution products of $\omega_i^{(\nu)}$ and $\omega_j^{(\mu)}$. Note that, if $i = j$, we have $\Delta a = 0$ and only the second term in $W_{ii}^{(11)}(x)$ is relevant.

Next, the pair distributions $g_{ij}(x) = h_{ij}(x) + 1$ can be calculated from the total correlation functions $h_{ij}(x)$, which are related to the direct correlation functions $c_{ij}(x)$ via the multicomponent Ornstein-Zernike equation

$$h_{ij}(x_1 - x_2) = c_{ij}(x_1 - x_2) + \sum_{l=1}^{K} \rho_l \int \mathrm{d}x_3\, c_{il}(x_1 - x_3)\, h_{lj}(x_3 - x_2)\,. \tag{E13}$$

The matrix solutions in Fourier space read

$$\hat{H}(q) = (\mathbf{1} - \hat{C}(q))^{-1} - \mathbf{1}\,, \tag{E14}$$

where the components of the auxiliary matrices $\hat{H}_{ij}(q) = \sqrt{\rho_i\rho_j}\hat{h}_{ij}(q)$ and $\hat{C}_{ij}(q) = \sqrt{\rho_i\rho_j}\hat{c}_{ij}(q)$ can be obtained by weighting the Fourier transforms $\hat{h}_{ij}(q)$ and $\hat{c}_{ij}(q)$ of $h_{ij}(x)$ and $c_{ij}(x)$, respectively, with the corresponding homogeneous densities. For hard rods in one dimension it is possible to determine an exact analytical solution of Eq. (E14) [47]. However, for simplicity, we perform the final inverse Fourier transform of $\hat{h}_{ij}(q)$ numerically.

Appendix F: Pair distributions for a one-dimensional carrier-cargo mixture

In this appendix, we provide further background on the relations, stated in Sec. II B 5, between the effective and physical pair distributions of the carrier-cargo mixture. For our minimal model of a carrier holding at most one cargo, the basic relation between the effective number densities, $\rho_{\bigcirc}$, $\rho_{\bullet}$ and $\rho_{\textcircled{\bullet}}$, and the total densities, $\rho_{\bigcirc}^{\mathrm{t}}$ and $\rho_{\bullet}^{\mathrm{t}}$, of the physical system is given by Eq. (11). For the pair distributions these relations are generally more involved since a CCC represents both carrier and cargo.

To determine the effective pair distributions $g_{ij}(x)$ with $i,j \in \{\bigcirc,\bullet,\textcircled{\bullet}\}$ for the mapped hard-rod system in one dimension and the pair distributions $g_{ij}^{\mathrm{t}}(x)$ with $i,j \in \{\bigcirc,\bullet\}$ for our physical carrier-cargo mixture, let us first recall from appendix E that the former follow directly from the exact direct correlation function, Eq. (E11), in the effective system. Moreover, following the structural equivalence of empty carriers and CCCs (both species have the same hard-core diameter $\sigma_{\bigcirc}$) we have

$$g_{\bigcirc\bigcirc} \equiv g_{\bigcirc\textcircled{\bullet}} \equiv g_{\textcircled{\bullet}\textcircled{\bullet}}\,. \tag{F1}$$

As a result, it is sufficient to determine the pair distribution for an effective binary mixture of hard rods with $\rho_{\bigcirc}^{\mathrm{t}} = \rho_{\bigcirc} + \rho_n$ and $\rho_{\bullet}$, as discussed in appendix D. For this reason, we apparently have $g_{\bigcirc\bigcirc}^{\mathrm{t}} = g_{\bigcirc\bigcirc}$ in Eq. (12). The remaining pair distributions of the physical system require additional care.

To understand the formulas in Sec. II B 5, we first point out that the relation, Eq. (11), between the one-body densities analogously applies to the two-body densities $\rho_i\rho_j g_{ij}$ and $\rho_i^{\mathrm{t}}\rho_j^{\mathrm{t}} g_{ij}^{\mathrm{t}}$. Solving for g_{ij}^{t} yields the basic structure of Eqs. (12) to (15) Specifically, $g_{\bigcirc\bigcirc}^{\mathrm{t}} = g_{\bigcirc\bigcirc}$, directly follows as

$$g_{\bigcirc\bigcirc}^{\mathrm{t}} = \frac{\rho_{\bigcirc}^2 g_{\bigcirc\bigcirc} + \rho_{\bigcirc}\rho_{\textcircled{\bullet}}(g_{\bigcirc\textcircled{\bullet}} + g_{\textcircled{\bullet}\bigcirc}) + \rho_{\textcircled{\bullet}}^2 g_{\textcircled{\bullet}\textcircled{\bullet}}}{(\rho_{\bigcirc}^{\mathrm{t}})^2}\,. \tag{F2}$$

Second, for the remaining pair distributions, we need to take into account the fact that the center of a cargo particle, which is contained in a CCC does not necessarily coincide with the center of the carrier but is uniformly distributed within the accessible space of length ℓ. Therefore, the effective distributions need to be blurred by calculating a convolution with the indicator function $\Theta(\ell/2 - |x|)$ in the corresponding coordinate(s). This is indicated by the superscript (b) in Eqs. (16) and (17). Third, specifically for the correlations between carrier and cargo particles in Eqs. (14) and (15), we need to manually account for the presence of a cargo particle within a carrier. This is achieved by redefining the effective two-body density $\rho_{\textcircled{\bullet}\textcircled{\bullet}}^{(2)}$ upon adding this self contribution (which for an ordinary fluid must be subtracted from the two-point correlation function to recover the two-body density). In practice, this amounts to setting $\rho_{\textcircled{\bullet}\textcircled{\bullet}}^{(2)}(x) \to \rho_{\textcircled{\bullet}\textcircled{\bullet}}^{(2)}(x) + \rho_{\textcircled{\bullet}}\delta(x)$, and then blurring the whole expression as described above. This yields the generalized contribution

$$G_{\textcircled{\bullet}\textcircled{\bullet}}^{(\mathrm{b})}(x_1 - x_2) := \frac{1}{\ell}\int \mathrm{d}x'\Theta(\ell/2 - |x_2 - x'|) \times \left(\rho_{\textcircled{\bullet}}^2 g_{\textcircled{\bullet}\textcircled{\bullet}}(|x_1 - x'|) + \rho_{\textcircled{\bullet}}\delta(x_1 - x')\right), \tag{F3}$$

which can be simplified to yield Eq. (18).

Appendix G: Mixtures with multiple carriers

The relations from Sec. II D can be easily generalized to describe mixtures involving cargo with fugacity $z_{\bullet}$ and now $\kappa - 1$ different carrier species with fugacities $z_{\bigcirc}^{[i]}$ for $i \in \{1,\ldots,\kappa-1\}$. In particular, introducing for each carrier the typical lengths $\ell^{[i]}$ entering in the $\ell_\nu^{[i]}$ (compare,

e.g., Eq. (35)), we can define as in Eq. (24) the effective fugacities $z_{\bullet\!\circ}^{[i,\nu]}$ of a CCC composed of one carrier of species i and exactly ν cargo. Thus, Eq. (29) generalizes to

$$z_{\bullet\!\circ}^{[i]} := \sum_{\nu=1}^{\infty} z_{\bullet\!\circ}^{[i,\nu]} = z_{\circ}^{[i]} \sum_{\nu=1}^{\infty} \left(\left(\ell_{\nu}^{[i]} \right)^{d} z_{\bullet} \right)^{\nu} . \tag{G1}$$

By accordingly rewriting Eqs. (27) and (28) as

$$\rho_{\bullet\!\circ}^{[i]} := \sum_{\nu=1}^{\infty} \rho_{\bullet\!\circ}^{[i,\nu]} , \quad \rho_{\circledast}^{[i]} := \sum_{\nu=1}^{\infty} \nu \rho_{\bullet\!\circ}^{[i,\nu]} \tag{G2}$$

for each carrier, we obtain from Eq. (23) the total number densities

$$\rho_{\circ}^{\mathrm{t}} = \sum_{i=1}^{\kappa-1} \rho_{\circ}^{([i],\mathrm{t})} , \tag{G3}$$

$$\rho_{\circ}^{([i],\mathrm{t})} = \rho_{\circ}^{[i]} + \rho_{\bullet\!\circ}^{[i]} , \tag{G4}$$

$$\rho_{\bullet}^{\mathrm{t}} = \rho_{\bullet} + \sum_{i=1}^{\kappa-1} \rho_{\circledast}^{[i]} . \tag{G5}$$

As an application, the results for the CCC fraction and loaded-carrier fraction of species i can be directly obtained for the respective occupation laws from Eqs. (37), (42) or (44) by simply introducing the superscript $[i]$ to $\ell \to \ell^{[i]}$ as a species label.

As a next step, let us consider the case $\kappa \to \infty$ of a polydisperse mixtures of carriers, whose engulfment strengths $\ell^{[i]} \to \ell$ are continuously distributed according to a normalized distribution $p(\ell)$, such that all sums

$$\sum_{i=1}^{\kappa-1} f^{[i]} \to \frac{1}{\ell^*} \int_0^{\ell^*} \mathrm{d}\ell \, f(\ell) \tag{G6}$$

turn into integrals and the superscript $[i]$ of a quantity $f^{[i]}$ turns into the argument ℓ of a function $f(\ell)$. By introducing the upper bound ℓ^* in Eq. (G6) we imply that the distribution $p(\ell > \ell^*) = 0$ vanishes beyond a maximal size ℓ^* to prevent a collapse towards (uncontrolled) infinite occupation for $\ell \to \infty$. Specifically, let us prescribe the function $p(\ell)$ such that the total number density $\rho_{\circ}^{\mathrm{t}}(\ell) = \bar{\rho}_{\circ}^{\mathrm{t}} p(\ell)$ of each carrier with engulfment strengths ℓ is a specified input quantity. Then we can recast Eq. (G3) in the continuous form

$$\bar{\rho}_{\circ}^{\mathrm{t}} = \frac{1}{\ell^*} \int_0^{\ell^*} \mathrm{d}\ell \, \rho_{\circ}^{\mathrm{t}}(\ell) = \frac{\bar{\rho}_{\circ}^{\mathrm{t}}}{\ell^*} \int_0^{\ell^*} \mathrm{d}\ell \, p(\ell) , \tag{G7}$$

where we chose the notation $\bar{\rho}_{\circ}^{\mathrm{t}}$ for the total number density of all carriers to indicate that it is an average of $\rho_{\circ}^{\mathrm{t}}(\ell)$. Moreover, Eq. (G5) becomes

$$\rho_{\bullet}^{\mathrm{t}} = \rho_{\bullet} + \frac{1}{\ell^*} \int_0^{\ell^*} \mathrm{d}\ell \, \rho_{\circledast}(\ell) \tag{G8}$$

in the polydisperse continuum.

[1] A. F. Thünemann, Prog. Polym. Sci. **27**, 1473 (2002).
[2] I. W. Hamley and V. Castelletto, Angew. Chem. Int. Ed. **46**, 4442 (2007).
[3] N. Vogel, M. Retsch, C.-A. Fustin, A. Del Campo, and U. Jonas, Chem. Rev. **115**, 6265 (2015).
[4] J. Yan, M. Han, J. Zhang, C. Xu, E. Luijten, and S. Granick, Nat. Mater **15**, 1095 (2016).
[5] J. Harder and A. Cacciuto, Phys. Rev. E **97**, 022603 (2018).
[6] H. Massana-Cid, D. Levis, R. J. H. Hernández, I. Pagonabarraga, and P. Tierno, Phys. Rev. Res. **3**, L042021 (2021).
[7] J. Wan, B. Fan, K. Putera, J. Kim, M. M. Banaszak Holl, and S. H. Thang, ACS nano **15**, 13721 (2021).
[8] A. Aubret, Q. Martinet, and J. Palacci, Nat. Commun. **12**, 6398 (2021).
[9] S. van Kesteren, X. Shen, M. Aldeghi, and L. Isa, Advanced Materials p. 2207101 (2023).
[10] B. V. Hokmabad, A. Nishide, P. Ramesh, C. Krüger, and C. C. Maass, Soft Matter **18**, 2731 (2022).
[11] N. Giri, M. G. Del Pópolo, G. Melaugh, R. L. Greenaway, K. Rätzke, T. Koschine, L. Pison, M. F. C. Gomes, A. I. Cooper, and S. L. James, Nature **527**, 216 (2015).
[12] J. Avila, L. F. Lepre, C. C. Santini, M. Tiano, S. Denis-Quanquin, K. Chung Szeto, A. A. Padua, and M. Costa Gomes, Angew. Chem. **133**, 12986 (2021).
[13] M. Karimi, H. Mirshekari, M. Aliakbari, P. Sahandi-Zangabad, and M. R. Hamblin, Nanotechnol. Rev. **5**, 195 (2016).
[14] X. Bo, Q. Zhang, X. Li, and Y. Zhao, J. Solgel. Sci. Technol. **93**, 324 (2020).
[15] X. Ma, H. Feng, C. Liang, X. Liu, F. Zeng, and Y. Wang, J. Mater. Sci. Technol. **33**, 1067 (2017).
[16] Y. Alapan, O. Yasa, O. Schauer, J. Giltinan, A. F. Tabak, V. Sourjik, and M. Sitti, Sci. Robot. **3**, eaar4423 (2018).
[17] Q. Sun, J.-F. Chen, and A. F. Routh, Expert. Opin. Drug. Deliv. **16**, 903 (2019).
[18] S. L. Perry and D. J. McClements, Molecules **25**, 1161 (2020).
[19] F. Madani, S. Lindberg, Ü. Langel, S. Futaki, and A. Gräslund, J. Biophys. **2011** (2011).
[20] N. Ma, C. Ma, C. Li, T. Wang, Y. Tang, H. Wang, X. Mou, Z. Chen, and N. He, J. Nanosci. Nanotechnol. **13**, 6485 (2013).
[21] S. Tan, T. Wu, D. Zhang, and Z. Zhang, Theranostics **5**, 863 (2015).
[22] E. R. Abels and X. O. Breakefield, Cell. Mol. Neurobiol. **36**, 301 (2016).
[23] Y. Mulla, A. Aufderhorst-Roberts, and G. H. Koenderink, Phys. Biol. **15**, 041001 (2018).
[24] J. Steinkühler, R. L. Knorr, Z. Zhao, T. Bhatia, S. M. Bartelt, S. Wegner, R. Dimova, and R. Lipowsky, Nat.

Commun. **11**, 905 (2020).
[25] S. Ashraf, A. Hassan Said, R. Hartmann, M.-A. Assmann, N. Feliu, P. Lenz, and W. J. Parak, Angew. Chem. Int. Ed. **59**, 5438 (2020).
[26] M. Clarke and L. Maddera, Eur. J. Cell Biol. **85**, 1001 (2006).
[27] S. H. Kaufmann and A. Dorhoi, Immunity **44**, 476 (2016).
[28] Y.-S. Cho, G.-R. Yi, J.-M. Lim, S.-H. Kim, V. N. Manoharan, D. J. Pine, and S.-M. Yang, J. Am. Chem. Soc. **127**, 15968 (2005).
[29] D. Zwicker, R. Seyboldt, C. A. Weber, A. A. Hyman, and F. Jülicher, Nat. Phys. **13**, 408 (2017).
[30] D. Zwicker, J. Baumgart, S. Redemann, T. Müller-Reichert, A. A. Hyman, and F. Jülicher, Phys. Rev. Lett. **121**, 158102 (2018).
[31] J. Grauer, F. Schmidt, J. Pineda, B. Midtvedt, H. Löwen, G. Volpe, and B. Liebchen, Nat. Commun. **12**, 6005 (2021).
[32] M. Paoluzzi, R. Di Leonardo, M. C. Marchetti, and L. Angelani, Sci. Rep. **6**, 1 (2016).
[33] H. R. Vutukuri, M. Hoore, C. Abaurrea-Velasco, L. van Buren, A. Dutto, T. Auth, D. A. Fedosov, G. Gompper, and J. Vermant, Nature **586**, 52 (2020).
[34] M. S. Peterson, A. Baskaran, and M. F. Hagan, Nat. Commun. **12**, 7247 (2021).
[35] V. Willems, A. Baron, G. Wolfisberg, E. Dufresne, and L. Alvarez, Active motion and division of phase separated soft biocomparments, in preparation.
[36] G. Kunti, Y. Wu, and G. Yossifon, Small **17**, 2007819 (2021).
[37] J. Palacci, S. Sacanna, A. Vatchinsky, P. M. Chaikin, and D. J. Pine, J. Am. Chem. Soc. **135**, 15978 (2013).
[38] Z. Rozynek and A. Józefczak, Eur. Phys. J.: Spec. Top. **225**, 741 (2016).
[39] F. Schmidt, B. Liebchen, H. Löwen, and G. Volpe, J. Chem. Phys. **150**, 094905 (2019).
[40] M. R. Evans, Europhysics Letters **36**, 13 (1996).
[41] F. Meng, D. Matsunaga, B. Mahault, and R. Golestanian, Phys. Rev. Lett. **126**, 078001 (2021).
[42] M. te Vrugt, T. Frohoff-Hülsmann, E. Heifetz, U. Thiele, and R. Wittkowski, arXiv preprint arXiv:2204.03018 (2022).
[43] J.-P. Hansen and I. R. McDonald, *Theory of simple liquids: with applications to soft matter* (Academic press, 2013).
[44] R. Evans, Adv. Phys. **28**, 143 (1979).
[45] J. Percus, J. Stat. Phys. **15**, 505 (1976).
[46] T. Vanderlick, H. Davis, and J. Percus, Chem. Phys. **91**, 7136 (1989).
[47] A. Santos, Phys. Rev. E **76**, 062201 (2007).
[48] H. Hansen-Goos and R. Roth, J. Condens. Matter Phys. **18**, 8413 (2006).
[49] R. Roth, J. Phys. Condens. Matter **22**, 063102 (2010).
[50] R. Roth, K. Mecke, and M. Oettel, J. Chem. Phys. **136**, 081101 (2012).
[51] K. Huang, *Introduction to statistical physics* (Chapman and Hall/CRC, 2009).
[52] S. Sacanna, M. Korpics, K. Rodriguez, L. Colón-Meléndez, S.-H. Kim, D. J. Pine, and G.-R. Yi, Nat. Commun. **4**, 1688 (2013).
[53] S. Sacanna, W. T. Irvine, P. M. Chaikin, and D. J. Pine, Nature **464**, 575 (2010).
[54] S. Sacanna, W. T. Irvine, L. Rossi, and D. J. Pine, Soft Matter **7**, 1631 (2011).
[55] Y. Wang, Y. Wang, X. Zheng, G.-R. Yi, S. Sacanna, D. J. Pine, and M. Weck, J. Am. Chem. Soc. **136**, 6866 (2014).
[56] M. Kamp, N. A. Elbers, T. Troppenz, A. Imhof, M. Dijkstra, R. Van Roij, and A. Van Blaaderen, Chem. Mater. **28**, 1040 (2016).
[57] Y. Wang, Y. Wang, D. R. Breed, V. N. Manoharan, L. Feng, A. D. Hollingsworth, M. Weck, and D. J. Pine, Nature **491**, 51 (2012).
[58] F. Li, D. P. Josephson, and A. Stein, Angew. Chem. Int. Ed. **50**, 360 (2011).
[59] E. Duguet, A. Désert, A. Perro, and S. Ravaine, Chem. Soc. Rev. **40**, 941 (2011).
[60] F. Kogler, O. D. Velev, C. K. Hall, and S. H. Klapp, Soft Matter **11**, 7356 (2015).
[61] H. Löwen, EPL **121**, 58001 (2018).
[62] E. S. Harper, G. van Anders, and S. C. Glotzer, Proc. Natl. Acad. Sci. **116**, 16703 (2019).
[63] Y. Martínez-Ratón and E. Velasco, Phys. Rev. E **104**, 054132 (2021).
[64] Y. Martínez-Ratón and E. Velasco, Phys. Fluids **34**, 037110 (2022).
[65] R. Wittmann, M. Marechal, and K. Mecke, J. Phys. Condens. Matter **28**, 244003 (2016).
[66] R. Wittmann, C. E. Sitta, F. Smallenburg, and H. Löwen, J. Chem. Phys. **147**, 134908 (2017).
[67] J. F. Lutsko, J. Condens. Matter Phys. **28**, 244020 (2016).
[68] A. Moncho-Jordá, A. B. Jódar-Reyes, M. Kanduč, A. Germán-Bellod, J. M. López-Romero, R. Contreras-Cáceres, F. Sarabia, M. García-Castro, H. A. Pérez-Ramírez, and G. Odriozola, ACS nano **14**, 15227 (2020).
[69] U. M. B. Marconi and P. Tarazona, J. Chem. Phys. **110**, 8032 (1999).
[70] A. J. Archer and R. Evans, J. Chem. Phys. **121**, 4246 (2004).
[71] M. te Vrugt, H. Löwen, and R. Wittkowski, Adv. Phys. **69**, 121 (2020).
[72] M. Popescu, M. Tasinkevych, and S. Dietrich, EPL **95**, 28004 (2011).
[73] L. Baraban, M. Tasinkevych, M. N. Popescu, S. Sanchez, S. Dietrich, and O. Schmidt, Soft Matter **8**, 48 (2012).
[74] H. D. Vuijk, H. Merlitz, M. Lang, A. Sharma, and J.-U. Sommer, Phys. Rev. Lett. **126**, 208102 (2021).
[75] P. L. Muzzeddu, É. Roldán, A. Gambassi, and A. Sharma, arXiv preprint arXiv:2302.08954 (2023).
[76] F. Martinez-Pedrero, A. Ortiz-Ambriz, I. Pagonabarraga, and P. Tierno, Phys. Rev. Lett. **115**, 138301 (2015).
[77] R. Niu, A. Fischer, T. Palberg, and T. Speck, ACS nano **12**, 10932 (2018).
[78] L. Alvarez, M. A. Fernandez-Rodriguez, A. Alegria, S. Arrese-Igor, K. Zhao, M. Kröger, and L. Isa, Nat. Commun. **12**, 4762 (2021).
[79] M. Odziomek, T. R. Sosnowski, and L. Gradoń, Int. J. Pharm. **433**, 51 (2012).
[80] T.-Y. Huang, H. Gu, and B. J. Nelson, Annu. Rev. Control Robot. Auton. Syst. **5**, 279 (2022).
[81] N. Metropolis, A. W. Rosenbluth, M. N. Rosenbluth, A. H. Teller, and E. Teller, J. Chem. Phys. **21**, 1087 (1953).

Chapter 4

Concluding remarks

The first publication **P1** *Topology of Orientational Defects in Confined Smectic Liquid Crystals* [20] aims to classify the previously little explored facet of defects in the orientation field of smectic liquid crystals. Those defects, which, as previously known, typically take the shape of extended grain boundaries in two dimensions, can be classified by a half integer index, that describes the rotation of local fluid particles around the whole defect. We found, that the fine structures of those defect lines, can be further resolved by considering it as an ensemble of point defects sitting at the respective nodes of the line. This comes, in particular, as a result of the properties of the smectic phase instead of the topological theory.

The second publication **P2** *Topological fine structure of smectic grain boundaries and tetratic disclination lines within three-dimensional smectic liquid crystals* [21] elevates the concept of the previous publication into the third dimension. The grain boundaries, which are lines in two dimensions, now take the shape of planes in three dimensions. We show that the fine structure of the planar grain boundary is still characterised by its topological boundary, i.e., lines wrapping around the surfaces. To this end, we introduce the concept of tetratic order in three dimensions, along with an appropriate order parameter. In three dimensions, where the topological charge is not in general a conserved quantity, the rigidity of the smectic phase, yet again, compliments the topological theory, by granting charge conservation via stacked quasi two-dimensional layers.

In the third publication **P3** *Smectic structures in button-like confinements: experiment and theory* [143] we study the influence of complicated confinements on the overall topology of the smectic structure. As a defining feature of this work, we bring four complementary approaches, experiment, density functional theory, Q-tensor theory and simulation together, and show that they display the same structural properties of the confined state. In particular, we show that the smectic layers in individual snapshots display a non-trivial symmetry breaking via a preferred angle to the confinements.

In the fourth publication **P4** *Network topology of interlocked chiral particles* [144], we utilise the conception of a smectic layer topology, which involves considering networks of smectic layers. We employ this network-topological model to the

analysis of more complicated chiral particles of the shape of the letter L. This is done, by constructing networks from the positions of both arms of the particles. We find, that the aspect ratio of the particles, is intricately connected to the topology of the emerging networks.

These studies of extended smectic defects show, how assumed symmetry of the system relates to the dimensionality of the defects. For instance: in 3d, planar nematic grain boundaries are wrapped by tetratic line defects on its rim. This invites further studies on, for instance, more complicated particles, with different symmetries than rods, where the material properties may be influenced differently by the underlying topological theory. It is known, how the topological charges characterise the dynamics of point defects within active nematic [79–81] and active smectic systems [85]. This seems to propose, that tetratic point charges, as introduced in our particle-resolved works, also bear certain dynamical properties. A future study may be of interest. The network topological model, as presented in **P4** may yield fruitful insight.

The fifth publication **P5** *Active particles using reinforcement learning to navigate in complex motility landscapes* [145] explores reinforcement learning models for microswimmers, whose target is to navigate complex environments in a preferably quick manner. This work's findings can be applied to the understanding of intelligent behaviour in biological life on microscopic length scales, and thus can be used in the engineering of microscopic technical components. Future endeavours may build upon this model to investigate more elaborate biological mechanisms, such as for instance the behaviour of bacteria in search of nutrition, with the explicit consideration of, e.g., a cell cycle [146, 147].

Finally, in the sixth publication **P6** *Statistics of carrier-cargo complexes* [148], we explore a statistical model for mixtures of colloidal particles, where one type is capable of engulfing the other to form a complex, which is a fairly common mechanism, e.g., in vesicles, which take up materials within their membrane (endocytosis) [149]. We find that the formation of complexes is largely steered by the respective densities of both components and show, that the microscopic structure of the system can be predicted from the model. We argue, that this work is relevant for predictive methods in medicine, which revolve around endocytic processes [150, 151]. This work may also stimulate research in the engineering of artificial functional carriers, and the various types of occupation laws may be appropriate to describe out-of-equilibrium phenomena such as engulfment and subsequent digestion.

Bibliography

[1] C. J. Hernandez and T. G. Mason, *Colloidal alphabet soup: Monodisperse dispersions of shape-designed lithoparticles*, J. Phys. Chem. C **111**, 4477 (2007).

[2] C. P. Lapointe, T. G. Mason, and I. I. Smalyukh, *Shape-controlled colloidal interactions in nematic liquid crystals*, Science **326**, 1083 (2009).

[3] C. Avendaño, G. Jackson, E. A. Müller, and F. A. Escobedo, *Assembly of porous smectic structures formed from interlocking high-symmetry planar nanorings*, PNAS **113**, 9699 (2016).

[4] M. Allen, G. Evans, D. Frenkel, and B. Mulder, *Hard convex body fluids*, Adv. Chem. Phys. **86**, 1 (1993).

[5] L. Onsager, *The effects of shape on the interaction of colloidal particles*, Ann. N. Y. Acad. Sci. **51**, 627 (1949).

[6] M. V. Kurik and O. Lavrentovich, *Defects in liquid crystals: homotopy theory and experimental studies*, Phys.-Uspekhi **31**, 196 (1988).

[7] O. D. Lavrentovich, *Phase transition altering the symmetry of topological point defects (hedgehogs) in a nematic liquid crystal*, Zh. Eksp. Teor. Fiz. **91**, 2084 (1986).

[8] O. D. Lavrentovich, *Topological defects in dispersed words and worlds around liquid crystals, or liquid crystal drops*, Liq. Cryst. **24**, 117 (1998).

[9] I. C. Gârlea, O. Dammone, J. Alvarado, V. Notenboom, Y. Jia, G. H. Koenderink, D. G. A. L. Aarts, M. P. Lettinga, and B. M. Mulder, *Colloidal liquid crystals confined to synthetic tactoids*, Sci. Rep. **9**, 1 (2019).

[10] G. Friedel, *Les états mésomorphes de la matière*, Ann. Phys. **18**, 273 (1922).

[11] M. A. Bates and D. Frenkel, *Phase behavior of two-dimensional hard rod fluids*, J. Chem. Phys. **112**, 10034 (2000).

[12] R. Wittmann, M. Marechal, and K. Mecke, *Fundamental measure theory for non-spherical hard particles: predicting liquid crystal properties from the particle shape*, J. Phys. Condens. Matter **28**, 244003 (2016).

[13] R. Wittmann, C. E. Sitta, F. Smallenburg, and H. Löwen, *Phase diagram of two-dimensional hard rods from fundamental mixed measure density functional theory*, J. Chem. Phys. **147**, 134908 (2017).

[14] R. Wittmann, M. Marechal, and K. Mecke, *Fundamental measure theory for smectic phases: Scaling behavior and higher order terms*, J. Chem. Phys. **141**, 064103 (2014).

[15] R. Wittmann, M. Marechal, and K. Mecke, *Elasticity of nematic phases with fundamental measure theory*, Phys. Rev. E **91**, 052501 (2015).

[16] G. Babakhanova, T. Turiv, Y. Guo, M. Hendrikx, Q.-H. Wei, A. P. Schenning, D. J. Broer, and O. D. Lavrentovich, *Liquid crystal elastomer coatings with programmed response of surface profile*, Nat. Commun. **9**, 456 (2018).

[17] D. Liu and D. J. Broer, *New insights into photoactivated volume generation boost surface morphing in liquid crystal coatings*, Nat. Commun. **6**, 8334 (2015).

[18] M. Schadt, *Liquid crystal materials and liquid crystal displays*, Annu. Rev. Mater. Sci. **27**, 305 (1997).

[19] B. Bahadur, *Liquid crystal displays*, Mol. Cryst. Liq. Cryst. **109**, 3 (1984).

[20] P. A. Monderkamp, R. Wittmann, L. B. G. Cortes, D. G. A. L. Aarts, F. Smallenburg, and H. Löwen, *Topology of orientational defects in confined smectic liquid crystals*, Phys. Rev. Lett. **127**, 198001 (2021).

[21] P. A. Monderkamp, R. Wittmann, M. Te Vrugt, A. Voigt, R. Wittkowski, and H. Löwen, *Topological fine structure of smectic grain boundaries and tetratic disclination lines within three-dimensional smectic liquid crystals*, PCCP **24**, 15691 (2022).

[22] T. Geigenfeind, S. Rosenzweig, M. Schmidt, and D. de las Heras, *Confinement of two-dimensional rods in slit pores and square cavities*, J. Chem. Phys. **142**, 174701 (2015).

[23] Y. Martínez-Ratón, J. A. Capitán, and J. A. Cuesta, *Fundamental-measure density functional for mixtures of parallel hard cylinders*, Phys. Rev. E **77**, 051205 (2008).

[24] H. Hansen-Goos and K. Mecke, *Fundamental measure theory for inhomogeneous fluids of nonspherical hard particles*, Phys. Rev. Lett. **102**, 018302 (2009).

[25] M. Ravnik and S. Žumer, *Landau–de gennes modelling of nematic liquid crystal colloids*, Liq. Cryst. **36**, 1201 (2009).

[26] A. Majumdar and A. Lewis, *Multistable nematic wells: modelling perspectives, recent results and new directions*, Liq. Cryst. **43**, 2332 (2016).

[27] G. P. Crawford and S. Zumer, *Liquid crystals in complex geometries: formed by polymer and porous networks* (CRC Press, Boca Raton, Florida, United States, 1996).

[28] T. Ohzono and J.-i. Fukuda, *Transition of frustrated nematic order and fluctuation of topological defects in microwrinkle grooves*, Soft Matter **8**, 11552 (2012).

[29] Y. Reznikov, O. Ostroverkhova, K. D. Singer, J.-H. Kim, S. Kumar, O. Lavrentovich, B. Wang, and J. L. West, *Photoalignment of liquid crystals by liquid crystals*, Phys. Rev. Lett. **84**, 1930 (2000).

[30] Y. Gu and N. L. Abbott, *Observation of Saturn-Ring Defects around Solid Microspheres in Nematic Liquid Crystals*, Phys. Rev. Lett. **85**, 4719 (2000).

[31] H. Stark, *Saturn-ring defects around microspheres suspended in nematic liquid crystals: An analogy between confined geometries and magnetic fields*, Phys. Rev. E **66**, 032701 (2002).

[32] P. E. Cladis, W. van Saarloos, P. L. Finn, and A. R. Kortan, *Dynamics of line defects in nematic liquid crystals*, Phys. Rev. Lett. **58**, 222 (1987).

[33] D. R. Link, J. E. Maclennan, and N. A. Clark, *Simultaneous observation of electric field coupling to longitudinal and transverse ferroelectricity in a chiral liquid crystal*, Phys. Rev. Lett. **77**, 2237 (1996).

[34] L. B. G. Cortes, Y. Gao, R. P. A. Dullens, and D. G. A. L. Aarts, *Colloidal liquid crystals in square confinement: isotropic, nematic and smectic phases*, J. Phys. Condens. Matter **29**, 064003 (2017).

[35] O. J. Dammone, I. Zacharoudiou, R. P. A. Dullens, J. M. Yeomans, M. P. Lettinga, and D. G. A. L. Aarts, *Confinement induced splay-to-bend transition of colloidal rods*, Phys. Rev. Lett. **109**, 108303 (2012).

[36] O. V. Manyuhina, K. B. Lawlor, M. C. Marchetti, and M. J. Bowick, *Viral nematics in confined geometries*, Soft Matter **11**, 6099 (2015).

[37] J. Dzubiella, M. Schmidt, and H. Löwen, *Topological defects in nematic droplets of hard spherocylinders*, Phys. Rev. E **62**, 5081 (2000).

[38] Y. Trukhina and T. Schilling, *Computer simulation study of a liquid crystal confined to a spherical cavity*, Phys. Rev. E **77**, 011701 (2008).

[39] S. Varga, Y. Martínez-Ratón, and E. Velasco, *Hard rods in a cylindrical pore: the nematic-to-smectic phase transition*, J. Phys. Condens. Matter **26**, 075104 (2014).

[40] P. E. Brumby, H. H. Wensink, A. J. Haslam, and G. Jackson, *Structure and interfacial tension of a hard-rod fluid in planar confinement*, Langmuir **33**, 11754 (2017).

[41] E. Basurto, P. Gurin, S. Varga, and G. Odriozola, *Ordering, clustering, and wetting of hard rods in extreme confinement*, Phys. Rev. Research **2**, 013356 (2020).

[42] K. H. Kil, A. Yethiraj, and J. S. Kim, *Nematic ordering of hard rods under strong confinement in a dense array of nanoposts*, Phys. Rev. E **101**, 032705 (2020).

[43] A. H. Lewis, I. Garlea, J. Alvarado, O. J. Dammone, P. D. Howell, A. Majumdar, B. M. Mulder, M. Lettinga, G. H. Koenderink, and D. G. A. L. Aarts, *Colloidal liquid crystals in rectangular confinement: theory and experiment*, Soft Matter **10**, 7865 (2014).

[44] C. E. Sitta, F. Smallenburg, R. Wittkowski, and H. Löwen, *Liquid crystals of hard rectangles on flat and cylindrical manifolds*, Phys. Chem. Chem. Phys. **20**, 5285 (2018).

[45] E. Allahyarov, A. Voigt, and H. Löwen, *Smectic monolayer confined on a sphere: topology at the particle scale*, Soft Matter **13**, 8120 (2017).

[46] P. Poulin, V. Cabuil, and D. A. Weitz, *Direct Measurement of Colloidal Forces in an Anisotropic Solvent*, Phys. Rev. Lett. **79**, 4862 (1997).

[47] R. W. Ruhwandl and E. M. Terentjev, *Monte carlo simulation of topological defects in the nematic liquid crystal matrix around a spherical colloid particle*, Phys. Rev. E **56**, 5561 (1997).

[48] D. Andrienko, G. Germano, and M. P. Allen, *Computer simulation of topological defects around a colloidal particle or droplet dispersed in a nematic host*, Phys. Rev. E **63**, 041701 (2001).

[49] S. Čopar, T. Porenta, V. S. R. Jampani, I. Muševič, and S. Žumer, *Stability and rewiring of nematic braids in chiral nematic colloids*, Soft Matter **8**, 8595 (2012).

[50] J. M. Ilnytskyi, A. Trokhymchuk, and M. Schoen, *Topological defects around a spherical nanoparticle in nematic liquid crystal: Coarse-grained molecular dynamics simulations*, J. Chem. Phys. **141**, 114903 (2014).

[51] S. Püschel-Schlotthauer, V. Meiwes Turrión, C. K. Hall, M. G. Mazza, and M. Schoen, *The impact of colloidal surface-anchoring on the smectic a phase*, Langmuir **33**, 2222 (2017).

[52] K. Chen, O. J. Gebhardt, R. Devendra, G. Drazer, R. D. Kamien, D. H. Reich, and R. L. Leheny, *Colloidal transport within nematic liquid crystals with arrays of obstacles*, Soft Matter **14**, 83 (2018).

[53] I. C. Gârlea, P. Mulder, J. Alvarado, O. J. Dammone, D. G. A. L. Aarts, M. P. Lettinga, G. H. Koenderink, and B. M. Mulder, *Finite particle size drives defect-mediated domain structures in strongly confined colloidal liquid crystals*, Nat. Commun. **7**, 12112 (2016).

[54] R. Wittmann, L. B. G. Cortes, H. Löwen, and D. G. A. L. Aarts, *Particle-resolved topological defects of smectic colloidal liquid crystals in extreme confinement*, Nat. Commun. **12**, 623 (2021).

[55] X. Yao and J. Z. Y. Chen, *Rodlike molecules in extreme confinement*, Phys. Rev. E **101**, 062706 (2020).

[56] X. Yao, H. Zhang, and J. Z. Chen, *Topological defects in two-dimensional liquid crystals confined by a box*, Phys. Rev. E **97**, 052707 (2018).

[57] X. Yao, L. Zhang, and J. Z. Y. Chen, *Defect patterns of two-dimensional nematic liquid crystals in confinement*, Phys. Rev. E **105**, 044704 (2022).

[58] C. Wagner, *Theorie der geordneten mischphasen. ii.*, Z. Phys. Chem. **1931**, 177 (1931).

[59] A. K. Cheetham, T. D. Bennett, F.-X. Coudert, and A. L. Goodwin, *Defects and disorder in metal organic frameworks*, Dalton Trans. **45**, 4113 (2016).

[60] B. Wu, Z. Pan, D. Ding, D. Cuiuri, H. Li, J. Xu, and J. Norrish, *A review of the wire arc additive manufacturing of metals: properties, defects and quality improvement*, J. Manuf. Process. **35**, 127 (2018).

[61] M. Kleman and O. D. Lavrentovich, *Soft Matter Physics - An Introduction* (Springer, New York, NY, 2003).

[62] N. D. Mermin, *The topological theory of defects in ordered media*, Rev. Mod. Phys. **51**, 591 (1979).

[63] G. P. Alexander, B. G.-g. Chen, E. A. Matsumoto, and R. D. Kamien, *Colloquium: Disclination loops, point defects, and all that in nematic liquid crystals*, Rev. Mod. Phys. **84**, 497 (2012).

[64] O. D. Lavrentovich, *Topological defects in dispersed words and worlds around liquid crystals, or liquid crystal drops*, Liq. Cryst. **24**, 117 (1998).

[65] Y.-K. Kim, S. V. Shiyanovskii, and O. D. Lavrentovich, *Morphogenesis of defects and tactoids during isotropic nematic phase transition in self-assembled lyotropic chromonic liquid crystals*, J. Condens. Matter Phys. **25**, 404202 (2013).

[66] M. Kléman, *Defects in liquid crystals*, Rep. Prog. Phys. **52**, 555 (1989).

[67] R. B. Meyer, B. Stebler, and S. T. Lagerwall, *Observation of Edge Dislocations in Smectic Liquid Crystals*, Phys. Rev. Lett. **41**, 1393 (1978).

[68] P. Chen and C.-Y. D. Lu, *Smectic Edge Dislocations under Shear*, JPSJ **80**, 094802 (2011).

[69] C. Zhang, A. M. Grubb, A. J. Seed, P. Sampson, A. Jákli, and O. D. Lavrentovich, *Nanostructure of Edge Dislocations in a Smectic-C* Liquid Crystal*, Phys. Rev. Lett. **115**, 087801 (2015).

[70] R. D. Kamien and R. A. Mosna, *The topology of dislocations in smectic liquid crystals*, New J. Phys. **18**, 053012 (2016).

[71] B. G.-g. Chen, G. P. Alexander, and R. D. Kamien, *Symmetry breaking in smectics and surface models of their singularities*, Proc. Natl. Acad. Sci. U.S.A. **106**, 15577 (2009).

[72] O. V. Yazyev and S. G. Louie, *Topological defects in graphene: Dislocations and grain boundaries*, Phys. Rev. B **81**, 195420 (2010).

[73] J. P. Bramble, S. D. Evans, J. R. Henderson, T. J. Atherton, and N. J. Smith, *Observations of focal conic domains in smectic liquid crystals aligned on patterned self-assembled monolayers*, Liq. Cryst. **34**, 1137 (2007).

[74] Y. H. Kim, D. K. Yoon, M.-C. Choi, H. S. Jeong, M. W. Kim, O. D. Lavrentovich, and H.-T. Jung, *Confined self-assembly of toric focal conic domains (the effects of confined geometry on the feature size of toric focal conic domains)*, Langmuir **25**, 1685 (2009).

[75] D. B. Liarte, M. Bierbaum, R. A. Mosna, R. D. Kamien, and J. P. Sethna, *Weirdest martensite: Smectic liquid crystal microstructure and weyl-poincaré invariance*, Phys. Rev. Lett. **116**, 147802 (2016).

[76] M. Kléman and O. Lavrentovich, *Grain boundaries and the law of corresponding cones in smectics*, Eur. Phys. J. E **2**, 47 (2000).

[77] H. Yokoyama, *Surface anchoring of nematic liquid crystals*, Mol. Cryst. Liq. Cryst. **165**, 265 (1988).

[78] Y. Sato, K. S. K. Sato, and T. U. T. Uchida, *Relationship between rubbing strength and surface anchoring of nematic liquid crystal*, JJAP **31**, L579 (1992).

[79] G. Tóth, C. Denniston, and J. M. Yeomans, *Hydrodynamics of Topological Defects in Nematic Liquid Crystals*, Phys. Rev. Lett. **88**, 105504 (2002).

[80] C. D. Muzny and N. A. Clark, *Direct observation of the Brownian motion of a liquid-crystal topological defect*, Phys. Rev. Lett. **68**, 804 (1992).

[81] S. J. DeCamp, G. S. Redner, A. Baskaran, M. F. Hagan, and Z. Dogic, *Orientational order of motile defects in active nematics*, Nat. Mater. **14**, 1110 (2015).

[82] A. Díaz-De Armas, M. Maza-Cuello, Y. Martínez-Ratón, and E. Velasco, *Domain walls in vertically vibrated monolayers of cylinders confined in annuli*, Phys. Rev. Research **2**, 033436 (2020).

[83] M. González-Pinto, F. Borondo, Y. Martínez-Ratón, and E. Velasco, *Clustering in vibrated monolayers of granular rods*, Soft Matter **13**, 2571 (2017).

[84] V. Narayan, N. Menon, and S. Ramaswamy, *Nonequilibrium steady states in a vibrated-rod monolayer: tetratic, nematic, and smectic correlations*, J. Stat. Mech. **2006**, 01005 (2006).

[85] Z.-F. Huang, H. Löwen, and A. Voigt, *Defect dynamics in active smectics induced by confining geometry and topology*, Commun. Phys. **5**, 294 (2022).

[86] T. Machon, H. Aharoni, Y. Hu, and R. D. Kamien, *Aspects of defect topology in smectic liquid crystals*, Commun. Math. Phys. **372**, 525 (2019).

[87] H. Aharoni, T. Machon, and R. D. Kamien, *Composite dislocations in smectic liquid crystals*, Phys. Rev. Lett. **118**, 257801 (2017).

[88] D. A. Beller, T. Machon, S. Čopar, D. M. Sussman, G. P. Alexander, R. D. Kamien, and R. A. Mosna, *Geometry of the cholesteric phase*, Phys. Rev. X **4**, 031050 (2014).

[89] B. J. Hocking, H. S. Ansell, R. D. Kamien, and T. Machon, *The topological origin of the peierls–nabarro barrier*, Proc. R. Soc. **478**, 20210725 (2022).

[90] R. Arnheim, *Entropy and art: An essay on disorder and order* (Univ of California Press, 1971).

[91] K. G. Denbigh, *Note on entropy, disorder and disorganization*, BJPS **40**, 323 (1989).

[92] D. Frenkel, *Order through entropy*, Nat. Mater **14**, 9 (2015).

[93] G. J. Vroege and H. N. Lekkerkerker, *Phase transitions in lyotropic colloidal and polymer liquid crystals*, Rep. Prog. Phys. **55**, 1241 (1992).

[94] V. N. Manoharan, *Colloidal matter: Packing, geometry, and entropy*, Science **349**, 1253751 (2015).

[95] T. Fließbach, *Statistische Physik: Lehrbuch zur Theoretischen Physik IV* (Springer-Verlag, 2018).

[96] C. J. Geyer, *Practical markov chain monte carlo*, Stat. Sci. (1992).

[97] S. Brooks, *Markov chain monte carlo method and its application*, J R Stat Soc Ser A Stat Soc **47**, 69 (1998).

[98] A. Van De Walle and M. Asta, *Self-driven lattice-model monte carlo simulations of alloy thermodynamic properties and phase diagrams*, Model Simul Mat Sci Eng **10**, 521 (2002).

[99] J. W. Gibbs, *Elementary principles in statistical mechanics: developed with especial reference to the rational foundations of thermodynamics* (Charles Scribner's Sons, 1902).

[100] P. Ehrenfest, *Phase transitions in the normal and generalized sense classified according to the singularities of the thermodynamic functions*, Proc. K. Ned. Akad. Wet. **36**, 10 (1933).

[101] W. Nolting, *Grundkurs Theoretische Physik 6: Statistische Physik* (Springer-Verlag, 2013).

[102] L. Boltzmann, *Lectures on gas theory* (Courier Corporation, 2012).

[103] N. Metropolis, *The beginning*, Los Alamos Sci **15**, 125 (1987).

[104] D. P. Kroese, T. Brereton, T. Taimre, and Z. I. Botev, *Why the monte carlo method is so important today*, Wiley Interdiscip. Rev. Comput. Stat. **6**, 386 (2014).

[105] R. Dufo-López, E. Pérez-Cebollada, J. L. Bernal-Agustín, and I. Martínez-Ruiz, *Optimisation of energy supply at off-grid healthcare facilities using monte carlo simulation*, Energy Convers. Manag. **113**, 321 (2016).

[106] D. Silver, A. Huang, C. J. Maddison, A. Guez, L. Sifre, G. Van Den Driessche, J. Schrittwieser, I. Antonoglou, V. Panneershelvam, M. Lanctot, et al., *Mastering the game of go with deep neural networks and tree search*, Nature **529**, 484 (2016).

[107] D. Silver, J. Schrittwieser, K. Simonyan, I. Antonoglou, A. Huang, A. Guez, T. Hubert, L. Baker, M. Lai, A. Bolton, et al., *Mastering the game of go without human knowledge*, Nature **550**, 354 (2017).

[108] G. Tesauro and G. Galperin, *On-line policy improvement using monte-carlo search*, Adv Neural Inf Process Syst **9**, (1996).

[109] D. L. McLeish, *Monte Carlo simulation and finance* (John Wiley & Sons, 2011).

[110] P. Jäckel, *Monte Carlo methods in finance* (J. Wiley, 2002).

[111] N. Metropolis, A. W. Rosenbluth, M. N. Rosenbluth, A. H. Teller, and E. Teller, *Equation of state calculations by fast computing machines*, J. Chem. Phys. **21**, 1087 (1953).

[112] N. Metropolis and S. Ulam, *The monte carlo method*, J. Am. Stat. Assoc. **44**, 335 (1949).

[113] N. Metropolis, A. W. Rosenbluth, M. N. Rosenbluth, A. H. Teller, and E. Teller, *Equation of State Calculations by Fast Computing Machines*, J. Chem. Phys. **21**, 1087 (1953).

[114] M. P. Allen and D. J. Tildesley, *Computer simulation of liquids* (Oxford university press, 2017).

[115] G. Hummer, *Fast-growth thermodynamic integration: Error and efficiency analysis*, J. Chem. Phys. **114**, 7330 (2001).

[116] M. J. Mitchell and J. A. McCammon, *Free energy difference calculations by thermodynamic integration: difficulties in obtaining a precise value*, J. Comput. Chem. **12**, 271 (1991).

[117] H. C. Andersen, D. Chandler, and J. D. Weeks, *Roles of Repulsive and Attractive Forces in Liquids: The Optimized Random Phase Approximation*, J. Chem. Phys. **56**, 3812 (1972).

[118] C. Bechinger, R. Di Leonardo, H. Löwen, C. Reichhardt, G. Volpe, and G. Volpe, *Active particles in complex and crowded environments*, Rev. Mod. Phys. **88**, 045006 (2016).

[119] M. R. Shaebani, A. Wysocki, R. G. Winkler, G. Gompper, and H. Rieger, *Computational models for active matter*, Nat. Rev. Phys. **2**, 181 (2020).

[120] M. C. Marchetti, J.-F. Joanny, S. Ramaswamy, T. B. Liverpool, J. Prost, M. Rao, and R. A. Simha, *Hydrodynamics of soft active matter*, Rev. Mod. Phys. **85**, 1143 (2013).

[121] J. Elgeti, R. G. Winkler, and G. Gompper, *Physics of microswimmers—single particle motion and collective behavior: a review*, Rep. Prog. Phys. **78**, 056601 (2015).

[122] M. E. Cates and J. Tailleur, *Motility-induced phase separation*, Annu. Rev. Condens. Matter Phys. **6**, 219 (2015).

[123] L. Caprini, U. M. B. Marconi, and A. Puglisi, *Spontaneous velocity alignment in motility-induced phase separation*, Phys. Rev. Lett. **124**, 078001 (2020).

[124] L. Caprini and H. Löwen, *Flocking without alignment interactions in attractive active brownian particles*, arXiv:2303.07746 (2023).

[125] Y. Zhang and R. Zhao, *Overall thermal sensation, acceptability and comfort*, Build. Environ. **43**, 44 (2008).

[126] M. Schweiker, X. Fuchs, S. Becker, M. Shukuya, M. Dovjak, M. Hawighorst, and J. Kolarik, *Challenging the assumptions for thermal sensation scales*, Build. Res. Inf. **45**, 572 (2017).

[127] H. Löwen, *Inertial effects of self-propelled particles: From active brownian to active langevin motion*, J. Chem. Phys. **152**, 040901 (2020).

[128] M. Z. Miskin, A. J. Cortese, K. Dorsey, E. P. Esposito, M. F. Reynolds, Q. Liu, M. Cao, D. A. Muller, P. L. McEuen, and I. Cohen, *Electronically integrated, mass-manufactured, microscopic robots*, Nature **584**, 557 (2020).

[129] P. Langevin, *Sur la théorie du mouvement brownien*, C. R. Acad. Sci. **146**, 530 (1908).

[130] H. Risken and H. Risken, *Fokker-planck equation* (Springer, 1996).

[131] X. Ma, K. Hahn, and S. Sanchez, *Catalytic mesoporous janus nanomotors for active cargo delivery*, J. Am. Chem. Soc. **137**, 4976 (2015).

[132] A. F. Demirörs, M. T. Akan, E. Poloni, and A. R. Studart, *Active cargo transport with janus colloidal shuttles using electric and magnetic fields*, Soft Matter **14**, 4741 (2018).

[133] D. Patra, S. Sengupta, W. Duan, H. Zhang, R. Pavlick, and A. Sen, *Intelligent, self-powered, drug delivery systems*, Nanoscale **5**, 1273 (2013).

[134] B. J. Nelson, I. K. Kaliakatsos, and J. J. Abbott, *Microrobots for minimally invasive medicine*, Annu. Rev. Biomed. Eng. **12**, 55 (2010).

[135] M. You, C. Chen, L. Xu, F. Mou, and J. Guan, *Intelligent micro/nanomotors with taxis*, Acc. Chem. Res. **51**, 3006 (2018).

[136] V. Balakrishnan, *Elements of nonequilibrium statistical mechanics* (Springer, 2008).

[137] M. Campbell, A. J. Hoane Jr, and F.-h. Hsu, *Deep blue*, Artif. Intell. **134**, 57 (2002).

[138] P. H. Winston, *Artificial intelligence* (Addison-Wesley Longman Publishing Co., Inc., 1984).

[139] M. A. Boden, *Artificial intelligence* (Elsevier, 1996).

[140] B. Mahesh, *Machine learning algorithms-a review*, IJSR **9**, 381 (2020).

[141] R. S. Sutton and A. G. Barto, *Reinforcement learning: An introduction* (MIT press, 2018).

[142] A. Nandy and M. Biswas, *Reinforcement learning: with open AI, tensorflow and keras using python* (Apress, 2017).

[143] R. Wittmann, P. A. Monderkamp, J. Xia, L. B. Cortes, I. Grobas, P. E. Farrell, D. G. Aarts, and H. Löwen, *Smectic structures in button-like confinements: experiment and theory*, arXiv:2303.01425 (2023).

[144] P. A. Monderkamp, R. S. Windisch, R. Wittmann, and H. Löwen, *Network topology of interlocked chiral particles*, arXiv:2301.09541 (2023).

[145] P. A. Monderkamp, F. J. Schwarzendahl, M. A. Klatt, and H. Löwen, *Active particles using reinforcement learning to navigate in complex motility landscapes*, MLST **3**, 045024 (2022).

[146] D. Breoni, F. J. Schwarzendahl, R. Blossey, and H. Löwen, *A one-dimensional three-state run-and-tumble model with a 'cell cycle'*, EPJ E **45**, 83 (2022).

[147] K. Qu, F. Guo, X. Liu, Y. Lin, and Q. Zou, *Application of machine learning in microbiology*, Front Microbiol **10**, 827 (2019).

[148] R. Wittmann, P. A. Monderkamp, and H. Löwen, *Statistics of carrier-cargo complexes*, arXiv:2303.04005 (2023).

[149] A. Morshed, B. I. Karawdeniya, Y. N. D. Bandara, M. J. Kim, and P. Dutta, *Mechanical characterization of vesicles and cells: A review*, J. Electrophor. **41**, 449 (2020).

[150] J. E. Ziello, Y. Huang, and I. S. Jovin, *Cellular endocytosis and gene delivery*, J. Mol. Med. **16**, 222 (2010).

[151] A. Akinc and G. Battaglia, *Exploiting endocytosis for nanomedicines*, Cold Spring Harb. Perspect. Biol. **5**, a016980 (2013).